THERMAL MODELLING AND OPTIMISATION OF A HIGH TEMPERATURE BLACKBODY RADIATOR

by

Khaled Chahine

B.E. (UTS), Post Grad. Dip. in Quality & Metrology (SUT)

CERTIFICATE OF AUTHORSHIP/ORIGINALITY

I certify that the work in this thesis has not previously been submitted for a degree nor has it been submitted as part of requirements for a degree except as fully acknowledge within the text.

I also certify that the thesis has been written by me. Any help that I have received in my research work and the preparation of the thesis itself has been acknowledged. In addition, I certify that all information sources and literature used are indicated in the thesis.

Signature of Candidate

_____

ABSTRACT

Blackbody radiators, or graphite tube furnaces, are commonly used in the calibration of pyrometers for temperature range up to 3 000 °C. These radiators are usually constructed from graphite cylindrical shaped cavities insulated by graphite felt or similar materials. The calibration uncertainties associated with one of these radiators, a 48 kW Thermogage furnace, are 1 °C at 1 000 °C and a wavelength of 650 nm rising to 2 °C at 2 000 °C. These uncertainties are mainly due to deviations of the blackbody emissivity from 100%. The emissivity has been calculated to be 99.2% at a temperature of 1 000 °C and a wavelength of 650 nm, increasing to 99.9% in some cases.

To improve this Thermogage furnace's temperature calibration uncertainty to the level required, the emissivity must be increased to 99.9% over the full temperature range. This can be achieved by improving the temperature uniformity of its cavity inner walls. Therefore, the aim of this work is to achieve this emissivity increase by optimising the temperature uniformity of the blackbody furnace graphite tube.

A quasi 2-D numerical model has been developed to predict the temperature profile of the Thermogage furnace's tube. This has been used to optimise the temperature uniformity based on input parameters such as the thermophysical properties of ATJ graphite and WDF graphite felt. These thermophysical properties have been thoroughly investigated and implemented into the quasi 2-D numerical model.

The numerical predictions generated have been validated by comparing them to the measured temperature profile and radial heat fluxes of the graphite tube. Once an agreement has been achieved between the measured and the modelled results, the quasi 2-D numerical model has been used to generate numerical predictions of the temperature profile based on design methodologies that include changing the cross sectional area and the length of the graphite tube as well as using different insulating gases.

With a new tube design, a better temperature uniformity has been achieved and thus improvement in the cavity emissivity resulting into temperature uncertainty of better than 0.02 °C for operating temperatures from 1 000 to 1 600 °C and at a wavelength of 650 nm.

ACKNOWLEDGMENTS

TABLE OF CONTENTS

LIST OF TABLES

LIST OF FIGURES

NOMENCLATURE

Roman Symbols		**First Occurrence**
a	Radius of an electrical wire	72
A	Area of the blackbody cavity hole	11
	Area of a disk	77
A_{A4}	Area of an A4 sized paper	194
A_{amb}	Area of the ATJ graphite tube's opening to the ambient	77
A_c	Cross sectional area	98
$A_{contact}$	Fibre-to-fibre contact area	34
A_{felt}	Area of a piece of a WDF graphite felt	194
A_g	Cross sectional area of a gap between two surfaces	123
A_i	Area at node i	87
A_j	Area at node j	87
A_{septum}	Area of the ATJ graphite tube's middle septum	77
A_{ring}	Surface area of a ring inside the ATJ graphite tube	98
A_{Silica}	Cross sectional area of the silica tube	124
A_{TC}	Cross sectional area of the Pt/Pt-Rh thermocouple wires	70
A_{WJ}	Cross sectional of the water jacket	127
c_0	Speed of light in vacuum	2
	Polynomial coefficient	32
c_1	Polynomial coefficient	32
c_2, c_3, c_4, c_5	Polynomial coefficients or used as constants	32
C	Constant used in the measurement of the thermal conductivity of WDF graphite felt	40
C_1	First radiation constant	3
C_2	Second radiation constant	3
C_{fr}	Experimentally determined radiation constant	39
c_I	Sinusoidal current sensitivity factor	110
$c_{k_{ATJ}}$	ATJ graphite thermal conductivity sensitivity factor	111
c_{M_i}	Radiant exitance at node i sensitivity factor	89
c_{M_j}	Radiant exitance at node j sensitivity factor	89
c_{M_w}	Middle septum radiant exitance sensitivity factor	89

Greek Symbols

μ_{TC}	Defined constant by Carslaw & Jaeger (1959)	69
v_g	Kinematic viscosity of air	31
v_1	Volume fraction of air	29
v_2	Volume fraction of fibre	29
ξ_{cond}	Distance offset – solution to the transmission line matrix	96
π	Pi	3
ρ_{ATJ}	Density of ATJ grade graphite	64
ρ_{felt}	Density of WDF graphite felt	194
$\rho_{water_{15°C}}$	Density of water at 15 °C	99
σ	Stefan-Boltzmann constant	38
σ_a	Absorption coefficient	38
σ_e	Extinction coefficient	38
σ_s	Diffusion coefficient	38
τ	Graphite fibre tortuosity	35
χ	Attenuation	98
υ_f	Frequency of graphite fibre crossing from one layer to another	35
ς	Schuhmeister first constant	29
ψ	Schuhmeister second constant	29
ω_{ATJ}	Electrical resistivity of ATJ graphite	58

Subscripts

amb	Ambient
ATJ	ATJ grade graphite
BB	Ideal blackbody surface
PSF	Perfectly stratified felt
rad	Radiation
radial	Radial direction
Real	Real blackbody surface
WJ	Water Jacket

Abbreviations

1-D	1-dimensional

2-D	2-dimensional
3-D	Three-dimensional
AC	Alternating current
AGA	Graphite material grade
AGOT	Graphite material grade
AGSR	Graphite material grade
AGSX	Graphite material grade
Ar	Argon gas
ATJ	Graphite material grade
ATL	Graphite material grade
CC	Carbon-composite
EXCEL	Microsoft EXCEL program
He	Helium gas
IKE	Institut für Kernenergetik, Universität Stuttgart
MTSP	Medium temperature standard pyrometer
N_2	Nitrogen gas
NMIA	National Measurement Institute, Australia
NMIJ	National Measurement Institute of Japan
USA	United States of America
VNIIOFI	All-Russian Research Institute for Optical and Physical Measurements
WDF	Graphite felt grade

1 INTRODUCTION & BACKGROUND

1.1 Introduction to Blackbody Emulators

Almost eve ry proc ess in n ature is tem perature depen dent so th at tem perature measurement is an essential tool for many fields such as m edicine, industry, metrology and science. For non-contact tem perature measurem ent applications, particularly those exceeding 1 000 °C, ra diation therm ometers or pyrom eters are commonly used. Applications in w hich pyrom eters are us ed vary fro m situations in which objects are in m otion to others in which conventional contact type thermometers cannot be used due to dam age that might be caused to the article whose temperature is to be m easured, o r b ecause the high tem perature of the objec t m ight result in damage to, or even melting of, the measuring device.

Pyrometers sense the radiant flux from an item and generate an output signal which, through a calibration algorithm , provides a m easure of the tem perature of the object (DeWitt & Nutter, 1988). Such instruments need to be appropriately calibrated in such a way as to ensure that their accuracy is adequate and that th e equipment used in the calibration can be easily "traced" to reference physical standards, thereby allowing the use of an algorithm relating the radiant flux m easurement to a tem perature output, as well as en abling the evaluation of the uncer tainties as sociated with their us e. Blackbodies are comm only used as reference standards in the calibration of radiation thermometers or pyrometers.

Blackbodies can be used for a very wide te mperature range from -40 °C or below in cryogenic applications to 20 000 °C for ra diometric applications. Many types of blackbody simulators have been developed over the last century to deal with this wide temperature range; to present all of them is beyond the scope of this thesis. Since excellent pyrom eter calibration facilities for temperatures below 1 000 °C already exist whereas facilities for tem peratures betw een 1 000 and 3 000 °C have m uch higher m easurement uncertainties, the disc ussion herein will be res tricted to blackbody radiators which operate in the 1 000 to 3 000 °C temperature range.

As m entioned above, the device employed in the calibration of pyrom eters is a blackbody whose surface is m aintained at a fi xed temperature with an em issivity of unity. Hence, two questions arise: what is a blackbody and what is surface emissivity?

Gustav Kirchhoff in 1859 first proposed the concept of a blackbody radiator and subsequently m any workers during the late 19 [th] centu ry and early 20 [th] centu ry attempted to explain the radiati on which such a body generated (Dewitt & Nutter, 1988). Kirchhoff suggested blackbodies as being ideal, or im agined, objects that abso rb all in cident rays so tha t they neithe r ref lect nor transm it any radiation. Then in 1879, Joseph Stephan found experim entally that the emissive power of such a radiator is proportional to the fourth power of its absolute tem perature (Siegel 2002, p.27), thereby laying the foundati on of radiation heat transfer. This relation was also derived by Ludwig Ed ward Boltzm ann in 1884 by analysing a Carnot cycle in which radiation pressure wa s assum ed to act as the p ressure of the working fluid (Siegel 2002, p.27). In 1891, W ien showed that the spectral em issive power of a blackbody is inversely proportional to the fifth power of the wavelength; a relationship now called "W ien Displacement Law". W ien's formula, however, could not be extended to the e missive power at short wavelengths and high tem peratures (Barr 1960). The Rayleigh-Jeans formula, de veloped by Lord Rayl eigh and Sir James Jeans in early 1900, has utility only for l ong-wave radiation such as radio waves (Siegel 2002, p.27). Sim ilar to W ien's for mula, it could not be extended to the full spectrum of temperatures and wavelengths of blackbodies.

In 1901, Planck combined the works of Wien and Rayleigh-Jeans to better explain the spectral emissivity of blac kbodies for all wavelengths and tem peratures. On the assumption that energy is quan tised, Planck sho wed that the spectral rad iance or the total intensity, I, emitted by a b lackbody is, as w as already known, a function of the wavelength, λ, and temperature T. That is: $I = I_{\lambda,b}(\lambda,T)$. More importantly he was able to show that the spectral radiance is given by (Dewitt & Nutter 1988, p. 41):

$$I_{\lambda,b}\left(\lambda,T\right) = \frac{2hc_0^2}{\lambda^5[e^{hc_o/\lambda kT} - 1]},$$
(1.1)

in which, $h = 6.6256 \times 10^{-34}$ J·s and $k = 1.3805 \times 10^{-23}$ J·K^{-1} are the universal Planck and Boltzmann constants respectively, $c_0 = 2.998 \times 10^8$ m·s^{-1} is the speed of light in vacuo, and T is the absolute temperature of the blackbody.

Unlike previous attempts, equation (1.1) applies at all temperatures and frequencies. The idea that energy is quantised has been used to develop quantum mechanics, which as well as being one of the cornerstones of modern physics has led to significant developments in technology that unfortunately are outside the scope of this thesis.

Equation (1.1) can be used to evaluate the spectral hemispherical emissive power $E_{\lambda,b}(\lambda,T)_{BB}$, which is defined as the rate at which radiative flux of wavelength λ is emitted in all directions per unit length from a surface. It is given as (Incropera 1996, pp 640):

$$E_{\lambda,b}\left(\lambda,T\right)_{BB} = \pi I_{\lambda,b}\left(\lambda,T\right). \ (1.2)$$

Here, π is the solid angle of a hemisphere in steradians.

The substitution of equation (1.1) in equation (1.2) gives,

$$E_{\lambda,b}\left(\lambda,T\right)_{BB} = \frac{C_1}{\lambda^5\left[e^{C_2/\lambda T} - 1\right]}, \ (1.3)$$

in which, the first and second radiation constants C_1 and C_2, are $C_1 = 2\pi h c_0^2 = 3.742 \times 10^8$ W·μm^4·m^{-2} and $C_2 = hc_o/k = 1.439 \times 10^4$ μm·K respectively. As may be seen in Figure 1.1, equation (1.3) can be used to generate the well known spectral radiance distribution of blackbodies at different temperatures.
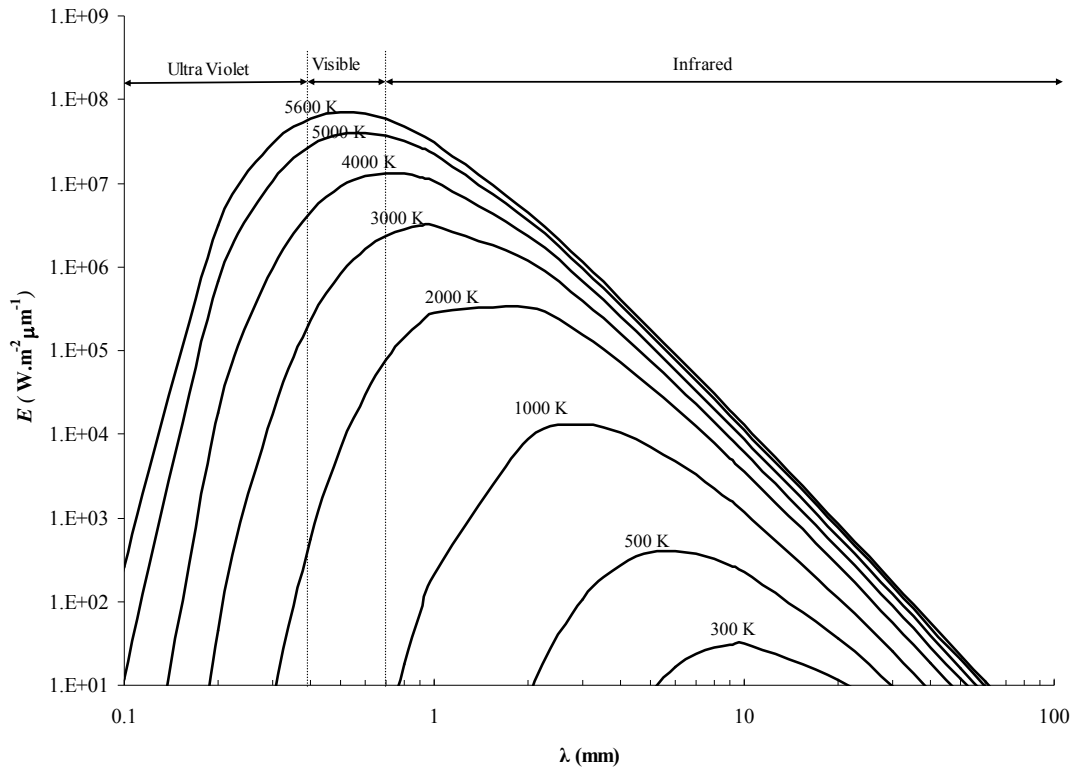
Figure 1.1. Spectral radiance of a perfect blackbody at different temperatures– Plank's Distribution.

Equations (1.1) and (1.3) are valid for a   perfect blackbody. Unfortunately, perfect blackbodies cannot be physically realised and do not exist naturally (Bartell 1989), so that an ob ject m aintained at a fixed tem   perature em its les s energy th an a perfect blackbody and therefore does not reproduce the distributions shown in Figure 1.1. An example of the difference between a real and an ideal blackbody spectral radiance at a temperature of 2 000 K is presented in Figure 1.2.
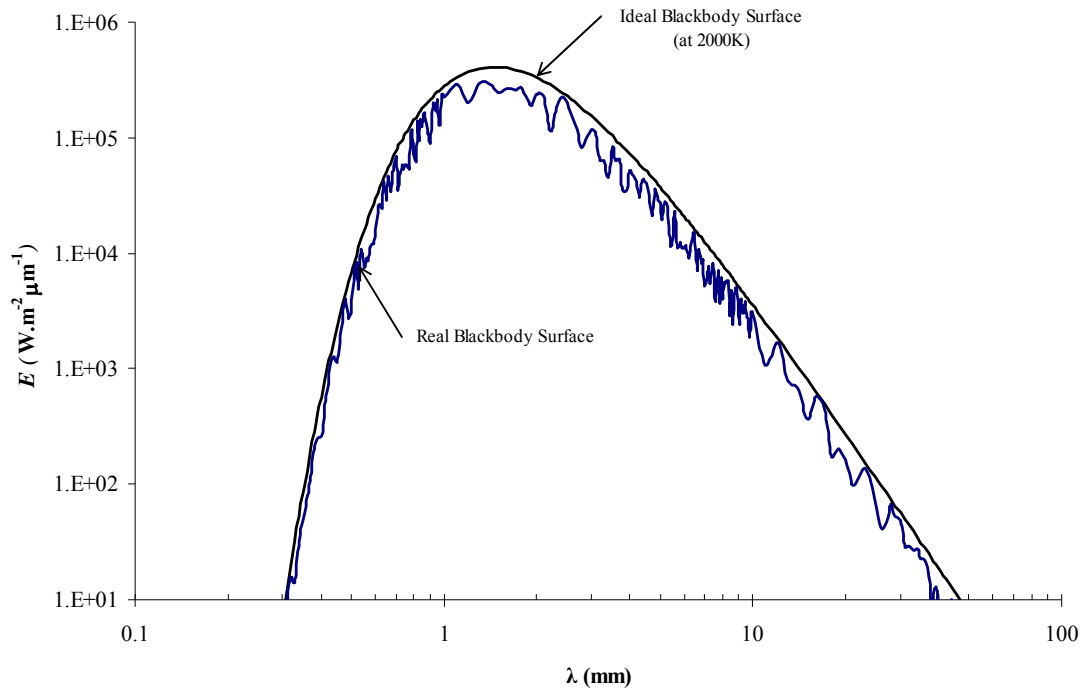
Figure 1.2. Plots of the spectral radiance *E* of an ideal and a real blackbody surfaces at a temperature of 2000 K as a function of the wavelength λ.

Similarly to the "efficiency" asso ciated with en gine performance, the em issivity is a measure of the ability of an object or surf ace to absorb and em it radiation. Th e spectral em issive power of a r eal body is usually written as (Dewitt & Nutter 1988, p.53):

$$E_{\lambda,b}(\lambda,T)_{Real} = \varepsilon(\lambda)E_{\lambda,b}(\lambda,T)_{BB} , (1.4)$$

in which, $E_{\lambda,b}(\lambda,T)_{Real}$ is the sp ectral emissive power for a real b lackbody, $E_{\lambda,b}(\lambda,T)_{BB}$ is the spectral em issive pow er for a perfect blackbody, and $\varepsilon(\lambda)$ is th e em issivity which is generally a function of the wavelength.

In order to achieve hig h accuracy in the ca libration of pyrom eters, the em issivity of the blackbody surface used needs to be as close as possible to unity at all frequencies.

The relation between the error in evaluating absolute temperature of a blackbody and its emissivity is given by Ballico (1998) as:

$$\frac{\Delta T}{T} = \frac{\lambda T}{C_2} \frac{\Delta \varepsilon}{\varepsilon}, \quad (1.5)$$

in which, $\Delta T/T$ is the relative temperature error caused by the relative change in the emissivity, $\Delta \varepsilon/\varepsilon$. Thus, for a blackbody surface at 2 000 K a 10% error in the emissivity at a wavelength of 0.85 μm, which is a common wavelength for pyrometers, yields 1.2 % error in the absolute temperature or 24 K. Since a measurement uncertainty of less than 1 K is needed, the relative error in the emissivity must be less than 0.4%, that is the blackbody emissivity must be greater than 99.6%, or 0.996.

Since perfect blackbodies do not exist, blackbody emulators have been developed for applications such as radiometric and pyrometric standards. A discussion of all of the different types of emulators which have been or are being used is certainly beyond the scope of this thesis. However, a survey of the current literature has led the present author to the conclusion that the most useful types of blackbody emulators for the calibration of pyrometers and radiometers which deal with temperatures up to 20 000 K are plasma arcs, lamps and graphite furnaces. Detailed descriptions and discussion of the advantages and disadvantages of each type are presented below.

1.1.1 Plasma Arcs

Plasma arcs are used as standards for spectral radiance. A schematic diagram of a plasma arc emulator is shown in Figure 1.3. Typically, the two electrodes are separated by a distance of few millimetres with the space between them filled with a gas. Plasma arcs form when a high voltage is applied between the electrodes. Once a current begins to flow the gas temperature rises to the point that ionisation occurs, leading to the resistance between the electrodes dropping and a very high current flowing between the electrodes. Currents as high as 40 A at a voltage of 800 V are

commonly encountered. This high energy release leads to high temperature generation in the re latively sm all volum e of gas in th e glass cas e. Arcs can be p roduced with almost any gas, however, the m ost common gas used is hydrogen. Hydrogen arcs are sometimes used in the realisation of standards for the violet and ultra violet spectrum . Their operating tem peratures can reach 20 000 K. The tem perature m easurement uncertainty of a hydrogen arc is ar ound 5% (Hattenburg 1967, Bridges 1977 and Key 1977).
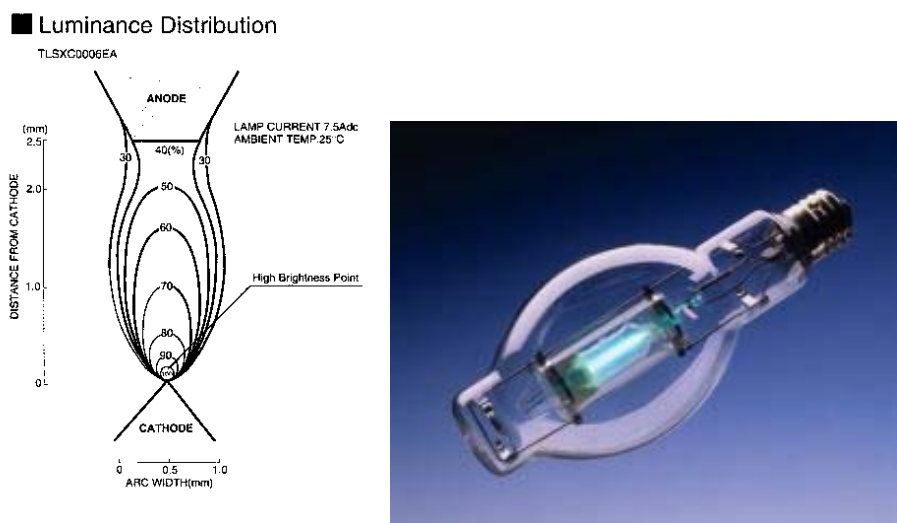
Figure 1.3. Schematic diagram and a picture of a plasma arc emulator.

Plasma arcs are cheap to operate, ho wever they are very un stable which results in th e high uncertainty m entioned above. Furtherm ore, the effective em issivity of such arcs changes as they continuously alter their sh ape, leading to a constant variance in emissivity of the in tervening media. Also, arcs can only op erate over a sm all part of the thermal radiation spectru m. Plasm a arcs are no longe r widely used as blackbody radiation sources in precision measurements.

1.1.2 Lamps

Lamps are broad-band light sources which are used as standards for pyrom etry and radiometry. There are a few types of lam ps, each type operating at different spectral ranges and tem peratures. Some lamps are used as standards in pyrom etry, others as spectral radiance and irradiance standards in radiometry and photometry.

Figure 1.4. Tungsten Strip Lamp.

Tungsten type lam ps operate in the visible and near infrared ranges. As shown in Figure 1.4, the lam p consists of a strip of tun gsten m aterial encas ed in glass. An electric current is passed thr ough the strip causing it to glow at a certain tem perature. The temperature versus current relationship is very stable and it is therefore read ily reproducible. The temperature range varies from 800°C to 1 700°C when the filament is operated in vacuo, and 1 300°C to 2 300°C when the lamp is filled with argon or any other inert gas. The gas is introduced to s low down the transp iration rate of the tungsten. Tungsten lamps are used as sec ondary standards in phot oelectric pyrometry (Jones 1971). The typical tem perature uncertainty of this type of lam p is around 2 K (McEvoy 96).

Quartz Tungsten Halogen (QTH) la mps also operate in the visibl e and near infrared range. Their operating tem perature is around 3 300 K. The em issivity of QTH la mps is around 0.4. This type of lamp is mainly used for photometry where the emissivity is not required to be known very accurately. The lamp (FEL model) shown in Figure 1.5 is a QTH lamp used as an irradiance spectral standard.

Figure 1.5. FEL lamp used as irradiance spectral standard.

Lamps are inexpensive and have long term stability. However, the disadvantage of using lamps as blackbo dy sources is that their em issivities are usually unknown and since lamps have to be encased in g lass, the spectral properties of the glass not only have to be known, but also reduce the in tensity of the trans mitted radiation thereby reducing th e ef fective em issivity of th e f ilament. Addition ally, th e tem perature variations along the filament are usually large, leading to the difficulty in determining a single temperature for the filament, so that high temperature uncertainties result.

Thus, it may be concluded that plasm a arcs and lamps are not suitable for use in h igh precision calib ration of pyrom eters. Fortunately, graphite cavity ty pe furnaces , commonly known as the graphite b lackbody furnaces, are availab le for the precisio n

calibration of pyrom eters. The different m anifestations of the fu rnace are presen ted below.

1.2 Graphite Blackbody Furnaces

In general, this type of blackbody emulator   is based on the prin   ciple of heating an element using electrical power. The elem ent is usually m ade of a material with ve ry high m elting point f ormed in the shape of   a tube. In m ost cas es, this m aterial is graphite which has an em issivity of around 80% (Mantell 1968). In graphite furnaces, the blackbody cavity is produced by having a divider (or se ptum) in the m iddle of, or at a specified distance from, the heater elements. As shown in Figure 1.6, the common cavity shape for this type of furnace is usually a hollow cylindrical tube.
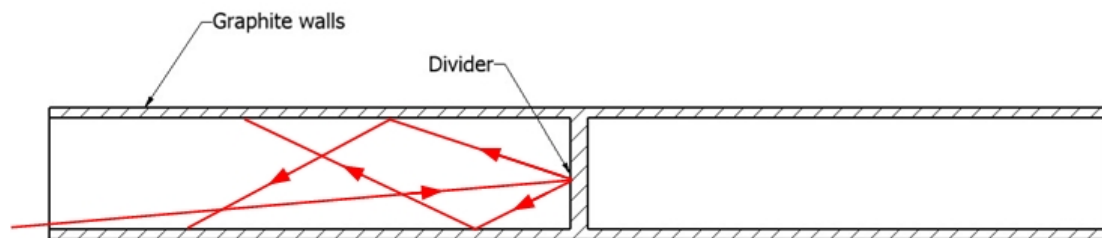
Figure 1.6. Schematic diagram of a cylindrical blackbody cavity. The incident ray-paths are shown to demonstrate the enhancement in absorptivity due to multiple reflections.

Dewitt & Nutter (1988, p. 663) suggest that such a cy lindrical cavity can be used to emulate a blackbody with an em   issivity as high as 0.99, perhaps higher. W   hen an incident-ray enters the cavity, th en, as shown i n Figure 1.6, such a ray gets partly absorbed and reflected   several tim   es be fore it em erges from the cavity. As a consequence there is a large chance of near total absorption of the ray, thereby closely emulating a blackbody surface. As it m   ay be readily apparent from Figure 1.6, a relationship must exist b etween the em issivity o f the cavity, and the surface area of the cavity divider and the depth of the cavity   . B allico (1998) showed that the longer the cavity the greater the absorption of the inci dent radiation. If the cavity walls are at

a uniform temperature, an estimate of the apparent emissivity of a cylindrical cavity ε_{BB} is,

$$\varepsilon_{BB} = 1 - \left(1 - \varepsilon_{surf}\right)\frac{A}{\pi d^2} \, , \quad (1.6)$$

in which, ε_{surf} is the emissivity of the surface material, A is the area of the cavity hole and d is the cavity depth. For example, the apparent emissivity of a graphite cavity 40 mm in diameter and 120 mm deep with an emissivity of 0.8 is 0.994. The estimated uncertainty in the calculation of this emissivity is around 1% so that equation (1.6) can only yield an *estimate* of the cavity depth required for a given apparent emissivity, emissivity of the surface material and septum hole area.

More accurate calculations of the effective emissivity of cylindrical shaped cavities were carried out by Jones & Tapping (1972) and later by Bedford & Ma (1975). They divided the cylindrical cavity into a number of small annuli and analytically calculated the radiation transfer between them based on surface temperature measurements of the cavity walls. Sapritsky & Prokhorov (1995) also calculated the effective cavity emissivity by using the Monte Carlo method. Based on these works, Ballico (1996) developed software to compute the effective emissivity of a cylindrical cavity based on the cavity's dimensions, thermophysical properties (mainly emissivity) and the cavity wall temperature. The modelling of the cylindrical cavity emissivity by Ballico (1996) indicated that it is dependent on the temperature gradient of these walls; the better the uniformity of the wall temperature the higher the emissivity. For the work presented here, the author's intention is to use Ballico's software to compute the effective emissivity of the cavity.

There are four major producers of graphite furnaces for spectral radiance standards for pyrometry and radiometry around the world, viz, Thermogage in the USA, IKE in Germany, Nagano in Japan, and Vega International in Russia-USA. All of these furnaces use cylindrical cavities manufactured from graphite material in order to emulate blackbody surfaces. Descriptions of these furnaces are as follows.

1.2.1 Thermogage Instruments Inc.

The principle adopted by Therm ogage Inst ruments Inc. in their design to em ulate blackbody surfaces is based on the principle of direct resistance heating of a graphite element, which has lo w electrical res istivity, using large AC curre nts as high as 1 000 A with voltages less than 15 V. The elem ent is a cylindrical tube with a small divider, or a septum , in the m iddle, whic h prod uces two cavities; on e on each side. One of these cavities is used for control, while the oth er is used as the em ulating blackbody surface for calibrating pyrometers. The tube is poorly insulated so it can be cooled as easily as it can be heated up. The tube is m ounted on two water-cooled copper wires. The internal tube diam eters vary between designs. Therm ogage manufactures tubes with an internal diameter of 16, 25, 38 or 51 mm. The length of each tube is at leas t 5 tim es greater than the inner diameter. Figure 1.7 is a pho to of one of the furnaces produced by Therm ogage, m odel 48kW , kept at the Nation al Measurement Institute, Australia (N MIA). The internal diam eter of the graphite tube of this furn ace is 24 mm, with a 3 00 mm length, and th e m anufacturer's sp ecified emissivity is 0.995. Thermogage had ceased manufacturing such a model.
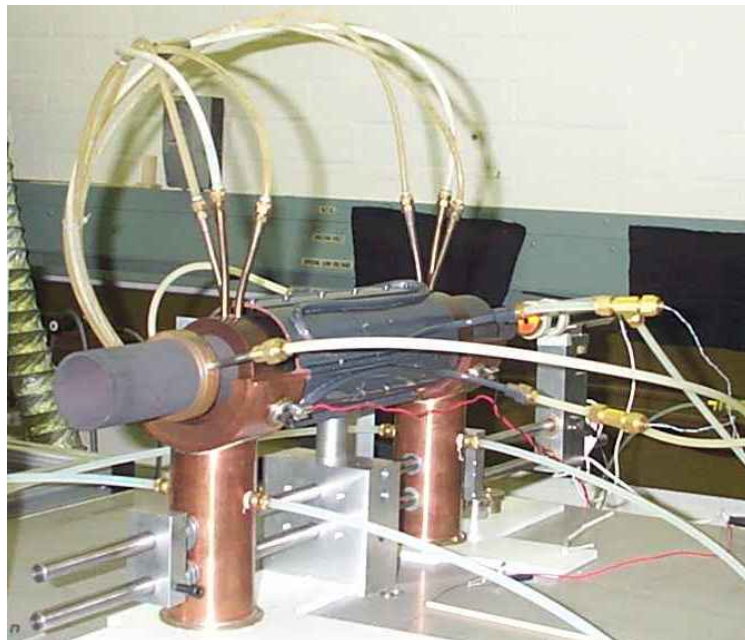
Figure 1.7. Photo of the 48kW Thermogage furnace at the National Measurement Institute, Australia.

Thermogage has produced two additional furnace models, which are the HT-5500 and HT-9500. These two models don't differ gr eatly from the 48kW m odel m entioned above except that their heater elements are enclosed in metal cases as shown in Figure 1.8 (copyright of Ther mogage website). An advantage of having the heater elem ents encased is to prov ide a better temperat ure contro l for the furn ace and b etter temperature profile along the graphite tube. However, it lim its the user from having the ability to conduct re search work on the gr aphite tube element in order to im prove its performance.

Figure 1.8. Thermogage furnace model HT-5500/9500.

On the other hand, the m ain difference between the two m odels, HT-5500 and HT-9500 is the capacity of their power supplies. The HT-5500 has 15 kW power supply while HT-9500 has 45 kW, which indicates that the operating tem perature of the HT-9500 is higher than th at of the HT-5500. The specifications of each m odel are presented in Table 1.1, which also incl udes the response tim e needed to attain maximum operating temperature for each model.

Table 1.1. Specifications of the HT5500 and HT9500 furnaces

HT-9500 Furnace Specifications				
Element Model	Inner Diameter (mm)	Temperature (K)	Response Time (s)	Emissivity
IA	15.9	500 - 3000	200	0.995
II	25.4	500 – 3000	300	0.995
III	38.1	500 - 3000	500	0.995
IV	50.8	500 – 2500	800	0.995
HT-5500 Furnace Specifications				
Element Model	Inner Diameter (mm)	Temperature (K)	Response Time (s)	Emissivity
IA	15.9	500 - 3000	200	0.995
II	25.4	500 – 2500	300	0.995
III	38.1	300 - 2000	450	0.995
IV	50.8	300 – 1400	600	0.995

Aside from the m etal encasing, the tw o models HT-5500 and HT-9500 do not differ greatly from the older 48kW model. The emissivity of these two m odels, as given by Thermogage, is still 0.995. The im provements made were carried ou t to enhance their response tim es and control sys tems but not their cav ity e missivities or tem perature uncertainties. The literature survey conducted b y the prese nt author in dicates tha t Thermogage do not have any known publ ished research literature on their manufacturing technology. Most of the l iterature published on Therm ogage furnaces is by end us ers, for exa mple scientists at Na tional Measurement Institutes around the world.

1.2.2 VNIIOFI/Vega International Inc.

The development of this type of blackbody fu rnace started with Victor I. Sapritsky in the e arly 19 70s whilst h e w as w orking w ith the "All-Russian Research Institute for Optical and Physical M easurements (VNIIO FI)". Later in 1994, Vega International Inc was established with Sapritsky as one of its directors, and development of these blackbody furnaces still continues at the time of writing this thesis.

Since 1975, m any blackbody source furnaces have been manufactured by VNIIOFI and later by Vega In ternational Inc.. A cr oss s ectional v iew of one such furnace is shown in Figure 1.9. Sim ilar to the Therm ogage graphite furnace, th ese furnaces are

heated ohmically. While the The rmogage's radiating cavity is m anufactured from a solid graphite cylinder, the rad iating cavity of th e VNIIOFI/Vega furnaces is formed by stacking graphite rings together with variable outs ide diam eters, enabling the optimisation of the cavity w all temperature (Ogarev *et al* 2004). These rings are held together with two sprin gs at bo th sides of th e furnace. A s m entioned earlier, the calibration of pyrometers up to 3 500 K is only of interest to the w ork presented here, and therefore the VNIIOFI/Vega furnaces wi th operating tem peratures between 8 00 and 3 500 K will only be discussed.
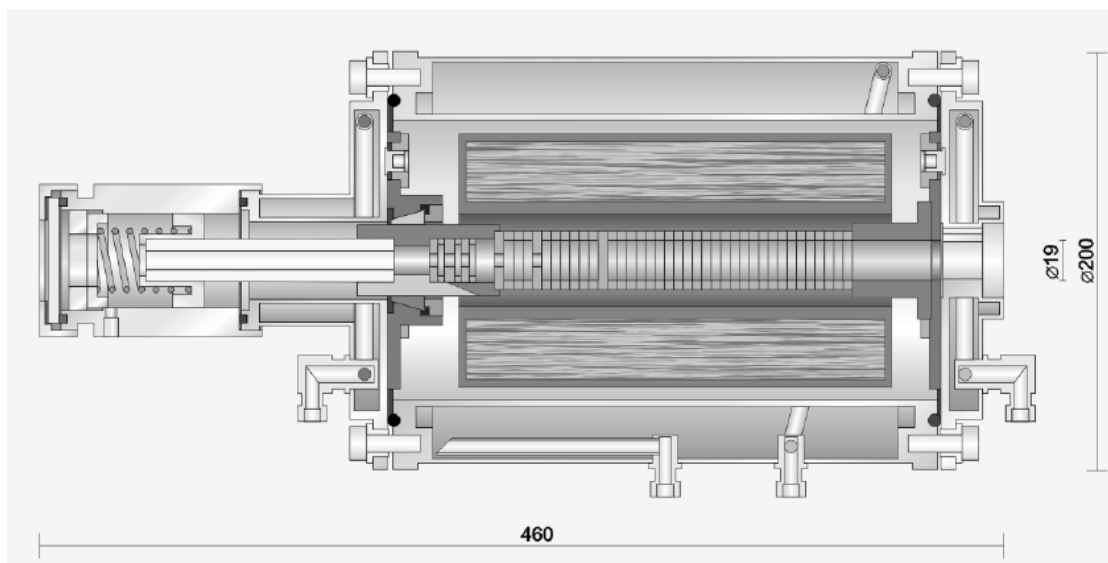
Figure 1.9. Cross sectional view of the VNIIOFI blackbody furnace model BB3400 ("BB-PyroG") with a 19 mm window (sourced from Ogarev *et al* 2004).

The BB2500 and BB2700 were the first two furnace m odels to be m anufactured at VNIIOFI in 1975. The BB2500 was m ade of carbon-glass and had a tem perature range from 2 000 to 2 500 K. The BB2700 was m ade from high- modulus carbon plastic and had a tem perature range from 2 000 to 2 700 K. Both furnaces have an opening of 12 mm and an em issivity of 0.998. The BB3000 was m anufactured in 1985. This model was made of thin-wall niobium carbide. It has an opening of 12 mm and an em issivity of 0.9 97. This furnace was employed at VNIIOFI as their Natio nal Primary Standard for radiom etry and pyrom etry (Sapritsky *et al* 1997). The BB14 graphite source was developed in 1990. Th e operating tem perature of this m odel

exceeded the previous ones, reaching 3 000 K. However, the opening of this model is only 8 mm, and it was demonstrated during an international comparison (Saunders 1996) that this model had substantial drawbacks due to this small opening size. The emissivity of the BB14 was 0.998.

The two models BB22p and BB39p were developed in 1992. Their radiators were manufactured from graphite and have an emissivity of 0.999 and 0.998 respectively (Sapritsky 1996). These furnaces were used for reliable and accurate measurements of spectral radiance and spectral irradiance in the spectral region starting from 250 nm (Sapritsky *et al* 2003). The opening diameters of these two models were 14 and 30 mm respectively, and their operating temperatures extend from 1 800 to 2 900 K. The BB22p model differs from the BB39p by being able to operate in vacuo or with an inert gas purging, and therefore this model would have the advantage of having no window.

Sapritsky *et al* (1996 and 2003) claimed that the model BB3200pg was developed after many years of research, however no detailed descriptions of this research could be found by the present author. This model was manufactured from pyrolytic graphite. The use of such a graphite grade in the manufacturing process made it possible to improve both the service life of the tube and attain higher operating temperatures. Sapritsky *et al* stated a value of 0.999 for the emissivity of the BB3200pg model and an operating temperature range between 1 800 and 3 300 K. In addition to this model, a BB3200pg model was manufactured using pyrolytic graphite however it had a wider opening with a diameter of 24 mm.

Table 1.2 presents the basic technical and operating parameters of the high temperature furnaces, with operational temperatures between 800 and 3 500 K, developed at VNIIOFI and Vega International.

Table 1.2. List of graphite furnaces developed by VNIIOFI and later Vega International.

Year	Type	Opening (mm)	Temperature (K)	Emissivity	Radiating Cavity
1975	BB2500	12	2000 to 2500	0.998	carbon glass
1975	BB2700	12	2000 to 2700	0.998	carbon plastic
1985	BB3000	12	2500 to 3000	0.997	niobium carbide
1990	BB14	8	1600 to 2500	0.998	graphite
1992	BB39p	30	1800 to 2900	0.998	graphite
1992	BB22p	14	1600 to 2900	0.999	graphite
1995 B	B2000	60	800 to 2000	0.995	graphite
1995	BB3200c	20	1800 to 3300	0.999	pyrolytic graphite
1995	BB3200pg	24	1800 to 3300	0.999	pyrolytic graphite
1997	BB3500	24	1500 to 3500	0.999	pyrolytic graphite

1.2.3 IKE

These blackbody furnaces, shown in Figure 1.10, are manufactured by the "Institut für Kernenergetik, Universität Stuttgart" in Germany. Similar to the two types of furnaces described above, the operation principle of this furnace is also resistance-heating of a graphite rod mounted on two water-cooled copper wires, which also serve as electrical power leads and provide support to mount the graphite rod. A coaxial cylindrical hole inside the graphite rod constitutes the cavity. Temperature distribution uniformity is achieved along the hole by varying the thickness of the graphite rod wall, which is schematically presented in Figure 1.10. The internal diameter of this cavity may vary between 7 mm and 12 mm. The outer diameter of the cavity is 28 mm. The length of the cylindrical hole, with a depth of 134 mm, abides by the 5:1 diameter to depth ratio requirement. The whole of the graphite element is placed inside a water-cooled cylindrical steel vessel. This vessel can be either evacuated or filled with a positively pressured inert gas, but it can not be run in purging mode. This results in the vessel and graphite rod being encased inside a glass window. As in the case of the QTH lamps discussed in section 1.1.2, the spectral properties of the encasing glass needs to be known and, furthermore, this glass limits the intensity of the emulated blackbody surface which inturn affects its effective emissivity. The inert gas must be used when a higher operating temperature range is desired. The operating temperatures of the IKE furnace are 1200 to 2200 K in vacuum, and up to 3000 K in an inert gas. Groll & Neuer (1972) give a value for the emissivity of the IKE graphite furnace of 0.995.

The manufacturing of this type of furnace has ceased at the University of Stuttgart. A literature survey found that publications related to the manufacturing of this technology seem to be very scarce. The present author could only find one publication by Groll & Neuer (1972) related to the IKE graphite furnace. In their publication, Groll and Neuer discussed the specifications of the IKE graphite furnace, however no discussion of the design m ethodology they a dopted in profiling th e cross sectiona l area of their furnace's heater element was presented.
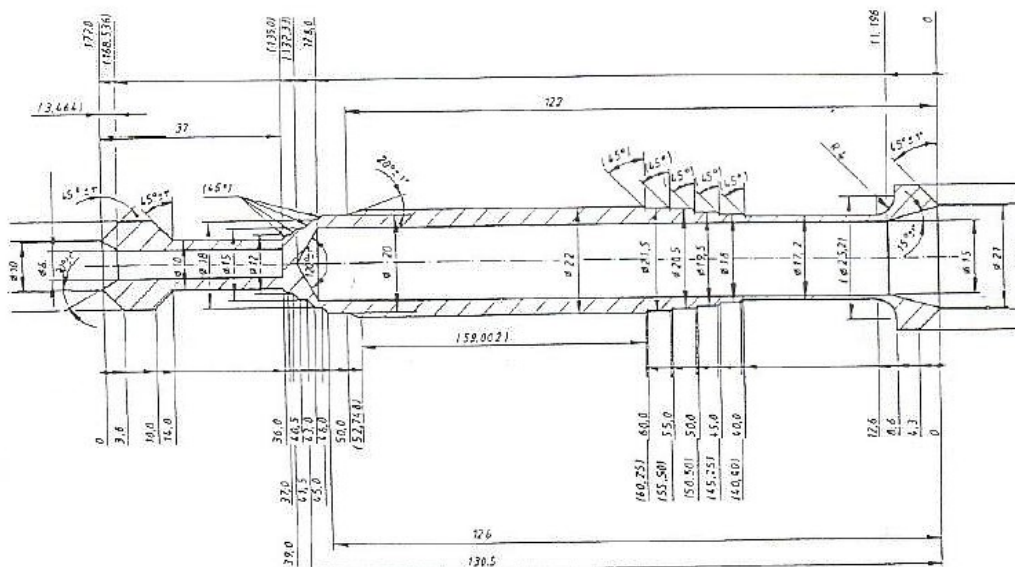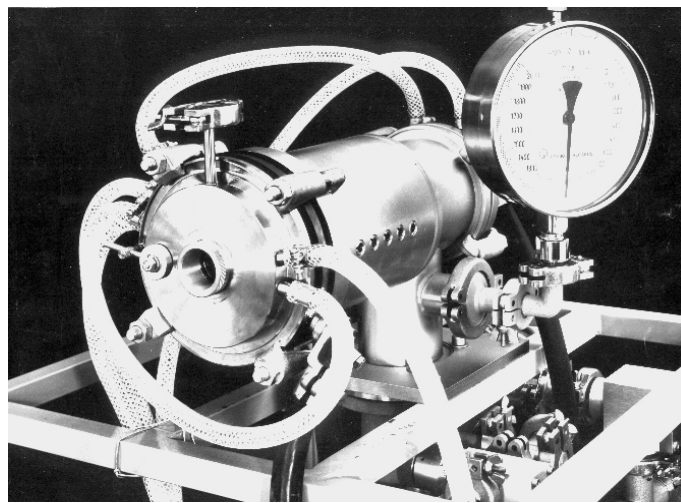
Figure 1.10. Photo of an IKE blackbody furnace (top), cross sectional view of an IKE blackbody furnace heater element (bottom).

1.2.4 Nagano Ltd.

Nagano Ltd. in Japan m anufacture graphite furnaces in collaboration with Dr. Y. Yamada from the National Measurem ent Institute of Japan, NMIJ (Yamada *et al* 2003). As shown in the cross sectional view in Figure 1.11, this furnace consists of three different sections or z ones nested on top of a carbon-composite (CC) graphite tube, which has an inner diam eter of 50 mm. Ea ch zone consists of an independent heater elem ent with an inde pendent tem perature con trol system . Fibre-optic radiation thermometers positioned at the centre of each zone are used to measure the temperatures of the three zones.
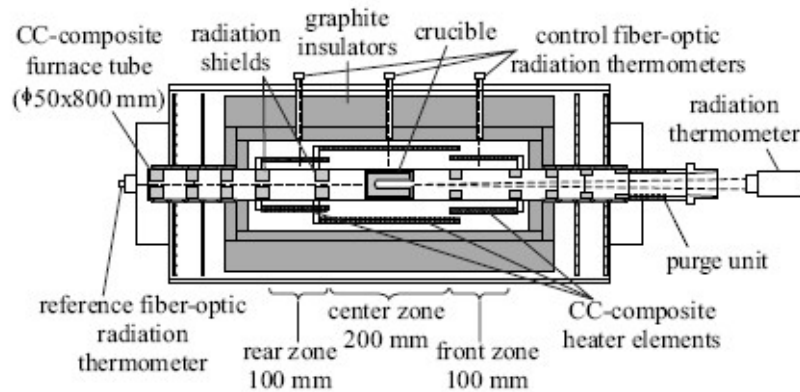
Figure 1.11. Cross sectional view of the Nagano three-zone CC-composite furnace at the NMIJ (sourced from Yamada *et al* 2003)

The heater elem ent c onsists of a car bon-fibre-reinforced-carbon-composite (CC-composite) with a thickness of approximately 1 mm. This material is strong enough to withstand any therm al shocks, however, th e fine thickness does not allow for any special tube profiling as in the case of the Thermogage and the IKE furnaces. On th e other hand, having a thin tube allows the use of lower currents and higher voltages during operation, which m eans that the copp er power cables used are kept with in reasonable sizes. The need for water-cooled h eat exchangers is s till necessary a cross these cables (for the th ree zones) to prevent them from melting when o perating the furnace at high tem peratures. This can be a d isadvantage when trying to optimise the

cavity wall temperature for best performance due to cold spots caused by these heat exchangers along the length of the heater element.

This furnace can operate without a window. The operating temperature is below 2 300 K when purged with pure Ar gas and to 2 800 K when using a mixture of Ar and nitrogen (N_2) gas. The uniformity of the temperature in this furnace is stated by Sasajima *et al* (2001) to be better than 0.5 K, however, there is no mention of the emissivity or temperature uncertainty.

The literature review conducted on the above four types of blackbody furnaces suggests that there are currently only two active manufacturers for this type of technology: Thermogage and VNIIOFI/Vega. It can also be concluded from this review that there are no published research works on the improvement of these four furnaces' emissivities and temperature uncertainties. Improvements on some models, as in the case of VNIIOFI/Vega, were not based on any active or known research works. In the case of the IKE furnace, the present author could find no publications on the methodology adopted in the design of their heater element.

1.3 Aims and Scope

The NMIA is responsible under the National Measurement Act 1961 to maintain and establish Australia's physical, chemical, biological and legal standards (DITR 2007). The role of the NMIA is the continuous improvement of these standards to respond to the needs of the national industry in order to stay competitive in both local and global environments. Based on this fact, it is important for the reader to note that the research presented in this thesis will aim at improving the standards used in the calibration of pyrometers, namely the Thermogage furnace, at NMIA.

At the NMIA, a 48kW Thermogage blackbody furnace is used as Australia's primary radiance standard for the temperature calibration of pyrometers up to 3 000 °C. The original design of the 48kW Thermogage furnace, shown schematically in Figure

1.12, consists of a 3.2 mm thick 289 mm long ATJ graphite grade heater element. The heater element is div ided in the m iddle by a septum and is surrounded by W DF graphite felt purged with an inert gas such as He, Ar or N $_2$. The felt is wrapped with two 0.5 mm thick graphite foils and inserted into a 2 mm silica tube. Th e ends of the tube are clamped by graphite-com posite ri ngs, which are in turn clamped to water-cooled copper rings. During operation, the graphite tube and graphite-composite rings are ohm ically heated b y a voltag e applied across the cop per ring s. This electrical power is dissipated by (i) conduction along th e graphite tube, (ii) radiation from the middle of the tube and (iii) radially through the insulation.
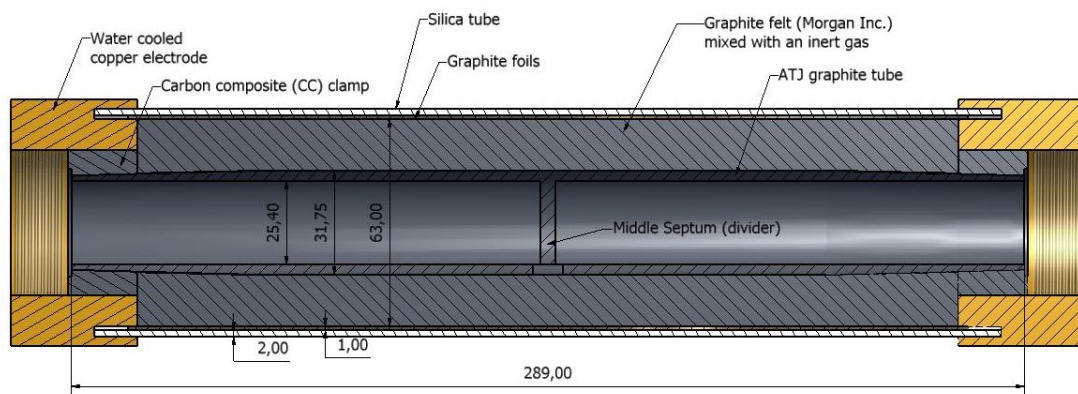
Figure 1.12. Cross sectional view of the 48kW Thermogage furnace at the NMIA (all dimensions are in mm).

As calculated by Ballico (1996), the emissivity of the Thermogage blackbody is 0.992 at an operating temperature of 1 000 °C and a wavelength of 650 nm. This leads to an uncertainty of 0.8% associat ed with the radiance of the The rmogage blackbody, or a temperature uncertainty of 0.6 °C at 650 nm. This uncertainty increases to almost 2 °C at 2 000 °C, which is mainly due to this emissivity value.

With continuous de mands by the various industries in Australia for the constant improvement of temperature measurements to meet new challenges, it follows that the direct aim of the work presented here is to improve the uncertainty associated with the calibration of pyrometers using the NMIA's 48kW Thermogage furnace to better than 0.1 °C for tem peratures up to 1 600 °C at a first stage and up to 3 000 °C at a later

one. In add ition to this direc t aim , it is also essential for the NMIA to grow and enhance the engineerin g expertise and scie ntific knowled ge necessary to m aintain these calibration standards.

The literature survey conduc ted in the previous secti ons on different m odels of blackbody furnaces sug gests that th ere is no current activ e research to im prove the emissivity of this technol ogy. Most of the w orks publ ished did not include any technique or m ethod to enhance the em issivity of these furnaces o r their tem perature uncertainties. It can also be deduced from this literatu re survey that although better cavity em issivities have been ach ieved fo r som e furnaces, this im provement did not encompass the full operating range of the fu rnaces or a wide wavelen gth spectrum. The lack of published research work on this technology m ay indicate that any improvements achieved in perform ance we re by tr ial and erro r of either the manufacturers or the sc ientists at va rious international measurement institutes sim ilar to the NMIA.

The 48kW Thermogage furnace at NMIA can be modified to obtain better cavity wall temperature uniform ity and consequen tly a better blackbody cavity effective emissivity. One method of improving the temperature uniformity is to manipulate the area profile of the heater elem ent sim ilar to the principles em ployed by IKE and VNIIOFI/Vega in th e design of th eir furnaces . The IKE f urnace's heater elem ent, described in section 1.2.3, was m anufactured from a graphite rod with varying wall thickness as shown in Figure 1.10. On th e other hand, the VN IIOFI/Vega furnace's heater elements cons ist of rings with different outside diam eters (section 1.2.2). Regardless of whether or not th e m anufacturer uses a profiled cavity wall or rings with different diam eters, the ultim ate desi gn co ncept is to improve the tem perature uniformity, and is thus the sam e for both furnaces. This concept depends on changing the dim ensions of the cross sectional area p erpendicular to the h eat flux directio n along the tube. By doing this it is possible to manipulate the cavity wall temperature, especially around the area close to the cavity . By reducing the cross sectional area of the wall, th e heat flux can be restricted cau sing the tem perature at this point to ris e and vice versa. Unlike the Nagano model, whi ch has a 1 mm thick CC heater element, the cross s ectional area of the NMIA Ther mogage heater elem ent, which has at least

3 mm of tube thickness, can be easily prof iled in order to im prove the cavity wall temperature.

Although the profiling of the cross sectional area may be one avenue to b e adopted to improve the ef fective em issivity of the   cavity, other design factors, such as the thermophysical properties of the ATJ graphite   and the graphite felt, also need to be considered. Prelim inary m easurements of th e ca vity w all te mperature p rofile show s that sign ificant change occurs when diffe   rent gases are used in purging the felt insulation. An example of this phenomenon is given in Figure 1.13.
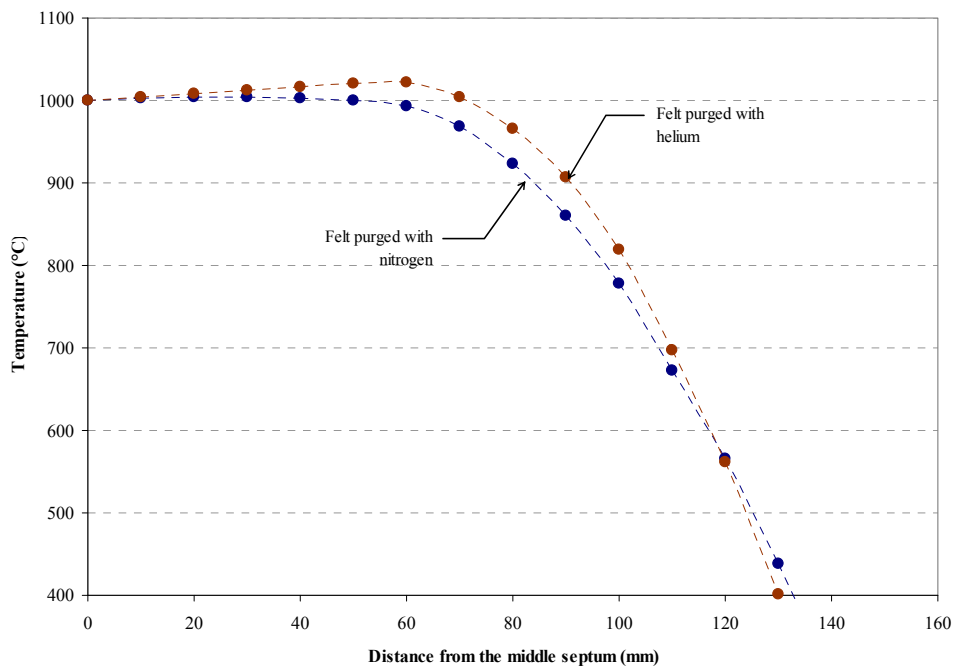
Figure 1.13. Measurements of the cavity wall temperature profile of the NMIA Thermogage graphite furnace at an operating temperature of 1 000 °C using felt insulation purged with N_2 and He.

As maybe seen, the temperatures of the cavity walls are measured as a function of the distance from the m iddle septum of the he ater element of the NMIA furnace, shown schematically in Figure 1.12. These m easurements are carried out first with nitrogen (N_2) and th en w ith helium (H e) a s the f elt purging gas. Up to   50 °C rise in temperature, within 60 mm from the m iddle septum, is obs erved when using helium.

This can be explained by the increase of the heat flux through the WDF felt due to the increase of its therm al conductivity caused by changing the felt purging gas from nitrogen to helium w hile m aintaining the te mperature of the m iddle of the tube at 1 000 °C; note that the thermal conductivity of helium is higher than that of nitrogen.

By considering these two fact ors, the tube design can be mathematically modelled to produce optimum results. However, an analy tical solution m ay not be possible due to the geometric complexity of both the heater element and other parts of the furnace. In addition, the temperature dependence of the thermophysical properties of the graphite materials c onstituting the heater elem ent and the in sulation pr ovide f urther complications. Since there is no analytical solution for the mathematical models of the furnace, numerical simulations need to be performed.

Prior to u sing num erical m odels to d esign the n ew heate r e lements, the thermophysical properties of the ATJ graphite and the W DF graphite felt need to be determined. Specifically the therm al conductivity and density of the graphite felt, and the specific heat, electrical resistivity a nd thermal conductivity of the ATJ graphite. For this reason, a literature survey of these properties is presented in chapter 2. In the first part of the survey, wo rks by various investigators on the therm al conductivity of fibrous materials in general and graphite felt in particular are investigated. Models for the thermal conductivity of gra phite felt are obtained based on this survey, and direct measurements are conducted to obtain geometrical factors needed for these models. In the second part of the survey th e e ffect of the m anufacturing process on the thermophysical properties of gr aphite is investigated, and equations for the electrical resistivity, specific heat, density and thermal conductivity are obtained by com paring works carried out by various investigators.

With the t hermophysical properties needed for the num erical simulation thus determined, accurate temperature m easurements are need ed, firstly to m easure th e temperature profile of the cavity walls, and secondly to calcul ate the heat transfer rate by conduction along the heater elem ent. Diff erent "direct-contact" techniques using platinum/platinum-rhodium (Pt/Pt-Rh) ther mocouples on one hand and a pyrom etric technique using optical fibres on the other hand are presented in chapter 3.

In chapter 4, descriptions are given of the experimental apparatus used for measuring the various heat transfer rates from and to the heater element of the Thermogage furnace (that is the ATJ graphite tube). In order to ensure that these measurements of the heat transfer rates are acceptable and with their measurement uncertainties, the electrically generated heat transfer rate by the ATJ graphite tube is then compared to the sum of the heat transfer rates dissipated (i) in the radial direction through the WDF graphite felt, (ii) along the ATJ graphite tube, and (iii) by radiation to the environment. These measurements were conducted using two newly manufactured graphite tubes. Furthermore, the results of these measurements are then used to justify any assumptions to be made in order to simplify the numerical model developed by the present author.

Having determined the thermophysical properties of the ATJ graphite and WDF graphite felt as well as quantifying the heat transfer rates and their directions, the software developed by the present author to simulate a new heater element design is then described in chapter 5. Based on the works presented in chapter 4, the assumptions made in developing this modelling software are discussed. The grid size and time step to be used in the simulation are determined, and validations of the software against analytical solutions are conducted.

In order to /use the numerical model to optimise the effective emissivity of the Thermogage furnace, the numerical model needs first to be validated against measured data. The numerical predictions of the temperatures of the inner walls of the graphite tube (temperature profiles) as well as the heat transfer rates in the radial directions generated using the software developed in chapter 5 are then compared to the measured ones. These comparisons are presented in chapter 6. A sensitivity study of the numerical model to the measurement uncertainties of various input parameters is also conducted in this chapter.

With the validation of the numerical models against measured data achieved, the design methodologies of a new heater element are discussed in chapter 7. Numerical simulations are conducted to obtain a new heater element design. Measurements of the cavity wall temperature of the newly designed tube are conducted. The new

calculated effective cavity em issivities at different operatin g tem peratures are also presented.

Having achieved the goal of the work presente d here, the conclusions are presented in chapter 8. R ecommendations are als o m ade as to how this can be further im proved, especially with respect to cavity emissivities in the temperature range above 1 600 °C.

2 LITERATURE REVIEW: WDF GRAPHITE FELT AND ATJ GRAPHITE THERMOPHYSICAL PROPERTIES

The WDF graphite felt, manufactured by MorganAM&T in the USA, and ATJ grade graphite, manufactured by a division of the Union Carbide Corporation in the USA, are commonly used in the manufacturing of blackbody graphite furnaces. As mentioned in chapter 1, it is essential that the thermophysical properties of both materials be determined in order to achieve accurate numerical modelling of such blackbody furnaces. In this chapter, a literature survey is conducted to determine these thermophysical properties, in particular the WDF felt thermal conductivity, which is presented in section 2.1, as well as the density, specific heat, electrical resistivity and thermal conductivity of ATJ graphite, presented in section 2.2.

2.1 WDF Graphite Felt Thermal Conductivity

The datasheet, supplied by MorganAM&T, for WDF graphite felt has an inconsistency in the value of thermal conductivity (MorganAM&T 2007). To illustrate the difficulty, the thermal conductivity of the WDF felt measured in vacuo and when argon fills the interstices in the felt, obtained from this datasheet, are plotted in Figure 2.1. It might have been expected that the difference between the thermal conductivities of the WDF felt measured in vacuo and when the argon pervades the voids in the felt should have been approximately equal to the thermal conductivity of argon gas. However, as may be seen from Figure 2.1, the difference is much greater; in fact it is a factor of 2 to 12 times larger. In addition, the measurement uncertainties of these thermal conductivities could not be found in the datasheet produced by MorganAM&T.

This puts the validity of the data produced by MorganAM&T in doubt so that they cannot be used with any certainty. As a result, a thorough literature survey of the thermal conductivity of graphite felt presented below became necessary so as to ensure that reliable values of the thermal conductivity of WDF graphite felt are

needed before an accurate model could be developed so that the research described in this thesis could proceed.
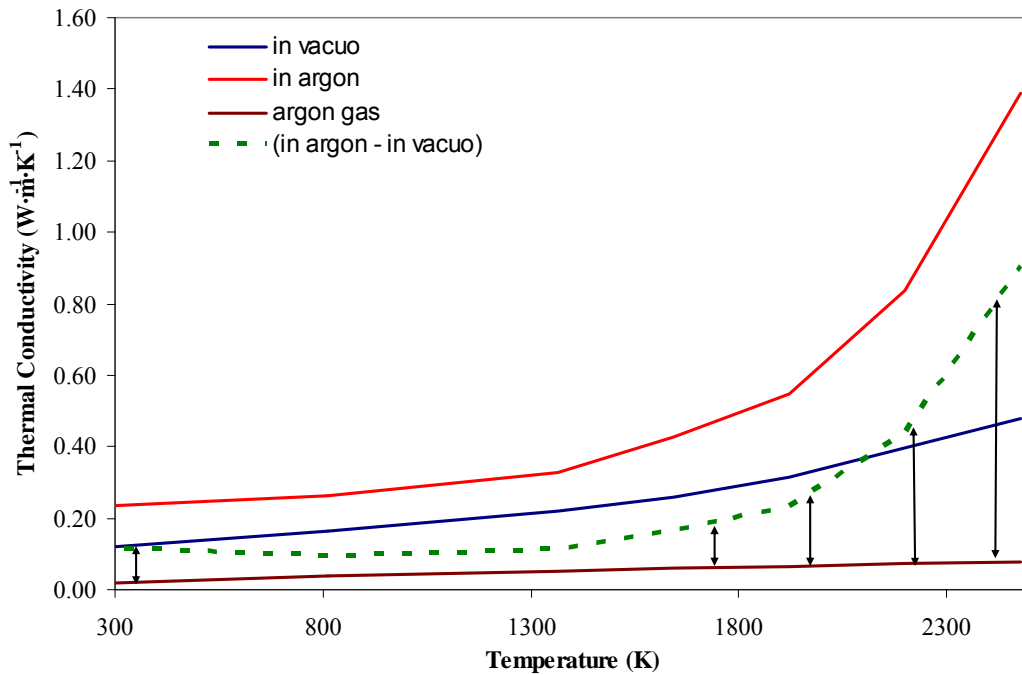
Figure 2.1. Thermal conductivity of WDF felt in argon and vacuo versus the absolute temperature as given by Morgan AM&T (MorganAM&T, 2007) with the plot of the calculated difference between them, as well as thermal conductivity of argon gas.

In the next section, studies of the thermal conductivity of fibrous materials in general and WDF graphite felt in particular, are examined. The different mechanisms of heat transfer in this type of material are discussed and a model is developed of the apparent thermal conductivity of graphite felt.

2.1.1 Review of Previous Work

Graphite felt is a fibrous material consisting of graphitised carbon fibres. To avoid ignition when using it as a high temperature insulator, the felt must be either in a vacuo or purged with an inert gas. Hence, the apparent thermal conductivity of fibrous

material is the product of the combined thermal conductivities of the solid part, which consists of fibres, and the gaps among these fibres, which can be either in vacuo or filled with an inert gas. A brief history of the development of methods for evaluating the thermal conductivity of fibrous materials is given below.

Pratt (1969) claims that the earliest work on calculating the thermal conductivity of a fibrous material was carried out by Schuhmeister in 1877. According to Pratt Schuhmeister proposed a simple form for the thermal conductivity of textile fabrics k_m to be,

$$k_m = \varsigma(k_1 v_1 + k_2 v_2) + \psi \frac{k_1 k_2}{k_1 v_2 + k_2 v_1},$$
(2.1)

in which, k_1 and k_2 are the thermal conductivities, v_1 and v_2 are the fractional volumes of air and fibre respectively. Further, Schuhmeister defined ς and ψ as two constants such that,

$$\varsigma + \psi = 1.$$
(2.2)

By using a simplified model in which the fabric is arranged as layers of slabs, he proposed ς as ⅓ so that ψ had to be ⅔. Pratt (1969) further indicates that in 1946, Baxter extended Schuhmeister work and obtained empirical values of 0.21 and 0.79 for ς and ψ respectively. These values were based on measurements of thin samples of cotton, wool and rayon fabrics. Schuhmeister and Baxter were only concerned with thermal conductivity of fibrous materials at room temperature, they assumed uniformly distributed fibres, and did not take into consideration other effects that could influence heat transfer through the felt such as the radiative exchanges among the fibres, or the complexity in their geometrical structure and distribution. It was found, by the present author, that the use of Baxter and Schuhmeister's values for ς and ψ led to an overestimate of the thermal conductivity of the WDF graphite felt.

A more comprehensive approach to the thermal conductivity of fibrous insulations was developed by Verschoor *et al* (1951), who were the first researchers to investigate the radiative heat transfer mechanism. They stated that the apparent thermal

conductivity of graphite felt, k_f, consists of five heat transfer mechanisms, viz, solid conduction along the fibres, gas conduction, gas convection, gas radiation and radiative exchanges among the fibres. These effects could be combined to yield

$$k_f = \frac{\left(k_{gc} + k_{fc} + k_{gr} + k_{fr} \right)}{1 - f} + k_{sc} . \qquad (2.3)$$

Here, k_{sc}, k_{gc}, k_{fc}, k_{gr} and k_{fr} are the thermal conductivities due to the solid conduction along the fibre paths, gas conduction, free convection, gas radiation, and radiation exchanges between the fibres respectively, and f is the graphite felt bulk material volume fraction. They introduced a theoretical approach for heat transfer by radiation and gas conduction which they combined with experimental results.

Various models were developed by different investigators for each of the five heat transfer mechanisms in equation (2.3). Discussions of these mechanisms are presented in the following paragraphs.

2.1.1.1 Radiation Mechanism From Interspatial Gas

As mentioned earlier, graphite felt used as an insulator needs to be purged with an inert gas which will prevent the solid material from igniting. Commonly used gases are nitrogen, argon and helium. These gases are transparent to infrared radiation and do not emit significantly (Siegell and Howell 2002, p. 464). Therefore heat transfer by gas radiation is negligible and consequently k_{gr} was set to zero.

2.1.1.2 Natural Convection Mechanism

Small cavities are formed by the entangled fibres of graphite felt, which can result in heat transferred by free convection inside them. This convective heat transfer is usually caused by the temperature difference between the fibres. To simplify the

calculation of heat transfer by free convection, the cavities are assumed to be rectangular prisms of high aspect ratio, which are heated from below by the lower, hot horizontal surface. This type of convective flow is termed Rayleigh-Bénard convection and it can be shown that it occurs only once the critical Rayleigh number, R_{a_L}, of 1708 is exceeded (Incropera and Dewitt 2002, p.562). R_{a_L} is defined as

$$R_{a_L} = \frac{g \beta_g \Delta T L^3}{\alpha_g \nu_g} ,$$

(2.4)

in which, g is the acceleration due to gravity, β_g is the coefficient of volumetric thermal expansion of the gas filling the gap, α_g is its thermal diffusivity, ν_g is its kinematic viscosity, ΔT is the temperature difference between the top and the bottom of the cavity, and L is the height of the cavity. The height L can be assumed, as a good approximation, to be equal to the free mean free path for molecule-fibre collision, l_f, which is given by (Pratt 1969)

$$l_f = 1.57 \frac{r}{f} ,$$

(2.5)

where r is the graphite fibre radius.

In this work, f and r were assumed to be 0.05 and 10.5 μm respectively (refer to Appendix A). Hence, the maximum value of R_{a_L} obtained when ΔT is 3 000 K was approximately 0.35, which is very much less than the critical value of 1 708, needed to produce motion. Therefore, heat transfer by free convection will not occur, so that k_{fc} can be safely also set to zero.

It follows that the apparent thermal conductivity of graphite felt is dependent upon conduction along the solid paths, gas conduction and radiative exchange mechanisms, allowing equation (2.3) to be simplified to,

$$k_f = \frac{\left(k_{gc} + k_{fr}\right)}{1-f} + k_{sc}.$$
(2.6)

2.1.1.3 Gas Conduction Mechanism

The most commonly gases used to purge the graphite felt when operating at high temperatures are helium, argon and nitrogen. The thermodynamic properties of these gases can be readily found in the literature and are reproduced in Figure 2.2 up to a temperature of 2 000 K (Vargaftik 1983).
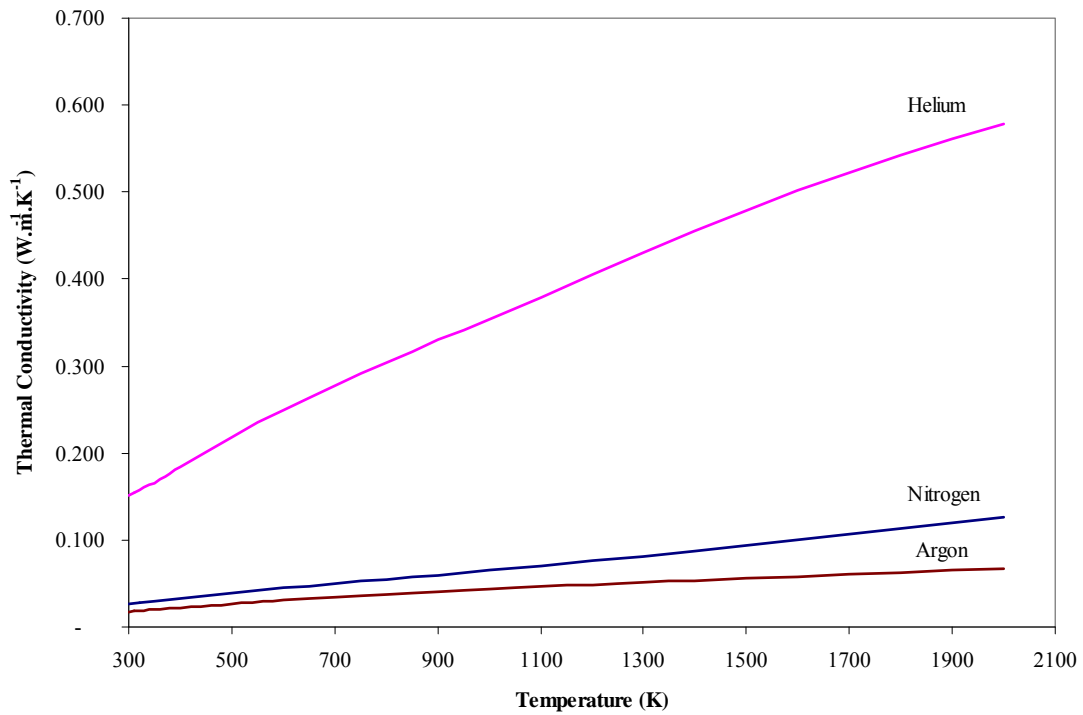
Figure 2.2. Thermal conductivities of helium, nitrogen and argon versus absolute temperature.

Fifth degree polynomial functions of the form

$$k_{gc}(T) = c_5 T^5 + c_4 T^4 + c_3 T^3 + c_2 T^2 + c_1 T + c_0,$$
(2.7)

in which, c_0 to c_5 are constant coefficients whose values depend on the gas, were fitted to the curves in Figure 2.2. Values of these coefficients for helium, argon and nitrogen are given in Table 2.1.

Table 2.1. Polynomial coefficients for helium, argon and nitrogen.

	Helium	Nitrogen	Argon
c_5	-2.3363×10^{-18}	-5.0736×10^{-19}	-1.0250×10^{-18}
c_4	-2.9313×10^{-14}	-7.8019×10^{-15}	4.6553×10^{-15}
c_3	1.7470×10^{-10}	4.9661×10^{-11}	-2.9810×10^{-12}
c_2	-3.4439×10^{-7}	-8.9523×10^{-8}	-1.7708×10^{-8}
c_1	5.4519×10^{-4}	1.1486×10^{-4}	5.9051×10^{-5}
c_0	1.1565×10^{-2}	-1.8605×10^{-3}	1.5875×10^{-3}

The standard error in the polynomials of helium, nitrogen and argon are 1.6, 0.5 and 0.8% respectively. Since the expected total uncertainty in determining the felt thermal conductivity can be as high as 10%, the contribution of these errors is small and therefore ignored.

2.1.1.4 Conduction along Solid Paths Mechanism

In fibrous materials, when two fibres come into contact, heat will be transferred by conduction from one fibre to the other. Most of the models developed for this mechanism are purely empirical, and their geometrical representation of the material texture is either vaguely described or crude, as in the cases of Schuhmeister and Baxter (Pratt 1969). For example, the thermal conductivity of graphite felt in air was determined to be 1.7 W·m^{-1}·K^{-1} based on Schuhmeister model and using equation (2.1), whilst direct measurement produced a value of 0.077 W·m^{-1}·K^{-1}. Schuhmeister's structural assumption of materials composed of slabs is thus not appropriate for graphite felt.

On the other hand, Strong *et al* (1960) assumed that the fibres have an orderly arrangement that form symmetrical layers with all fibres having the same diameters.

They calculated the thermal conductivity by estimating the number of fibre-to-fibre contacts, n_{fibre}, from the values of the fibre radius and the bulk material volume fraction, which was given as,

$$k_{sc_{Strong\ et\ al}} = \frac{r ln\left(8\pi r^2 / A_{contact}\right) + 2 l_{fibre}}{4 n_{fibre} \pi r^2 k_s(T)},$$ (2.8)

in which, $A_{contact}$ is the fibre-to-fibre contact area, l_{fibre} is a length of fibre equal to one-half the distance between successive fibre junctions, and $k_s(T)$ is the thermal conductivity of the bulk material as a function of the absolute temperature T. The model did not take into account the crossing of fibres from one layer to another. Unfortunately, the experimental results obtained by Strong *et al* were at variance with their theoretical model. They explain that this discrepancy arose because they had overestimated the number of fibre-to-fibre contacts. The need to make assumptions about the number of fibre-to-fibre contacts as well as estimate values for $A_{contact}$ and l_{fibre} made this approach somewhat limited.

Bankvall (1973) also assumed uniformly and symmetrically arranged fibres, obtaining the thermal conductivity due to conduction from only values of volume fraction, f, and the bulk material thermal conductivity, $k_s(T)$, to be,

$$k_{sc_{Bankvall}} = \frac{32 f^2 k_s(T)}{\pi \left(3 + \dfrac{\pi}{4f}\right)}.$$ (2.9)

Although Bankvall's equation requires fewer parameters to be determined than that of Strong *el al*'s, it unfortunately fails to predict the experimental results accurately. For example, thermal conductivity of WDF graphite felt in vacuo calculated using equation (2.9) is $0.14\ \text{W·m}^{-1}\text{·K}^{-1}$ in comparison with the measured value of $0.064\ \text{W·m}^{-1}\text{·K}^{-1}$.

A more complex approach to the modelling of heat transfer by conduction along the solid paths of fibres was adopted by Bardon & Danes (1994). Based on works by

Strong *et al* and Bankvall, they developed two models to predict the conduction thermal conductivity for carbon fibres. Their first model was developed for the case of perfectly stratified felt (PSF), in which heat is transferred from one felt layer to another across the contact spots. The equation for the thermal conductivity, k_{PSF}, in this model is

$$k_{PSF} = \frac{1.5 k_s(T)(f/\tau)^2}{\alpha - 0.838 + 0.231(\tau^2/f)} .$$ (2.10)

Here α is the ratio of fibre radius to contact spot radius, and τ is the fibre tortuosity defined as the ratio of its actual length to the distance between the two contact points of this fibre. However, fibres in the felt can often cross from one layer to the other with a frequency υ_f. Bardon and Danes' second model was for imperfect stratified felt (ISF) and therefore was adopted by the present author to determine the thermal conductivity of graphite felt due to conduction along the solid paths, k_{sc}. This model is given by Bardon and Danes as,

$$k_{sc} = (1 - \upsilon_f) k_{PSF}(T) + \frac{4 f^2 k_s(T) \upsilon_f}{\pi \tau^3} .$$ (2.11)

As may be seen from equations (2.10-11), k_{sc} is dependent on $k_s(T)$, α, υ_f, f and τ. At room temperature, values for $k_s(T)$ can be obtained from the literature. The thermal conductivity of the felt fibres is not well accounted for, but exhibits the same patterns as any graphite materials, thereby can be considered to be similar to common graphite grade such as pyrolytic, ATJ or ATJS (Mantell 1968). Figure 2.3 is a plot of the thermal conductivity of the bulk material of the fibre.

The figure shows thermal conductivity versus temperature with the best fit curve function:

$$k_{graphite} = -5.099\text{x}10^{-18}T^5 + 6.728\text{x}10^{-14}T^4 - 4.051\text{x}10^{-18}T^3 + 1.294\text{x}10^{-6}T^2 - 2.152\text{x}10^{-3}T + 234.7$$
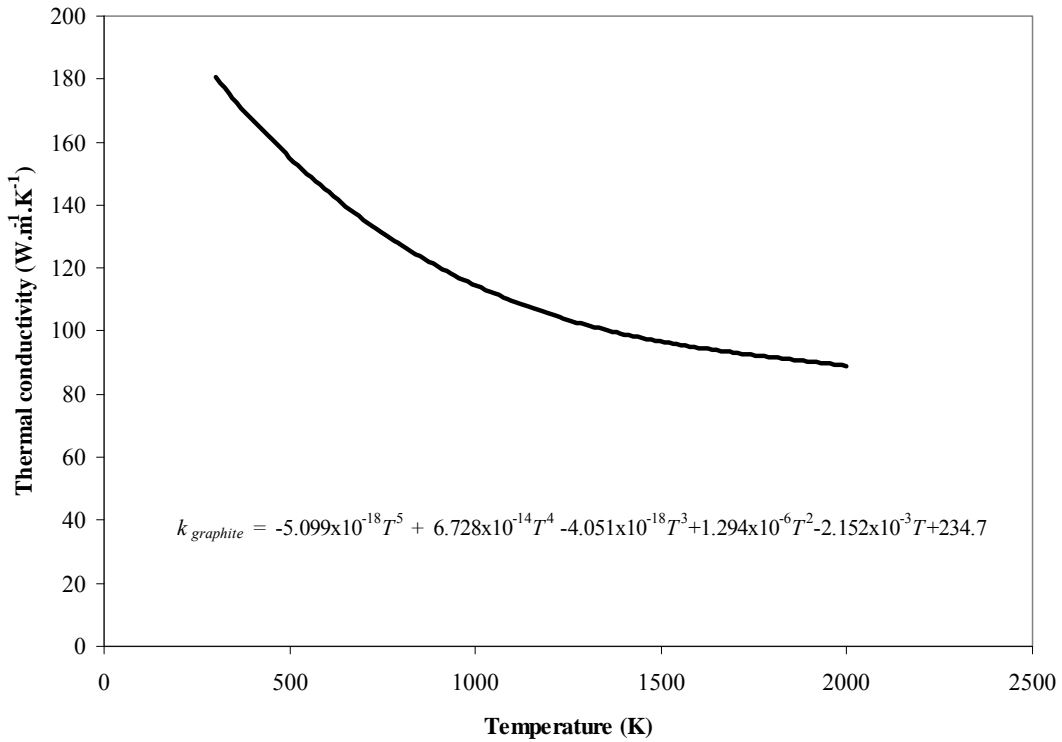
Figure 2.3. Thermal conductivity of graphite bulk material versus temperature with the best fit curve function.

Despite the fact that the value for α obtained from contact spot radii values (between 5 and 20 nm) and the average radius of the fibre (measured to be 10.5 μm) can vary from 500 to 2 000, a variation of less than 1% is obtained in the thermal conductivity resulting from conduction along the solid paths of the fibres of the felt.

The expected value of υ_f is given by Bardon and Danes (1994) as being between 0.13 and 0.15. However, this apparently small range of values leads to a 10% variation in k_{sc}. Figure 2.4 is a plot of k_{sc} calculated using equation (2.11) as a function of the absolute temperature for υ_f values of 0.13 and 0.15.

For a perfectly stratified felt (as assumed by Strong *et al* 1960 and Bankvall 1973) τ is equal to one. Because of fibre entanglement, as in the case of the WDF graphite felt used in the present research, the value of τ is greater than one. The thermal

conductivity (by conduction) as a function of the absolute temperature is presented in Figure 2.4, for different values of τ and υ_f.
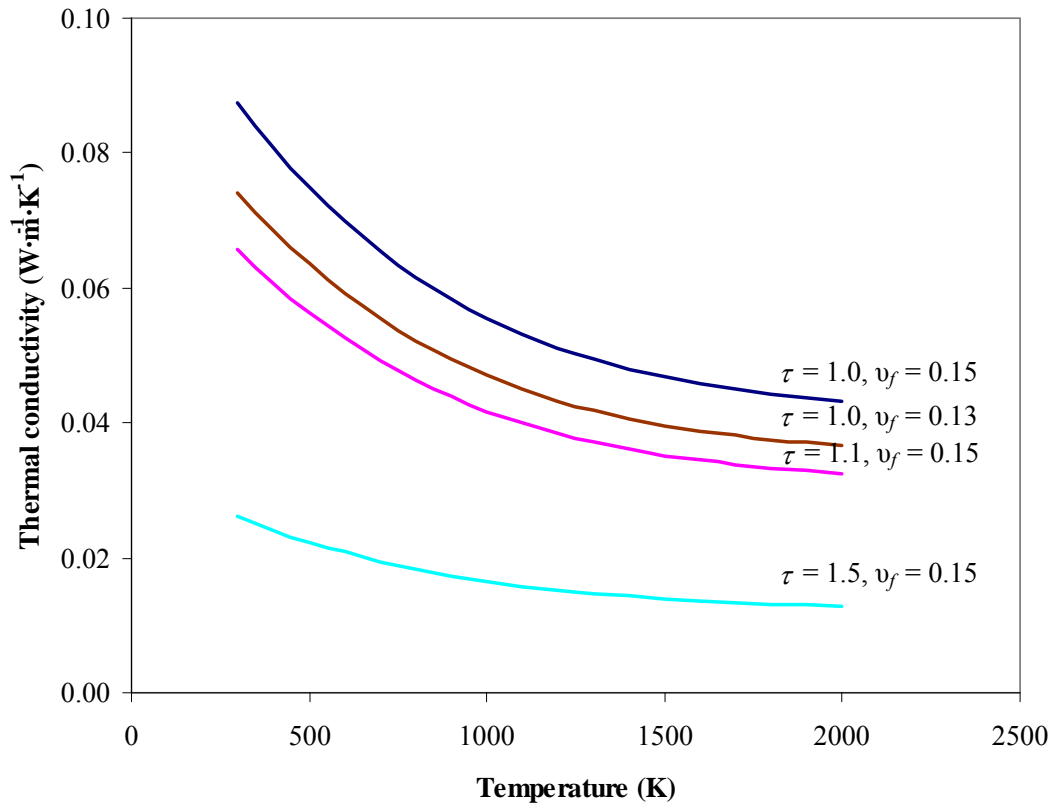
Figure 2.4. Plot of the thermal conductivity of graphite felt due conduction along the solid paths versus the absolute temperature for different values of υ_f and τ.

As can be seen in Figure 2.4, the thermal conductivity is very sensitive to variation in the tortuosity τ, a 10% change in τ leads to an almost 25% change in k_{sc}. Bardon and Danes (1994) stated that value of τ cannot be determined theoretically due to the geometrical complexity of the felt structure. Therefore, measurements of the thermal conductivity at room temperature are necessary to determine values for τ, and subsequently obtain k_{sc} as a function of the absolute temperature T.

2.1.1.5 Radiative Exchange Mechanism

The operating temperatures under which the graphite felt is used reach up to 3 000 K. This means that heat transfer by radiative exchange between the fibres is expected to be the dominating mechanism. The researchers on radiative exchanges among the fibres have found that the radiative thermal conductivity is proportional to T^3 (e.g.: Verschoor *et al* 1951 and Strong *et al* 1960). A list of investigators, who studied the radiative heat transfer mechanism, together with their correlations for k_{fr} are summarised in Table 2.2[1].

Table 2.2. Summary of k_{fr} values obtained by various investigators.

Investigator	k_{fr}	Experimentally determined factors.
Verschoor *et al*	$\dfrac{2\pi\sigma}{\alpha_f^2}\dfrac{r}{f}T^3$	$\dfrac{1}{\alpha_f^2}$ Opacity factor
Strong *et al*	$\dfrac{2\pi H\sigma}{\varepsilon}\dfrac{r}{f}T^3$	Emissivity, ε, and geometrical factor ,H.
Hager *et al*	$9\sigma\dfrac{r}{f}T^3$	None.
Bankvall	$\dfrac{2\pi\sigma}{\alpha_f^2}\dfrac{r}{f}T^3$	Opacity factor, $\dfrac{1}{\alpha_f^2}$.
Birekbak *et al*	$\dfrac{4F\sigma}{\varepsilon}\dfrac{r}{f}T^3$	Emissivity, ε, and geometrical factor ,F.
Tong *et al*	$\dfrac{4\sigma}{\beta\sigma_e}T^3$	Extinction factor, σ_e, and scattering function, β
Uny	$\dfrac{4\sigma}{\sigma_a+2\sigma_s}T^3$	Absorption and diffusion coefficients, σ_a and σ_s.

As can be seen in Table 2.2, the correlations for k_{fr} developed by Verschoor *et al* (1951), Strong *et al* (1960), Hager *et al* (1967), Bankvall (1973) and Birekbak *et al* (1979) are all proportional to $\dfrac{r}{f}$. These models, however, simplified or even neglected the radiative properties of the fibres such as the absorption and extinction coefficients.

---

[1] Some entries in the table were obtained from Tong and Tien (1980).

Alternatively, correlations obtained by Tong *et al* (1980, 1981 and 1983) and Uny's (1986) were developed on "two-flux" models derived from electromagnetic theory. They also took into consideration the radiation properties of the fibres. They assumed that each fibre is an absorbing, scattering and emitting medium. They emphasized that radiative heat transfer among the fibres is a strong function of the wavelength.

On the other hand, Hager *et al*'s model is the only model in Table 3 that does not have an experimentally determined factor. However, this model is only valid for a felt with large fibres, defined as having diameters greater than 100 μm. Such fibres are larger than the graphite felt fibres so cannot be used to predict the radiant heat transfer of graphite felts. Similar to the conduction along the solid paths discussed in the previous section, the remainder of the correlations have experimentally determined geometrical factors.

It may be noted from Table 2.2 that the radiative thermal conductivity can be calculated using a relation of the form,

$$k_{fr} = C_{fr}\sigma\frac{r}{f}T^3 .$$
(2.12)

Here σ is the Stefan-Boltzmann constant and C_{fr} is a radiation constant that is determined experimentally.

2.1.2 Ex perimental Determination of τ and C_{fr}

It appears therefore that direct measurements of felt thermal conductivity are necessary in order to calculate the conduction and radiation constants τ and C_{fr} respectively, as well as other felt properties, such as the density and the average fibre

radius used in the determination of the volume fraction f. These measurements are discussed in this section.

As mentioned in the introduction of this chapter, the felt used in our application is a graphite felt grade WDF manufactured by the MorganAM&T in the USA. Its density was measured, by the present author, to be 80 kg·m^{-3}. The radius of the graphite fibres was also measured using a projector magnifier. The measurements were carried out on a sample of fibres extracted from the felt. The results showed that the radius, r, varies between 7 and 13 μm. The arithmetic average of all measurements taken was 10.5 μm with a 3.2 μm standard deviation. Detailed descriptions of measuring the graphite felt density and average fibre radius are found in Appendix A.

The bulk density of the graphite fibres was obtained from the literature as between 1500 and 1770 kg·m^{-3} (Mantell 1968). The volume fraction, f, of the felt is defined as the ratio of the felt density to the bulk material density, so that 4.5%$<f<$5.5%. A value of 5% for f is therefore assumed.

Further to the work by Chahine *et al* (2005b), measurements of the thermal conductivity of WDF felt were carried out at NMIA using the "Hot-Wire" technique (Schneider 1998). This technique was used because of its suitability for materials with low thermal conductivity. A heating copper wire for room temperature testing and platinum wire for high temperature testing were sandwiched between two layers of WDF felt, with each layer being 80 mm long, 50 mm wide and 20 mm thick. A current of 7 A was passed through the wire causing its temperature to rise. The rise in temperature was obtained from a measurement of the voltage drop in the wire between two points 55 mm apart. The temperature rise was then plotted against time. The thermal conductivity, k, can be calculated from the solution to the transient heat conduction equation, given by Schneider (1998) as

$$\Delta T = \frac{P}{4\pi k}\left(ln\left(\frac{4\alpha_g t}{d_v^2}\right) - C \right),$$ (2.13)

in which, P is the power per unit length, α_g is the thermal diffusivity, t is the time, d_v is the distance between the contact points where the voltage is measured, and C is a constant.
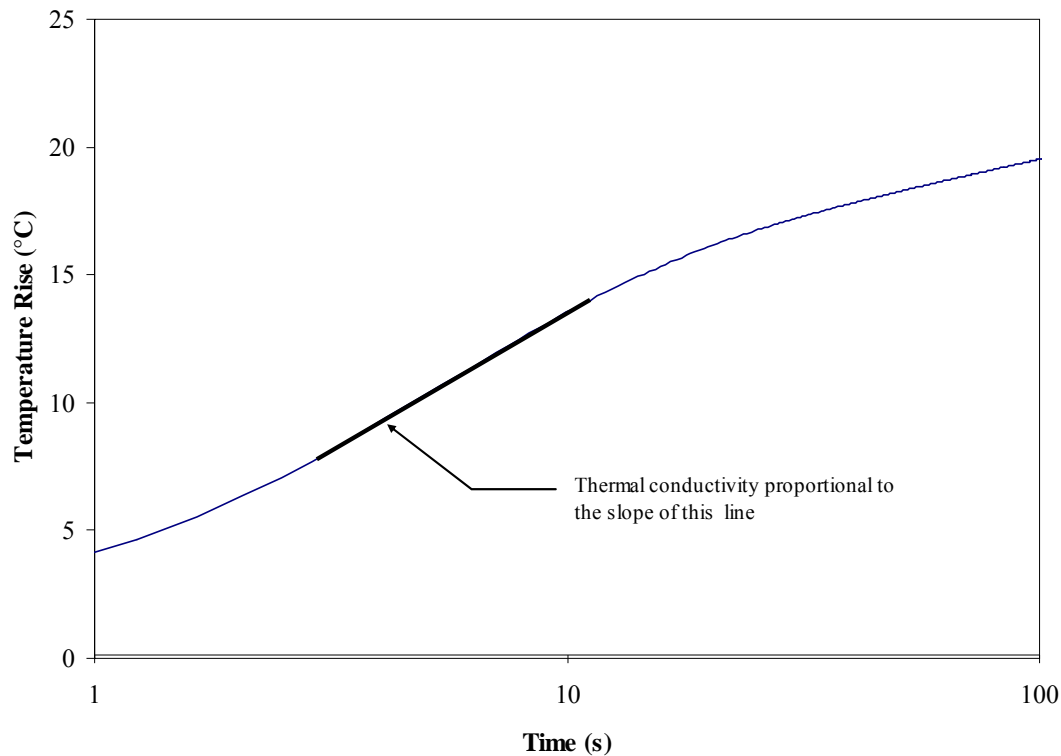
Figure 2.5. Rise in temperature due to heating of a copper wire sandwiched inside WDF graphite felt.

Figure 2.5 is a plot of the temperature rise in the middle of the felt versus time. The readings in the first few seconds were affected by the initial transients establishing the temperature field in and around the heating wire, and therefore they were discarded. The slowing of the temperature rise at the top end of the curve was taken to indicate that heat transfer had reached the edge of the felt. The straight line section of the plot indicated that heat was transferred in the felt only, and hence this section was used to calculate the thermal conductivity. This technique was validated by measuring Perspex thermal conductivity and comparing the measured values with that obtained from the literature. The results showed agreement within the specified uncertainties.

Two sets of measurements were carried out. The first set was conducted at room temperature in vacuo, air and nitrogen to determine τ, and the second set was conducted in nitrogen and helium at temperatures up to 700 °C to determine C_{fr}.

At room temperature, air was used because it is readily available and has similar thermal conductivity to nitrogen and argon. The results obtained in vacuo, air and He are presented in Table 2.3.

Table 2.3. Measured thermal conductivities of WDF graphite felt measured at room temperature in vacuo, air and helium.

Measured in	Thermal Conductivity W·m^{-1}·K^{-1}	Uncertainty W·m^{-1}·K^{-1}
vacuo	0.064	0.013
air	0.077	0.016
helium	0.232	0.034

The repeatability of the measurements given in the above table was found to be less than 5%; the repeatability is defined here to be the standard deviation of the repeated measurements. The uncertainty expected in the measurement of the thermal conductivity is around 10-20% (Lutkov *et al* 1975). The difference between the measurement in vacuo and the one in helium is 0.168±0.04 W·m^{-1}·K^{-1}, with the thermal conductivity of He at room temperature being 0.151 W·m^{-1}·K^{-1}. Also, the difference between the measurement in vacuo and the one in air is 0.013±0.014 W m^{-1} K^{-1}, while the air thermal conductivity at room temperature is 0.026 W·m^{-1}·K^{-1}. Hence, the results obtained are all in agreement within their uncertainties.

In the absence of any gas at room temperature, heat transfer occurs by conduction only. Using (i) equation (2.11), (ii) the measurement in vacuo from Table 2.3, and (iii) assuming a value of $\upsilon_f = 0.15$ and $\alpha = 500$ then the tortuosity ratio τ can be calculated to be 1.11. This value indicates that 11% of the felt fibres cross from one layer to another, which is considered to be a realistic expectation.

Substituting the values of υ_f, α and τ into equation (2.11) leads to the following equation:

$$k_{sc}(T) = 3.53985 \times 10^{-4} k_s(T), \qquad (2.14)$$

which can be used to calculate the graphite felt thermal conductivity due to conduction along solid paths.

The second set of measurements was conducted in N_2 and He and at temperatures up to 700 °C. These results are plotted in Figure 2.6 and Figure 2.7 respectively.
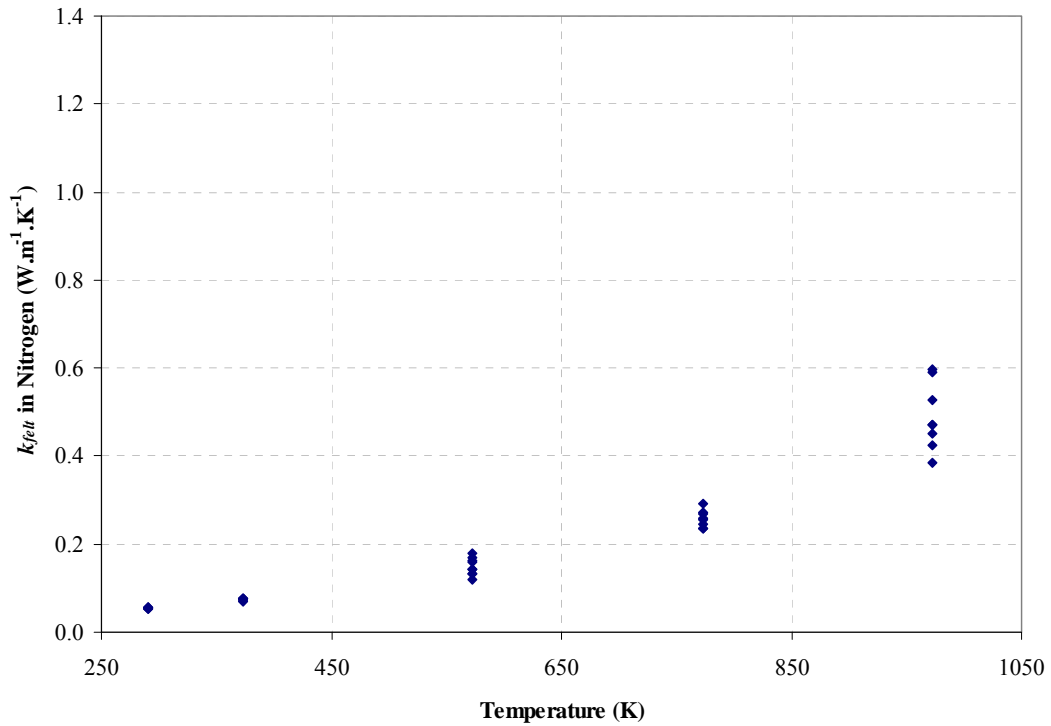
Figure 2.6. Plot of the measured graphite felt thermal conductivity in nitrogen at the NMIA.
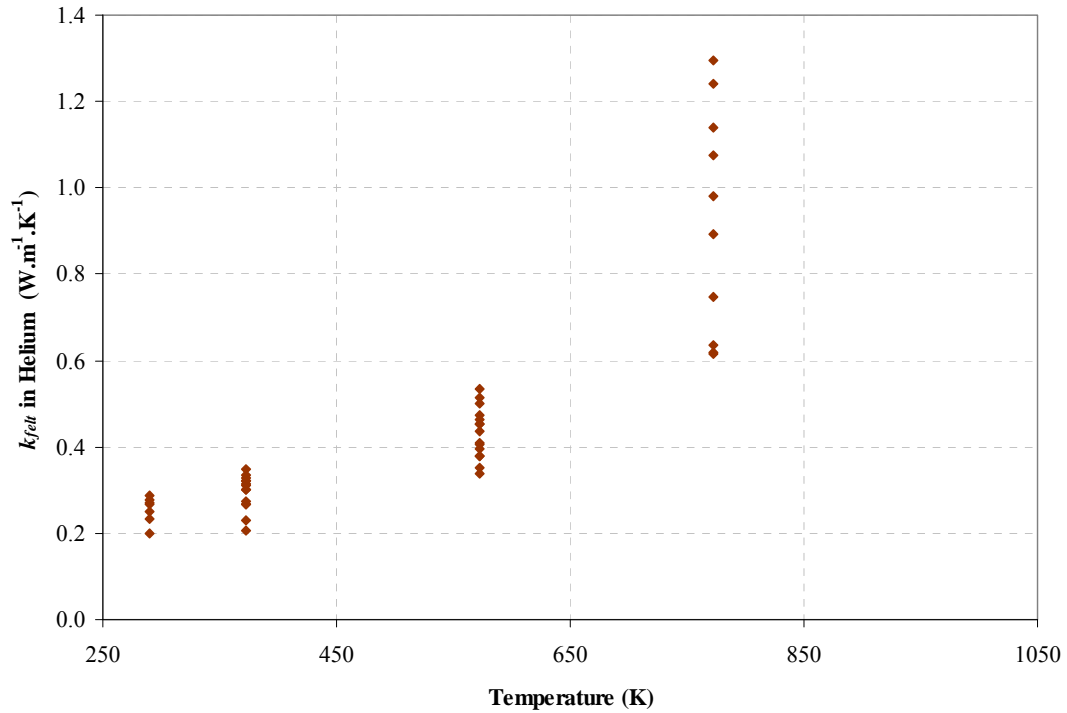
Figure 2.7. Plot of the measured graphite felt thermal conductivity in helium at the NMIA.

As can be seen from the plots, the scatter in the thermal conductivity measurements increases with the temperature. This may be caused by the small size of the sample used (limited by the furnace dimensions), and the heat losses along the hot wire with the increased temperatures. Using (i) equation (2.12), (ii) r =10.5 μm and f =0.05, and (iii) the measured felt thermal conductivity values, C_{fr} is calculated to be between 10 and 35, which is a large span and needs to be narrowed down.

A better estimation of C_{fr} can be obtained by cross examining thermal conductivity measurement of similar felt based on the felt density. A literature survey undertaken by the present author obtained measured thermal conductivity of similar felt by Lutkov *et al* (1975) on graphite and carbon felts. The physical properties of Lutkov *et al*'s felt were similar to the graphite felt used in this work. Their felt density was 50 to 100 kg·m^{-3} compare to 80 kg·m^{-3} for the WDF graphite felt.

Lutkov *et al*'s measurements of the felt thermal conductivity were carried out in vacuo, argon and helium in the range of 300 to 1 100 K. This allowed a mean for

comparing their results to the ones presented here. Lutkov *et al*'s results are shown in Figure 2.8. These results have an uncertainty of 20%.
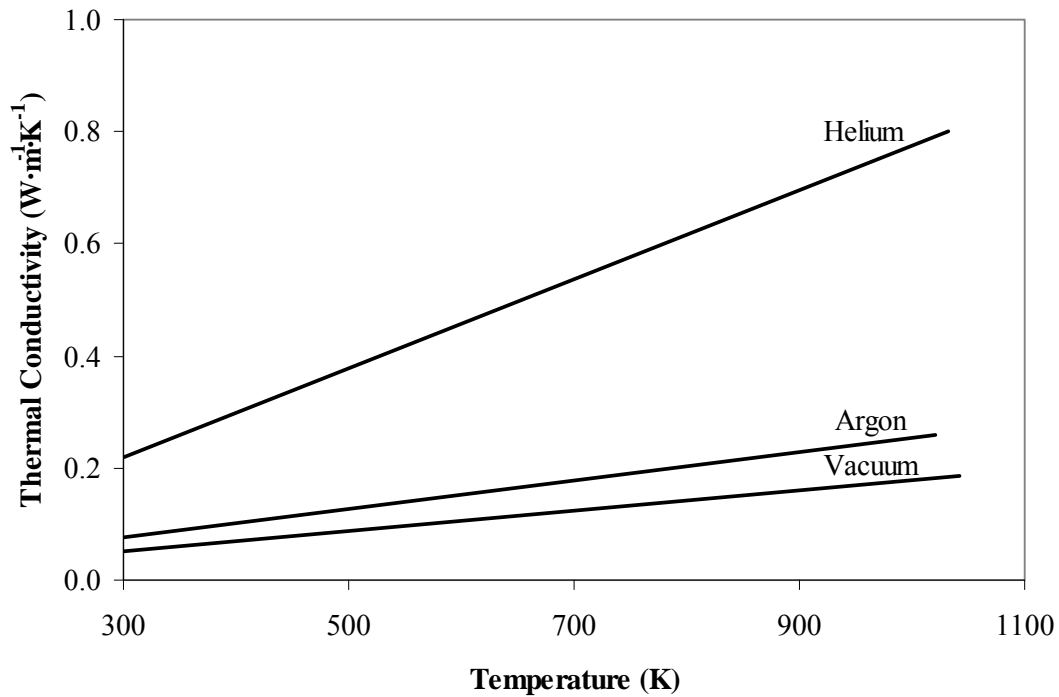
Figure 2.8. Thermal conductivity of graphite felt as a function of the absolute temperature given by Lutkov *et al* (1975).

Referring to Figure 2.8, the thermal conductivity in vacuo at a temperature of 900 K is 0.166 W·m^{-1}·K^{-1}, and therefore C_{fr} is calculated to be 15.0. This narrowed the value for C_{fr} to be 15.0.

2.1.3 Final Thermal Conductivity

The apparent thermal conductivity of the WDF graphite felt given in equation (2.6) can now be rewritten to include equations (2.12) and (2.14) and the calculated value of C_{fr} =15.0, giving:

$$k_f(T) = \frac{k_{gc}(T) + 15.0\sigma\frac{r}{f}T^3}{1 - f} + 3.53985 \times 10^{-4} k_s(T).$$ (2.15)

This equation can be used to calculate the apparent thermal conductivity at any temperature T. In addition, it can be used to calculate the apparent thermal conductivity for felt with different fibre radius and volume fraction. As an example, the apparent thermal conductivity versus the absolute temperature for two felts with densities of 50 and 80 kg·m^{-3} are plotted in Figure 2.9. The heat transfer mechanisms for each felt are also plotted in this figure.

At low temperatures (less than 500 K), the felt thermal conductivity is dominated by the solid and gas conduction mechanisms. At higher temperatures, radiation and to some extent gas conduction (based on the gas used), overwhelm heat transfer in the felt. The radiative heat transfer mechanism is very sensitive to any change in the felt density, but other heat transfer mechanisms do not change substantially.

The measurement uncertainty of k_f can be determined from the mathematical model in equation (2.15). It consists of the measurements uncertainties of T, k_{gc}, k_s, r and f. The measurement uncertainty in T is less than 0.1% and therefore can be ignored (temperatures can be measured to better than 0.1% using conventional thermocouples). Although the uncertainty in k_s can be as high as 10%, its contribution to k_f is small especially at high temperatures (where the contribution of conductive heat transfer is negligible, refer to Figure 2.9) and hence can be ignored. Similarly, the contribution of the measurement uncertainty of k_{gc} is minimised by the fact that its contribution to k_f is also small. As shown in Appendix A, the measurement uncertainty of r is negligible. On the other hand, the measurement uncertainty of f was calculated to be 2.2% (see also Appendix A).
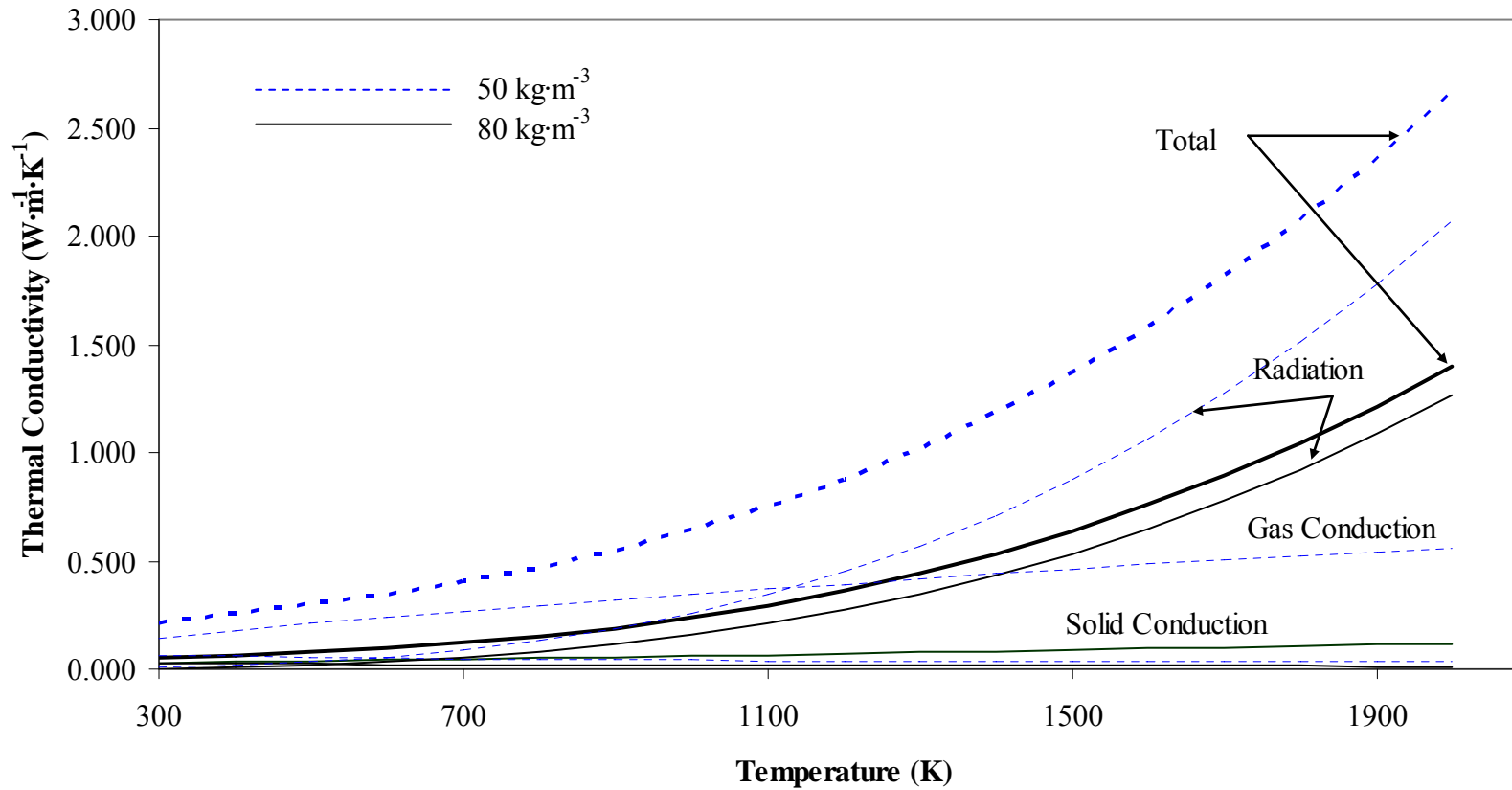
Figure 2.9. Plots of the apparent thermal conductivity of two felts with densities of 50 (blue) and 80 (black) kg·m⁻³ and their heat transfer mechanisms versus the absolute temperature.

Hence it can be deduced from the above that the measurement uncertainty of k_f should be less than 2.5%. However, it is important to note that the value of k_f relies also on the accurate determination of C_{fr}, which was determined in section 2.1.2 to be 15.0. However, this value relied mainly on the measurement uncertainty of the thermal conductivity of graphite felt at high temperatures, which was in the order of 10-20%. On the other hand, by cross examining the results with that of Lutkov *el al*, the uncertainty of C_{fr} can be narrowed to 10%, and hence resulting in similar measurement uncertainty for k_f.

2.1.4 Conclusions on the Graphite Felt Thermal Conductivity

It was apparent form the literature review that the determination of thermal conductivity of fibrous material in general and graphite felt in particular is a complicated matter, which requires a combination of theory and experiments. While the gas conduction heat transfer mechanism is fairly straightforward and values for the thermal conductivities of the gases could be easily obtained, the conduction and radiative mechanisms proved to be more complex and problematic due to the intricate geometry of the felt. Most of the conductivity models are still purely empirical and they could not predict the conduction thermal conductivity without resorting to experimental results. Similarly, most of the radiative mechanism models reviewed have geometrical factors, which must be determined experimentally. As a conclusion, the apparent thermal conductivity of the WDF felt cannot be obtained on a purely theoretical basis. In this work, an empirical model for the thermal conductivity of graphite felt has been developed which allows for different density, fibre diameter and gas conduction as a function of temperature.

2.2 Thermophysical Properties of ATJ Graphite

2.2.1 Over view

Graphite is considered by many investigators (Mantell 1968 and Tyler 1953) to be one of the better materials for use in high temperature applications such as ballistic vehicles, rocket engines, nuclear power sources and blackbody graphite furnaces. Although graphite can be formed naturally from carbon, this is rare, and most of the available graphite is produced artificially by graphitisation process (Union Carbide 1964), which is the transformation of amorphous carbon to artificial graphite. It follows that the thermophysical properties of graphite may be influenced by this graphitisation process. An overview of this process is presented herein.

Prior to graphitisation, the coal is crushed by mills and sized into a series of fractions through screens. This produces raw materials with different grain sizes varying from 0.2 to 20 mm, which are collectively referred to as "coke". The crushed material is then combined with coal tar pitch to make a formable plastic mix; which is then heated to assure homogeneity (Union Carbide 1964). The mix is then subjected to a "first bake" in a large furnace purged with N_2 to develop infusible carbon bonds between the pieces constituting the mix (Mantell 1968). This is done by heating the mix to a temperature between 750 and 900 °C. Following the first bake is the graphitisation process, which transforms carbon to graphite. During graphitisation, the graphite crystals in the mix are rearranged in an ordered pattern of stacked parallel planes. The process of graphitisation involves the gradual heating of the mix up to 3 000 °C. From room temperature to about 1 500 °C there are no significant dimensional changes, between 1 500 and 2 000 °C a volume expansion of 0.2 to 0.6% occurs, and above 2 000 °C crystallite growth predominates up to 2 600 °C. In general, graphitisation starts at approximately 2 200 °C but in order to produce better quality graphites with high purity, high temperatures ranging from 2 700 to 3 000 °C are sometimes used (Union Carbide 1964). High purity graphite consists of at least 98% carbon. During baking, the raw material is heated at different temperatures and for a long period, then it is pressed and place under pressure. Baking affects the density and the porosity of the graphite produced. This effect could vary depending on

the method used for baking. The higher the temperature and pressure used, the denser is the produced graphite.

The graphitisation process is important in determining the thermophysical properties of the resulting graphite. During the production process, the thermophysical properties such as the electrical and thermal conductivities increase with temperature. For the formed graphite, any deviations observed in its final properties are the results of variations of the production process. These production variations can be caused by many effects including the grain size and shape of the raw materials used, the forming method and the effect of the first bake and graphitisation (Mantell 1968, p. 330).

The particle or grain size of the raw materials used affects the density of the produced graphite; the density varying inversely with the grain size. For example, the density of graphite varies from $1\,550\,\text{kg·m}^{-3}$ for a grain size of 0.4 mm to $1\,440\,\text{kg·m}^{-3}$ for a grain size of 37 mm. In addition, this grain size has an effect on the anisotropy of the graphite, with large grain sizes resulting in more anisotropic graphite. Table 2.4, (data obtained from Mantell 1968, p. 336), demonstrates the effect of the grain size on the density and specific electrical resistance.

Table 2.4. Effect of grain size on the density and electrical resistivity of graphite.

	Fine Grain 0.4 mm	Medium Grain 3 mm	Coarse Grain 37 mm
Density (kg·m^{-3})	1 550	1 540	1 440
Specific electrical resistance ($\Omega\cdot\text{cm}$)	8.5×10^{-4}	8.9×10^{-4}	11.9×10^{-4}
Ratio of specific electrical resistance (with-the-grain/across-the-grain)	0.51	0.79	0.85

The forming method employed during the graphitisation process combined with the grain size and shape of the particles affect the homogeneity of the produced graphite. During the forming process, the raw material can either be extruded by applying pressure to the material, or moulded into different shapes. The shape of the grains is closer to a rod than a cube, and during forming the grains tend to take a preferred orientation along their axes. The "with-the-grain direction" refers to the direction

parallel to the direction of extrusion in an extruded piece of graphite and perpendicular to the direction of moulding pressure in a moulded piece, whilst the "across-the-grain" direction is defined as the direction perpendicular to extrusion and parallel to the moulding. For example, for the same fine-grained raw material with 0.4 mm in size, the density of the produced graphite varies from 1 640 kg·m^{-3} when it is extruded to 1 750 kg·m^{-3} when moulded.

Hence, the thermophysical properties of graphite change depending on the forming method used. An example of property changes is illustrated in Table 2.5, in which values of specific electrical resistance and density, for extrusion and moulding methods, are compared.

Table 2.5. Difference in properties for a fined-grained graphite when extruded and moulded.

	Extruded	Moulded
Density (kg·m^{-3})	1 640	1 750
Specific electrical resistance (Ω·cm)		
With-the-grain	8.60×10^{-4}	9.60×10^{-4}
Across-the-grain	16.20×10^{-4}	13.20×10^{-4}
Ratio	0.53	0.73

The combined effects of the grain size and the forming method on the thermal conductivity and density of different types of graphite were also investigated. Table 2.6 summarises the densities and the "with-the-grain" and "across-the-grain" thermal conductivities at room temperature for various graphite products by Union Carbide Corporation (Union Carbide 1964).

Table 2.6. Different types of graphite with their characteristics, densities and thermal conductivities.

Graphite Type	Forming Method	Grain Size	Density	Thermal Conductivity	
				with-the-grain	across-the-grain
		(mm)	(kg·m^{-3})	(W·m^{-1}·K^{-1})	(W·m^{-1}·K^{-1})
AGSR	Extruded	0.4	1580	155	87
AGSX	Extruded	0.4	1670	162	97
ATL	Extruded	0.8	1730	146	121
AGOT	Extruded	0.8	1700	950	577
AGA	Moulded	12.7	1650	125	119
ATJ	Moulded	0.2	1730	118	90

To some extent, the thermal conductivities of the extruded graphite types (AGSR, AGSX, ATL and AGOT) increase with increasing densities in both directions (with-the-grain and across-the grain). It is also apparent that the thermal conductivity in the "with-the-grain" direction is considerably higher than the "across-the-grain" direction for all types; this higher thermal conductivity may be explained by better heat transfer along the "with-the-grain" direction where the material is less porous. On the other hand, it can be noted that the difference in thermal conductivity between the two directions is considerably less in the moulded graphite. This is due to the fact that when the raw material is moulded, it is not subjected to one directional pressure that tends to align the grain in one direction. However, the extruded graphite types exhibit much higher conductivities in general, especially along the "with-the grain" direction. Also, based on the above tabulated values, it can be concluded that there is no relation between the density of graphite and its thermal conductivity. For example, the AGOT type has a similar density to ATJ but the thermal conductivity of the later is around a factor of 8 less.

Other physical properties are affected by the manufacturing process of extruding or moulding of the graphite, however only the density, specific heat, electrical resistivity and thermal conductivity of the ATJ will be discussed in this literature survey.

As stated before, understanding the effects of the graphite manufacturing processes (grain size, baking temperature and forming method) on the thermophysical properties is important in order to estimate the uncertainty associated with the data obtained for

these properties. It can be concluded from the above that the major variances arise due to imperfection and variation in the manufacturing processes. For example, when crushing the raw material, the grain size produced can vary from one mill to another, which leads to variation in the thermophysical properties of the produced graphite. Another example may be the difference in the baking furnace temperature uniformity, which can affect the homogeneity of the produced graphite and thus its thermophysical properties.

2.2.2 ATJ Graphite

ATJ is a grade of graphite produced by Carbon Products Division at the Union Carbide Corporation. It is extremely fined-grain with a maximum size of 0.2 mm. ATJ is a high-strength essentially flaw free premium quality graphite. It can be machined to very close tolerances with sharp details and fine surface finishes (Union Carbide 1964). ATJ graphite is formed by moulding it into blocks with different lengths and diameter sizes. This type of graphite was designated as GBH type during development stage (Ho *et al* 1968). ATJ is used in applications which require a superior surface finish and high strength; for example moulds for metal casting operations, rocket motor nozzle inserts and blackbody furnaces.

The heating element of the 48kW graphite furnace at NMIA is made of ATJ graphite. The density, specific heat, electrical resistivity and thermal conductivity of the ATJ graphite have to be known to obtain accurate numerical models of the Thermogage furnace, which are then used in the optimisation of the its performance.

2.2.2.1 Density

The density of the ATJ graphite was found in the literature to be $1\,730\ \mathrm{kg \cdot m^{-3}}$ by Ho *et al* (1968), Mantell (1968, p. 328) and Union Carbide (1964). Also, the value for the density was found to be $1\,700\ \mathrm{kg \cdot m^{-3}}$ by Taylor *et al* (1969) and $1\,760\ \mathrm{kg \cdot m^{-3}}$ by

Touloukian (1970, p.11). In addition, the ATJ density was measured by the present author at NMIA using the water displacement method and it was found to be 1 700 kg·m^{-3}. These density values are summarised in Table 2.7.

Table 2.7. Table of ATJ graphite bulk density by different investigators.

Source	Bulk Density (kg·m^{-3})
Ho *et al* (1968)	1 730
Mantell (1968)	1 730
Union Carbide Handbook (1964)	1 730
Taylor (1969)	1 700
Touloukian (1970)	1 760
NMIA (local measurement in 2003)	1 700

The average of the above values is 1 730 kg·cm^{-3} and it can be deduced from the maximum and minimum values that the density of ATJ graphite varies up to 3.5%. This variation can be explained by the variation in the ATJ graphite manufacturing processes. The density of ATJ material was measured at NMIA and by the listed investigators in Table 2.1 to better than 1%.

2.2.2.2 Specific Heat

Mantell (1968) stated that the values of specific heat at temperatures above room temperature for all types of natural and manufactured graphite are essentially the same. At temperatures below room temperature, the difference between natural and manufactured graphite can reach up to 10%. However, specific heat below room temperature is not relevant for this thesis, and therefore will not be discussed in this literature review.

Figure 2.10 is a collection of different graphs of specific heat versus temperature ranging from 0 to above 3 000 K. These graphs are based on experimental results collated by Touloukian (1970) and Mantell (1968). The results of Touloukian are for different types of natural and manufactured graphites. Type 3474 is a fine-grained and

uniform graphite with a density of around 1 040 kg.cm^{-3}, and the reported uncertainty of the specific heat values given by Touloukian is 5.0%. The carbon graphite type has a high purity with a reported uncertainty of 5.0%. The ATJ type consists of 99.5% carbon and 0.5% carbides (e.g. Silicon, Iron and other traces) with a density of around 1 760 kg·cm^{-3}, and the reported uncertainty of less than 5.0%. The specific heat values of ATJ in He have a reported uncertainty of 2.9% or better. The GBH type is similar to ATJ, and there was no mention on the reported uncertainty.
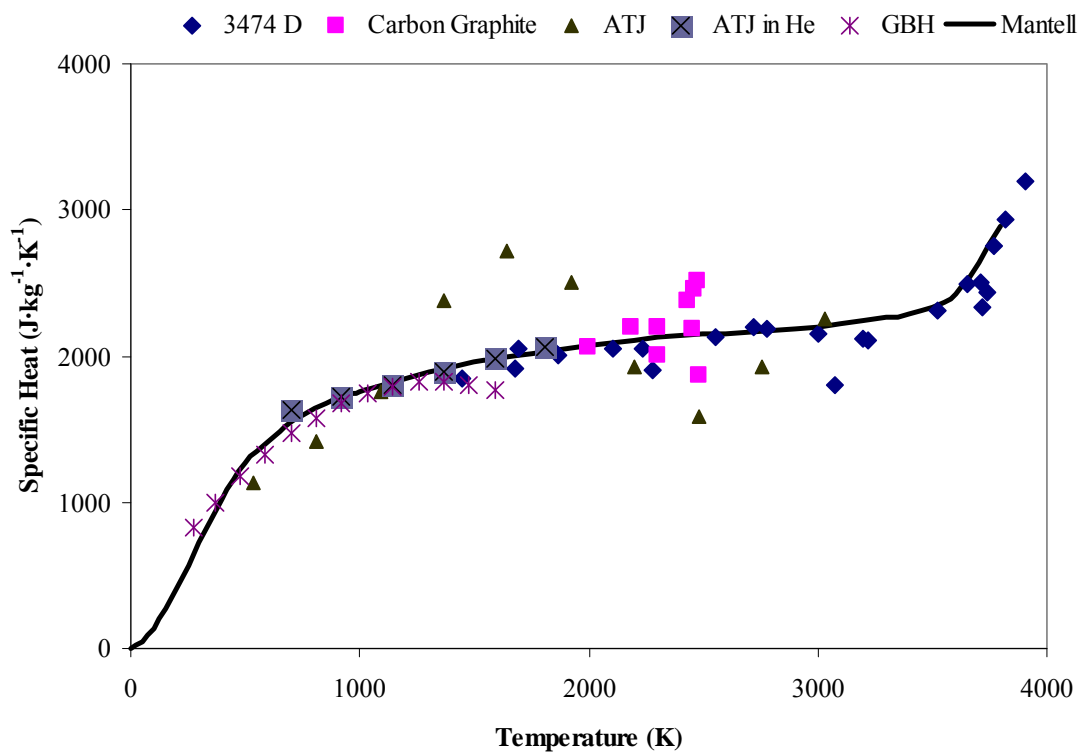
Figure 2.10. Specific Heat versus temperature for different type of graphites.

The best fit curve given by Mantell (1968),

$$C_p = 0.44391 + 0.30795 \times 10^{-4} T - 0.61257 \times 10^5 T^{-2} + 0.10795 \times 10^8 T^{-3}$$, (2.16)

55

is in agreement with the results taken from Touloukian (1970) within their given uncertainties. Here, C_p is the specific heat of graphite in J·kg^{-1}·K^{-1} and T is the absolute temperature in Kelvin. This equation can be used in the numerical model to obtain the specific heat of graphite at temperatures ranging from 300 to 3 200 K. According to Mantell (1968), the above equation is reliable to better than 2%. On the other hand, the associated uncertainty given by Touloukian (1970) is 5%.

2.2.2.3 Electrical Resistivity

During the operation of the 48kW Thermogage furnace, the ATJ graphite tube is heated ohmically by passing a high current through it. Therefore, values for the resistivity of the graphite are needed to calculate the electrical power generated across the tube.

Kinchin (1953) stated that the first recorded electrical resistivity measurements of graphite in the "with-the-grain" direction were carried out by Washburn in 1915 and Ryschewitsch in 1923 using Ceylon Graphite. However, their measurements were obtained at room temperature with values ranging from 4×10^{-5} to 8×10^{-5} Ω·m. In his review, Kinchin (1953) also stated that Roberts in 1913 and Meissner *et al* in 1932 conducted measurements at different temperatures. Their measurements were made in the "across-the-grain" direction. Kinchin (1953) observed that works carried out by Washburn and Krishnan *et al* concluded that the electrical resistivity in the "with-the-grain" direction is substantially greater than that of the "across-the-grain direction" by more than 10% difference.

Measurements on pyrolytic graphite, which has a low anisotropic quality and high density, were made by Klein (1966). He published extensive studies on graphite properties in both directions. More measurements were made by Taylor (1972) on different grades of graphite, namely ATJ-S which is a slightly denser grade than ATJ with higher thermal conductivity. The results obtained by Taylor, plotted in Figure 2.11, confirmed the findings by Washburn and Krishnan *et al* that the electrical resistivity in the "with-the-grain" direction is higher than the "across-the-grain". His

results also showed linear relationship between the electrical resistivity and the absolute temperature between 1 400 and 2 400 K.
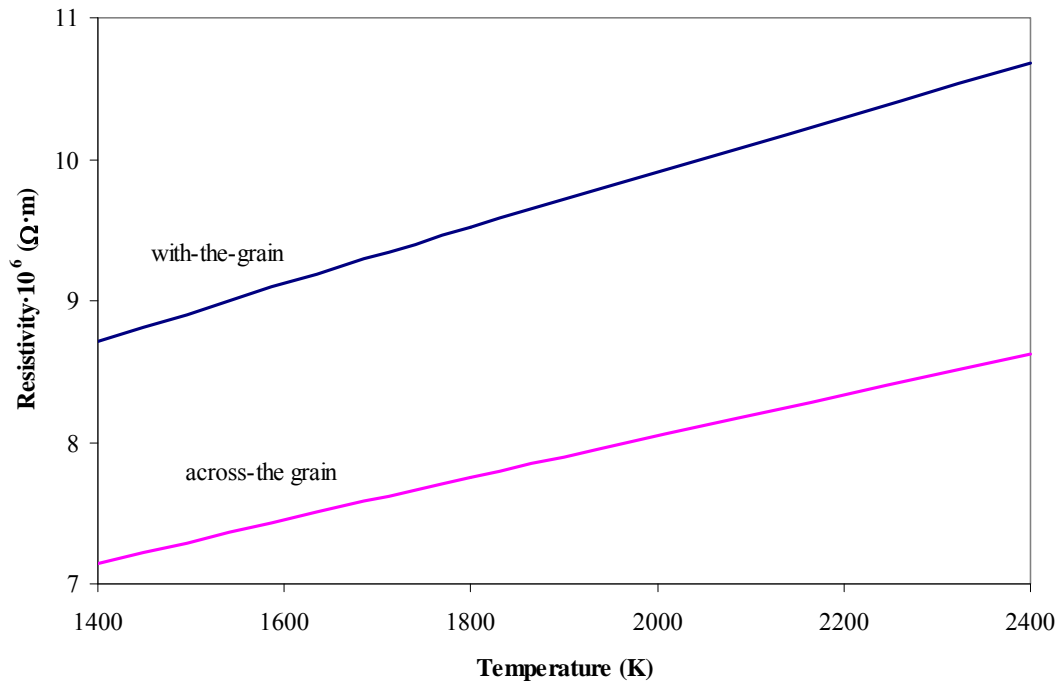
Figure 2.11. Graphite electrical resistivity in the "with-the-grain" and "across-the grain" directions at different temperatures (Taylor 1972).

It can be concluded that the electrical resistivity can vary substantially within the graphite itself depending on the measured direction. As demonstrated above by Taylor (1972), the variation in the resistivity can reach up to 20%. Usually, the orientation of the grain in a piece of graphite can not be accounted for by visual inspection and therefore the difference in resistivity caused by the grain direction can become a major uncertainty component in determining the electrical resistivity of the graphite.

Investigations carried out on the electrical resistivity of the ATJ grade graphite found data for only the electrical resistivity in the "with-the grain" direction (Horn 2000). Horn's data are then compared to Taylor's as shown in Figure 2.12.
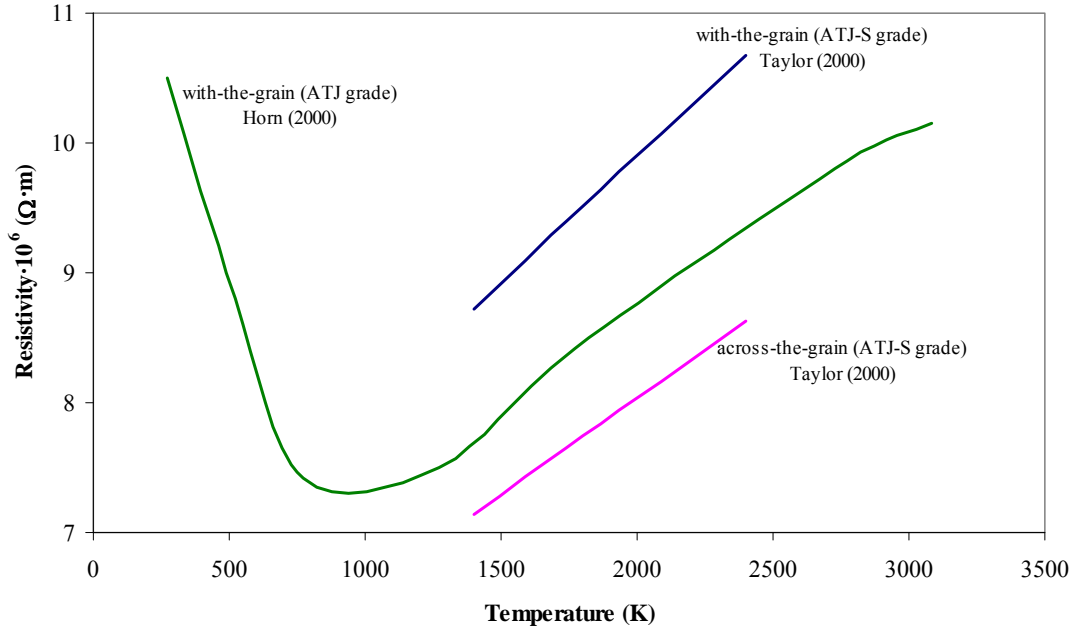
Figure 2.12. Plots the ATJ graphite electrical resistivity given by Horn (2000) and Taylor (1972).

Referring to the Figure 2.12, the ATJ graphite electrical resistivity given by Horn (2000) drops to its minimum around 1 000 K, or it can be said that ATJ graphite is most conductive at 1 000 K. Above this temperature, the relation between the temperature and the electrical resistivity rises in a linear manner, which confirms Taylor's findings. The direction of the grain is not well accounted for and hence the uncertainty associated with using these data can be as high as 20%.

In the numerical model, the values given by Horn (2000) can be used in the determination of the ATJ graphite electrical resistivity. These values are fitted to a 4th degree polynomial with the form,

$$\omega_{ATJ}(T) = 4.628 \times 10^{-19}T^4 - 4.247 \times 10^{-15}T^3 + 1.374 \times 10^{-11}T^2 \\ -1.688 \times 10^{-8}T + 1.424 \times 10^{-5} \qquad . \quad (2.17)$$

Here ω_{ATJ} is the electrical resistivity of ATJ graphite and T is the absolute temperature.

2.2.3 ATJ Graphite Thermal Conductivity

The thermal conductivity of graphite at different temperatures had been investigated by many researchers: Rasor *et al* (1960), Ho *et al* (1968), Mantell (1968), Reynolds (1968), Touloukian (1970), Taylor (1972), Bapat & Nickel (1973). It was found that the general features of the variation in thermal conductivity with the absolute temperature follow in general the trend plotted in Figure 2.13.
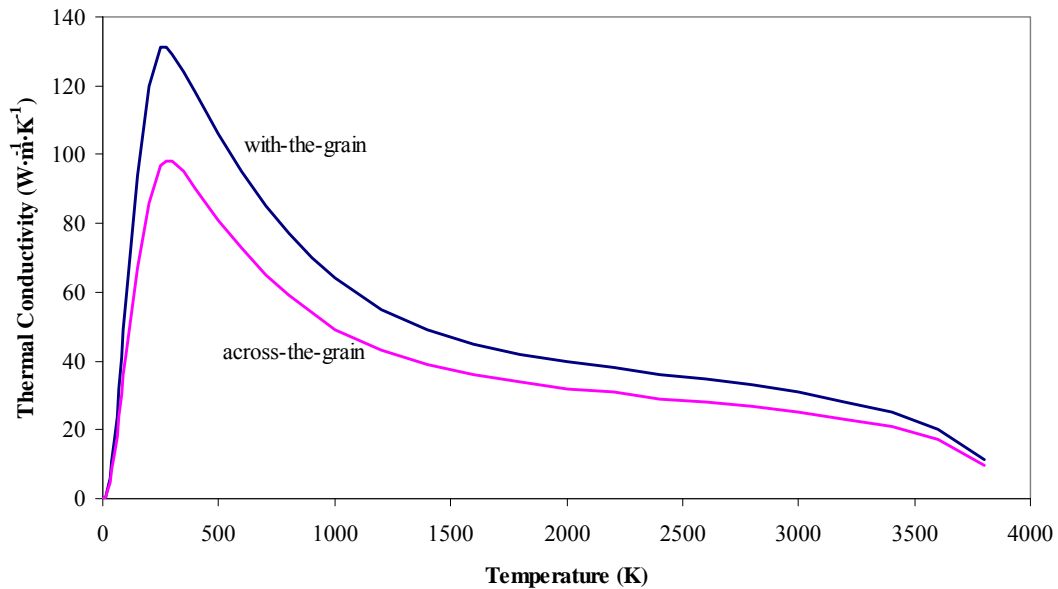
Figure 2.13. Plots of the "with-the-grain" and "across-the-grain" thermal conductivity versus the aboslute temperature (Touloukian *et al*, 1970).

The maximum thermal conductivity of graphite is obtained around room temperature. According to Mantell (1968, p. 363), the graphite thermal conductivity below room temperature follows a T^2 trend (T being the temperature), and a T^{-1} trend above it. As mentioned earlier, only values of the graphite thermophysical properties above room temperature are of interest to this work and hence its thermal conductivity within this range is surveyed.

Recalling that, due to the anisotropic nature of graphite, the thermal conductivity is higher in the "with-the-grain" direction in comparison with the "across-the-grain", and referring to Figure 2.13, it can be seen that the maximum difference was observed to occur at around room temperature.

Values of the thermal conductivity of the ATJ grade graphite, in the "with-the-grain and "across-the-grain" directions, as a function of the absolute temperature given by Ho *et al* (1968), Mantell (1968) and Touloukian (1970) were collated and are plotted in Figure 2.14.
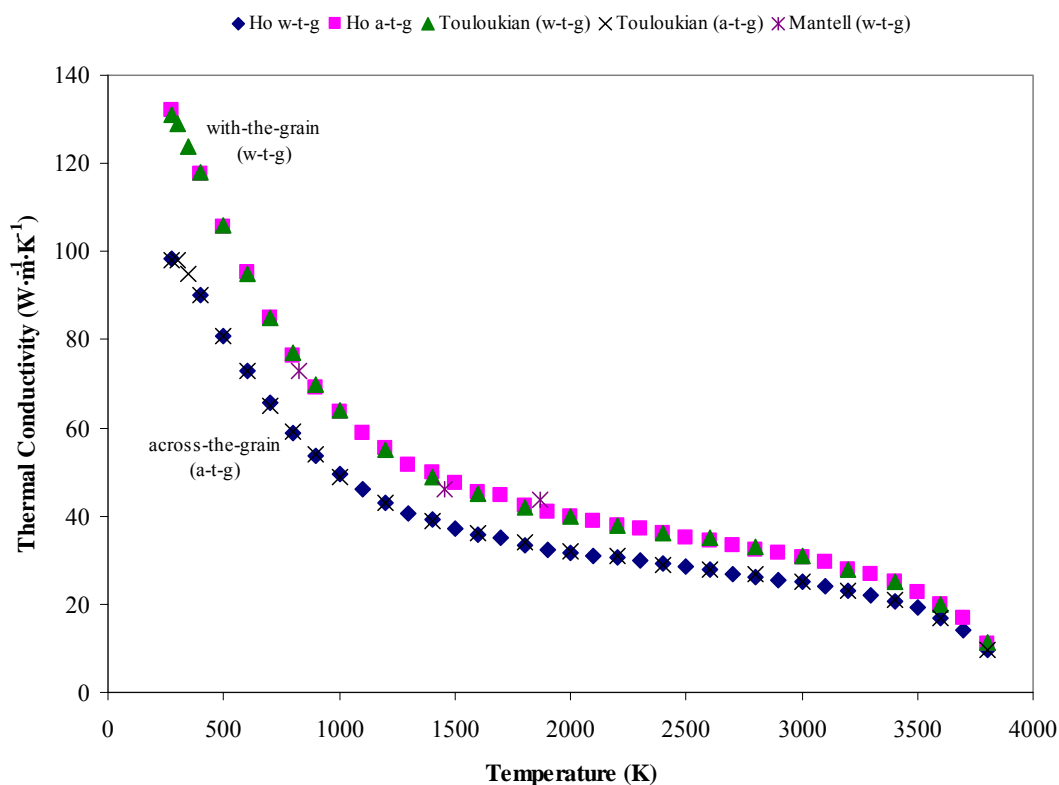
Figure 2.14. Values of the ATJ graphite thermal conductivity given by Ho *et al* (1968), Mantell (1968) and Touloukian (1970) as a function of the absolute temperature.

As can be observed, the values of the ATJ graphite thermal conductivity given by the different investigators agree within 2%. On the other hand, the uncertainty in the thermal conductivity values was given by Ho *et al* (1968) to be 10%. There was no

mention of uncertainty by the data given by Touloukian (1970) or Mantell (1968). Therefore, the uncertainty given by Ho *et al* can be adopted and the average values of the three sets of data can be calculated and taken with 10% uncertainty as the ATJ thermal conductivity.

Since the grain direction in a piece of graphite cannot be easily determined when inspected visually, it is best to use the average thermal conductivity, $k_{average}$, calculated using the equation given as (Pratt 1969),

$$k_{average} = 1/3\, k_{across} + 2/3\, k_{with}\,, \qquad (2.18)$$

in which, k_{across} and k_{with} are the "across-the-grain" and "with-the-grain" thermal conductivities respectively. The plots in Figure 2.15 were obtained by averaging the values obtained by the different investigators in Figure 2.14 and using equation (2.18).
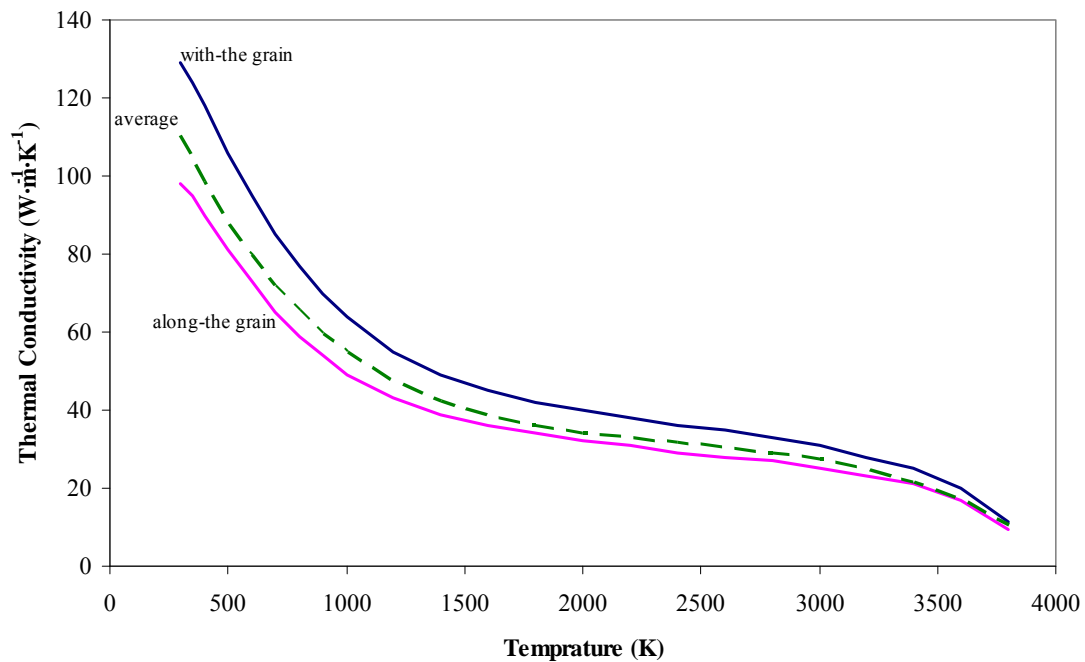
Figure 2.15. Plots of the ATJ graphite "with-the-grain" and "across-the-grain" and their average thermal conductivities.

The calculated average values above, shown as the green dotted line, can be fitted to a 5th degree polynomial to give,

$$k_{ATJ}(T) = -5.749 \times 10^{-16} T^5 + 7.176 \times 10^{-16} T^4 - 3.984 \times 10^{-8} T^3$$
$$+ 1.183 \times 10^{-4} T^2 - 0.1867T + 156.6 \qquad (2.19)$$

This equation can then be used in the numerical modelling of the 48 kW Thermogage furnace to calculate the ATJ graphite thermal conductivity as a function of the absolute temperature.

2.2.4 Conclusions on the ATJ Graphite Thermophysical Properties

The density, specific heat, electrical resistivity and thermal conductivity of the ATJ grade graphite have been determined as functions of the absolute temperatures. These properties, along with the graphite felt thermal conductivity are important factors in the development of a numerical model to be used in the optimisation of the 48kW Thermogage furnace. On the other hand, the development of measurement techniques to be used to measure accurately the temperatures of the inner walls of the graphite tube is essential in the calculation of the effective emissivity of the ATJ graphite tube cavity. In the next chapter, temperature measurement techniques using Pt/Pt-Rh thermocouples and optical methods are presented.

3 TEMPERATURE PROFILE MEASUREMENT

3.1 Introduction

Measurement of the graphite tube cavity wall temperatures and the estimation of their uncertainties are important for two reasons. Firstly, to calculate the cavity effective emissivity and its uncertainty using these measurements (chapter 1). Secondly, to measure the temperature gradients along the tube ($\delta T/\delta x$), which is essential in the calculation of the heat transfer rate by conduction along the graphite tube. The latter is used in the validation of the quasi 2-D numerical model presented in chapter 5.

The cavity wall temperature profile was measured using platinum/platinum-rhodium (Pt/Pt-Rh) thermocouples encased inside alumina tubes. Measurements were conducted by direct contact of the alumina tube with the surface of the graphite tube, on the other hand the tip of the thermocouple was located of at a distance of ½ of the alumina tube's diameter above the surface, shown schematically in Figure 3.1. As described in chapter 1, during operation the copper rings that surround the carbon composite clamps are cooled by water at 15 °C in order to avoid melting of the power supply copper wires. A steep temperature profile could occur, as a result of this water cooling, inside the tube. For example, measurements of the temperature profiles conducted at an operating temperature of 1 600 °C resulted in temperature gradient exceeding 100 °C·cm^{-1} near the graphite tube ends.

Figure 3.1. Cross sectional view of the temperature measurement setup of the graphite furnace tube using Pt/Pt-Rh thermocouple encased inside an alumina tube.

As a result of these steep temperature gradients near the ends of the graphite tube, temperature measurements using the Pt/Pt-Rh thermocouples may include corrections due to the heat transfer along the Pt/Pt-Rh wires and the alumina tube. It is therefore essential for this work to investigate and assess the magnitude of these corrections, which are caused by heat transfer along the thermocouple wires and alumina tubes, as well as to validate these temperature measurements and to calculate their uncertainties.

In the present work, three Pt/Pt-Rh thermocouples with different alumina tube diameters and tip configurations are used to measure the temperature profiles of the graphite tube by direct contact. In addition, a pyrometrical technique using a bent optical fibre is also used to measure the temperature profile in order to validate these measurements. These two techniques will now be presented.

3.2 Pt/Pt-Rh Thermocouple Technique

As shown in Figure 3.2, three Pt/Pt-Rh thermocouples were used with two encased fully inside the alumina tubes while the third has its wires formed into a circular ring or loop with a diameter of 25 mm, which is the same as the inside diameter of the graphite tube. In the case of the first two thermocouples, the temperature profile was measured by simply placing them on the inner surface of the furnace tube as shown in Figure 3.1. The platinum wires and the alumina tube have high thermal conductivity and therefore, when placed in the very steep temperature gradients inside the furnace tube (over 100 °C·cm^{-1}), will conduct heat away from the measurement point resulting in a lower measured temperature. In the region near the middle of the tube where the temperatures are higher, there is very significant radiated heat flux from the furnace tube inner surface (mainly due to the cold parts of the tube). When the thermocouple is placed on the surface then it will, to some extent, act as a "blanket" reducing radiative surface losses and causing a higher temperature to be measured.
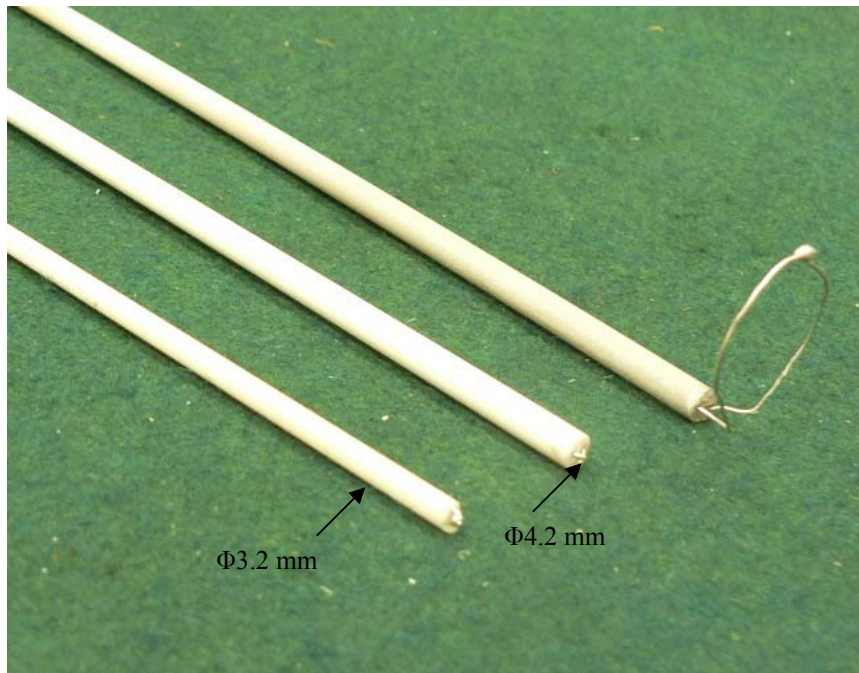
Figure 3.2. Pt/Pt-Rh thermocouple wires with 0.5 mm diameter, two are inside alumina tubes with outside diameters of 4.2 and 3.2 mm, and the third with its tip formed in a circular (loop) shape with a diameter of 25 mm.

In the case of the third thermocouple, heat transfer away from the measurement point is minimised by having the wire outside the alumina tube, as may be seen in Figure 3.3. Furthermore, using this configuration means that the circular shape thermocouple wire is in contact with the inner surface area of the furnace tube where the temperature is measured. The temperature of each ring is uniform due to the symmetrical shape of the furnace tube along the axial direction. This means that heat transfer from or to the thermocouple tip is minimised.
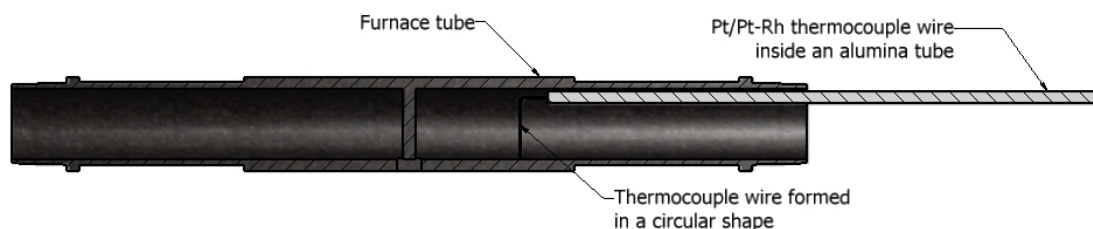
Figure 3.3. Cross sectional view of the temperature measurement setup of the graphite furnace tube using Pt/Pt-Rh thermocouple with a circular (loop) shape wire.

In a preliminary test, the temperature profile of a 289 mm long graphite tube at an operating temperature of 1 000 °C was measured from its centre to its end at 10 mm intervals using the three thermocouple configurations presented above. These thermocouples were mounted on a high precision displacement stage with a positioning accuracy better than 0.5 mm; this was done to ensure that the temperature uncertainty due to distance, especially in the high temperature gradient areas, is minimised. The results of the measurements are plotted in Figure 3.4.
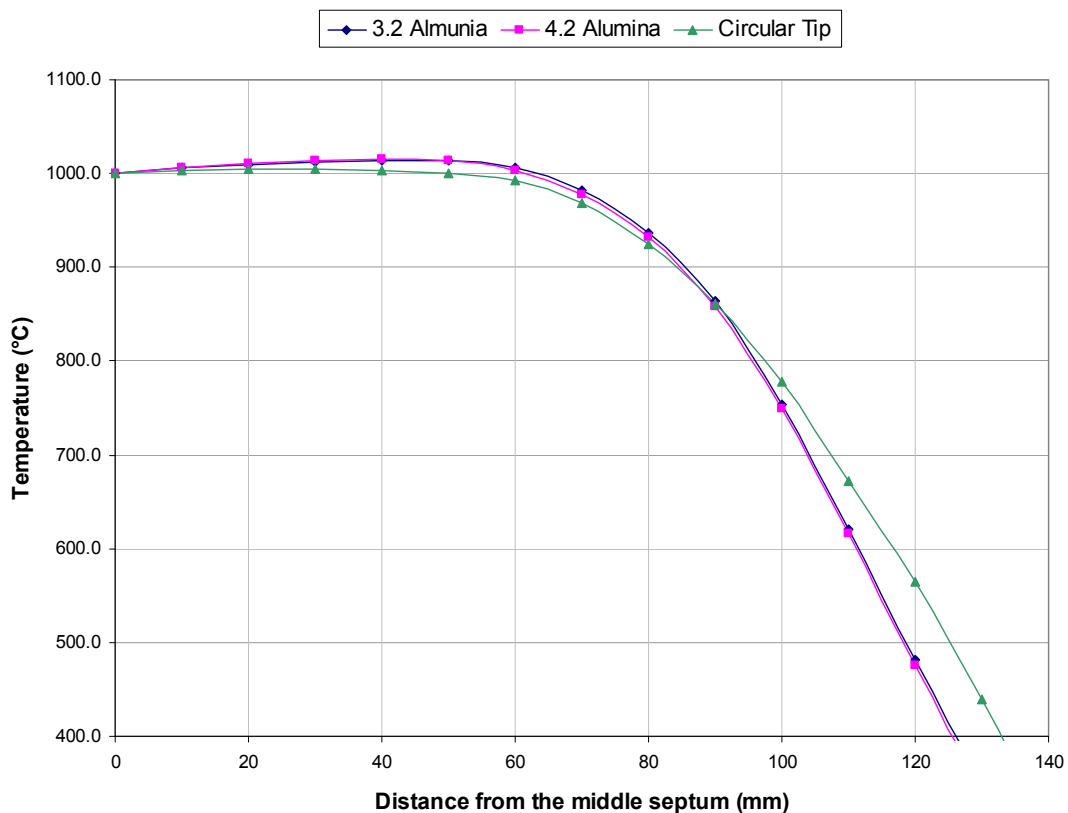
Figure 3.4. Temperature distribution in the graphite tube measured with Pt/Pt-Rh thermocouple wires in alumina tubes with 3.2 and 4.2 mm diameter and Pt/Pt-Rh thermocouple with a circular-tip wire versus distance from the furnace tube middle septum.

As may be seen from the graphs, the temperatures measured by the Pt/Pt-Rh thermocouples inside the alumina tube with 3.2 mm are higher than those of the 4.2 mm tube, with the differences becoming larger at higher temperature gradients. This suggests that heat transfer from the tip of the thermocouple wires inside the 4.2 mm alumina tube is higher than that of the 3.2 mm, this is due of course to the

4.2 mm alumina tube having larger cross sectional area perpendicular to the direction of the heat transfer. On the other hand, both set of temperature measurements measured by the 3.2 and 4.2 mm thermocouples indicate that they have higher temperatures than the circular wire thermocouple in the area near the centre, this may be credited to:

1. Radiation from the middle area of the tube onto the alumina tube, with an emissivity of around 0.4, resulting in additional heating and consequently a temperature rise of the thermocouple wires.
2. Heat transfer by conduction by the alumina tube is minimised in low temperature gradient areas; within 90 mm of the middle septum of the furnace tube where the temperature profile is near isothermal.
3. The surface of the thermocouple platinum wire is shiny with an emissivity of ~0.05, which means that radiative heat transfer from other areas of the tube onto the wire is mostly reflected and hence minimised.

In the area near the end of the tube, 90 to 130 mm from the middle septum, the temperatures measured by the 3.2 and 4.2 mm thermocouples are lower than the circular wire one. This is due to:

1. Heat transfer by the alumina tubes with 3.2 and 4.2 mm diameters result in the cooling of the tip of the Pt/Pt-Rh thermocouple wires, and consequently the measured temperature appears to be lower.
2. Heat transfer by conduction when using the circular wire thermocouple is minimised by the fact that the Pt/Pt-Rh thermocouple wire is formed in a loop shape and placed on a surface which has a uniform temperature, furthermore the radiative exchanges between the wire's surface and the surroundings may be negligible due to its low emissivity (~0.05).

It follows from the above that in order to achieve better measurements of the temperature profile then errors associated with these measurements using the three thermocouples need to be evaluated. Also, it is important to quantify the temperature measurement uncertainties, which are needed in estimating the uncertainty of the blackbody cavity effective emissivity.

3.2.1 Measurement Errors of the Pt/Pt-Rh Thermocouples

The errors in measuring temperatures using the Pt/Pt-Rh thermocouple wires placed inside the 3.2 and 4.2 mm alumina tubes may be calculated using the correlations to transmission line matrix found in textbooks dealing with electromagnetic theory (for example Christopoulos 1995). It follows that the thermal resistances between the different parts of the thermocouple and alumina assemblies, such as the thermal contact resistances between the Pt/Pt-Rh wires and the alumina tubes and the contact resistances between the alumina tubes and the cavity wall surfaces, are required to be determined.

Attempts by the present author to calculate the errors due to transmission line effects for the thermocouples with 3.2 and 4.2 mm alumina tube diameters did not unfortunately yield to any realistic results due to the complexity in determining the various thermal resistances, especially between the Pt/Pt-Rh thermocouple wires and the insulating alumina tubes. Instead more effort was given to the calculation of these errors for the case of the circular shape thermocouple since the thermal resistances between the Pt/Pt-Rh wires and the cavity wall surface could be easily determined.

For the circular shape Pt/Pt-Rh thermocouple wires, the heat transfer problem can be simplified to an 80 mm long and 0.5 mm in diameter Pt/Pt-Rh wire with its ends at a temperature T_{end}. The wire is mounted on top of a flat graphite surface with a uniform temperature T_s, shown schematically in Figure 3.5.
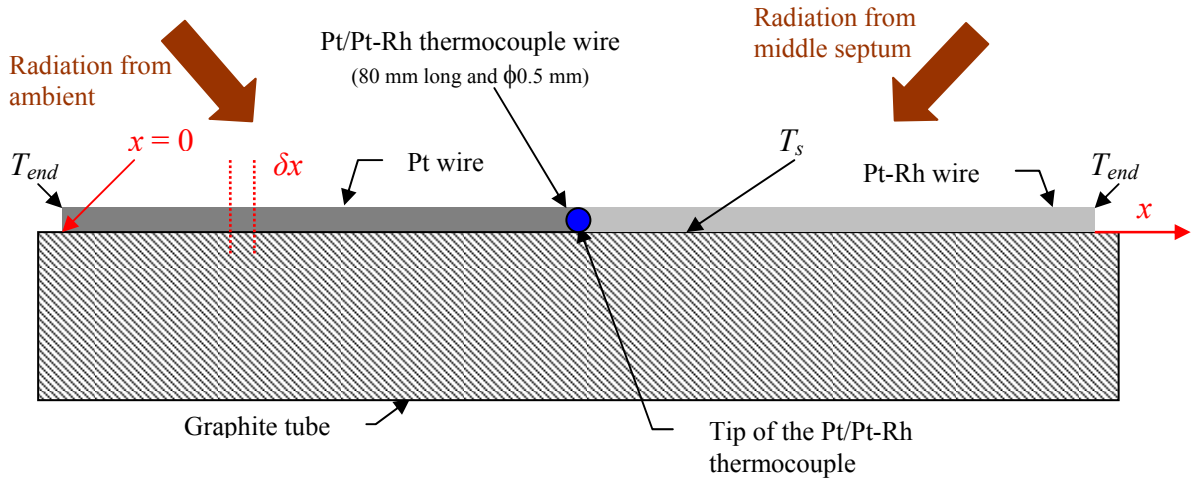
Figure 3.5. Schematic diagram of the Pt/Pt-Rh thermocouple wires on top of a graphite surface at a temperature T_s.

When measuring a temperature profile heat is transferred away from the surface of the thermocouple wire mainly by two mechanisms: (i) by conduction from the graphite surface to the wire and then through it (conduction errors) caused by the difference in temperature between T_{end} and T_s, and (ii) by radiative exchanges between the thermocouple wire on one hand and the cavity walls, the middle septum and the outside environment on the other (radiation errors). The measurement errors caused by these two heat transfer modes are calculated separately below.

3.2.1.1 Temperature Errors Due to Conduction

As shown in Figure 3.5, the thermocouple wire can be simplified to a finite rod on a surface with temperature (T_s) while the ends of the rod are maintained at a fixed temperature (T_{end}). The temperature distribution across the wire ($T_{TC}(x)$), which is caused by the temperature difference between T_{end} and T_s, can be determined using (Carslaw & Jaeger 1959, p. 140)

$$T_{TC}(x) = T_s + (T_{end} - T_s)\frac{cosh[\mu_{TC}(L-x)]}{cosh[\mu_{TC}L]},\qquad(3.1)$$

where,

$$\mu_{TC}^2 = \frac{G_s p_{TC}}{k_{TC}(T_s) A_{TC}},$$
(3.2)

in which G_s is the surface conductance between the thermocouple wire and the surface of the graphite tube, p_{TC} is the perimeter of the wire, k_{TC} is the thermal conductivity of the thermocouple and A_{TC} is the cross sectional area of the wire. Due to the similarities in the thermophysical properties of the metal element Pt and the compound Pt-Rh, the thermal conductivity of the thermocouple (k_{TC}) is assumed to be for platinum only whose values can be obtained from Touloukian (1970). A schematic diagram of the equivalent circuit of the thermocouple wire for a control volume with a width δx is shown in Figure 3.6.
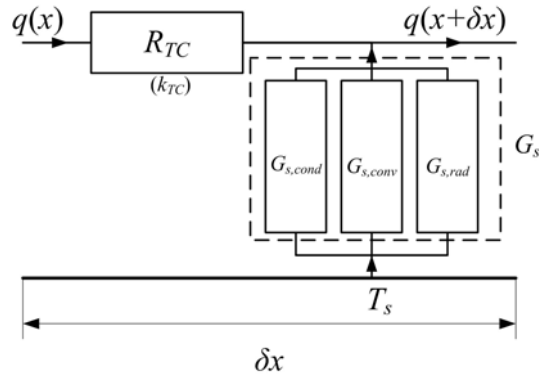
Figure 3.6. The equivalent thermal circuit diagram of the Pt/Pt-Rh thermocouple wire control volume with a width δx.

In order to calculate G_s, the thermocouple wire and the graphite tube surface may be assumed to have a contact area, with an average gap of g=0.1 mm, across which heat is transferred *viz* three mechanisms: (i) gas conduction, (ii) free convection inside the gap, and (iii) by radiative exchanges between the surfaces of the thermocouple wire and the graphite tube. However, the convective mechanism can be ignored due to the small size of the gap between the wire and the graphite tube. Hence, G_s is calculated using,

70

$$G_s = G_{s,cond} + G_{s,rad}.$$ (3.3)

Here $G_{s,cond}$ and $G_{s,rad}$ are the surface conductances due to conduction and radiation respectively, these are calculated next.

$G_{s,cond}$ can be calculated based on the above assumption of the thermocouple wire and the graphite surface being separated by a 0.1 mm gap filled with a gas (nitrogen or helium). Equation for $G_{s,cond}$ can be obtained by using the analogy to electromagnetic theory for the case of leakage resistance between two transmission wires separated by a symmetry line, shown schematically in Figure 3.7. As it may be seen from the figure, the two thermocouple wires are considered as two electrical wires with one taken as an imaginary side, while the graphite tube is taken as the line of symmetry that separates both wires.
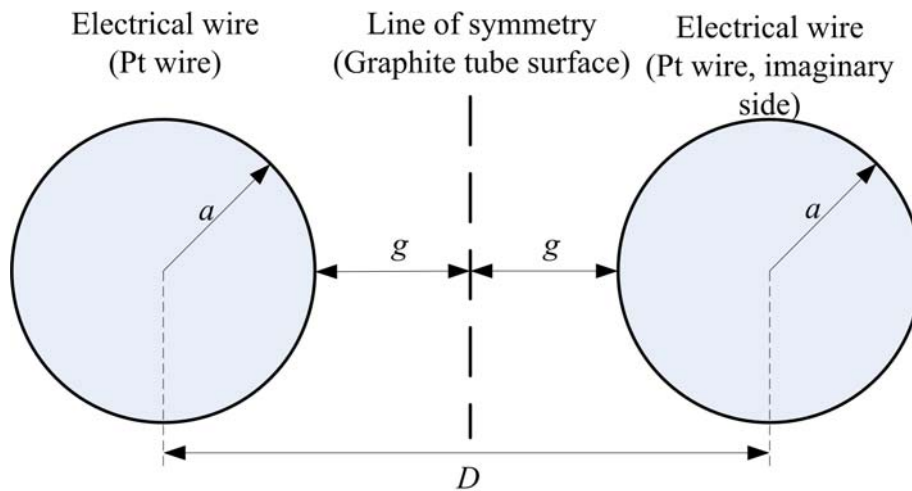
Figure 3.7. Cross sectional view of two platinum wires with radius *a*, in addition to the line of symmetry between them (the graphite tube surface).

The equation for calculating the leakage electrical resistance (R_{elec}) for the case presented above, refer to Figure 3.7, is given as (Cheng 1983, p. 189),

$$R_{elec} = \frac{1}{\pi \kappa} ln \left[\frac{D}{2a} + \sqrt{\left(\frac{D}{2a}\right)^2 - 1} \right],$$ (3.4)

in which, κ is the electrical conductivity, a is the wire radius and $D=2a+2g$ is the distance between the two wires' centres. By substituting the electrical conductivity κ with that of the thermal conductivity of gas, k_{gas}, then equation (3.4) can be modified to obtain the thermal resistance, $R_{s,cond}$, to be,

$$R_{s,cond} = 2 \times \frac{1}{\pi k_{gas}(T_s)} ln \left[\frac{D}{2a} + \sqrt{\left(\frac{D}{2a}\right)^2 - 1} \right].$$ (3.5)

It is important to emphasise here that a multiple of two is used in order to obtain the thermal resistance between the wire and the graphite tube surface; the surface is taken as the symmetry line between the two wires shown in Figure 3.7. Also, it is noteworthy that the thermal conductivity of the gas (k_{gas}) is a function of the absolute temperature of the surface of the graphite tube, T_s. Using equation (3.5) and value of $p_{TC}=0.5\pi$ mm, $G_{s,cond}$ can be calculated from,

$$G_{s,cond} = \frac{1}{R_{s,cond} p_{TC}}$$ (3.6)

On the other hand, $G_{s,rad}$ can be obtained using (Incropera & Dewitt 2002, p. 10),

$$G_{s,rad} = 4\varepsilon_{r,eff} \sigma T_s^3.$$ (3.7)

Here $\varepsilon_{r,eff}$ is the radiative effective emissivity between the graphite surface and the thermocouple wire, with temperature-dependent emissivities $\varepsilon_g(T_s)$ and $\varepsilon_{Pt}(T_s)$ consecutively, calculated using,

$$\varepsilon_{r,eff} = \frac{1}{1/\varepsilon_g(T_s) + 1/\varepsilon_{Pt}(T_s) - 1},$$ (3.8)

given by Siegel & Howell (2002, p. 299) for the case of two infinite parallel plates. The graphite surface and the thermocouple wire were assumed to behave as two infinite parallel plates due to the large ratio of the wire length to the width of the wire-to-surface contact area.

Using equations (3.3-8), values for $G_{s,cond}$ and $G_{s,rad}$ were obtained for temperatures varying between 200 and 1 600 °C and are plotted along with their combined values (G_s) in Figure 3.8.
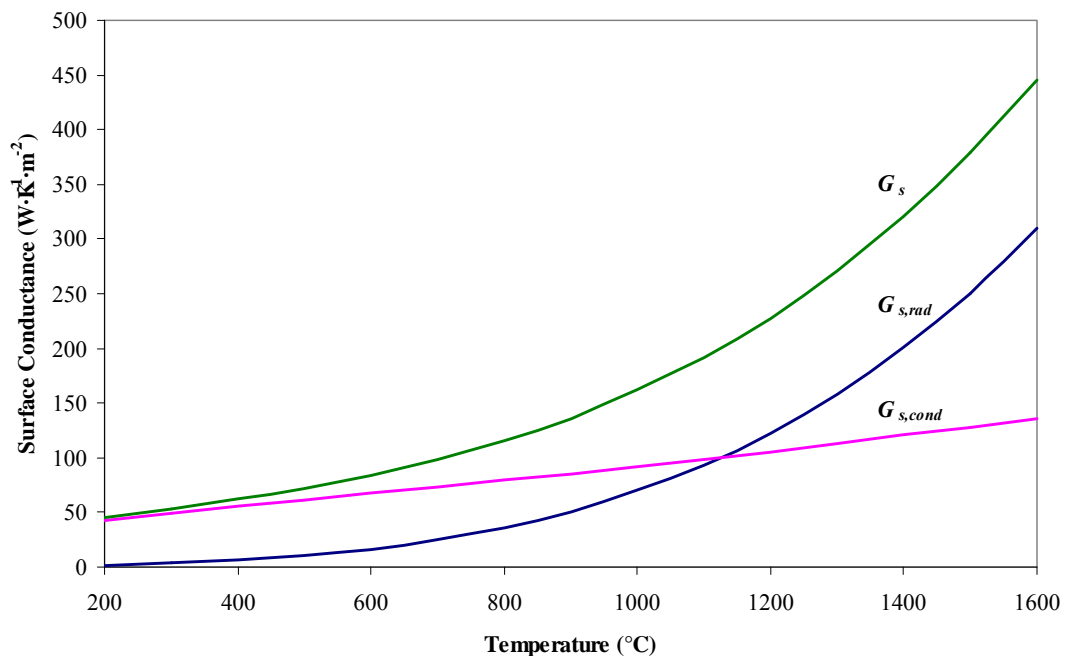
Figure 3.8. Graphs of the surface conductances $G_{s,cond}$ and $G_{s,rad}$ along with their combined values G_s as a function of the surface temperature T_s.

As may be seen from the graphs, heat transfer between the thermocouple wire and the graphite tube occurs mainly by conduction for temperatures below 1 000 °C. Radiative heat transfer, which is proportional to T_s^3, becomes the dominant mechanism for temperatures above 1 200 °C. It can be therefore deduced that measurement erroneous due to bad contact between the wire and the graphite tube surfaces is minimised at high temperatures; unlike the conductive heat transfer

mechanism, the radiative heat transfer mechanism is independent of the size of the contact area and the distance between the two surfaces.

Having determined the values of G_s, equation (3.1) can now be used to calculate the conduction errors at the location of the Pt/Pt-Rh thermocouple junction ($x= L/2$). As an example, for a surface temperature of the graphite tube of 1 000 °C (or T_s=1 000 °C) and a temperature of the thermocouple ends of 980 °C (or T_{end}=980 °C), the temperature difference between the thermocouple wire and temperature of the graphite surface (T_s) at the location of the thermocouple wire junction (where the *emf* is generated) was calculated to be -0.14 °C, or $T_{TC}(x= L/2)-T_s = -0.14$ °C. To better understand the effect of conduction errors on the temperature measurements over a range of surface temperatures (T_s), values of $T_{TC}(x= L/2)$ were calculated for various values of T_{end} and T_s and are plotted in Figure 3.9.
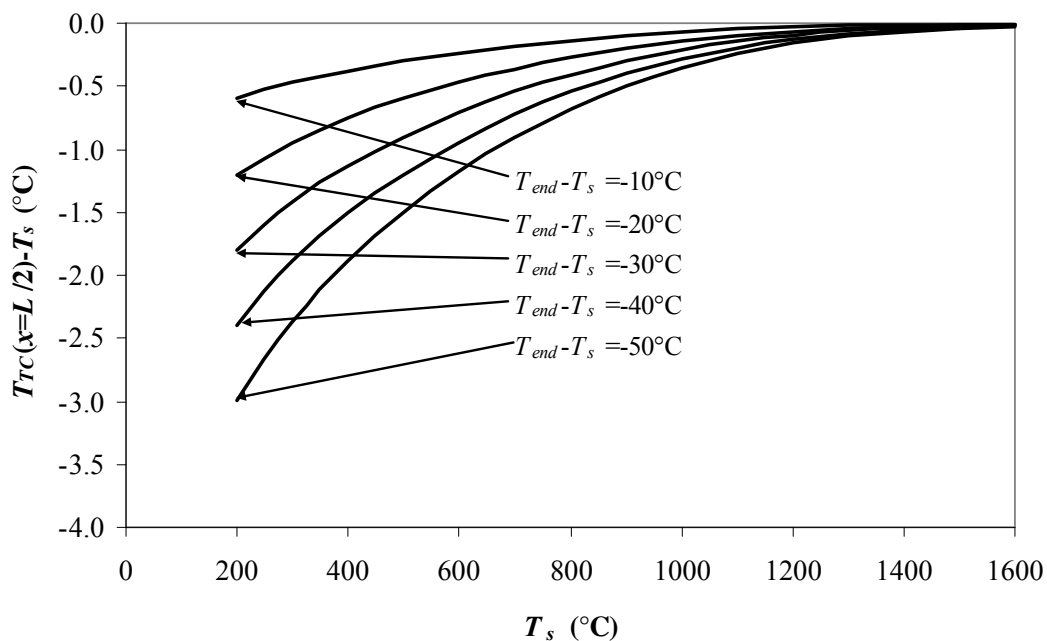
Figure 3.9. Graphs of the temperature rise at the tip of the Pt/Pt-Rh thermocouple wire ($T_{TC}(x=L/2)-T_s$) versus the surface temperature of the ATJ graphite tube (T_s) for different values of the temperature difference between the ends of the thermocouple wire and the surface temperatures ($T_{end}-T_s$).

As expected, the errors in the temperature measurements ($T_{TC}(x=L/2)-T_s$) are proportional to the temperature differences ($T_{end}-T_s$) with values varying from 0.01 °C for T_s=1 600 °C and ($T_{end}-T_s$)=10 °C to over 3.0 °C for values of T_s and ($T_{end}-T_s$) of 200 °C and 50 °C respectively. This difference can be credited to the high values of thermal conductivity of the thermocouple wire when compared to that of the surface conductance (G_s) of the contact area between the thermocouple wire and the surface of the graphite tube (refer to Figure 3.8) at lower temperatures. For T_s of 1 000 °C, these errors reduce to less than 1.0 °C and to less than 0.03 °C for T_s of 1 600 °C for all cases of ($T_{end}-T_s$). This is of course credited to the increase in the thermal surface conductance (G_s) between the thermocouple wire and the surface of the graphite tube where radiative exchanges dominate at higher temperatures.

As mentioned in the introduction to this chapter, measurements of the temperature gradients showed a worst case scenario of 100 °C·cm^{-1} at operating temperature of 1 600 °C, this steep temperature gradient occurred in the regions near the water cooled clamps (refer to chapter 1). Assuming that T_{end} is situated at 1 mm from the ends of the thermocouple wire wring (refer to Figure 3.5) then this results in ($T_{end}-T_s$) of -10 °C. As may be seen from the graphs in Figure 3.9, a ($T_{end}-T_s$) of 10 °C will yield to 0.5 °C error at T_s of 200 °C with this error dropping to less than 0.01 °C at T_s of
1 600 °C. For the work presented here, the expected measurement uncertainties of temperatures vary from 0.5% to 6.0% for operating temperatures ranging from 1 000 to 1 600 °C, which translate to measurement uncertainties of temperatures of at least 5 °C. It can therefore be deduced that the uncertainty contribution of 0.5 °C caused by the conduction errors is therefore negligible and can be ignored.

3.2.1.2 Temperature Errors Due to Radiation

When measuring the graphite tube temperature profile, radiative heat exchanges occur between the Pt/Pt-Rh wire on one side and the graphite tube cavity walls, the middle septum and the outside environment on the other side (refer to Figure 3.3). These

radiative exchanges can add to the heating or cooling of the thermocouple wire and as a result introducing systematic errors to the measurements. Therefore, it is important for the work presented here to evaluate these radiative errors and their contributions to the total measurement uncertainties of temperatures.

In order to estimate the corrections due to radiation when using the circular shape thermocouple wire, the following assumptions need to be made:

1. the heat transfer is steady state,
2. the thermal resistance through the wire is negligibly small due to its high thermal conductivity and small diameter,
3. the thermocouple wire (circular shape) can be assumed to be a circular flat surface perpendicular to the cavity walls and parallel to the middle septum and the outside opening to the ambient with an inner diameter of 23.4 mm and a thickness of 1 mm, and
4. the thermal resistance between the wire and the cavity walls can be ignored since the cavity wall temperature is similar or very close to that of the wire's temperature.

Based on these assumptions, the equivalent thermal circuit for the circular shape thermocouple wire, the graphite tube and the ambient can be constructed as shown in Figure 3.10.
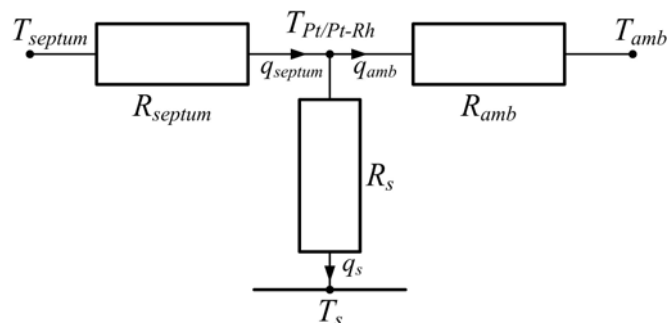
Figure 3.10. Equivalent thermal circuit for radiative exchanges between the Pt/Pt-Rh wire, the ATJ graphite tube middle septum and the ambient.

As may be seen from the circuit diagram, the temperature errors due to radiative exchanges is the temperature drop across the thermal resistor R_s and it is defined as $\Delta T_s = T_{Pt/Pt-Rh} - T_s$. Using the analogy to the electrical theory, in which thermal heat transfer rate is considered to be equivalent to that of an electrical circuit, the following equation can be written, based on the circuit diagram shown in Figure 3.10, as,

$$q_s = q_{septum} - q_{amb} .$$
(3.9)

Here q_s, q_{septum} and q_{amb} are the heat transfer rates between the Pt/Pt-Rh thermocouple wire and the ATJ graphite tube surface, the middle septum and the ambient respectively. The negative sign on the right hand of the equation indicates that q_{septum} and q_{amb} are of opposite directions since the temperature of middle septum is assumed to be the highest inside the cavity.

Defining ΔT_{septum} and ΔT_{amb} as the temperature drops between the Pt/Pt-Rh wire and the middle septum and the ambient respectively and using equation (3.9), the temperature drop (or correction) ΔT_s is calculated using,

$$\Delta T_s = R_s \left(\frac{\Delta T_{septum}}{R_{septum}} - \frac{\Delta T_{amb}}{R_{amb}} \right),$$
(3.10)

in which, R_{septum} and R_{amb} are the thermal resistors between the thermocouple wire and the middle septum and the ambient respectively. Both resistors may be calculated using the following equations (Incropera & Dewitt 2002, p. 91),

$$R_{septum} = \frac{1}{F_{ss}\varepsilon_{Pt}(T_s)A_{septum}\sigma\left(T_{septum} + T_s\right)\left(T_{septum}^2 + T_s^2\right)}, \text{ and}$$
(3.11)

$$R_{amb} = \frac{1}{F_{as}\varepsilon_{Pt}(T_s)A_{amb}\sigma\left(T_{amb} + T_s\right)\left(T_{amb}^2 + T_s^2\right)}.$$
(3.12)

Here T_{septum} and T_{amb} are the absolute temperatures of the middle septum and ambient respectively, A_{septum} and A_{amb} are the surface areas of the of the middle septum and the tube opening to the ambient respectively, and F_{ss} and F_{as} are the view factors

calculated using the *configuration-factor algebra* given as (Siegel & Howell 2002, p. 167-9),

$$F_{ss} = F_{ss,r=25.4/2} - F_{ss,r=23.4/2} \text{ , and}$$ (3.13.a)

$$F_{as} = F_{as,r=25.4/2} - F_{as,r=23.4/2} \text{ .}$$ (3.13.b)

Here $F_{ss,r=25.4/2}$ and $F_{ss,r=23.4/2}$ are the view factors between the middle septum and the surface areas of the two circles used in determining the thermocouple surface area and having radii of 25.4/2 and 23.4/2 mm respectively. Similarly, $F_{as,r=25.4/2}$ and $F_{as,r=23.4/2}$ are the view factors between the ambient and the thermocouple area and may be used to calculate F_{as}. These view factors are determined using equations of view factors for the case of "*parallel circular disks with centres along the same normal*" (Siegel & Howell 2002, p. 845) with the general form (F_{xx}) given as,

$$F_{xx} = \frac{1}{2}\left[X - \sqrt{X^2 - 4\left(\frac{R_2}{R_1}\right)^2} \right],$$ (3.14.a)

in which,

$$R_1 = \frac{25.4/2}{x},$$ (3.14.b)

$$R_2 = \frac{23.4/2}{x}, \text{ and}$$ (3.14.c)

$$X = 1 + \frac{1 + R_2^2}{R_1^2}.$$ (3.14.d)

Note that x is taken to be the distance between the location of the thermocouple wire and the middle septum when calculating F_{ss}. On the other hand, x is taken to be the distance between the thermocouple wire and the ambient when calculating F_{sa}.

For the measured temperature profile presented in Figure 3.4, values for ΔT_s are calculated using equations (3.10-14). These are plotted as a percentage of the

measured temperature versus the distance from the middle septum of the ATJ graphite tube in Figure 3.11.
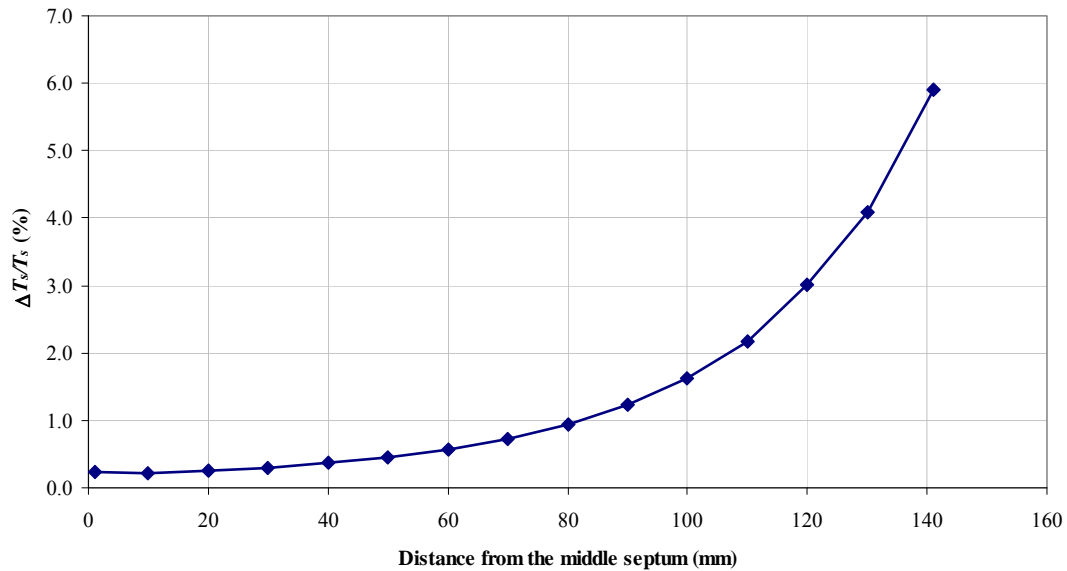
Figure 3.11. Graph of the temperature drop due by radiative exchanges between the Pt/Pt-Rh thermocouple wire with circular shape tip and the middle septum and the ambient at an operating temperature of 1 000 °C while using nitrogen as the graphite felt purging gas, this drop is expressed as % of the temperature reading.

As can be deduced from the graph, the temperature errors are minimised for the area of the graphite tube over which the temperature is uniform; less than 0.5% within 50 mm from the middle septum. These low corrections are attributed firstly to temperature uniformity of this part of the graphite tube, and secondly to the comparably long distance between the middle septum and the ambient resulting from the low values of the view factor, F_{as}; calculated to be between 0.0012 and 0.0046 when the thermocouple wire is located between the middle septum and 70 mm from it. On the other hand, these errors start to increase when the circular shape thermocouple wire is used near the graphite tube end where radiative heat transfer from this thermocouple wire to ambient is larger. At 140 mm from the middle septum ΔT_s reaches approximately 6.0%.

Determining values for the temperature drop ΔT_s for a given measured temperature profile provides a means to evaluate the uncertainty component of the temperature measurement due to the radiative exchanges. It may be deduced that unlike conduction errors, which were discussed in section 3.2.1.1, radiation errors are larger and must be taken into account in the measurement uncertainty budgets. These budgets are presented next.

3.2.2 Pt/Pt-Rh Thermocouple Temperature Measurement Uncertainties

As mentioned in chapter 1, the graphite tube blackbody cavity emissivity is estimated from measured temperatures of the graphite tube cavity inner walls (or the temperature profile) and, therefore, it follows that the uncertainty in the calculated emissivity is directly related to the uncertainty in the temperature measurements. It is, therefore, important for the work presented here to determine these measurement uncertainties of temperatures. As has been demonstrated in the previous section, the best method to measure the temperature profile is by using Pt/Pt-Rh thermocouple with circular-tip configurations, therefore only the uncertainty pertinent to this type of thermocouple will be discussed.

The temperature measurement uncertainty may be calculated with the use of the "Guide to the Expression of Uncertainty in Measurement", which is better known as the "ISO Guide" (ISO 1993). This guide is commonly used by metrologists for the estimation of measurement uncertainties. The uncertainty of the temperature measurements consists of a number of components with some having small contributions to the final uncertainty, such as the calibration uncertainty of the thermocouple wire (<0.5 °C). Other components, such as radiation errors, have larger contribution. These uncertainty components are:

1. the thermocouple calibration standard uncertainty, which is given by the calibration laboratory to be 0.5 °C, u_{cal},

2. the radiative contact resistance standard uncertainty, $u_{s,rad}$, between the Pt/Pt-Rh wire and the graphite tube (discussed in details in section 3.2.1.2), and

3. the standard uncertainty due to the positioning of the thermocouple, which is a function of the temperature gradient, u_{pos}.

In addition to these standard uncertainty components, the thermocouple readout resolution and the standard deviation of the temperature sampling readings also contribute to the final uncertainty. According to the "ISO Guide" the contribution of the readout may be taken to be 0.1/2√3 °C (ISO 1993), which amounts in the worst case scenario to less than 0.01% of the measured temperature. On the other hand, it was observed by the present author that the standard deviation of the temperature readings when conducting measurements did not exceed the 0.05 °C, or less than 0.01% of the lowest measured temperature. Both values are negligible in comparison to the other uncertainty components and therefore can be ignored.

The positioning uncertainty component is due to the uncertainty in the length measurement from the middle septum to the Pt/Pt-Rh thermocouple. As mentioned previously, during measurement the thermocouple was mounted on a high precision stage with an uncertainty better than 0.5 mm. Consequently, the resulted temperature uncertainty due to this length uncertainty is therefore proportional to the measured temperature gradient inside the tube. For the temperature profile presented in Figure 3.4, the uncertainty component due to length is found to vary between 0.01% for the uniform temperature area and 1.2% for the steep temperature gradient area.

The total temperature uncertainty, u_T, can be calculated for the temperature profile in Figure 3.4 using the equation (ISO 1993),

$$u_T = \sqrt{u_{cal}^2 + u_{s,rad}^2 + u_{pos}^2} \; . \qquad\qquad (3.15)$$

Values of the standard uncertainty u_T are calculated using the equation above and together with the uncertainty components u_{cal}, $u_{s,rad}$ and u_{pos} are plotted as a function of the distance from the graphite tube middle septum in Figure 3.12. Note that all

these components are expressed in the graphs as relative uncertainties in respect to the measured temperatures.
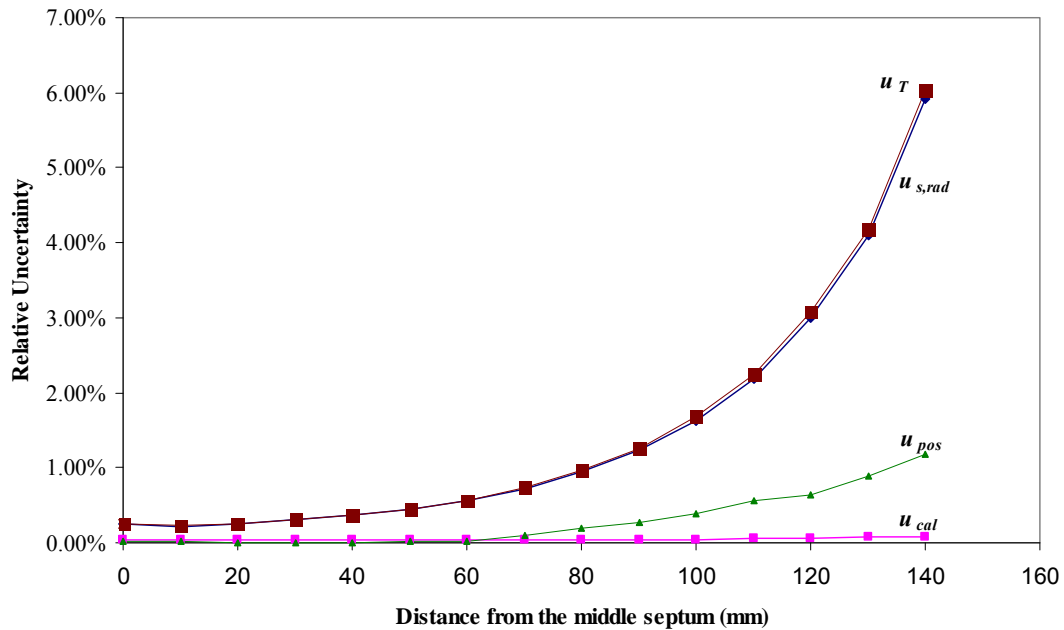
Figure 3.12. Graphs of the of the relative uncertainty (at 95% C.L.) of the temperature measurement u_T versus the distance from the graphite tube middle septum, as well as its uncertainty components $u_{s,rad}$, u_{pos} and u_{cal}.

As may be seen from the plots, the uncertainty in the near isothermal (or uniform temperatures) area of the tube is small due to firstly low temperature gradient and secondly to low radiative exchanges between the Pt/Pt-Rh and the cooler part of the tube. This uncertainty increases toward the end of the tube where the thermocouple wire is used in a steep temperature gradient where the thermocouple has greater exposure to the cool ambient resulting in an increase in radiative exchanges. Subsequently, it can be observed from the plots that the total uncertainty u_T is dominated by the uncertainty due to radiative exchanges u_{rad}.

However, for the work presented here, the temperature measurements toward the ends of the tube are mainly important for measuring the temperature gradient ($\delta T/\delta x$) in order to calculate the conductive heat flux along graphite tube. This uncertainty is

then minimised by the fact that the measured temperatures have correlated uncertainties and therefore given this fact the uncertainty in the temperature difference is minimised. It is important to point to the reader's attention at this stage that the conduction heat transfer rate is only required to be known to no better than 5-10%.

3.3 Optical Fibre Technique

When possible, the use of different measurement techniques in metrology is common in order to provide a mean of validating and giving more confidence in the measurements. It follows that in order to validate the temperature profile measurements using the Pt/Pt-Rh thermocouple (refer to the previous section), an alternative technique needs to be devised using say, radiometric or pyrometric technique. This measurement technique and the uncertainty associated with it are described next.

The graphite tube, used in this measurement, is 289 mm long and 25.4 mm in diameter and contains a wall septum in the middle, as shown in Figure 3.13. To view a measurement region with a spatial resolution of a few millimetres, most commercial pyrometers require F/20 to F/50 viewing optics (i.e. a viewing cone with an apex angle of 1-2°). Measuring the temperature of the wall close to the centre of the furnace tube thus requires near tangential viewing. For graphite, the specular reflection component then becomes very significant and will tend to merely reflect the temperature of the furnace septum. Other means have to be devised to collect light from the furnace wall surface for the pyrometer.

The solution to this problem is to bend a silica optical fibre to an angle of 45° to collect radiation or light from the graphite furnace tube surface. The cladding of the silica fibre is first removed, then the fibre is heated by a hydrogen (H_2) flame until it starts to bend under its own weight, then heating is stopped when the bend angle reaches around 45°. Removal of the cladding and deformation introduced around the bend and the heated area can result in light leakage from the fibre. The light leakage

was investigated and the measurement uncertainty caused by this leakage was quantified at a wavelength of 850 nm, which is the operating wavelength of the pyrometer.
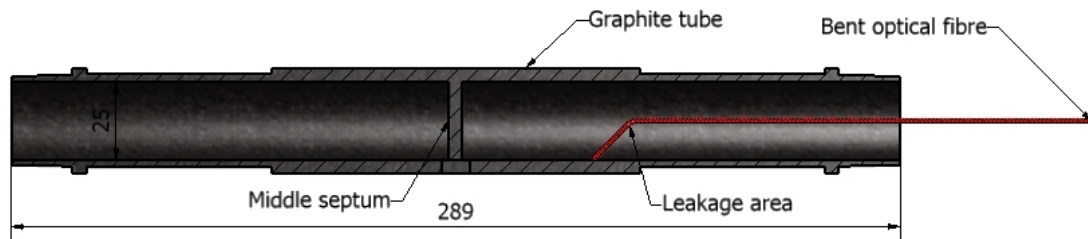
Figure 3.13. Schematic diagram of the graphite tube and the fibre optic.

The bent silica fibre was connected to a multimode fibre, the end of which is viewed with the NMIA medium temperature standard pyrometer, or MTSP, which has F/10 optics and a 1 mm target spot. The voltage of the signal from the detector (V_m) is converted to a temperature using Planck's law,

$$V_m \propto E = \frac{2\pi C_1}{\lambda^5 (e^{C_2/\lambda T} - 1)} \, , \tag{3.16}$$

where E is the energy, C_1 and C_2 are the first and second Planck's constants, λ is the wavelength and T is the absolute temperature. The pyrometer used has a 10 nm bandwidth filter at 850 nm. The MTSP has a voltage output V_m varying from ~10 V at 1 000 °C to less than 0.05 V below 500°C. For a fixed wavelength λ of 850 nm the value of $C_2/\lambda T \gg 1$, therefore equation (3.16) becomes:

$$V_m = V_o e^{-C_2/\lambda T} \, , \tag{3.17}$$

in which, V_o is a constant. This constant can be determined by calibrating the pyrometer against a thermocouple reading in an isothermal environment. This calibration method automatically includes any fibre coupling or transmission losses. In this situation, the optical fibre is placed in the middle of the graphite tube and then

V_o is calculated from the measured voltage and the value of the absolute temperature, which is measured by a calibrated thermocouple.

The leakage from the bent area is measured using the experimental setup shown in Figure 3.14. Light from a tungsten halogen (QTH) lamp is collimated, filtered with an 850 nm interference filter, and is focussed into a 1 mm multimode fibre by a fibre coupler. This is coupled to the bent silica fibre, the end of which is placed inside a 100 mm integrating sphere. An HP3458A multimeter is used to measure the photocurrent of a silicon photodiode mounted on the sphere.
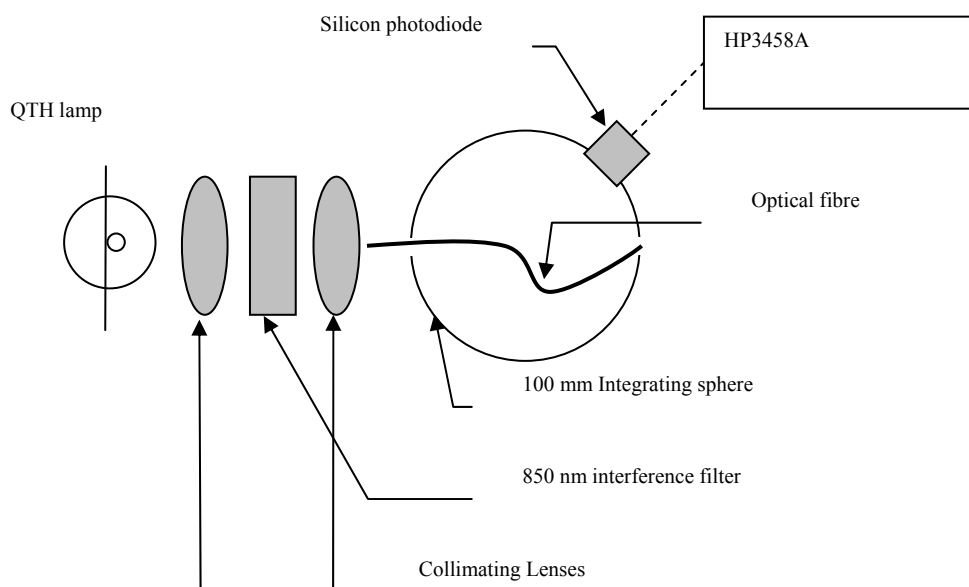
Figure 3.14. Schematic diagram of the leakage testing setup.

The total optical power E, launched into the fibre, is assessed by placing it wholly inside the integrating sphere. The power leaking from the bent area, ΔE, is measured by carefully aligning the fibre tip, so that light directly radiated from the tip escapes through a small hole in an aperture placed in the sphere wall. A ratio of $\Delta E/E=7.3\%$ was measured. Although the measured leakage is relatively large, the contribution of

this leakage to the total temperature uncertainty is minimised by the fact that the bent area, shown in Figure 3.13, is almost on the top of the fibre tip where measurement occurs. Any leakage from and to the fibre is mainly due to the radiation from and to the measured area. The leakage to other areas of the tube should not be more than 10% of the leakage, or $\Delta E/E$ can be reduced to 0.73%.

For a narrow bandwidth optical pyrometer, equation (3.17) is used to calculate the error in temperature ΔT arising from an error in measured optical signal (Ballico 1998),

$$\frac{\Delta T}{T} = \frac{\lambda T}{C_2} \frac{\Delta E}{E} .$$ (3.18)

Using equation (3.18), the uncertainty in temperature for the measurements is calculated to be no more than 0.05% or 0.7 °C at 1 000 °C. Taking into consideration that the expected measurement uncertainties of temperatures vary from 5 to 30 ° at an operating temperature of 1 000 °C (refer to section 3.2.2) then the contribution of 0.7 °C to the total uncertainty is therefore negligible and can be ignored.

3.3.1 Silica Optical Fibre Corrections

Having assessed the uncertainty due to the leakage around the bent area of the optical fibre, measurements of the temperature profile of the graphite tube were conducted with this fibre. The furnace temperature was set at a temperature of 1 000 °C. Similarly to the way that the thermocouple measurements were performed, the surface temperature of the graphite tube was measured from the centre of the graphite tube to its end at different positions at distances 10 mm apart.

For the work presented here, the only temperature measurements of interest are within the first 120 mm from the centre as this is the area of the tube that mostly affects the emissivity of the graphite cavity.

The radiant exitance measured by the pyrometer at a position i consists of the radiant exitance due to the thermal radiation arising from the surface temperature and the irradiances reflected from other places inside the graphite tube. This can be expressed as,

$$M_i = \varepsilon_{ATJ} M_{p(T),i} + \left(1 - \varepsilon_{ATJ}\right) E_i \,, \tag{3.19}$$

where M_i is the radiant exitance measured by the pyrometer at a node i, ε_{ATJ} is the emissivity of graphite, $M_{p(T),i}$ is the radiant exitance due to the surface temperature, and E_i is the total irradiance from other surfaces inside the graphite tube onto the node i. Rearranging equation (3.19) and solving for $M_{p(T),i}$ gives,

$$M_{p(T),i} = \frac{M_i}{\varepsilon_{ATJ}} - \frac{\left(1 - \varepsilon_{ATJ}\right)}{\varepsilon_{ATJ}} E_i \,, \tag{3.20}$$

which can be used to calculate the radiant exitances due to surface heat and then convert them into temperature readings using Planck's radiation law.

To simplify the computation of E_i, the graphite tube was assumed to be divided into 10 mm wide ring elements (w_{ring}); the 10 mm width was chosen because this was the distance between measuring positions. The total irradiance E_i on one ring element consists of the other ring elements' irradiances and the irradiance from the middle wall inside the graphite tube (refer to Figure 3.13). This is given by,

$$E_i = \sum_{j=0}^{n} M_{j,r} F_{ji} \frac{A_j}{A_i} + M_{i,w} F_{wi} \frac{A_{septum}}{A_i} \,. \tag{3.21}$$

The substitution of E_i from equation (3.21) into equation (3.20) yields,

$$M_{p(T),i} = \frac{M_i}{\varepsilon_{ATJ}} - \frac{\left(1 - \varepsilon_{ATJ}\right)}{\varepsilon_{ATJ}} \left[\sum_{j=0}^{n} M_j F_{ji} \frac{A_j}{A_i} + M_w F_{wi} \frac{A_{septum}}{A_i} \right] \,, \tag{3.22}$$

in which, n is the number of ring elements, M_j and M_i are the radiant exitances from other rings and the middle septum respectively, F_{ji} and F_{wi} are the view factors between two ring elements and wall ring element respectively, A_i and A_j are the areas of the ring elements, and A_{septum} is the area of the middle septum. Schematic diagrams of these two view factor configurations are shown in Figure 3.15.
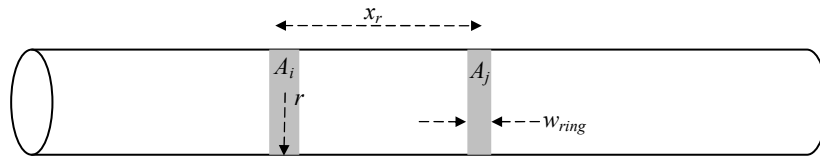
Case of two ring elements on the interior of a right circular cylinder
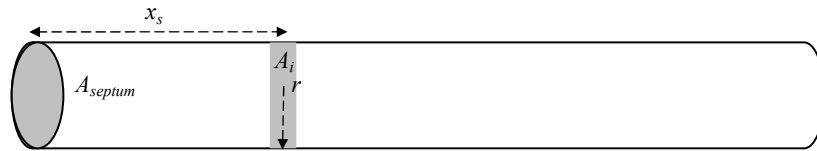
Case of ring element on interior of right circular cylinder to circular disk at a distance x_s.

Figure 3.15. Schematic diagram of two view factor configurations.

The view factors were calculated from (Siegel & Howell 2002, p. 848),

$$F_{ji} = \left[1 - \frac{2X_r^3 + 3X_r}{2(X_r^2 + 1)^{\frac{3}{2}}} \right] dX_i, \text{ and} \qquad (3.23.a)$$

$$F_{wi} = \frac{X_s^2 + \frac{1}{2}}{\sqrt{X_s^2 + 1}} - X_s, \qquad (3.23.b)$$

where,

$$X_r = \frac{x_r}{2r} \qquad (3.23.c)$$

$$X_s = \frac{x_s}{2r} \qquad (3.23.d)$$

$$dX_i = \frac{w_{ring}}{2r}$$ (3.23.e)

The radiant exitance $M_{p(T),i}$ at each position along the tube is calculated using equations (3.22) and (3.23.a-e). To simplify these calculations, all surfaces are assumed to follow *Lambert's cosine law* where they are assumed to be independent of their viewing angle; in other words the emissivities of these surfaces are independent of the viewing angles (Siegel & Howell 2002, p. 11). Due to the high emissivity of graphite, ε_{ATJ}= 0.85 (Touloukian 1970), only first order reflections were taken into consideration. Values for $M_{p(T),i}$, at each node i due only to the surface temperature are calculated and then converted into temperatures.

3.3.2 Uncertai nty in $M_{p(T),i}$

The uncertainty in $M_{p(T),i}$ consists of the uncertainties $u_{\varepsilon_{ATJ}}$, u_{M_i}, u_{M_w} and u_{M_j} in the emissivity ε_{ATJ} and the measured signals M_i, M_w and M_j respectively. The uncertainties due to the view factors and areas are small and therefore are ignored. For example, the ATJ graphite tube was machined and measured at the NMIA with a tolerance of 0.02 mm or better, this translates into a measurement uncertainty in the diameter (25.4 mm) of 0.08%, which is considered to be negligible when compared to the expected total uncertainty in the temperature measurements of 0.5 to 6.0%.

On the other hand, the uncertainties of the measured signals u_{M_i}, u_{M_w} and u_{M_j} were obtained from the standard deviations of the pyrometer readouts and were found to be about 1.4% each. According to the "ISO Guide" (ISO 1993), the total uncertainty $u_{M_{P(T),i}}$ is calculated using,

$$u_{M_{p(T),i}} = \left[\left(c_{\varepsilon_{ATJ}} u_{\varepsilon_{ATJ}} \right)^2 + \left(c_{M_i} u_{M_i} \right)^2 + \left(c_{M_w} u_{M_w} \right)^2 + \sum_{\substack{j=0 \\ j \neq i}}^{n} \left(c_{M_j} u_{M_j} \right)^2 \right]^{1/2} , \text{(3.24)}$$

in which, $u_{M_i} = u_{M_j} = u_{M_w} = 1.4\%$ of the measured signal, and $c_{\varepsilon_{ATJ}}$, c_{M_i}, c_{M_w} and c_{M_j} are the sensitivity factors given by the partial differential equations (ISO 1993),

$$c_\varepsilon = \frac{\partial M_{p(T),i}}{\partial \varepsilon_{ATJ}} = \frac{1}{\varepsilon_{ATJ}^2}\left[-M_i + M_w F_{wi}\frac{A_{septum}}{A_i} + \sum_{\substack{j=0 \\ j\neq i}}^{n}\left(M_j F_{ji}\frac{A_j}{A_i}\right)\right], \quad (3.25.a)$$

$$c_{M_i} = \frac{\partial M_{p(T),i}}{\partial M_i} = \frac{1 - F_{ii} + \varepsilon F_{ii}}{\varepsilon}, \quad (3.25.b)$$

$$c_{M_w} = \frac{\partial M_{p(T),i}}{\partial M_w} = -\frac{1 - \varepsilon_{ATJ}}{\varepsilon_{ATJ}}F_{wi}\frac{A_{septum}}{A_i}, \text{ and} \quad (3.25.c)$$

$$c_{Mj} = \frac{\partial M_{p(T),i}}{\partial M_j} = -\frac{1 - \varepsilon_{ATJ}}{\varepsilon_{ATJ}}F_{ji}\frac{A_j}{A_i}. \quad (3.25.d)$$

It is important to bring to the reader's attention that the value in equation (3.25.d) is only for one value of j. In addition, the summation in equation (3.24) is for all values of j from 0 to n except for the case of $j=i$.

Measurements of the graphite tube temperature profile were conducted using the NMIA pyrometer MTSP with a bent optical fibre at an operating temperature of 1 000 °C. The corrections and uncertainties are calculated, using the above equations, and applied to the measured data and plotted in Figure 3.16.
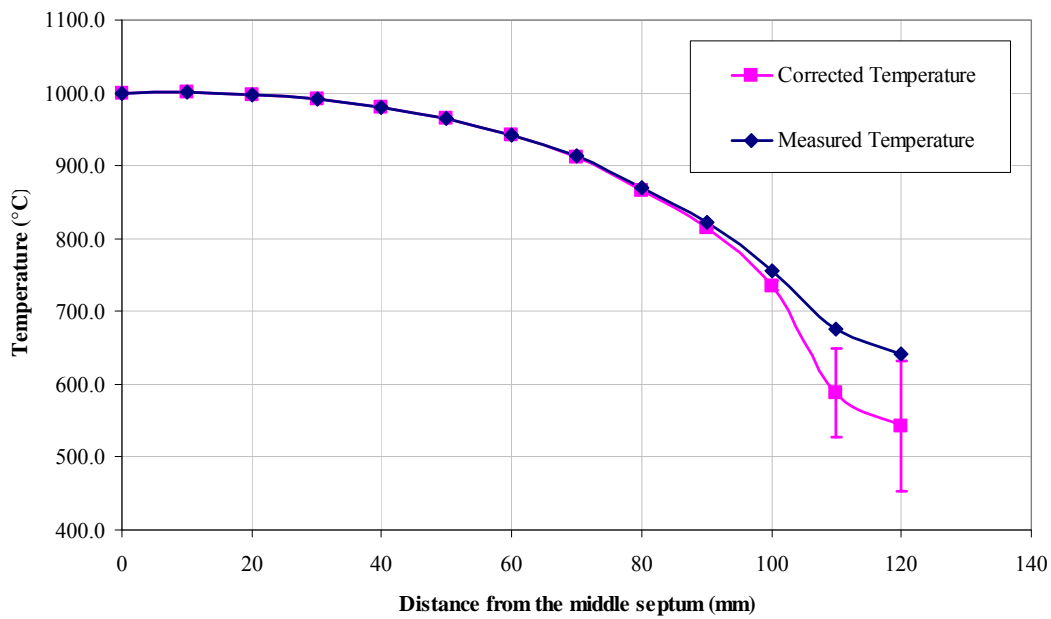
Figure 3.16. Graph of the optical fibre measured temperature compared with the corrected results with their uncertainties bars at 95% confidence limit.

As may be observed from the plots in Figure 3.16, the reflection corrections to the optical fibre measurements are small within 80 mm from the centre of the tube, due to the near isothermal conditions in this area. These corrections become larger in the cooler regions, where the radiated optical power is very small compared with the reflections from the hotter (central) area of the graphite tube. For example the blackbody radiance at 850 nm is 50 times larger at 1 000 °C than at 700 °C. The measurement uncertainties also increase toward the tube ends, mainly due to the low ratio of the voltage-to-temperature signal of the pyrometer in use (the NMIA MTSP pyrometer is best suitable for temperature measurements above 700 °C), as well as an increase of reflections from the ambient and the tube middle septum.

3.3.3 Measurement Comparison of the Optical Fibre and Pt/Pt-Rh Thermocouple Techniques

Measurements of the temperature profile of the graphite tube using the Pt/Pt-Rh thermocouple encased in the 3.2 and 4.2 mm alumina tubes and the Pt/Pt-Rh thermocouple with a circular tip as well as the bent optical fibre are compared in Figure 3.17. These measurements were conducted at an operating temperature of 1 000 °C. On the other hand, the same data are plotted in Figure 3.18 but on an expanded scale.
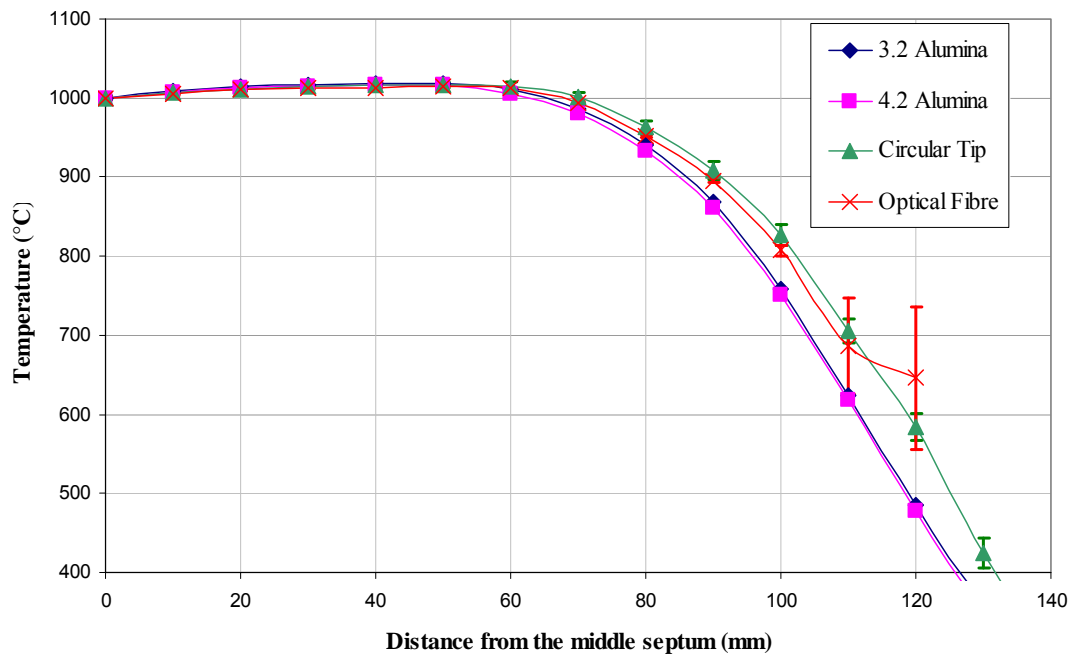
Figure 3.17. Graphs of the optical fibre corrected results and the circular-tip Pt/Pt-Rh thermcouple measurements with their uncertainty bars compared with the measurements taken by Pt/Pt-Rh thermocouple wires in alumina tubes with 3.2 and 4.2 mm diameter.
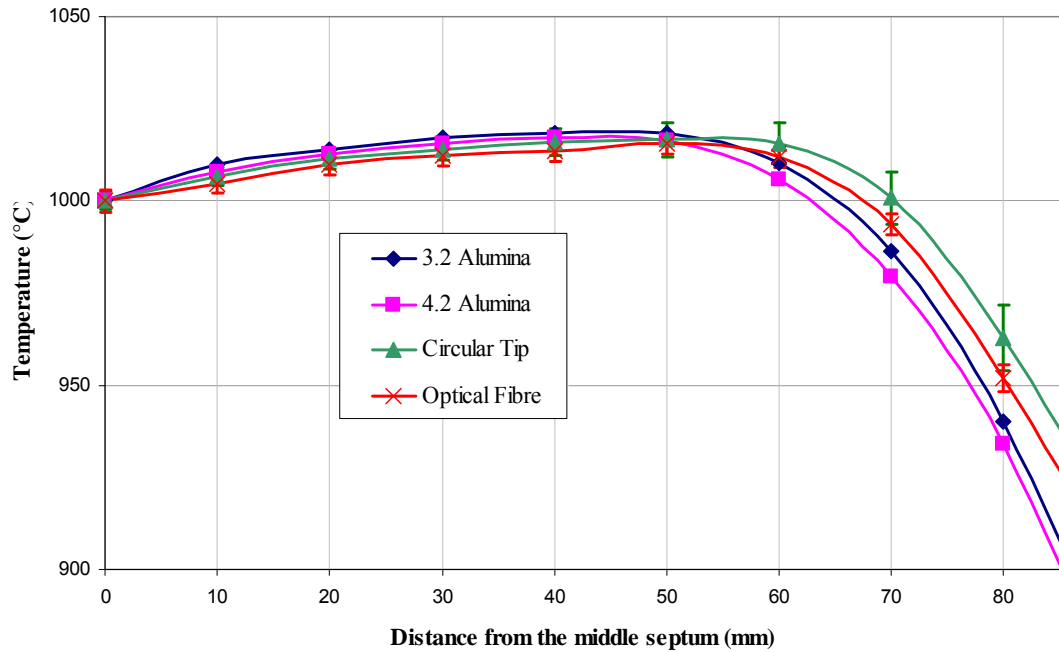
Figure 3.18. Graphs of the optical fibre corrected results and the circular-tip Pt/Pt-Rh thermcouple measurements with their uncertainty bars compared with the measurements taken by Pt/Pt-Rh thermocouple wires in alumina tubes with 3.2 and 4.2 mm diameter within 80 mm of the graphite tube centre.

It can be deduced from the graphs that the measurements by the optical fibre and all of the Pt/Pt-Rh thermocouples agree within their measurement uncertainties in the region of the tube where the temperatures are near isothermal, which is within 50 mm from the middle septum. However, in the steep temperature gradient region the difference between the Pt/Pt-Rh thermocouples placed inside the 3.2 and 4.2 mm alumina tubes, and the optical fibre and the circular-tip Pt/Pt-Rh thermocouple starts to increase as a result of the transmission line effect. On the other hand, the graphs show a good agreement within the uncertainty of measurements between the optical fibre and the circular-tip Pt/Pt-Rh thermocouple.

3.4 Overview of the Temperature Measurement Techniques

It was found from the work presented in this chapter that the most robust method of measuring the temperature profile of the graphite tube is to use the circular-tip

thermocouple, as it does not require complex and time-consuming reflection calculations, and additionally it is better suited for the measurement of full temperature range and has lower measurement uncertainties. It is therefore the intention of the present author to use this circular-tip thermocouple in all of the temperature measurements presented in this research.

Having developed a reliable technique to measure the temperature profiles of the graphite tube, a numerical model can now be developed to predict these profiles and compared them to the measured ones. However, before this model could be developed, an experimental apparatus was constructed to measure various quantities such as the heat transfer rates from and to the graphite tube. Using this apparatus, measurements of the heat transfer rates and heat balance check are conducted first before it could be used in the validation of the numerical predictions. At the same time, the apparatus was used to quantify the different heat transfer rates from and to the graphite tube, which helped in the development of the numerical model. Description of the apparatus and validation of the measurements of the heat transfer rates as well as the quantification of these rates are presented in the next chapter.

4 DESCRIPTION & VALIDATION OF THE EXPERIMENTAL APPARATUS

4.1 Introduction

As stated in chapter 1, a numerical model may be used to predict the temperature profile of the graphite tube inner walls as a function of the distance from the tube middle septum. However, it is important to firstly understand the heat transfer dynamics of the 48kW Thermogage furnace before attempting to develop any such numerical model. This can be done by measuring various heat transfer rates from and to the ATJ graphite tube. Recall that heat is generated by the tube electrically by passing a high current through it, heat is then dissipated from the tube *via* radiation from its inner wall to the environment, by conduction along the graphite tube and radially through the graphite felt. In order to evaluate the effectiveness of the experimental apparatus, the heat transfer rates generated electrically by the tube can be compared with the measured heat transfer rates dissipated out of the tube. This can be referred to as a "heat balance check".

In this chapter, the experimental apparatus used for the work presented in this thesis is described. Heat balance checks are conducted using this experimental apparatus by measuring the heat transfer rates to and from the Thermogage furnace. The results of these measurements are discussed and conclusions are made.

4.2 Experimental Apparatus

Modifications were carried out on the initial design of the 48kW Thermogage furnace, described in chapter 1, in order to make it safer to use. The main modification to the design was the installation of a brass jacket cooled by water at 15 °C, shown schematically in Figure 4.1. This was primarily done to ensure that the 48kW Thermogage furnace abided by the NMI occupational health and safety guidelines. Prior to this installation the users were at risk of being exposed to the hot surface of

the silica tube when the furnace is in operation; the temperatures of the outside surface of the silica tube can reach up to 1 100 °C. In addition to safety, the jacket provided a means to measure the heat transfer rate in the radial (P_{radial}) direction. This is done by using a K-type differential thermocouple to measure the temperature rise in the water and a flowmeter to measure the mass flowrate of the cooling water, refer to Figure 4.1. Note that a heat exchanger is used in a closed loop with the brass jacket (shown schematically in blue) to maintain the temperature of the water at 15 °C.
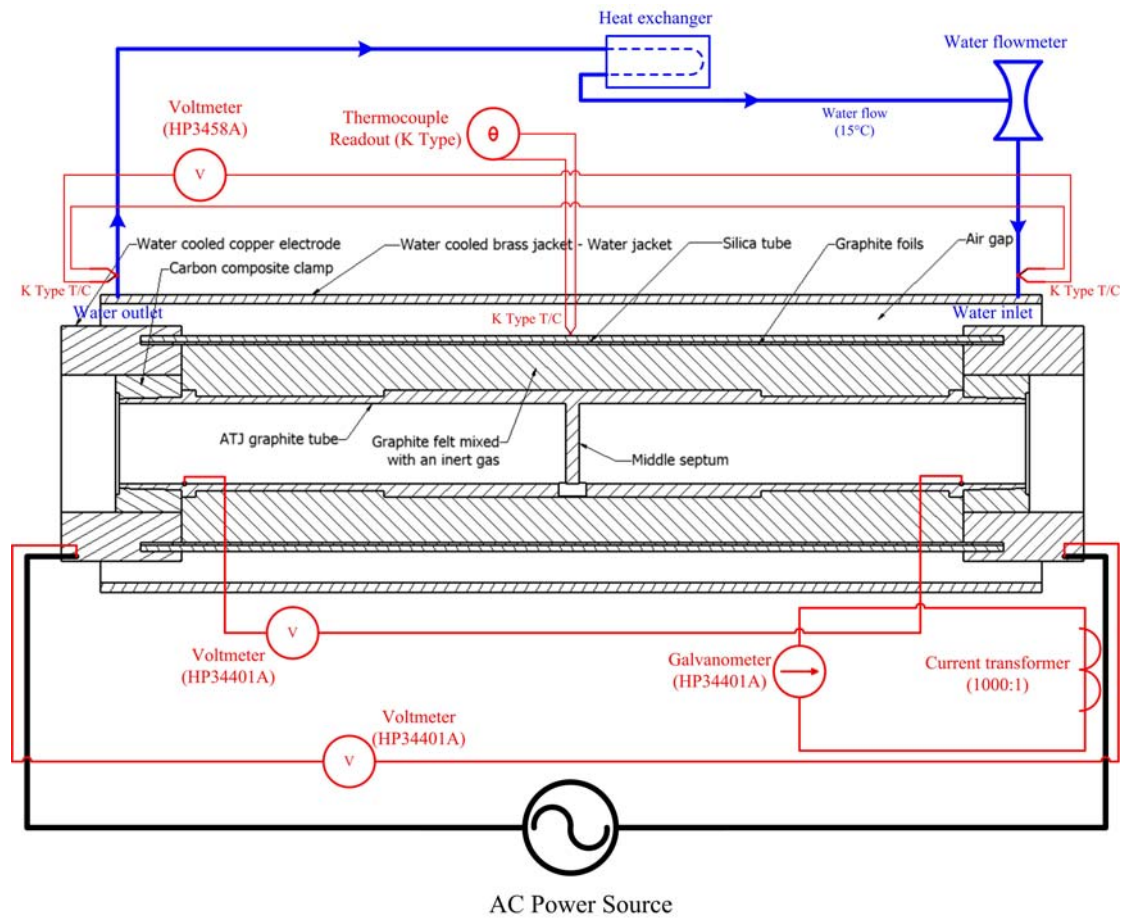
Figure 4.1. Schematic diagram of the NMIA 48 kW Thermogage furnace experimental apparatus.

As mentioned before, the ATJ graphite tube is electrically heated by passing a high current through it. The electrically generated heat ($P_{electrical}$) is then dissipated by radiation to the ambient ($P_{radiation}$), by conduction along the graphite ($P_{conduction}$) and radially through the graphite felt (P_{radial}). This can be written as,

96

$$P_{electrical} = P_{radiation} + P_{conduction} + P_{radial} \,. \tag{4.1}$$

These heat transfer rates can be calculated from direct temperature, electrical current and voltage measurements. Details of these measurements are described next.

$P_{electrical}$ is calculated from direct measurements of the root mean square (RMS) of the sinusoidal current I_{RMS} and voltage V_{RMS}, and measurements of the phase angle θ between them, given by (Dorf 2000, p. 83),

$$P_{electrical} = I_{RMS} V_{RMS} \cos(\theta). \tag{4.2}$$

Referring to the schematic diagram in Figure 4.1, I_{RMS} is measured with a calibrated (1 000:1) current transformer in conjunction with HP34401A-galvanometer. V_{RMS} is measured using HP34401A-voltmeter, however as it can be seen from the schematic diagram that this voltage is measured at two positions: (i) between the outer surfaces of the water cooled copper electrodes (V_{out}), and (ii) the inner surfaces of the ATJ graphite tube (V_{in}). These measurements are necessary in the calculation of the full electrical power delivered to the furnace assembly including the two carbon composite (CC) ends, and that delivered only to the ATJ graphite tube. It is important to note at this stage that due to the geometrical complexity of the CC clamps, these clamps will be modelled as special nodes. Whilst V_{out} can be used to calculate the overall power delivered by the Thermogage furnace, V_{in} is however more relevant to the numerical model since it can be used to calculate the electrical power delivered only by the graphite tube. It follows that the measured values of V_{in} are to be used to calculate $P_{electrical}$ (or $V_{RMS}=V_{in}$). On the other hand, the phase angle (θ) was measured using a power meter and found to be 0.00° and thus $\cos(\theta)=1.00$. This indicates that there is no significant phase shift between the current and the voltage.

The radiation power $P_{radiation}$ is the radiative exchanges from the tube inner surfaces, constituting the middle septum and the cylindrical walls to the ambient. $P_{radiation}$ can be calculated using the view factor concept and by considering only the radiative exchanges to ambient. This can be written as,

$$P_{radiation} = \begin{Bmatrix} \sigma\varepsilon_{ATJ}A_{ring}\sum_{i=1}^{m}\left[F_{ia}\left(T_{amb}^4 - T_i^4\right)\right] + \\ \sigma\varepsilon_{ATJ}A_{septum}F_{sa}\left(T_{amb}^4 - T_s^4\right) \end{Bmatrix}.$$ (4.3)

Here F_{ia} and F_{sa} are configuration (or view) factors, and A_{ring} and A_{septum} are the areas of the ring i and the middle septum respectively. Equations for F_{ia} and F_{sa} can be obtained from textbooks that deal with radiative exchanges, e.g.: Siegel & Howell (2002, p. 845 and p. 848), for the two cases of "*ring element on interior of right circular cylinder to circular disk at a distance x*" (F_{ia}) and "*parallel circular disks with centres along the same normal*" (F_{sa}), these equations were previously given in section 3.3.1 (refer also to Appendix B).

On the other hand, the heat transfer rate by conduction ($P_{conduction}$) at any position x can be calculated using Fourier's law,

$$P_{conduction} = k_{ATJ}\left(T_{ave}\right)A_c\frac{\delta T}{\delta x},$$ (4.4)

in which, k_{ATJ} is the thermal conductivity of ATJ graphite (see chapter 2), T_{ave} is the average temperature measurement of the readings conducted to obtain the temperature gradient $\delta T/\delta x$, and A_c is the cross sectional area of the graphite tube. The temperature gradient $\delta T/\delta x$ is calculated from the differences between measurements of the cavity wall temperatures, δT, and the distance between these temperatures, δx. These gradients are measured at the tube ends, just before the CC ends, where $\delta T/\delta x$ is largest. It is important to note at this stage that the above equation can be used to calculate $P_{conduction}$ was based on the assumptions that the internal heat generation within the small section, where $\delta T/\delta x$ is measured, is small in comparison to the overall conductive heat transfer rate flowing into it. As an example, the expected heat transfer rate by conduction for the case of a middle septum temperature of 1 000 °C is around 320 W, whereas the heat rate generated electrically by a section of the graphite tube with a length of 5 mm is calculated from the measured current I_{RMS} (~370 A), the resistivity (~10^{-5} Ω·m) and the cross sectional area of the graphite tube (~0.001 m²) to be 7 W. This constitutes less than 2% of the measured $P_{conduction}$. Hence, this

demonstrates that the contribution of the internally generated electrical power for the section of the graphite where the temperature gradients are measured is small and can be ignored; note that the expected uncertainty of the heat transfer rates in general is 8%.

As mentioned earlier, a brass jacket cooled by water (shown schematically in Figure 4.1) was installed around the silica tube to measure the radial heat transfer rate P_{radial}. The determination of P_{radial} using complex approximation of the heat transfer rate by free convection and the silica tube surface temperatures can be avoided when using this method since,

$$P_{radial} = C_{p_{water}} \rho_{water_{15°C}} V_{water} \Delta T_{water},$$ (4.5)

where $C_{p_{water}}$ is the specific heat of water, $\rho_{water_{15°C}}$ is the density of water at 15 °C, V_{water} is the volumetric flow rate measured with a calibrated domestic flowmeter, and ΔT_{water} is the temperature difference between the inlet and outlet of the jacket, which was measured using a K-type differential thermocouple in conjunction with a high accuracy HP3458A-voltmeter. The differential thermocouple is shown in red and the water inlet and outlet are shown in blue in Figure 4.1.

With $cos(\theta)$ taken to be 1.00 and by combining equations (4.1) to (4.5) a "heat balance" equation, pertinent to the NMIA's 48 kW Thermogage furnace, is obtained as,

$$I_{RMS}V_{RMS} = 2 \times \sigma \varepsilon_{ATJ} \left\{ \begin{array}{l} A_{ring} \sum_{i=1}^{m} \left[F_{ia} \left(T_{amb}^4 - T_i^4 \right) \right] \\ + A_{septum} F_{sa} \left(T_{amb}^4 - T_s^4 \right) \end{array} \right\} +$$

$$2 \times k_{ATJ}(T_{ave}) A_c \frac{\delta T}{\delta x} + C_{p_{water}} \rho_{water_{15°C}} V_{water} \Delta T_{water}$$ (4.6)

As it can be seen from Figure 4.1, the graphite tube is divided equally in the middle by a septum therefore the terms for the radiative and conductive heat transfer rates in

equation (4.6) above are multiplied by two to take account of the heat transfer rates at both ends.

In addition to the measurements of heat transfer rate described above, temperature measurements of the outside surface of the silica tube (inline with the middle septum) can be used in the validation of the thermal conductivity model of graphite felt developed in chapter 2 (see also Appendix C). The thermocouple was wrapped in a full circle around the silica tube to prevent measurement errors that might be caused by the effect of heat transmission line.

When trying to carry out validation measurements on the existing tube it was found that, due to the extensive use of the ATJ graphite tube at high temperatures, graphite dust, evaporating from the tube, condenses inside the graphite felt resulting in a significant change of the thermal conductivity of the insulating felt. Consequently, the temperature profile also changes due to this dust "loading" of the felt. Furthermore, the heat transfer rate in the radial direction also changes. It can be deduced that this change in the heat transfer rate in the radial direction can be used as an indicator of a change in the temperature profiles of the graphite tube. Hence, periodic measurements of P_{radial} can be employed as a quick mean to alert the users of the 48 kW Thermogage to any changes to the temperature profiles, which might be caused by the dust loading of the graphite felt.

With the problem of the dust loading identified by the present author, two new ATJ graphite tubes were then manufactured to be used for the work presented here. The first tube was a 289 mm long, referred to as the "short tube", with a 2 mm deep and 60 mm long cut. The second tube was a 400 mm long tube, referred to as the "long tube" with a 1.25 mm deep and 80 mm long cut. Schematic diagrams of these two tubes are shown in Figure 4.2.
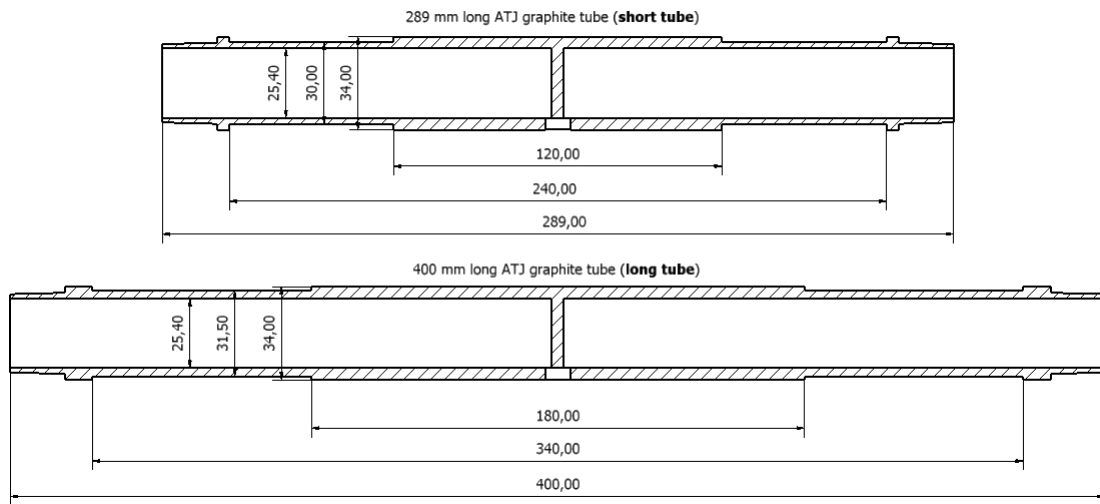
Figure 4.2. Schematic diagrams of the cross sectional views of 289 mm and 400 mm long ATJ graphite tubes (heater elements of the 48kw Thermogage furnace), referred to as the "short tube" and "long tube" respectively, manufactured at the NMIA.

Measurements of the heat transfer rates were conducted using both tubes and the results are presented in the next section. Note that the full details of these measurements can be found in Appendix B.

4.3 Heat Balance Measurements

As mentioned in the introduction to this chapter, measurements of the heat transfer rates were conducted to compare electrically generated heat by the ATJ graphite with the dissipated heat rates via radiation to ambient, conduction along the graphite tube and radially through the graphite felt; which are expressed mathematically in equation (4.6). Conducting this heat balance testing ensures that the balance of energy, within the specified measurement uncertainties, is achieved resulting in higher confidence in the experimental apparatus. A summary of the measurement results for the "short tube" and the "long tube" are presented in the next two sub sections. Detailed descriptions of these measurements can be found in Appendix B.

4.3.1 Short Tube

Measurements of the "short tube" temperature profile were conducted at two operating temperatures of 1 000 and 1 500 °C with the graphite felt purged with nitrogen. Temperature measurements were conducted from the tube middle septum to its end at 10 mm intervals. These measurements are presented in Figure 4.3.
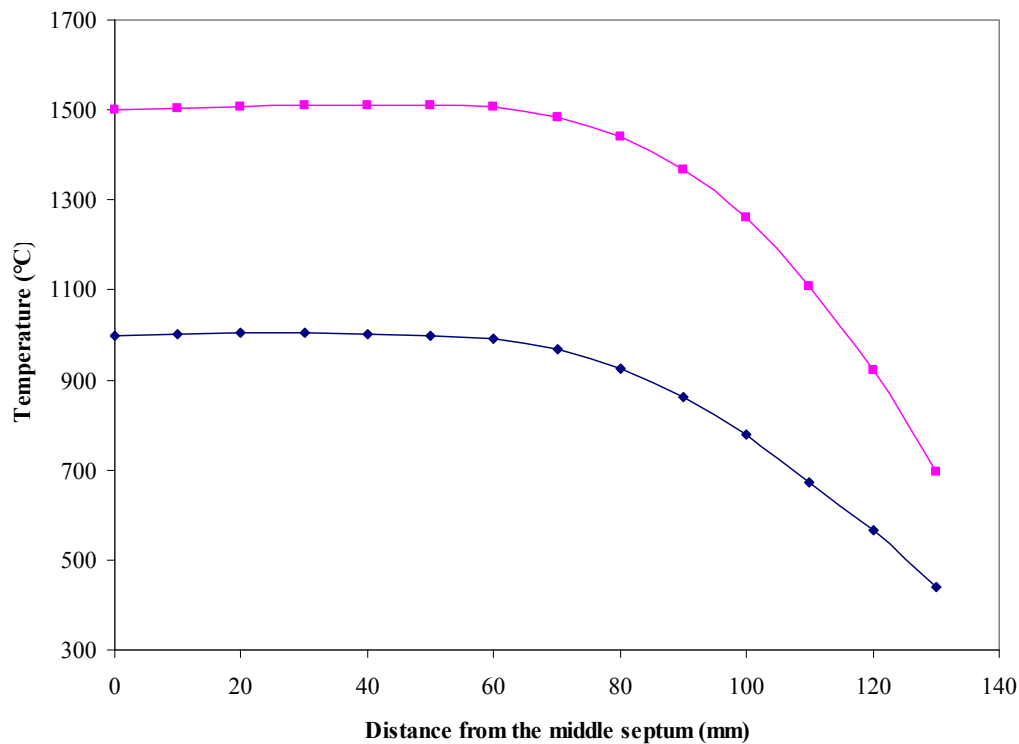
Figure 4.3. Graphs of the 289 mm ATJ graphite tube (short tube) temperature profile measurements at operating temperatures of 1 000 and 1 500°C with the graphite felt purged with nitrogen.

Using these temperature measurements, the radiative heat transfer rate, $P_{radiation}$, was calculated. In the calculations, the inner walls of the graphite tube were divided into 10 mm wide rings with the ambient circular opening positioned at 117.5 mm from the middle septum; the position at which the CC clamps were located. Recall that the voltage (V_{in}) across the inside of the graphite tube was measured at these points in order to calculate the heat rate generated electrically by the tube only, which did not include the CC clamps.

The conductive heat transfer rate, $P_{conduction}$, was calculated from equation (4.4) and measurements of the temperature gradients of the graphite tube inner walls conducted at the furnace operating temperatures of 1 000, 1 200, 1 400, 1 500 and 1 700 °C. Measurements of the temperature gradients, using nitrogen as the felt purging gas, are presented in Figure 4.4.
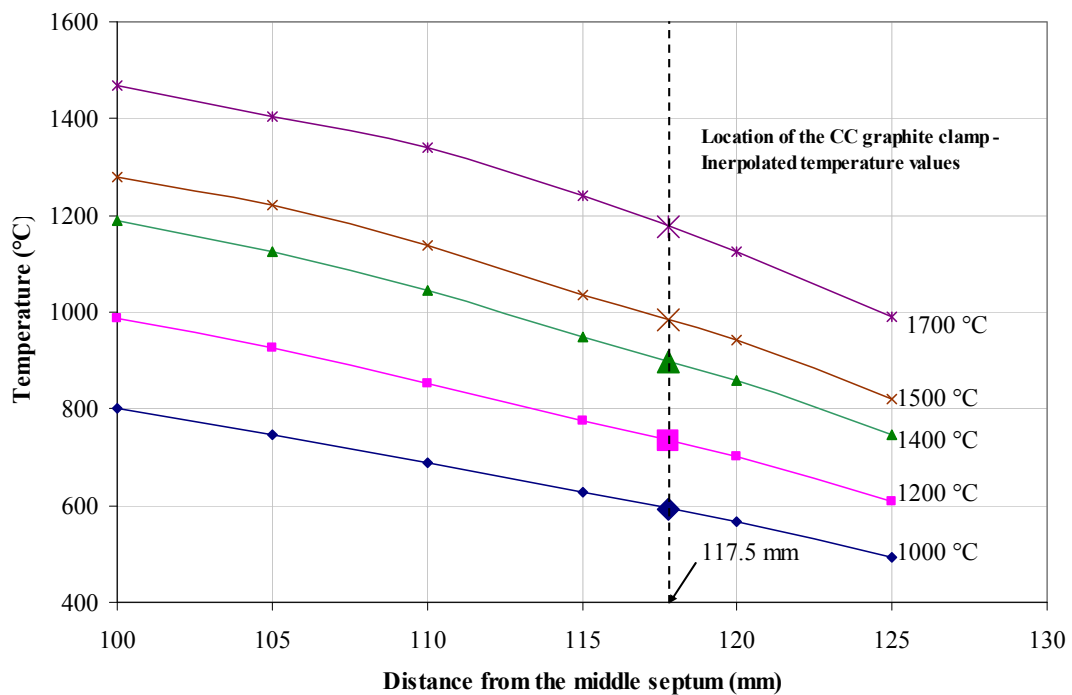
Figure 4.4. Graphs of the 289 mm ATJ graphite tube (short tube) inner wall temperatures versus the distance from the middle septum at operating temperatures of 1 000, 1 200, 1 400, 1 500 and 1 700 °C.

Referring to the plots in Figure 4.4, the temperatures at the location of the CC clamps are interpolated and values of $\delta T / \delta x$ are calculated using these temperatures.

The radial heat rate, P_{radial}, is calculated using equation (4.5) and measurements of the brass jacket cooling water temperature rise, ΔT_{water}, and its flow rate, V_{water}, which are measured using differential thermocouples and a calibrated water flowmeter respectively, refer to Figure 4.1. During testing, the flow rate V_{water} was measured to

be 4.16 L·min^{-1}. The temperature rise ΔT_{water} was also measured and plotted, as a function of the tube middle septum temperatures, in Figure 4.5.
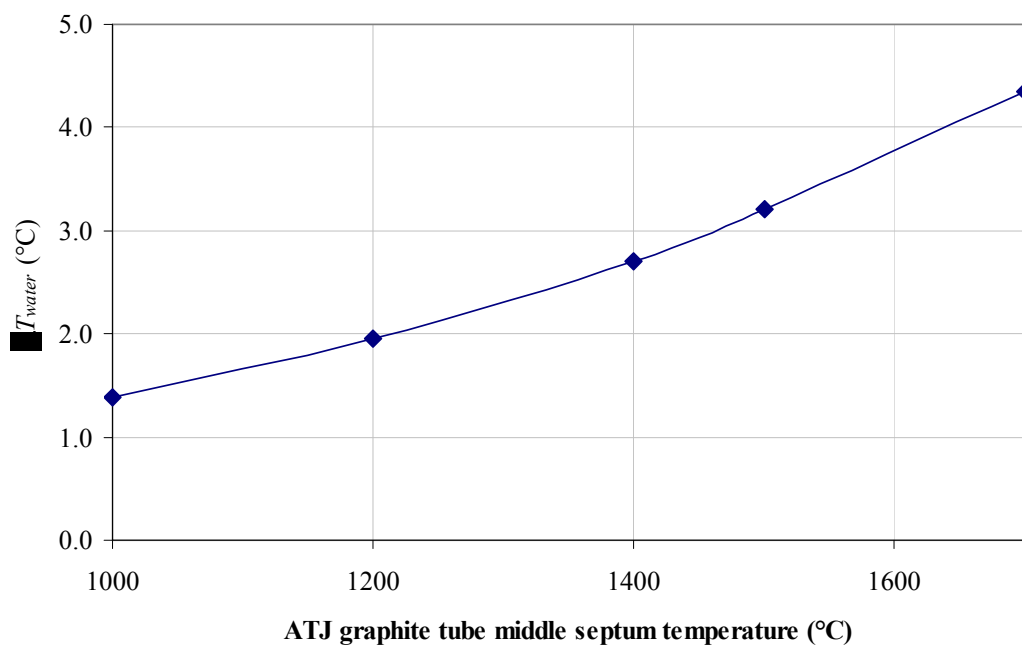
Figure 4.5. Graph of the temperature rise of the brass jacket cooling water, ΔT_{water}, as a function of the 289 mm ATJ graphite tube (short tube) middle septum temperature (or the furnace operating temperature).

The calculated values of $P_{electrical}$, $P_{radiation}$, $P_{conduction}$ and P_{radial} were then used in a heat balance check on the "short tube" with nitrogen as the felt purging gas and the results are shown in Figure 4.6.
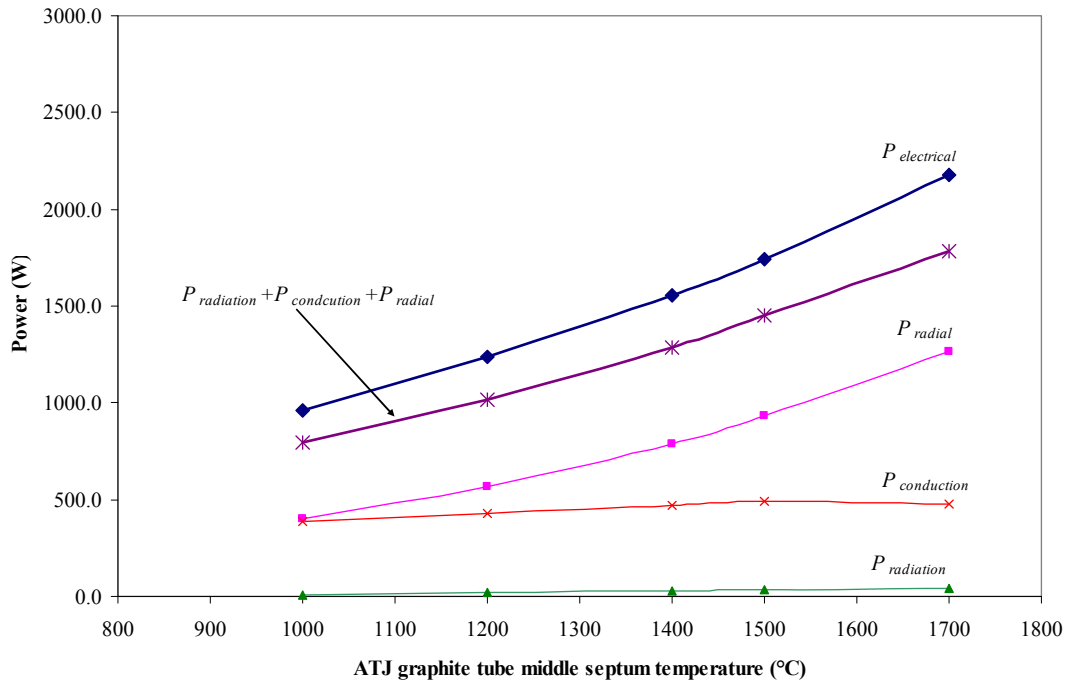
Figure 4.6. Graphs of the NMIA 48 kW Thermogage furnace heat transfer rates $P_{electrical}$, $P_{radiation}$, $P_{conduction}$ and P_{radial} as well as their sum at operating temperatures of 1 000, 1 200, 1 400 and 1 600 °C for the case of the 289 mm ATJ graphite tube (short tube). The measurements were conducted with nitrogen as the graphite felt purging gas.

Referring to the figure above, it may be noted that the contribution of $P_{radiation}$ to the total output heat transfer rate ($P_{radiation}+P_{conduction}+P_{radial}$) varies between 1.0% at 1 000 °C to a maximum of 2.3% at 1 700 °C (refer to Appendix B for the exact values of $P_{radiation}$). As mentioned before, measurements of temperature profiles were conducted at operating temperatures of 1 000 and 1 500 °C. However, using these profiles the values of $P_{radiation}$ were interpolated at the middle septum temperatures of 1 200 and 1 400 °C and extrapolated at a temperature of 1 700 °C. As can be deduced, the contribution of $P_{radiation}$ to the total heat transfer rate output is small. However, this does not lead to the conclusion that radiative exchanges are of no importance since most of these exchanges occur within the interior walls of the graphite tube and only a small portion of these exchanges is emitted to the ambient.

While the contribution of the conductive heat transfer rate $P_{conduction}$ to the total heat transfer rate ($P_{radiation}+P_{conduction}+P_{radial}$) is significant (in some cases up to 48% at 1 000 °C), it can be observed from the plots that most of the electrically generated energy $P_{electrical}$ is dissipated in the radial direction through the felt; P_{radial} varies from

51% at 1 000 °C to 71% at 1 700 °C. It can be also concluded that heat is transferred one-dimensionally in the radial direction through the graphite felt, while it is transferred one-dimensionally along the graphite ATJ in the axial direction. Noteworthy at this stage is that with these heat transfer rates ($P_{conduction}$ and P_{radial}) being found to be one-dimensional, the numerical model for the Thermogage furnace can be developed in a way that it can be simplified based on these findings.

On the other hand, the comparison between the electrical input energy or heat transfer rate, $P_{electrical}$, with the sum of all dissipated (output) heat transfer rates, $P_{radiation}+P_{conduction}+P_{radial}$, shows a difference of 17%-18% with $P_{electrical}$ being the larger. This implies that losses existed in the experimental apparatus that could not be accounted for (rather than erroneous in measurements). In order to decrease this difference, a new tube was manufactured with a length of 400 mm ("long tube") and with improvements made to the experimental apparatus. Similar to the "short" tube, a heat balance check was also carried out on the "long tube". Descriptions of these improvements and results of the heat balance check are presented next.

4.3.2 Long Tube

As mentioned earlier, improvements were made on the experimental apparatus in order to get better agreement between the heat flow rates, $P_{electrical}$ and $P_{radiation}+P_{conduction}+P_{radial}$. This was done by better insulating the edges of the water cooled brass jacket (shown in Figure 4.1) to ensure that radial heat is fully captured. In addition, it was observed by the author that the original graphite felt used by the manufacturer of the Thermogage furnace was not evenly wrapped around the tube, which would have affected the temperature profile of the graphite tube, especially the uniformity of these temperatures along the axial direction. This problem was resolved by reinstalling the graphite felt in even layers. On the other hand, measurements of $P_{conduction}$ were improved by using a precision stage to better measure the distances used in the calculations of the temperature gradients ($\delta T/\delta x$). With these improvements, a heat balance check was conducted on the "long tube" and the measurements are presented next (see also Appendix B).

Similarly to the case of the "short tube", measurements of the heat rates were conducted using the "long tube" at operating temperatures of 1 000, 1 200, 1 400 and 1 600 °C. Results for the cavity inner wall temperature profiles used in the calculation of $P_{radiation}$ are presented in Figure 4.7. The measured temperature gradients at 167.8 mm, at which the CC clamps are located, are plotted in Figure 4.8. These were used in the calculation of $P_{conduction}$. The measured temperature rise ΔT_{water}, used in the calculation of P_{radial} as a function of the middle septum temperature (that is the same as the furnace operating temperatures), is plotted Figure 4.9. In addition to these measurements, the cooling water average flow rate V_{water} was measured to be 2.85 L·min^{-1}. Values of ΔT_{water} and V_{water} were used in the calculation of P_{radial}. Note that Appendix B contains detailed descriptions of these measurements.
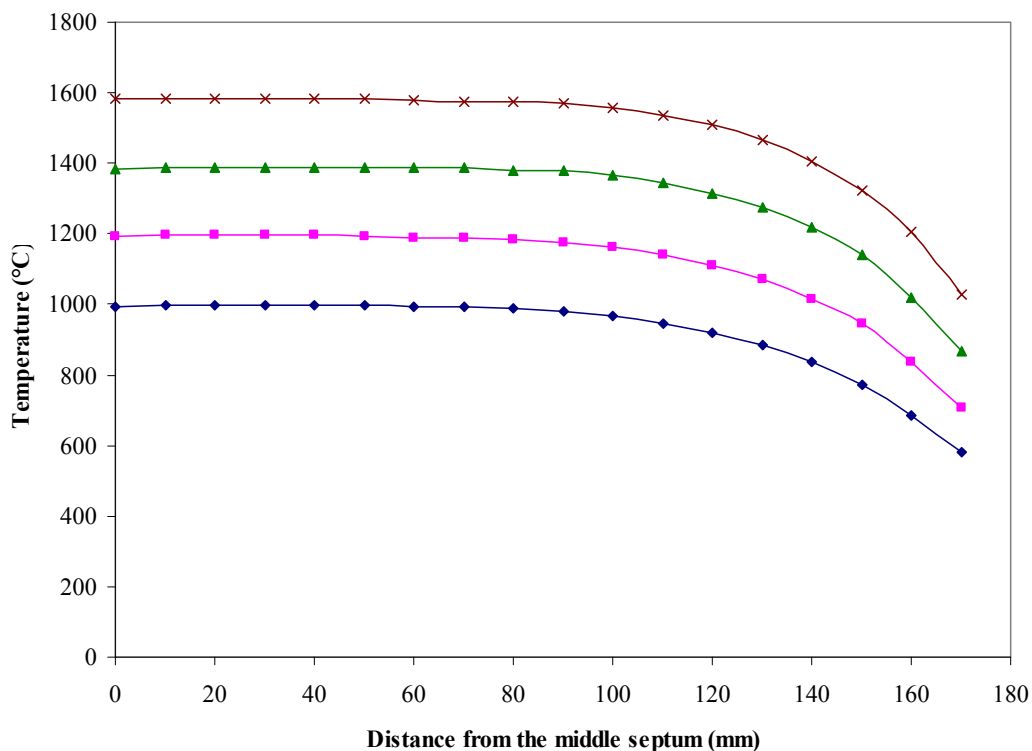
Figure 4.7. Plots of the 400 mm ATJ graphite tube (long tube) temperature profile measurements at operating temperatures of 1 000, 1 200, 1 400 and 1 600°C with the graphite felt purged with nitrogen.
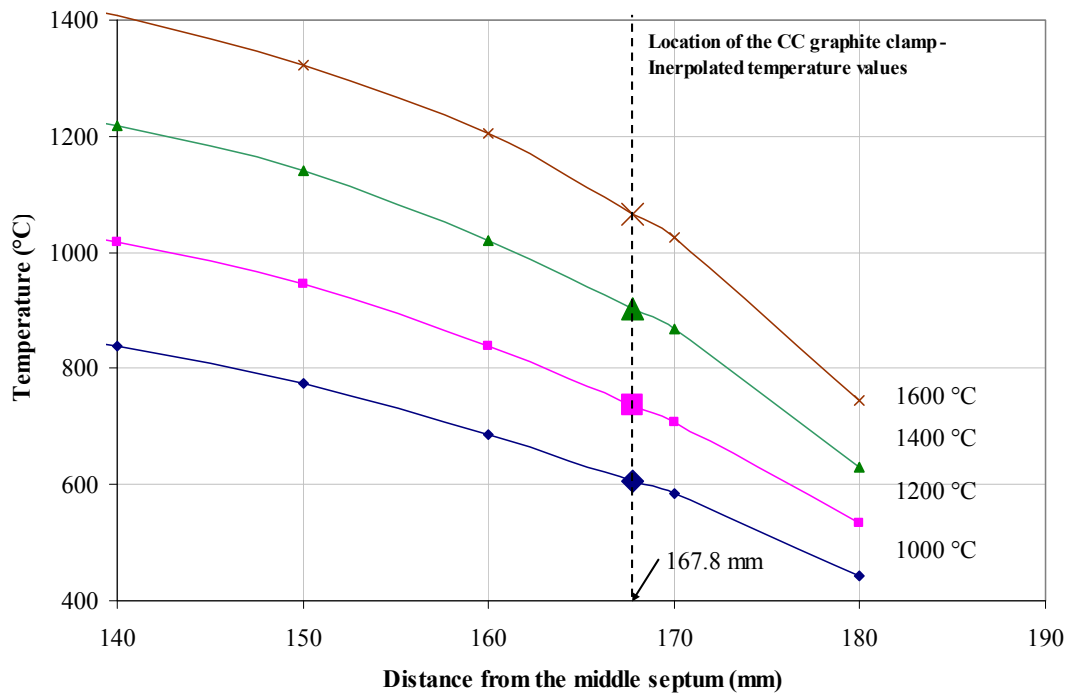
Figure 4.8. Plots of the 400 mm ATJ graphite tube (long tube) inner wall temperatures versus the distance from the middle septum at operating temperatures of 1 000, 1 200, 1 400 and 1 600 °C.
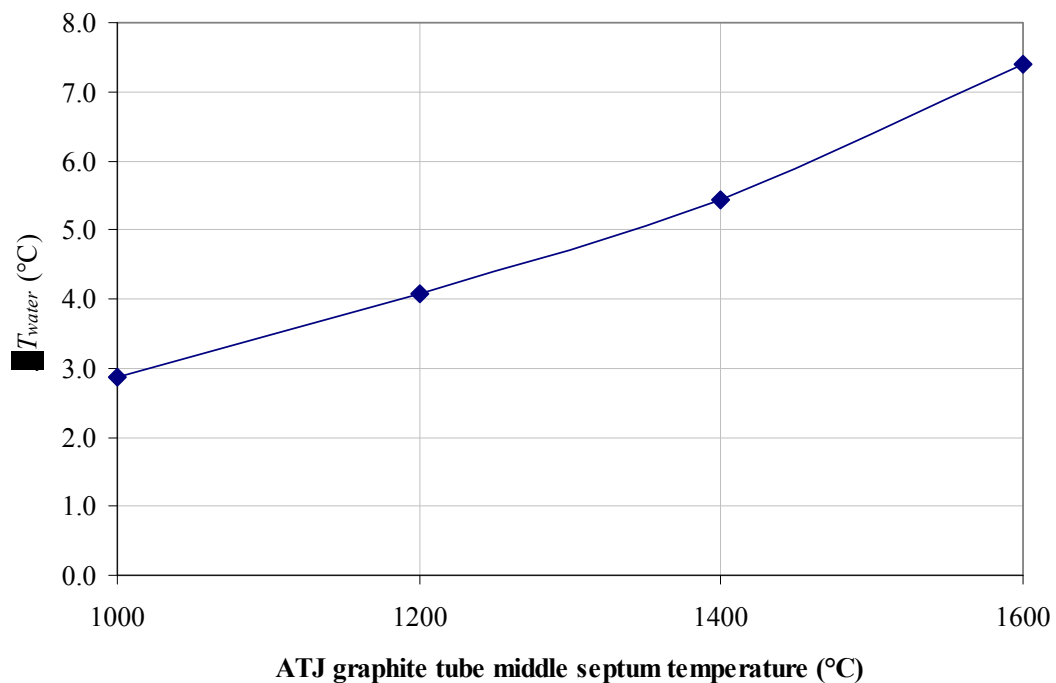
Figure 4.9. Plot of the temperature rise of the brass jacket cooling water, ΔT_{water}, as a function of the 400 mm ATJ graphite tube (long tube) middle septum temperature (or the furnace operating temperature).

Using the calculated values of $P_{electrical}$, $P_{radiation}$, $P_{conduction}$ and P_{radial}, a heat balance check was also conducted on the "long tube" with nitrogen used as the felt purging gas and the results are plotted in Figure 4.10.
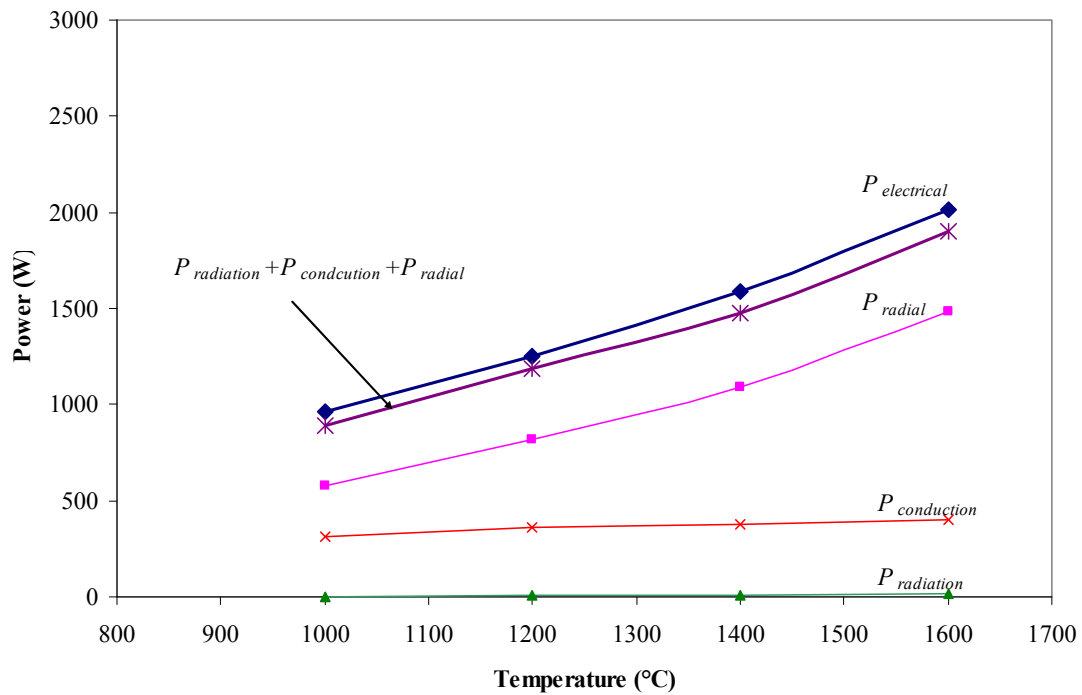
Figure 4.10. Graphs of the NMIA 48 kW Thermogage furnace's heat transfer rates $P_{electrical}$, $P_{radiation}$, $P_{conduction}$ and P_{radial} as well as their sum at operating temperatures of 1 000, 1 200, 1 400 and 1 600 °C for the case of the 400 mm ATJ graphite tube (long tube). The measurements are conducted with nitrogen as the graphite felt purging gas.

The contribution of $P_{radiation}$ is less than 1% at all operating temperatures, which is similar or close in value to that of the "short tube". On the other hand, the contribution of $P_{conduction}$ to the total output heat transfer rate varies between 35% at 1 000 °C to 21% at 1 600 °C. However, as can be seen from the graphs P_{radial} is the dominant heat transfer rate, which varies between 64% at 1 000 °C to 78% at 1 600 °C. The increase in the percentage of P_{radial} for the case of the "long tube" in comparison to that of the "short tube" is attributed to the increase of the length of the graphite tube.

Also, it may be noted from the graphs above that the discrepancy between the electrical input heat transfer rate ($P_{electrical}$) and the sum of all output heat transfer rates

109

($P_{radiation}$+$P_{conduction}$+P_{radial}) is decreased due to the improvements made on the experimental apparatus; better insulations at the edges of the brass jacket, evenly wrapped graphite felt and more accurate measurements of the temperature gradients. This discrepancy now varies between 5% to 8%, which is a factor of two to three better than the results obtained previously for the "short tube". The input heat rate agrees well with the sum of all output heat rates when taking into consideration the expected values of measurement uncertainties associated with these heat rates, which are discussed in the next section.

4.4 Uncertainty Analysis

The large discrepancy between and the input and output heat transfer rates for the "short tube" indicate that large systematic errors existed prior to the improvements on the experimental apparatus being carried out. Therefore, uncertainty analysis of the "short tube" will not be further discussed in this thesis as these systematic errors were not accounted for.

In the case of the "long tube", the uncertainties between the input and output heat transfer rates can be calculated from the models given in equations (4.1) and (4.6). However, the uncertainty contributions of the various surface areas (A_{ring}, A_{septum} and A_c), emissivity (ε_{ATJ}), configurations factors (F_{ia} and F_{sa}), density of water ($\rho_{water_{15°C}}$) and ambient temperature (T_{amb}) are small in comparison to other quantities and therefore can be ignored. Note that all of these terms have an uncertainty of less than 0.1%.

For the electrical input power $P_{electrical}$, the two dominant uncertainty components are the electrical current I_{RMS} and the voltage V_{RMS} with negligible uncertainty contribution by the phase shift θ. The electrical transfer rate standard uncertainty $u_{P_{electrical}}$ can be calculated using the ISO Guide (ISO 1993) to be,

$$u_{P_{electrical}} = \sqrt{(c_I u_I)^2 + (c_V u_V)^2} \ . \tag{5.7}$$

Here $c_I=V_{RMS}$ and $c_V=I_{RMS}$ are the sensitivity factors, and u_I and u_V are the standard uncertainties in measuring I_{RMS} and V_{RMS} respectively. Values of u_I and u_V were obtained from their calibration reports and the standard deviations of the measurements of I_{RMS} and V_{RMS} during testing. These uncertainties were calculated to be 0.5% of the average reading of I_{RMS} and V_{RMS} respectively. Note that this uncertainty value of 0.5% was due mainly to the fluctuation in I_{RMS} and V_{RMS} rather than to the accuracy of the multimeters used to measure these quantities. Using a coverage factor $k=2.0$, $u_{P_{electrical}}$ is calculated at 95% confidence limit to be ±1.4% of the reading. Note that the coverage factor k is a numerical factor used as a multiplier of the combined standard uncertainty in order to obtain an expanded uncertainty (ISO 1993).

The measurement uncertainty of the radiative heat transfer $u_{P_{radiation}}$ is due mainly to the temperature profile measurement uncertainty. However, as it has been indicated in the previous section that the contribution of $P_{radiation}$ to the total sum of all output heat transfer rate is less than 1% and hence any contribution caused by the uncertainty in measuring the temperature profile has negligible effect on the total uncertainty and therefore may be ignored.

On the other hand, the standard uncertainty of the conductive heat transfer rate ($u_{P_{conduction}}$) consists of the uncertainties due to the ATJ graphite thermal conductivity ($u_{k_{ATJ}}$) and the temperature gradient measurement ($u_{\partial T/\partial x}$), and can be calculated using (ISO 1993),

$$u_{P_{conduction}} = \sqrt{\left(c_{k_{ATJ}} u_{k_{ATJ}}\right)^2 + \left(c_{\partial T/\partial x} u_{\partial T/\partial x}\right)^2} \ , \tag{5.8}$$

in which, $c_{k_{ATJ}} = 2A_c\, \delta T/\delta x$ and $c_{\partial T/\partial x} = 2A_c k_{ATJ}\left(T_{ave}\right)$ are the sensitivity factors for $u_{k_{ATJ}}$ and $u_{\delta T/\delta x}$ respectively. Values for $u_{k_{ATJ}}$ are obtained from section 2.2.3, to be 10%. On the other hand, the temperature gradient uncertainty $u_{\delta T/\delta x}$ may be obtained

from section 3.2.2, which is a function of the tube ends temperature or the furnace operating temperature.

The standard uncertainty of the radial heat transfer rate ($u_{P_{radial}}$), which consists of the standard uncertainty of the cooling water flow rate ($u_{V_{water}}$) and the standard uncertainty of the water temperature rise ($u_{\Delta T_{water}}$), is calculated using,

$$u_{P_{radial}} = \sqrt{\left(c_{V_{water}} u_{V_{water}}\right)^2 + \left(c_{\Delta T_{water}} u_{\Delta T_{water}}\right)^2} \ . \tag{5.9}$$

Here the sensitivity factors for $u_{V_{water}}$ and $u_{\Delta T_{water}}$ are $c_{V_{water}} = C_{p_{water}} \rho_{water_{15°C}} \Delta T_{water}$ and $c_{\Delta T_{water}} = C_{p_{water}} \rho_{water_{15°C}} V_{water}$ respectively. Values of $u_{V_{water}}$ can be obtained from combining calibration uncertainty of the flow meter and the variability of the flow rate and water temperature. This was estimated by visually inspecting the readings of the flowmeter and found to be 0.5%. The uncertainty in the temperature rise measurement $u_{\Delta T_{water}}$ can be calculated from the thermocouple calibration report, the repeatability of the temperature readings during testing and the efficiency of the water jacket to capture all of the radial heat, this uncertainty component was estimated to be 0.1 °C at all the furnace's operating temperatures.

It follows from the above that the standard uncertainty of the sum of all the output heat rates, u_{out}, can be calculated by combining all the standard uncertainties above, in accordance with the ISO Guide (ISO 1993), as,

$$u_{out} = \sqrt{u_{P_{conduction}}^2 + u_{P_{radial}}^2} \ . \tag{5.10}$$

The measurement uncertainties $u_{P_{electrical}}$, $u_{P_{conduction}}$ and $u_{P_{radial}}$, and the total output heat transfer rate standard uncertainty u_{out} were all calculated at one standard deviation and are plotted in Figure 4.11.
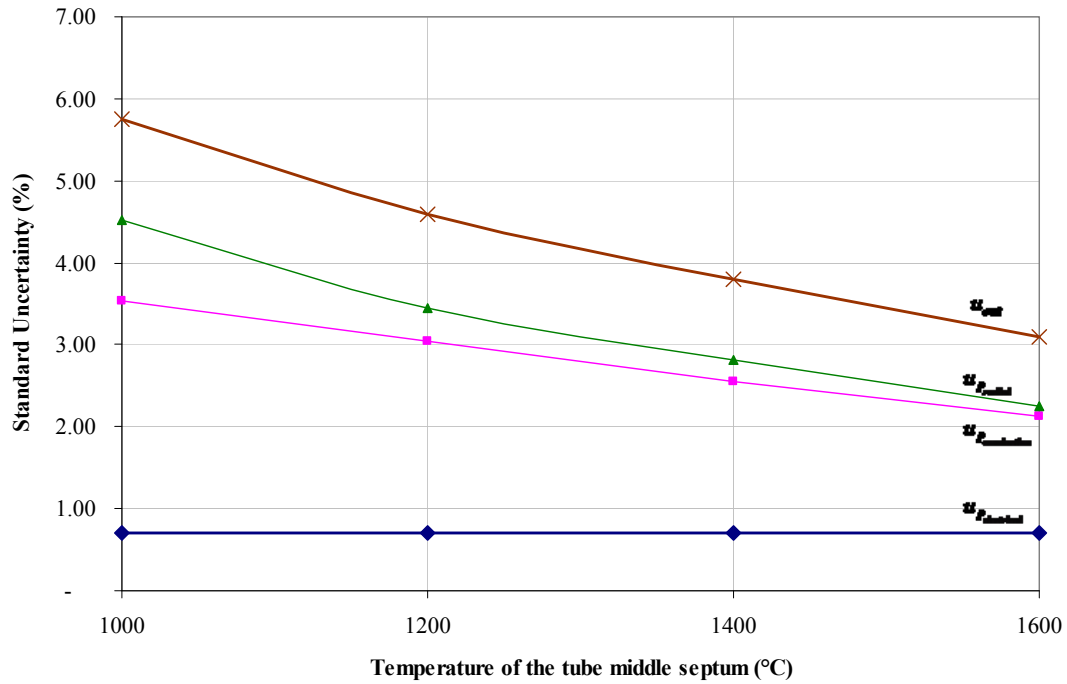
Figure 4.11. Plots of the electrical power standard uncertainty $u_{Pelectrical}$, the standard uncertainty components $u_{Pconduction}$ and $u_{Pradial}$, and the total output heat transfer rate standard uncertainty u_{out} as a function of the tube middle septum temperatures (or the furnace operating temperatures).

As can be seen from the plots, the dominant uncertainty contributor to the total output uncertainty u_{out} is the radial one, $u_{P_{radial}}$; this is mainly due to the high proportion of the radial heat transfer rate P_{radial} to the sum of all output heat transfer rates.

Using the uncertainty values above, the input ($P_{electrical}$) and output ($P_{radiation}+P_{conduction}+P_{radial}$) heat transfer rates for the measurement results in Figure 4.10 are compared using these uncertainties at 95% confidence limit with a coverage factor of 2.0. The results are presented in Figure 4.12.
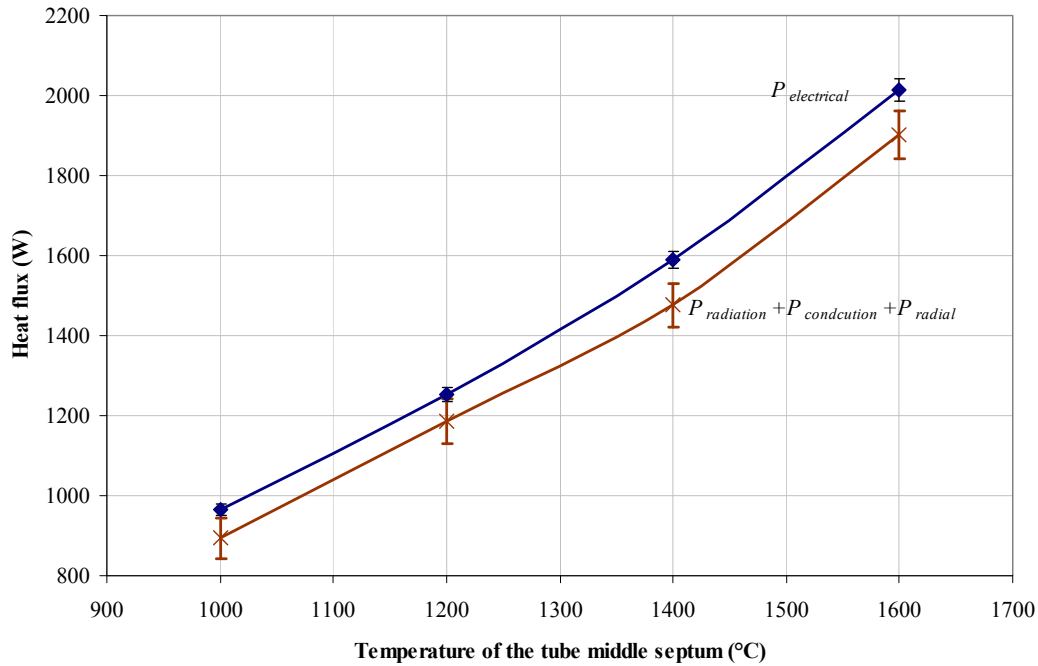
Figure 4.12. Graphs of the input electrical heat transfer rate $P_{electrical}$ and the sum of all output heat transfer rates ($P_{radiation}$+$P_{conduction}$+P_{radial}) for the case of the "long tube" versus the temperature of the ATJ tube middle septum along with their uncertainty bars calculated at 95% confidence limit.

As can be observed from the graphs, a good agreement can be found between $P_{electrical}$ and $P_{radiation}$+$P_{conduction}$+P_{radial} within their measurement uncertainties at operating temperatures of 1 000 and 1 200 °C. However, at the higher temperatures of 1 400 and 1 600 °C, the difference between $P_{electrical}$ and ($P_{radiation}$+$P_{conduction}$+P_{radial}) becomes larger. As it can be seen from the plots, this difference shows that the measured output heat transfer rates are always smaller than the input one. This suggests that there are small heat leakages that are not accounted for when measuring the output heat transfer rates. Another possibility of a heat leakage may occur at the edges of the graphite felt and the water cooled copper electrodes, shown in Figure 4.1, since no insulation exists between the felt and these electrodes.

4.5 Conclusions

It was shown that the measurement discrepancies (17-18%) between the heat transfer rates for the "short tube" were not acceptable as they were much higher than the expected uncertainties. This was improved by constructing the "long tube". The measurements on this tube showed better agreement (8%) between the heat transfer rates.

It was also found that the brass jacket used for safety reasons and, at the same time, to measure the heat transfer rate dissipated in the radial direction could as well be used to check for any change in the temperature profile of the inner walls of the ATJ graphite tube. This could be done by monitoring changes in the measured radial heat transfer rate, which could be affected by changes in the thermal conductivity of the WDF graphite felt that surrounds the graphite tube.

Most importantly, it was shown in this chapter that heat transfer rate through the graphite felt is mostly one-dimensional in the radial direction and also one-dimensional in the axial direction along the ATJ graphite tube. Based on these findings, the numerical model to be used to predict the temperature profiles of the inner walls of the ATJ graphite tube can now be developed. Details of this numerical model are presented in the next chapter.

5 QUASI 2-D NUMERICAL MODEL

5.1 Introduction

Advances in electronic computing in the last three decades have greatly reduced the difficulty of solving complex linear and non linear equations, thereby making numerical modelling a practical tool for solving engineering problems. As a consequence, the prediction of the behaviour of engineering designs and the optimisation of their performance and efficiency is now an everyday occurrence.

The optimisation of the performance, specifically the emissivity, of the 48kW Thermogage blackbody graphite furnace, described in chapter 1, requires as a first step that there should be a validated model of the existing furnace which includes the graphite tube and its insulation. The numerical models would of course have to simulate the graphite tube temperature profile and heat transfer rates which are functions of the operating parameters used. These parameters are the electrical current flowing through the graphite, the profile of the ATJ graphite tube, the thermal conductivity of the insulating felt and the ATJ graphite and other thermal boundary conditions. In this chapter, a description of the development and validation of a quasi-two dimensional (2-D) numerical model to simulate the behaviour of the graphite furnace, when it is electrically heated, are presented and discussed.

5.2 Thermogage Furnace

The Thermogage blackbody furnace consists of an ATJ graphite tube surrounded by insulating material, which consists of graphite felt purged with an inert gas wrapped with two layers of graphite foils and inserted into a silica tube. As was seen in Figure 1.12, the original design of the tube consisted of a 289 mm long tube whose outside diameter was 31.8 mm and whose wall thickness was 3.2 mm; machined from ATJ grade graphite rods. However, upon close inspection of this tube by the present

author, it was found that the insulating felt was loaded with graphite powder. This might have been caused by the ATJ graphite particles evaporating, when the rod was heated to temperatures above 2 000 °C, and condensing in the relatively cooler insulating felt. Therefore, to properly validate the numerical model, a new tube was needed and therefore constructed. With the new tube, the outside diameter was increased to 34 mm, providing a wall thickness of 4.3 mm. Two symmetrical cuts on the outside of the tube were machined at 24.5 mm from both ends of the tube. Both cuts are 2 mm deep and 60 mm long, shown schematically in Figure 5.1. It is important to point to the reader's attention at this stage that, in addition to the need of a new rod with uncontaminated insulation for validation purposes, these cuts were introduced as an initial attempt to improve the uniformity of the temperature distribution in the area near the middle septum of the tube.
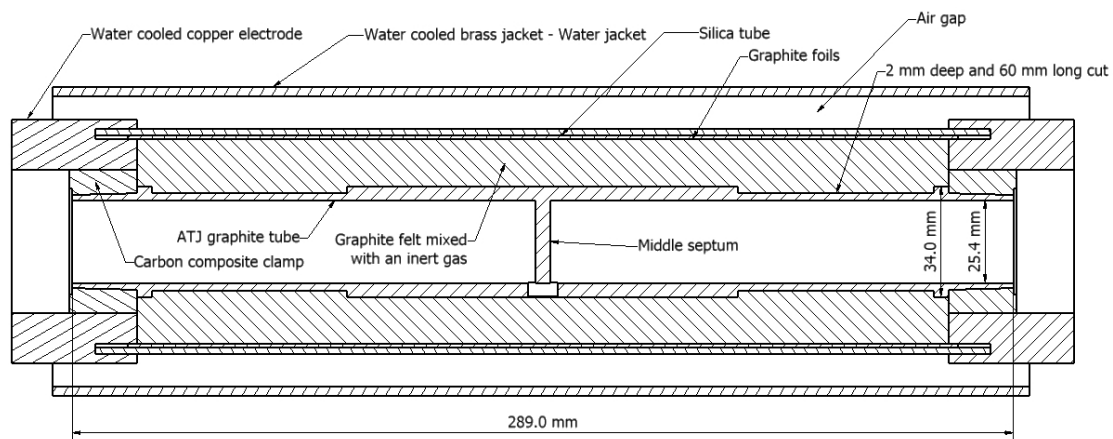
Figure 5.1 Schematic diagram of the Thermogage graphite furnace at the NMIA.

The graphite felt with a 21 μm-diameter fibres, manufactured by MorganAM&T, has a measured density of 80 kg·m^{-3} (see chapter 2 and Appendix A). The graphite tube with its insulation, contained inside a silica tube, are surrounded by a water cooled jacket whose function is to prevent accidental contact with the hot surface of the silica tube and to capture the radial heat transfer rate where it can be measured calorimetrically (refer to chapter 4). The ends of the tube are clamped by graphite-composite rings, which are in turn clamped to water cooled copper rings. The furnace is powered by a 48-kW AC power generator.

117

5.3 Numerical Model

During operation, a voltage applied across the copper rings causes an electric current to flow through the graphite thereby heating the graphite tube. Applying the law of conservation of energy, the electrical power supplied to the tube, q_e, is dissipated by:

(i)   conduction along the ATJ graphite tube,

(ii)   radiation from the middle of the tube to the outside, and

(iii)   radiation, convection and conduction radially through the graphite felt insulation.

It was concluded from the measurements of the heat transfer rates and the heat balance checks, refer to chapter 4, that the heat flows in the system are one-dimensional along the graphite tube and through the graphite felt. Based on these findings, the heat flows can now be separated into a succession of one dimensional (1-D) heat transfer problems with non-coupled thermal resistances in the axial and radial directions, as may be seen schematically in Figure 5.2. Hence, the numerical model then becomes a quasi 2-D one. On the other hand, the graphite-composite rings, clamped at both end of the tube, pose a special challenge as they have a complex three-dimensional (3-D) structure and are affected by contact resistances which are difficult to determine. The rings are therefore modelled as lumped electrical and thermal resistances, R_{cc}, which were determined experimentally

Radiative exchanges occur between the surfaces of the inner cylindrical walls of the tube and at the same time between these surfaces and the tube middle septum. In addition, radiative heat transfer also occurs between these surfaces and the septum on one side and the outside environment on the other side. Based on the above, the equivalent thermal circuit diagram of the ATJ graphite furnace is then constructed and presented in Figure 5.2. An analytic solution of the heat transfer rates and temperatures of the nodes of this equivalent thermal circuit is impossible to determine due to the number of components and the complexity of the problem. Fortunately, the

heat transfer rates and temperatures at the nodes of this circuit can be evaluated numerically.
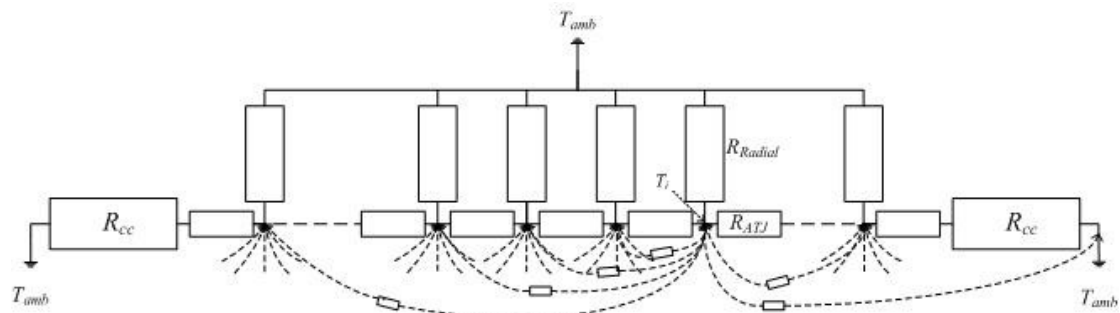
Figure 5.2. Equivalent thermal circuit diagram of the ATJ graphite furnace at NMIA.

The numerical model is assumed to be symmetrical about the axis of the graphite tube (axisymetric). The graphite tube is divided into *m* nodes with the carbon-composite clamps considered as special nodes at *i*=1 and *i*=*m*. The nodal network of the ATJ graphite tube for all the graphite tube nodes (except for the two special end nodes) is presented in Figure 5.3. For the nodes with 2≤*i*≤(*m*-1), heat is generated by resistance heating, q_e, where part of this energy is stored internally, q_{st}. The rest of the energy transfer occurs by:

i. conduction to/from the left of the node (node *i*-1), $q_{L,cond}$,

ii. conduction to/from the right of the node (node *i*+1), $q_{R,cond}$,

iii. conduction, convection and radiation radially through the felt insulation, q_{radial}, and

iv. radiative exchanges with other nodes, middle septum and the outside environment, q_{rad}.
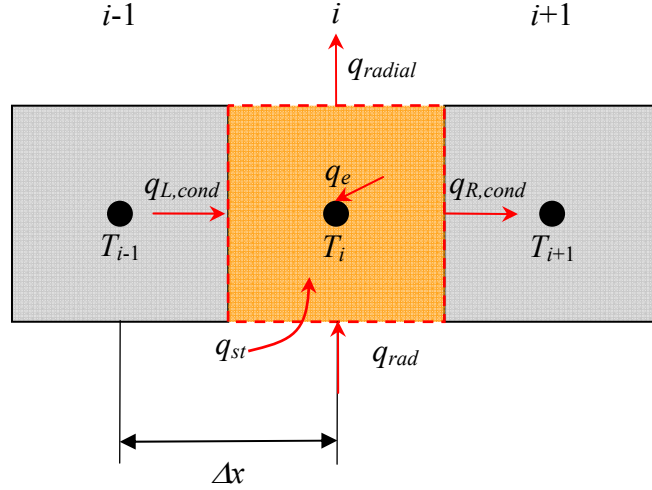
Figure 5.3. Nodal network diagram of the ATJ graphite tube for the case of 2≤*i*≤(*m*-1).

It is not possible to know *a priori* the direction of the heat flow into and out of a particular node as this can be different from one node to another. However, it is better practice to formulate the energy equation by assuming certain direction for the energy rates and to express their equations in a manner consistent with the assumptions made. Applying the principle of energy conservation at a node *i* gives,

$$q_{L,cond_i} + q_{rad_i} + q_{e_i} - \left(q_{R,cond_i} + q_{radial_i}\right) = q_{st_i}. \tag{5.1}$$

It follows that, for 2≤*i*≤(*m*-1), the above energy rates equation can rewritten as

$$\left[\frac{T_{i-1} - T_i}{R_{ATJ}\left(\frac{T_{i-1} + T_i}{2}\right)} + \sum_{j=1}^{m} q_{rad,j} + I^2 R_e(T_i) - \left(\frac{T_i - T_{i+1}}{R_{ATJ}\left(\frac{T_i + T_{i+1}}{2}\right)} + \frac{T_i - T_{amb}}{R_{radial}(T_i)} \right) \right] = \rho_{ATJ} A_c(x) \Delta x C_p(T_i) \frac{dT}{dt}, \tag{5.2}$$

in which, R_{ATJ} is the thermal resistance of the node, $\sum_{j=1}^{m} q_{rad,j}$ is the sum of all radiative energy exchanges between each node and other parts of the graphite tube including the middle septum and the outside environment, I is the electrical current passing through the node, R_e is its electrical resistance calculated using values of the resistivity of the ATJ graphite which were determined in chapter 2, $R_{radial}(T_i)$ is the thermal resistance of the felt insulation, ρ_{ATJ} ($=1\ 730\ \text{kg·m}^{-3}$) is the density of the ATJ graphite (chapter 2), $A_c(x)$ is the cross sectional area of the node as a function of the axial coordinate x, C_p is the specific heat capacity of the graphite (chapter 2), and t is time.

The thermal resistance of the ATJ graphite, $R_{ATJ}(T_i)$, is readily calculated from the definition of thermal conductivity (e.g.: Incropera& Dewitt 2002, p. 90) to yield

$$R_{ATJ}(T_i) = \frac{\Delta x}{k_{ATJ}(T_i)A_c(x)}, \tag{5.3}$$

in which, $k_{ATJ}(T_i)$ is the thermal conductivity of ATJ graphite at a temperature T_i and whose values were determined in chapter 2.

On the other hand, the radial thermal resistance $R_{Radial}(T_i)$, the radiative heat exchanges $\sum_{j=1}^{n} q_{rad,j}$, and the graphite-composite thermal resistance R_{cc} are more complex to determine and these are examined fully in the next three sections.

5.3.1 Radial Thermal Resistance, R_{radial}

Based on the assumption of 1-D heat transfer in the radial direction, heat generated by the ATJ graphite tube flows in the radial direction through a 14.5 mm of graphite felt layer, two 0.5 mm thick graphite foils, a 2 mm thick silica tube and a 10 mm thick air gap that separates the silica tube from a water cooled brass jacket.
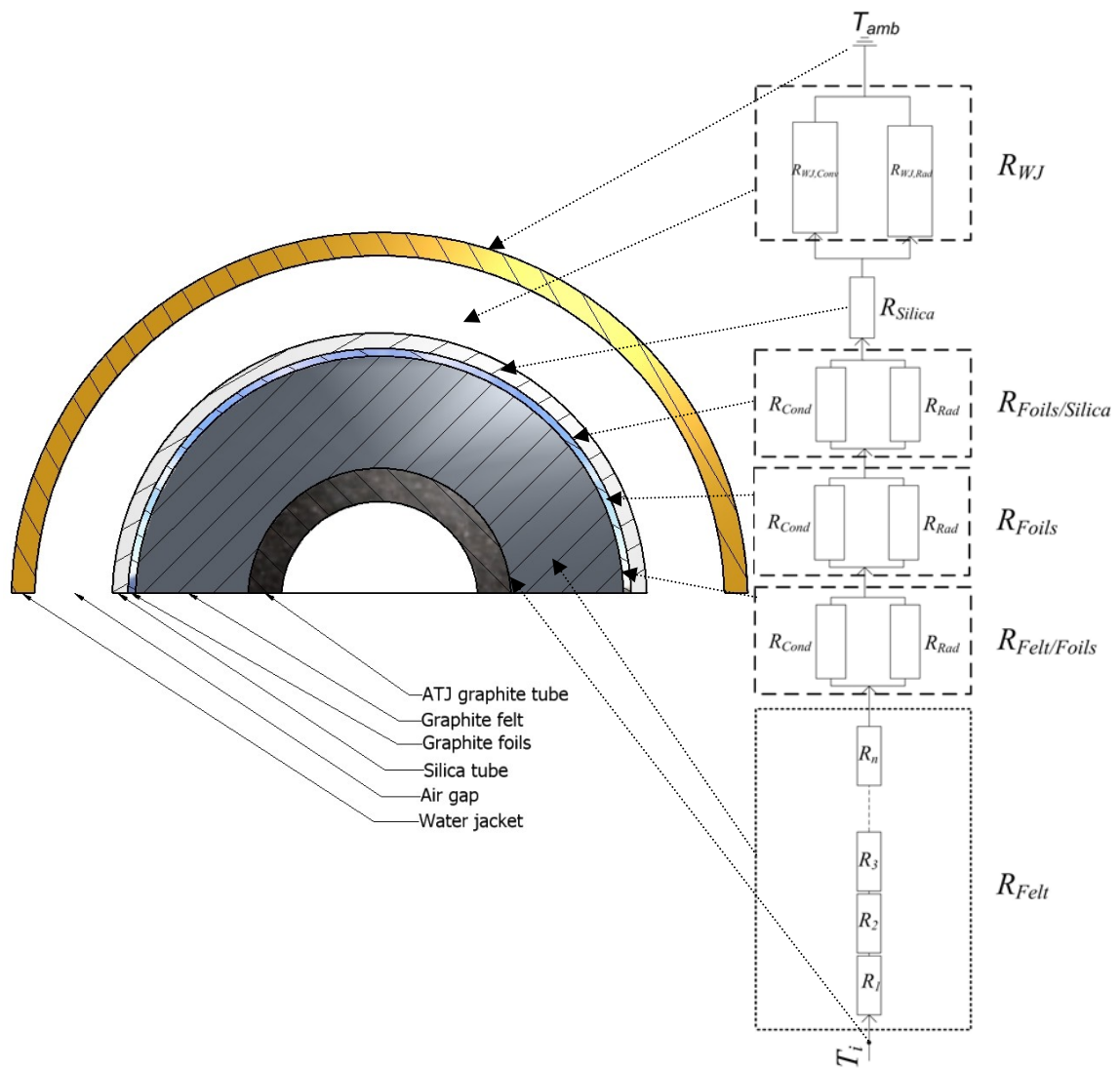
Figure 5.4. (left) Cross sectional view of the 48 kW Thermogage graphite furnace at the NMIA and (right) its radial equivalent thermal circuit diagram.

As shown on the schematic diagram and the equivalent thermal circuit in Figure 5.4, the radial thermal resistance R_{radial} consists of six resistances in series, which are:

i. R_{WJ}, the thermal resistance caused by the air gap between the silica tube and the water jacket,

ii. R_{Silica}, the thermal resistance of the silica tube,

iii. $R_{Foils/Silica}$, the contact thermal resistance between the graphite foils and the silica tube,

iv. R_{Foils}, the thermal resistance of the graphite foils,

v. $R_{Felt/Foils}$, the contact thermal resistance between the graphite foils and the graphite felt, and

vi. R_{Felt}, the thermal resistance of the graphite felt divided into n small resistors for iteration purposes.

It therefore follows that at a node i, R_{radial} can be expressed as,

$$R_{radial_i} = \sum_{k=1}^{n} R_k + R_{Felt/Foils_i} + R_{Foils_i} + R_{Foils/Silica_i} + R_{Silica_i} + R_{WJ_i} \,. \quad (5.4)$$

The two contact resistances $R_{Foils/Silica}$ and $R_{Felt/Foils}$ and the thermal resistance of the graphite foils, R_{Foils}, are treated as very small air gaps between two surfaces (refer to as surface 1 and surface 2) with a width of 0.5 mm. Since the size of this air gap is small resulting in the Rayleigh number being less than one, the heat transfer due to convection is negligibly small. Hence, heat transfer occurs across this gap by conduction and radiation only.

The resistance of the foils due to conduction is given by a relation similar to equation (5.3) and since their thermal conductivity is high and their thickness small, this leads to the conclusion that the thermal resistance of the foils due to their finite conductivity of approximately 100 W·m^{-1}·K^{-1} and their small thickness of 0.5 mm is also negligibly small.

The radiative and the conductive thermal resistance across the proposed cavities can be calculated from

$$R_{Cond} = \frac{g}{k_{gas}(T)A_g}\,, \qquad\qquad (5.5.a)$$

$$R_{Rad} = \frac{1}{4\varepsilon_{eff}\sigma T^3}\,, \text{ and} \qquad\qquad (5.5.b)$$

$$\varepsilon_{s,eff} = \frac{1}{1/\varepsilon_1 + 1/\varepsilon_2 - 1}\,, \qquad\qquad (5.5.c)$$

in which, g is the width of the gap between the two surfaces (between the foils and the silica, the two foils or the foils and the felt), $k_{gas}(T)$ is the thermal conductivity of the gas filling the gap, A_g is the area of the gap, *viz*, $A_g = 2\pi r_g \Delta x$ in which r_g is the radius of the gap, $\varepsilon_{s,eff}$ is the effective thermal emissivity, ε_1 is the emissivity of surface 1 and ε_2 is the emissivity of surface 2.

The silica thermal resistance R_{Silica} per unit length can be calculated using the following equation,

$$R_{Silica} = \frac{1}{k_{Silica}(T)A_{Silica}} .$$
(5.6)

Here, A_{Silica} is the area of the silica tube, and $k_{Silica}(T)$ is the thermal conductivity of the silica whose values can be obtained from Touloukian (1970). The variation of the thermal conductivity of the silica as a function of the absolute temperature is presented graphically in Figure 5.5.
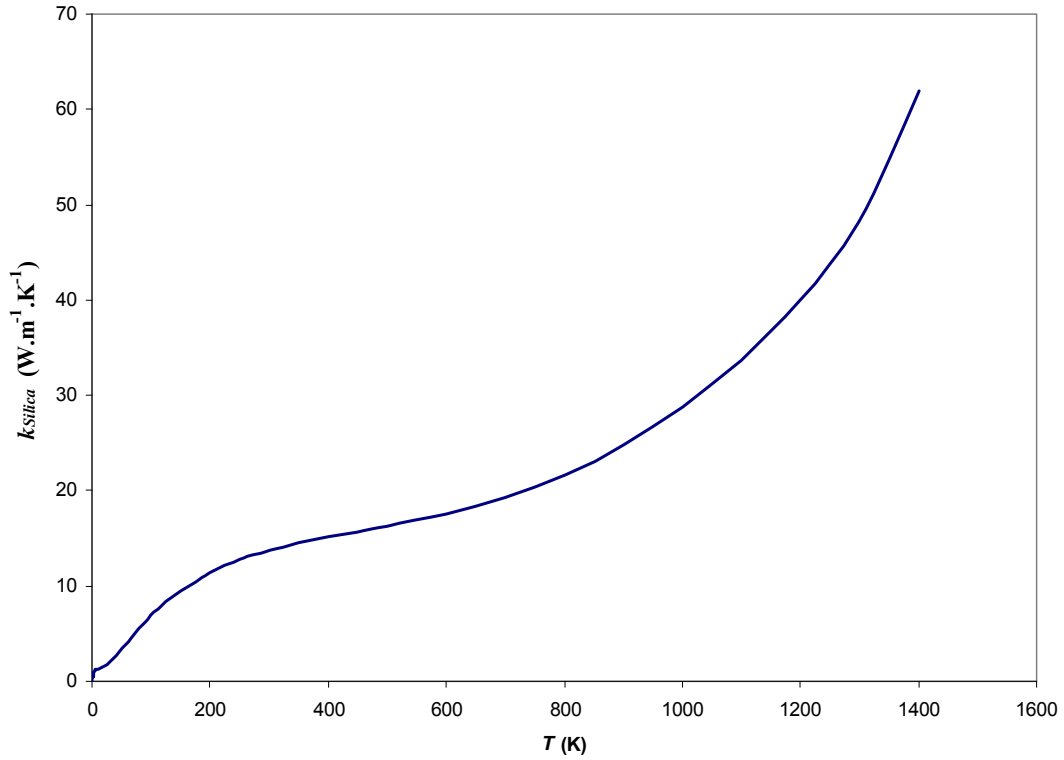
Figure 5.5. Graph of the silica thermal conductivity k_{Silica} versus the absolute temperature T.

The felt thermal resistance, R_{Felt}, is divided into n resistors so as to be able to more closely approximate the value of R_{radial} as a function of the temperature which varies across the felt gap. Each resistor R is calculated using the well known relation for the thermal resistance of a cylindrical wall (Incropera & Dewitt 2002, p. 106),

$$R = \frac{\ln\left(\frac{r_2}{r_1}\right)}{2\pi L k_{Felt}(T)},$$
(5.7)

where r_2 and r_1 are the radii of the two sides of each resistor, L is the graphite felt length (which is the same as the length of the ATJ graphite tube), and $k_{Felt}(T)$ is the thermal conductivity of the felt.

The water jacket thermal resistance R_{WJ} per unit length is calculated using the definition of thermal resistivity to be

$$R_{WJ} = \frac{T_{Silica} - T_{WJ}}{q'_{WJ,Total}},$$
(5.8)

in which, T_{Silica} is the silica tube absolute temperature, T_{WJ} is the water jacket absolute temperature fixed at 15 °C, and $q'_{WJ,Total}$ is the total heat transfer rate per unit length. Heat transfer across the air gap between the water jacket and the silica tube occurs mainly by radiation and free convection. The air free convection heat transfer also includes heat transfer by conduction. Thus, the total heat transfer rate $q'_{WJ,Total}$ can be expressed as:

$$q'_{WJ,Total} = q'_{WJ,Conv} + q'_{WJ,Rad},$$
(5.9)

where $q'_{WJ,Conv}$ and $q'_{WJ,Rad}$ are the heat transfer rates per unit length by free convection and radiation consecutively. The free convection heat transfer rate $q'_{WJ,Conv}$ per unit length is calculated using equations obtained from Incropera & Dewitt (2002, p. 564) based on the works by Raithby & Hollands (1998, Chap. 4) for the case of an annular space between long horizontal concentric cylinders, they are:

$$q'_{WJ,Conv} = \frac{2\pi k_{eff}}{ln(D_{WJ}/D_{Silica})}(T_{Silica} - T_{WJ}),$$
(5.10.a)

$$\frac{k_{eff}}{k} = 0.386\left(\frac{Pr}{0.386 + Pr}\right)^{1/4}\left(Ra_c^*\right)^{1/4},$$
(5.10.b)

$$Ra_c^* = \frac{[ln(D_{WJ}/D_{Silica})]^4}{g_{WJ}^3\left(D_{Silica}^{-3/5} + D_{WJ}^{-3/5}\right)^5}Ra_L.$$
(5.10.c)

Here D_{WJ} and D_{Silica} are the water jacket and silica tube diameters consecutively, k_{eff} is the effective thermal conductivity, Pr is the Prandtl number, g_{WJ} is the distance between the silica tube and the water jacket, Ra_c^* is the modified Rayleigh number, and Ra_L is the Rayleigh number.

The radiative heat transfer rate $q'_{WJ,Rad}$, on the other hand, is calculated using equation obtained from Siegel & Howell (2002, pp. 299) for the case of two infinitely long

concentric cylinders with a specular internal cylinder (the silica tube) and a diffuse external cylinder (the brass water jacket), as,

$$q'_{WJ,Rad} = \frac{A_{Silica}\sigma\left(T^4_{Silica} - T^4_{WJ}\right)}{1/\varepsilon_{Silica} + \left(A_{Silica}/A_{WJ}\right)\left(1/\varepsilon_{WJ} - 1\right)} \times \frac{1}{L}, \qquad (5.11)$$

in which, L is the length of the cylinders, A_{Silica} and A_{WJ} are the surface areas of the silica tube and the brass water jacket with emissivities of ε_{Silica} and ε_{WJ} consecutively.

Hence, R_{WJ} is calculated using the above equations for different silica tube temperatures and the results are plotted in Figure 5.6.

Having determined all the above thermal resistances, R_{radial} can be determined as a function of T_i using iterative over-relaxation method on $n+2$ finite elements in EXCEL. This was solved for a number of temperatures to give a simple polynomial for the temperature dependence of the total radial thermal resistance $R_{radial}(T)$. Different polynomials are generated for $R_{radial}(T)$ for the case of the graphite felt purged with helium or nitrogen and the results are plotted in Figure 5.7.
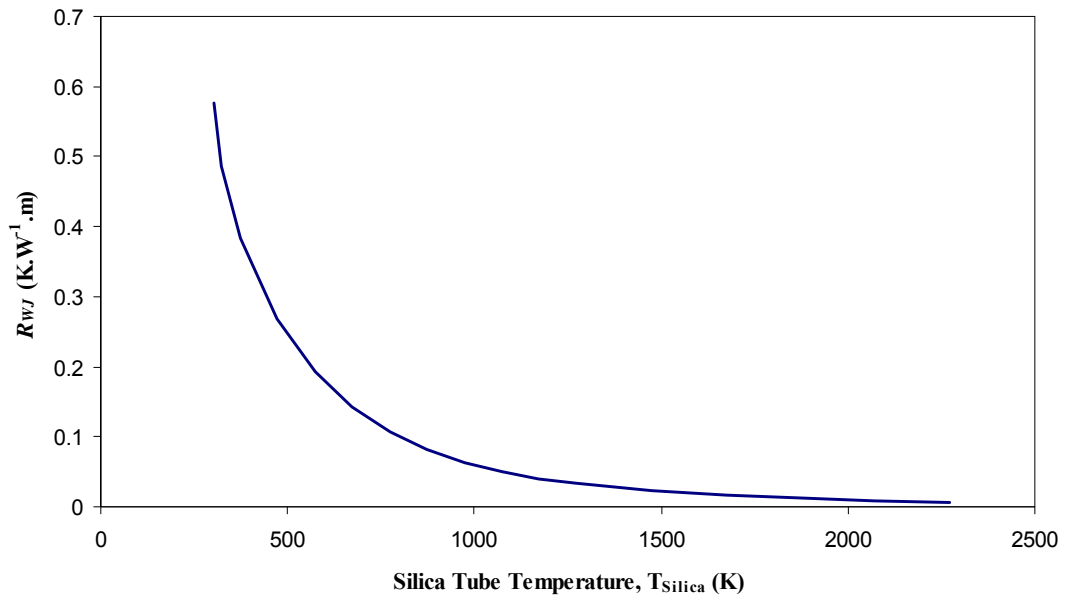
Figure 5.6. Graph of the calculated thermal resistance of the air gap between the silica tube and the brass water jacket of the Thermogage graphite furnace at NMIA as a function of the silica tube absolute temperature.
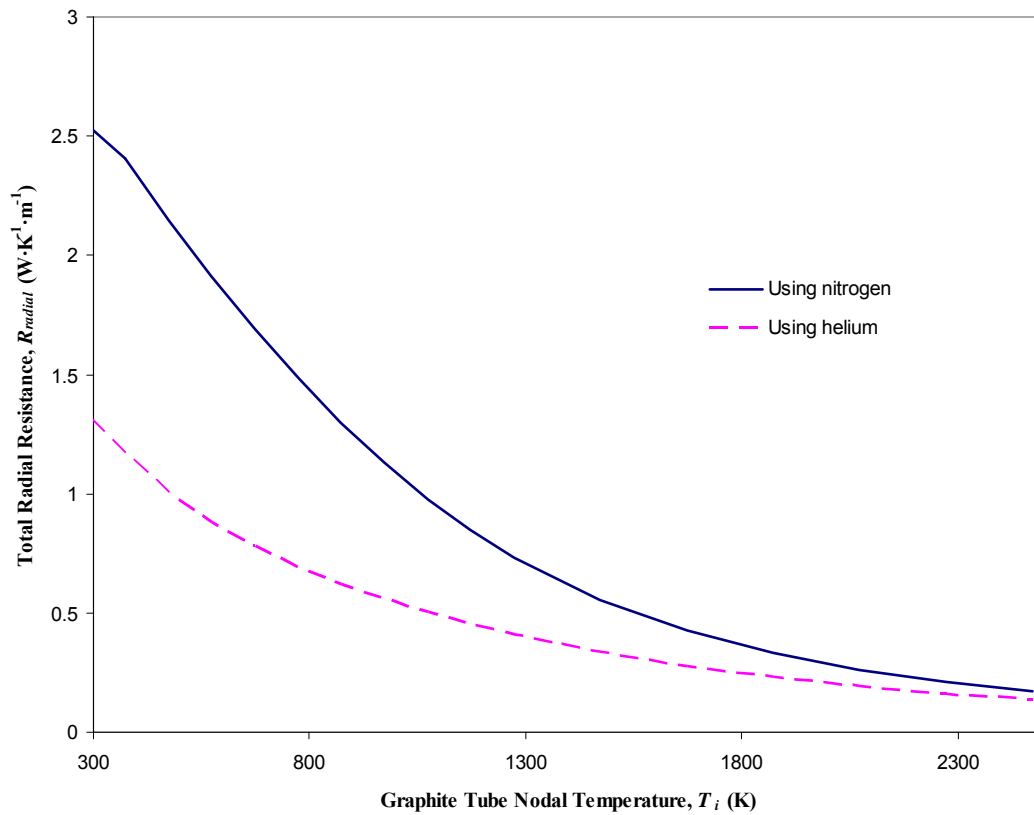
Figure 5.7. Plots of the total radial resistance per unit length R_{radial} versus the nodal absolute temperature T_i in the cases of graphite felt purged with He and N$_2$ as well as C_{fr}=15.0.

The full calculation details and an example on the calculations of R_{radial} for values of C_{fr} varying between 10.0 and 35.0 and for the cases of helium and nitrogen used as the felt purging gas are found in Appendix B.

5.3.2 Tube End Thermal Resistance, R_{cc}

As mentioned previously, the two ends of the graphite tube are held in short graphite-composite sleeves (see Figure 5.1), which contribute significant electrical heating and have complex 3-D geometry contact resistances making them difficult to model numerically. It was demonstrated that regardless of the design used for the graphite tube or insulation system, these end sections remained the same, and therefore their thermal and electrical behaviours are always constant. An empirical approach is adopted to model these ends, where they are considered as lumped elements, or special nodes, whose electrical and thermal resistances are determined experimentally. As may be seen from the nodal network in Figure 5.8, heat is internally generated ohmically by the graphite-composite material, $q_{e,cc}$. Heat transfer also occurs by conduction from the adjacent nodes, q_{cond}, in addition to heat transfers in the radial direction and by radiative exchanges as well as the stored energy.
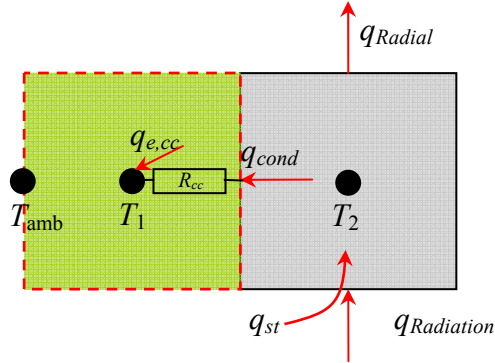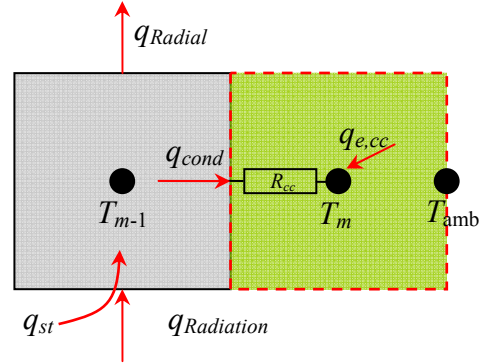
Figure 5.8. Nodal network diagram of the ATJ graphite tube's two special nodes (graphite-composite ends) at *i*=1 and *i*=m.

Based on this nodal network, the lumped resistance R_{cc} can be calculated using the following equations:

$$T_1 - T_{amb} = R_{cc}\left(\frac{T_1 + T_{amb}}{2}\right)\left[kA\frac{\delta T}{\delta x} + \frac{IV_{cc}}{2}\right] \text{ for } i=1, \text{ and} \qquad (5.12.\text{a})$$

$$T_{amb} - T_m = R_{cc}\left(\frac{T_{amb} + T_m}{2}\right)\left[kA\frac{\delta T}{\delta x} + \frac{IV_{cc}}{2}\right] \text{ for } i=m. \qquad (5.12.\text{b})$$

Both equations have two parts, the heat transfer rate $kA\dfrac{\delta T}{\delta x}$ coming from the end of the ATJ tube, and the electric power IV_{cc} heating it. The factor of two in the electrical heating arises because the power is assumed to be distributed evenly throughout the graphite-composite sleeve, not at the "hot" end only. Values of R_{cc} as a function of the average of T_{amb} and the adjacent node are calculated using the measured values of V_{cc}, I and $\delta T/\delta x$. Based on these measurements and the above equations, the calculated values of R_{cc} are plotted in Figure 5.9 along with the electrical resistance values calculated using measured values of V_{cc} and I. Note that T_{amb} is considered here to be the temperature of the water used to cool the copper electrodes described in section 5.2.
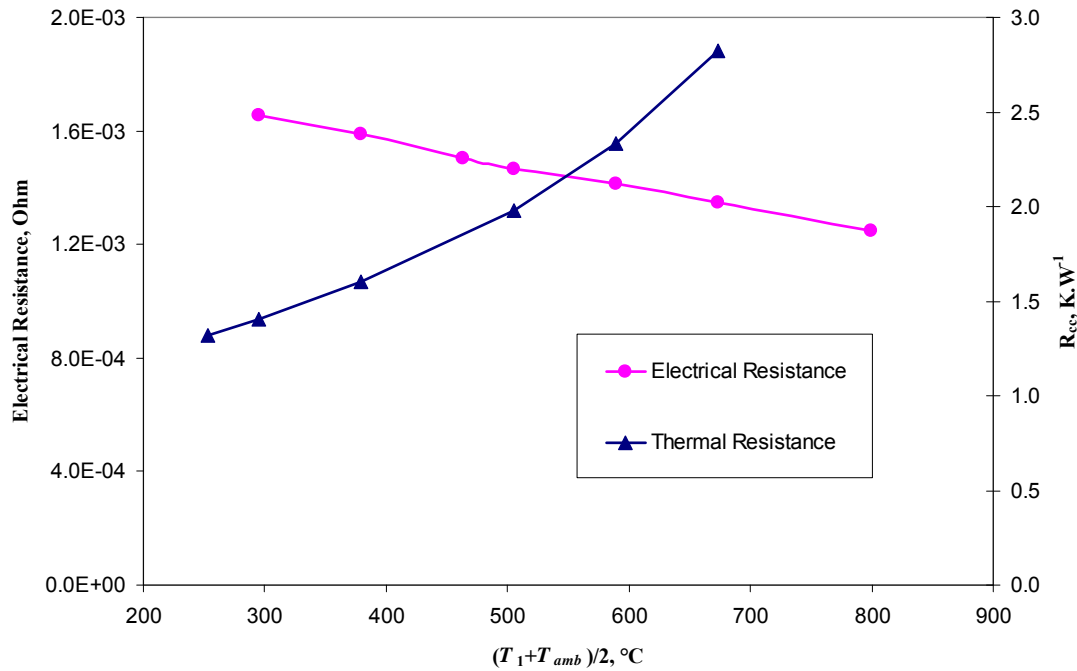
Figure 5.9. Graphs of the measured electrical resistance of the graphite-composite sleeve and the lumped thermal resistance R_{cc} versus the average of the ambient and the adjacent node temperatures (T_1 is given here as an example, it can be also T_m).

5.3.3 Radiative Thermal Exchanges

Radiative heat transfer inside the graphite tube is important since the operating temperatures of the ATJ graphite furnace exceed 1 000 °C at all times. The outside of the ATJ graphite tube is shielded for radiation by the graphite felt. However, its interior is of interest as it is there that most of the radiative exchanges between surfaces occur. Note that the septum in the middle divides the ATJ tube into two sections and at the same time acts as a radiation shield between them. Therefore, there is no radiation coupling between these two symmetrical sections. Due to this symmetry, only one section is discussed. As shown in Figure 5.10, for each section of the tube the radiative exchanges occur between:

i.   the interior cylindrical wall and the middle septum,

ii.   the cylindrical wall and the outside environment, and

iii. the middle septum and the outside environment.

131

In the numerical model, the ATJ graphite tube is divided into node elements of circular shape rings with each having a width of Δx , and the middle septum is considered as a special node with infinitely small width at node $m/2$. For all the ring nodes, the radiative heat transfer rate $q_{rad,i}$ at node $\underline{i}$ can be algebraically expressed as,

$$q_{rad,i} = \sum_{j=1}^{(m/2)-1} q_{ji} + q_{si} + q_{ai} , \qquad (5.13)$$

in which, $\sum_{j=1}^{(m/2)-1} q_{ji}$ is the sum of all radiative exchanges from all adjacent ring nodes onto node i, with q_{si} and q_{ai} being the radiative heat transfer rates between node i and the middle septum and the outside environment respectively.
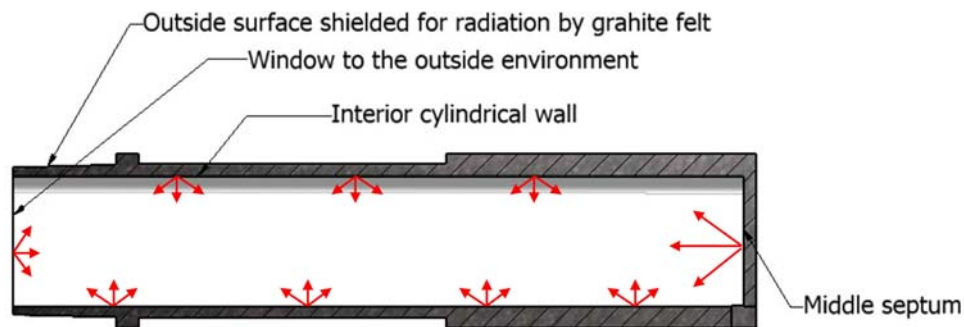
Figure 5.10. Cross sectional view of one section of the ATJ graphite tube with radiative heat exchanges between its interior surfaces.

On the other hand, the radiative heat transfer rate at the middle septum $q_{rad,s}$ is calculated using,

$$q_{rad,s} = \sum_{j=1}^{(m/2)-1} q_{js} + q_{as} . \qquad (5.14)$$

Here $\displaystyle\sum_{j=1}^{(m/2)-1} q_{js}$ is the sum of all radiative heat transfer rates from all cylindrical nodes onto the septum with an area A_{septum}, and q_{as} is the radiative heat transfer rate with the ambient with an area A_{amb}; note that both areas have a diameter of 25.4 mm.

The above radiative heat transfer rates at each node can be calculated using the concept of configuration or view factors which is based on the fact that a fraction of the radiation leaving a surface j (A_j) is intercepted by a surface i (A_i) and on the assumption that these surfaces act as blackbodies. Since both surfaces, i and j, are assumed to be black, there can be no reflections (Incropera & Dewitt 2002, p. 790). Also, the ATJ graphite emissivity is taken to be constant with a value of 0.85. Hence, equations (5.13) and (5.14) need to be rewritten using the configuration, or view, factor concept as,

$$q_{rad,i} = \left[\begin{array}{l} \sigma A_j \varepsilon_{ATJ} \displaystyle\sum_{j=1}^{(m/2)-1} F_{ji}\left(T_i^4 - T_j^4\right) + \sigma A_{septum}\varepsilon_{ATJ}F_{si}\left(T_i^4 - T_s^4\right) \\ + \sigma A_{amb}\varepsilon_{amb}F_{ai}\left(T_i^4 - T_a^4\right) \end{array} \right], \text{ and} \quad (5.15.a)$$

$$q_{rad,s} = \sigma A_j \varepsilon_{ATJ} \sum_{j=1}^{(m/2)-1} F_{js}\left(T_s^4 - T_j^4\right) + \sigma A_{amb}\varepsilon_{amb}F_{as}\left(T_s^4 - T_a^4\right), \quad (5.15.b)$$

in which σ is the Stefan-Boltzmann constant, ε_{ATJ} and ε_{amb} are the emissivities of the ATJ graphite and the ambient respectively. The view factors F_{ji}, F_{si}, F_{ai}, F_{js} and F_{as} are determined from well established relations which depend on the configuration factors, as illustrated in Figure 5.11 and which can be obtained from many text books dealing with radiation, for example Siegel & Howell (2002, p. 845 and p. 848). The configurations used in this work are (a)"*parallel circular disks with centres along the same normal*" with equal radius r and distance h between them (F_{as}), (b)"*two ring elements on the interior of a right circular cylinder*" (F_{ji}), and (c)"*ring element on interior of right circular cylinder to circular disk at a distance x*" (F_{si} and F_{js}). The configuration factors can be evaluated from,

$$F_{d1-2} = \frac{1}{2}\left[X_F - \sqrt{X_F^2 - 4}\right] \qquad \text{for case (a),} \qquad (5.16.a)$$

$$F_{d1-2} = \left[1 - \frac{2X_F^3 + 3X_F}{2\left(X_F^2 + 1\right)^{3/2}}\right]dX_F \qquad \text{for case (b), and} \qquad (5.16.b)$$

$$F_{d1-2} = \frac{X_F^2 + \frac{1}{2}}{\sqrt{X_F^2 + 1}} - X_F \qquad \text{for case (c)} \qquad (5.16.c)$$

with

$$X_F = 2 + \frac{x^2}{r^2} \qquad \text{for case (a), and} \qquad (5.16.d)$$

$$X_F = \frac{x}{2r} \qquad \text{for cases (b) and (c).} \qquad (5.16.e)$$

Equation (5.16.c) can be used to solve for the two view factors, F_{si} and F_{ai}, in conjunction with the *reciprocity relation* (Incropera & Dewitt 2002, p. 791) given as,

$$A_1 F_{d1-2} = A_2 F_{d2-1}. \qquad (5.17)$$

Here A_1 and A_2 are the areas of the ring element and the circular disk respectively.
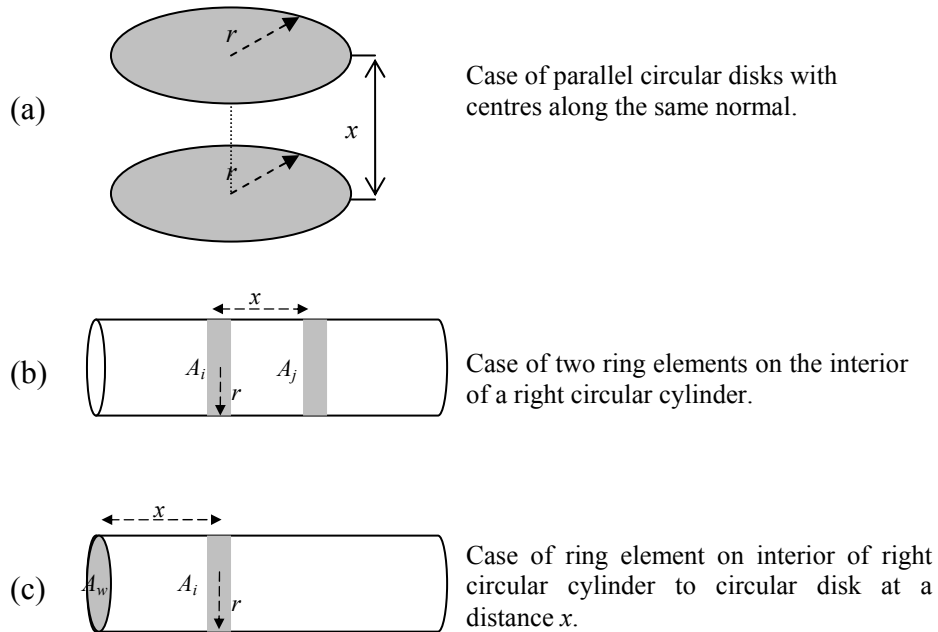
Figure 5.11. Schematic diagram of three view factor configurations (Siegel and Howell 2002, p. 848).

5.4 Code Validation

The aim of this section is to "verify" that the difference equations used in the numerical model are solved correctly and with some order of accuracy. The numerical model assumes a 1-D heat transfer with all nodes having an equal width h of L/m, where L is the length of the ATJ graphite tube. It is important to test the effect of the grid width refinement on the solution as well as to check the stability of the model with different combinations of h and the time steps dt. The solution can be for example the heat transfer rate in the radial direction, middle temperature or any other calculated output. Once the accuracy and the stability of the solution are determined then the selection of the grid size and the time step to be used can be decided.

Another method of validation is to compare the numerical model to that of an exact analytical solution of a similar problem. This provides a mean to verify the codes used; for example the comparison of the temperature profile obtained by numerical model to that of an exact solution. Details and discussions of these two validation methods are presented next.

5.4.1 Effect of the Grid size and Time Steps

The effect of the grid size (or node width in this case) h on the numerical solution can be observed by using the numerical model to generate solutions for different values of h. However, it is important first to determine the relation between the width size h and the accuracy of the numerical model. Then the question that may arise: is the numerical model a first order or a second order accurate or a combination of both?

It is fair to assume at first glance that the quasi 2-D numerical model is 1st order accurate when testing for grid convergence simply because the physical problem to be solved is linear with smooth functions. However, the introduction of the tube end thermal resistance R_{cc} as a measured entity (refer to Figure 5.9 for the graphs of R_{cc}) to the software adds more complexity. This can be best illustrated by comparing the

135

plots of the grid convergence results for the cases of the numerical model with and without R_{cc}.

The total radial heat rate, q_{radial}, was selected as the numerical solution to test for the case of the quasi 2-D numerical with and without R_{cc}. Values of q_{radial} were calculated using different grid sizes varying from a coarse mesh of 12 mm to a fine grid of 1 mm in width, and with the temperature of the middle of the graphite tube is fixed at 1 000 °C. Values of the thermophysical properties of ATJ graphite and WDF graphite felt, obtained from chapter 2, were used in these numerical simulations. The calculated values of q_{radial} as a function of h for the cases of "with R_{cc}" and "without R_{cc}" are then plotted in Figure 5.12 and Figure 5.13 respectively.
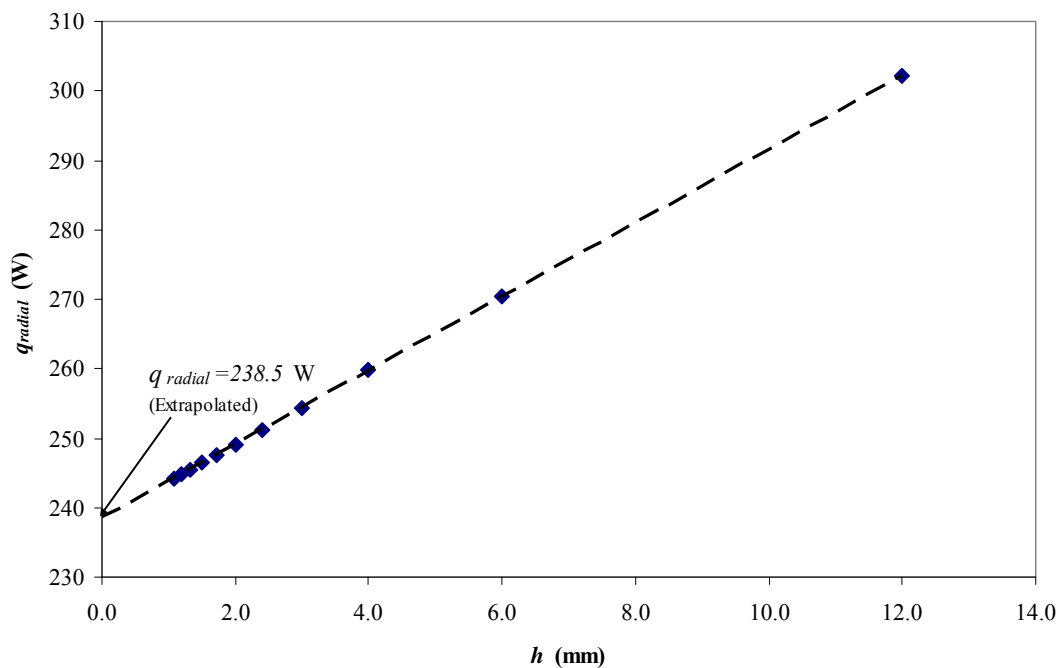
Figure 5.12. Graph of the total radial heat rate, q_{radial}, versus the grid size h for the case of the numerical model without R_{cc}.
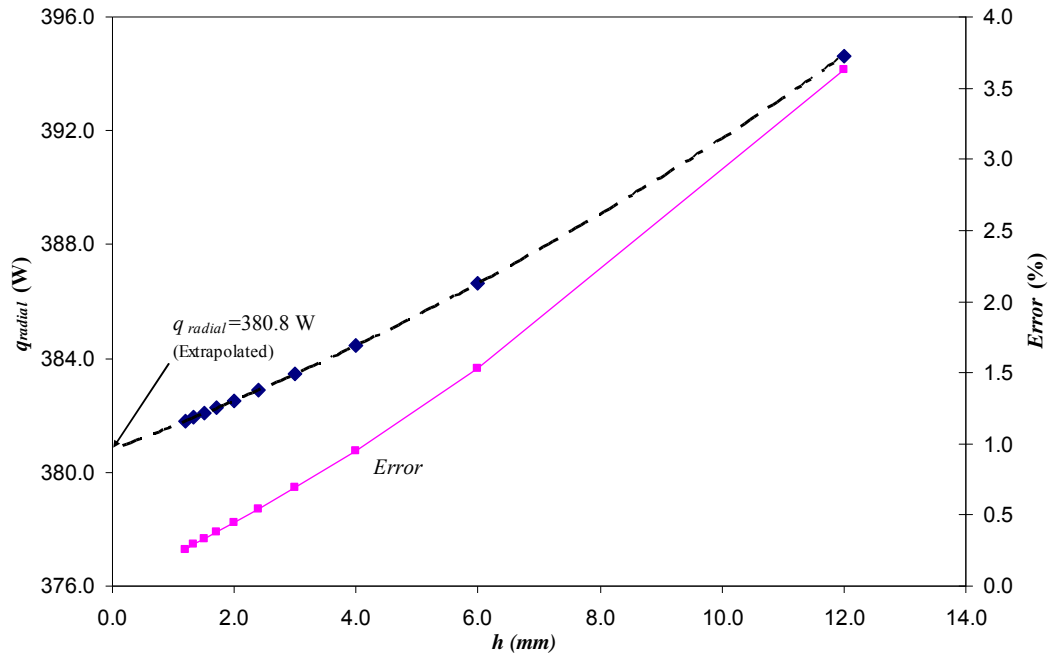
Figure 5.13. Graph of the total radial heat rate, q_{radial}, versus the grid size h for the case of the numerical model with R_{cc}.

The figures above confirm that the numerical model is no longer 1st order accurate when R_{cc} is introduced. Methods to extrapolate for the exact solution, which is in this case q_{radial}, such as the Richardson Extrapolation method (also known as the "h^2 extrapolation"), cannot be used because the grid convergence for the "with R_{cc}" case, mainly caused by the non-linearity and complexity of R_{cc}, exhibits a mixture between a first and second order accuracy. However, the results show that the grid convergence follows a second order polynomial, which can be used to extrapolate for q_{radial}. Similar results were also obtained when the quasi 2-D numerical model was used to test for other outputs, such as the temperature at each node and radiative and conductive heat rates.

Using the value obtained for q_{radial}, the percentage difference between the values of q_{radial} for each grid size and its extrapolated one are then calculated. These values are plotted on the secondary axis of Figure 5.13. As may be observed from this graph, for a coarse grid size of 12.0 mm wide, corresponding to 20 nodes, the solution obtained differs by 3.6% from the predicted one. However, this difference drops to less than 1% for any grid size smaller than 4.0 mm, corresponding to 60 nodes. Assuming that

137

a 1% error is acceptable in the prediction of the numerical model output then a numerical model with a 100-node, in which an error of less than 0.5% can be obtained, is therefore acceptable. On the other hand, it is important to point to the reader's attention that the increase in the extrapolated values of q_{radial}, shown in Figure 5.12 and Figure 5.13, can be justified by the increase in the temperature of the graphite tube walls when R_{cc} is introduced.

Another important consideration in the quasi 2-D numerical model is its stability when using different combinations of time step dt and node width h. The time step dt is not a factor in the accuracy of the solution, q_{radial}, but rather it is important for the convergence of the numerical model. The graph in Figure 5.14 gives an example of the area of stability for different combinations of h and dt. The points on the graph are obtained by iteration. A line was then fitted to these points to create two regions where the numerical model converges (stable region) or not (unstable region).
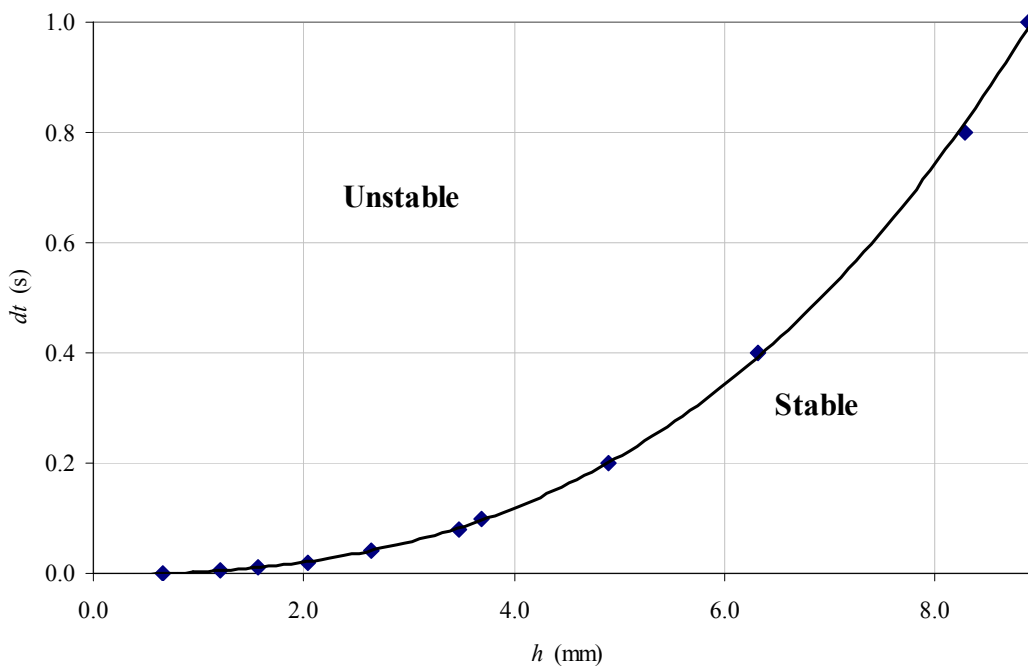
Figure 5.14. Graph of the solution f versus the grid size h and the quasi 2-D numerical model stable and non stable areas.

As may be seen from the plot in Figure 5.14, the relation between *dt* and *h* follows a second order polynomial. This clearly agrees with the *stability requirement* of the quasi 2-D numerical model, which can be obtained from various textbooks to be (e.g.: Anderson 1995, p.161),

$$\alpha_N \frac{dt}{h^2} \leq \frac{1}{2},$$ (5.18)

in which α_N is a constant.

5.4.2 Code Verification: Comparison with an Exact Solution

The ATJ graphite tube model is similar to that of an insulated heater wire with the ATJ graphite acting as the electrically heated wire and the graphite felt as its insulation. The dependence of the ATJ graphite and graphite felt thermophysical properties on temperature, the complexity of the graphite tube profile, radiative exchanges among the inner surfaces of the graphite tube make finding an analytical solution very difficult if not impossible. However, in order to compare the numerical model with an analytical solution then the ATJ physical problem must be first simplified. This can be done by assuming the following:

i.   steady state with internal heat generation q_e,

ii. constant cross sectional area A_c of the ATJ graphite tube,

iii. axisymetric model along the *x* direction with symmetry line in the middle ($dT/dx = 0$ at $x=0$), refer to Figure 5.15,

iv. constant thermophysical properties of the ATJ graphite and the graphite felt with the ATJ graphite thermal conductivity $k_{ATJ} = 100$ W·m^{-1}·K^{-1} and resistivity $\rho_{ATJ} = 10^{-5}$ Ω·m, and felt thermal conductivity $k_{Felt} = 0.3$ W·m^{-1}·K^{-1},

v.   negligible temperature drop across the ATJ graphite tube in the radial direction, or $dT/dr \approx 0$,

vi. no radiative heat exchanges among the inner surfaces of the graphite tube,

$$\sum_{j=1}^{n} q_{Rad,j} = 0, \text{ and}$$

vii. uniform heat transfer rate generated by resistance heating at the outer surface of the ATJ tube.
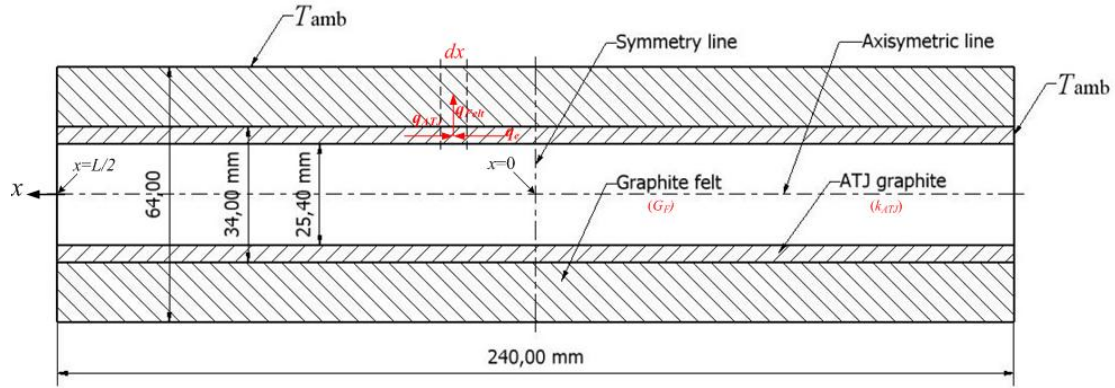
Figure 5.15. Schematic diagram of a ATJ graphite tube simplified design and the differential control volume $A_c dx$ for conduction analysis.

Applying an energy balance to the differential control volume $A_c dx$, shown in Figure 5.15, yields,

$$k_{ATJ} A_c \frac{d^2 T}{dx^2} - G_F \left(T(x) - T_{amb}\right) + \frac{V^2}{R_e L} = 0, \tag{5.19}$$

in which, $G_F = 2\pi k_{Felt}/ln(r_3/r_2)$ is the effective thermal conductivity of the graphite felt with $r_2 = 17$ mm and $r_3 = 32$ mm, T_{amb} is the ambient temperature, V is the applied voltage, $R_e = \rho_{ATJ} L/A_c$ is the electrical resistance of the graphite tube, and $L = 240$ mm is the tube length. The analytical solution to the above differential equation was obtained to be,

$$T(x) = c_1 e^{-\left(\sqrt{\frac{G_F}{k_{ATJ} A_c}}\right)x} + c_2 e^{\left(\sqrt{\frac{G_F}{k_{ATJ} A_c}}\right)x} + \left[T_{amb} + \frac{V^2}{G_F R_e L} \right], \tag{5.20}$$

where c_1 and c_2 are two constants (with the unit of Kelvin) to be determined using the following boundary conditions:

- at $x=0 \Rightarrow$ the partial derivative $\delta T / \delta x = 0$, and

- at $x=L/2 \Rightarrow T(L/2)=T_{amb}=288.15$K.

For $V=3$V and $T_{amb}=288.15$ K (15 °C), equation (5.20) reduces to,

$$T(x) = -663.9\left(e^{-8.618x} + e^{+8.618x}\right) + 2391.8 \,. \tag{5.21}$$

The values of T were calculated at different positions x and are plotted in Figure 5.16 and compared to the graphs of the temperature profiles generated by the quasi 2-D numerical model using node width h of 1.0 and 4.0 mm. These node widths are chosen in order to demonstrate the accuracy of the temperature profile predicted by the quasi 2-D numerical model when using different h values.
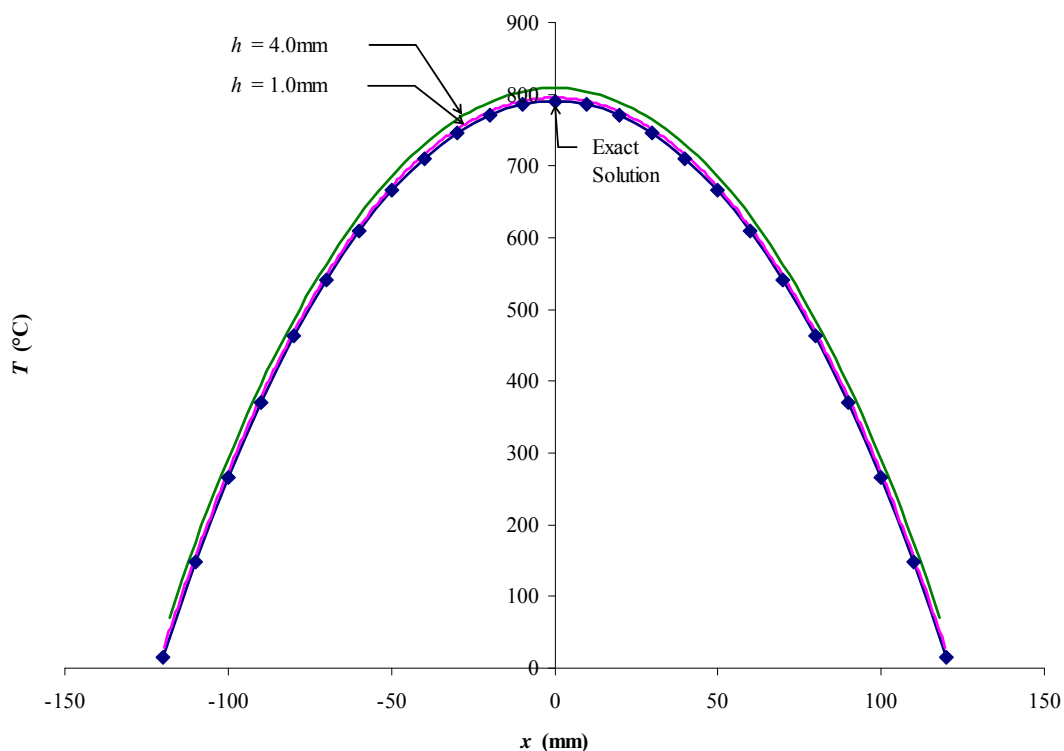
Figure 5.16. Graphs of the temperature profiles of the ATJ graphite tube obtained using an exact analytical solution and the quasi 2-D numerical model with h=1 mm and 4 mm.

It can be deduced from the graphs in Figure 5.16 that the exact analytical solution (in blue) agrees very well with the numerical model predictions (in orange and green), which demonstrates that the code is correctly programmed. The discrepancies between the analytical solution and the simulations can be accounted for by the grid convergence errors (discussed above in section 5.4.1). In conclusion, the choice of a node width h depends on whether the simulation is required to be either quick or accurate. Values of h=4.0 mm and dt=0.1 s (giving less than 1% error) can be used for quick and coarse simulations, which takes less than one minute in computational time. Values of h=1 mm and dt=0.001 (giving less than 0.4% error) can alternatively be used for more accurate but slower simulations, which takes more than half an hour to complete.

Having successfully developed and partially validated and verified the software, it can now be used to predict the temperature profile of the inner surface of the ATJ graphite furnace when it is electrically heated, as well as the heat rates in the radial direction through the WDF graphite felt and by conduction along the ATJ graphite tube. The numerical model can also be used to predict radiative exchanges from the inner surfaces of the graphite tube to the outside environment. However, it is important that this numerical model be firstly validated against measured data. Therefore, the predictions of the temperature profiles and heat transfer rates generated using the quasi 2-D numerical model are compared to measured ones and the results of this comparison are presented in the next chapter.

6 VALIDATION OF THE NUMERICAL MODEL

6.1 Introduction

In section 5.4.2, the code of the quasi 2-D numerical model developed by the present author was verified by comparing the simulated temperature profile of the ATJ graphite tube cavity walls with that of a "simplified" analytical solution using constant values for the cross sectional area of the tube and the thermophysical properties of the ATJ graphite and WDF graphite felt as well as constant temperatures at the graphite tube ends.

In this chapter, the simulated heat transfer rates and the temperature profiles of the ATJ graphite tube are compared with the data measured in order to validate the quasi 2-D model. Measurements of the heat transfer rates and temperature profiles are conducted using the experimental apparatus described in chapters 3 and 4. Furthermore, the sensitivity of the results of the numerical model is presented due to (i) the uncertainties in the thermophysical properties of the ATJ graphite and WDF graphite felt, and (ii) the effects of the measurement uncertainties of the temperature gradients ($\delta T/\delta x$), which were used in the determination of R_{cc}.

For the validation tests presented here, the "short tube" and the "long tube" used in the experimental setup validation (refer to chapter 4) are also used; recall that the two tubes have variable cross sectional areas with cuts with widths varying from 60 to 80 mm and depths from 1.25 to 2 mm (see Figure 4.2). The comparison between the modelled and measured data using these two tubes can be divided into two sections: "heat transfer rate" and "temperature profile" comparisons. Furthermore the temperatures at the middle of the silica tube are measured and checked against the modelled values generated using the numerical models developed for the calculation of the effective thermal resistance in the radial direction (R_{radial}), which is discussed in detail in section 5.3.1 and Appendix C. The results are included with the "heat transfer rate" section. For each tube, measurements were conducted at operating

temperatures ranged from 1 000 to 1 700 °C and with nitrogen and helium used as the graphite felt purging gases. The results of these measurements are presented next.

6.2 Validation of the Numerically Predicted Heat Transfer Rates & Silica Tube Middle Temperatures

In this section, heat transfer rates predic ted by the quasi 2-D m odel (see chapter 5) and the m iddle tem peratures of the m iddle of the silica t ube predicted by the numerical model of the therm al conductivity of the graphite felt (s ee chapter 2 and Appendix C) are com pared with the m easured ones. The agreem ent of these predictions with the m easurements will gi ve more conf idence in the se num erical models.

As can be recalled from section 5.3.2, th e end nodes of the num erical m odel are treated as special nodes with a therm al resistor, R_{cc}, wit h values determ ined from direct measurements of the tem perature gradients ($\delta T/\delta x$). These m easured gradients ($\delta T/\delta x$) are also used, chapter 4, in the calcul ation of the heat transfer rate b y conduction ($P_{conduction}$). As a conclusion, th e comparison of the conductive m easured and m odelled heat rates is not necessary as both are based on the sam e direct measurements of $\delta T/\delta x$.

Furthermore, as was shown in chapter 5, the contribution of the radiative power ($P_{radiation}$) is calculated from the measured temperature profiles to be less than 2% for the "short tube" and less than 1% for the "long tube" (which are substantially sm aller than the m easurement uncertainties). In addition, the m odelled radiative heat tr ansfer rates are calculated from the m odelled tem perature profiles and these are validated against the m easured temperature p rofiles, shown later in this ch apter. Taking in to consideration this sm all contribution of $P_{radiation}$ to the tota l output hea t transf er rate ($P_{radiation}+P_{conduction}+P_{radial}$) and th e valida tion o f the m odelled tem perature profiles then the comparison of the modelled radiative heat transfer rates to the measured ones is also not necessary for the works presented here.

On the other hand, the heat transfer rate in the radial direction (P_{radial}) was calculated calorimetrically from measurements of the volume flowrate and the temperature rise of the water coolant of the brass jacket (described in details in section 4.2). Unlike $P_{conduction}$ and $P_{radiation}$, the determination of P_{radial} does not rely on the measurements of the temperature profiles in addition P_{radial} is the largest heat transfer rate from the graphite tube (50-80%). Hence, only P_{radial} is to be validated in the work presented as it is the heat transfer rate that can mostly influence the temperature profile of the inner walls of the ATJ graphite tube.

As mentioned earlier, the "short tube" and the "long tube" are used in these numerical model validations. For both tubes, measurements are conducted at temperatures ranging from 1 000 to 1 700 °C and with the insulating graphite felt purged with nitrogen and helium. Numerical model simulations for both tubes were generated using an 80 node mesh and values for the graphite thermal conductivity with a radiation constant C_{fr} set to 15 (see chapter 2) purged with nitrogen and helium. Note that for WDF graphite felt, the value for C_{fr} of 15 was determined experimentally in section 2.1.2. Predictions of the heat transfer rates in the radial direction (P_{radial}) are then compared with the measured ones and are plotted in Figure 6.1 and Figure 6.2. In addition to these graphs and in order to better quantify the discrepancies between the modelled and measured P_{radial}, the modelled heat transfer rates versus the measured ones are plotted in Figure 6.3 and Figure 6.4 and are compared with the line of perfect agreement (when measured P_{radial} is equal to the modelled P_{radial}) along with a ±20% upper and lower limits. Note that this value of ±20% for the upper and lower limits was selected based on (i) the values of the measurement uncertainties of the heat transfer rates (see section 4.4), which was found to be up to a value of 5%, (ii) the discrepancies between the input and output heat transfer rates (see section 4.3), which was found to vary between 8% and 18%, and (iii) using an expanded measurement uncertainties with a confidence limit of 95% (ISO 1993). Combining these values gives a ball park figure of around 20%, which is can be used in the purpose of the work presented in this chapter.
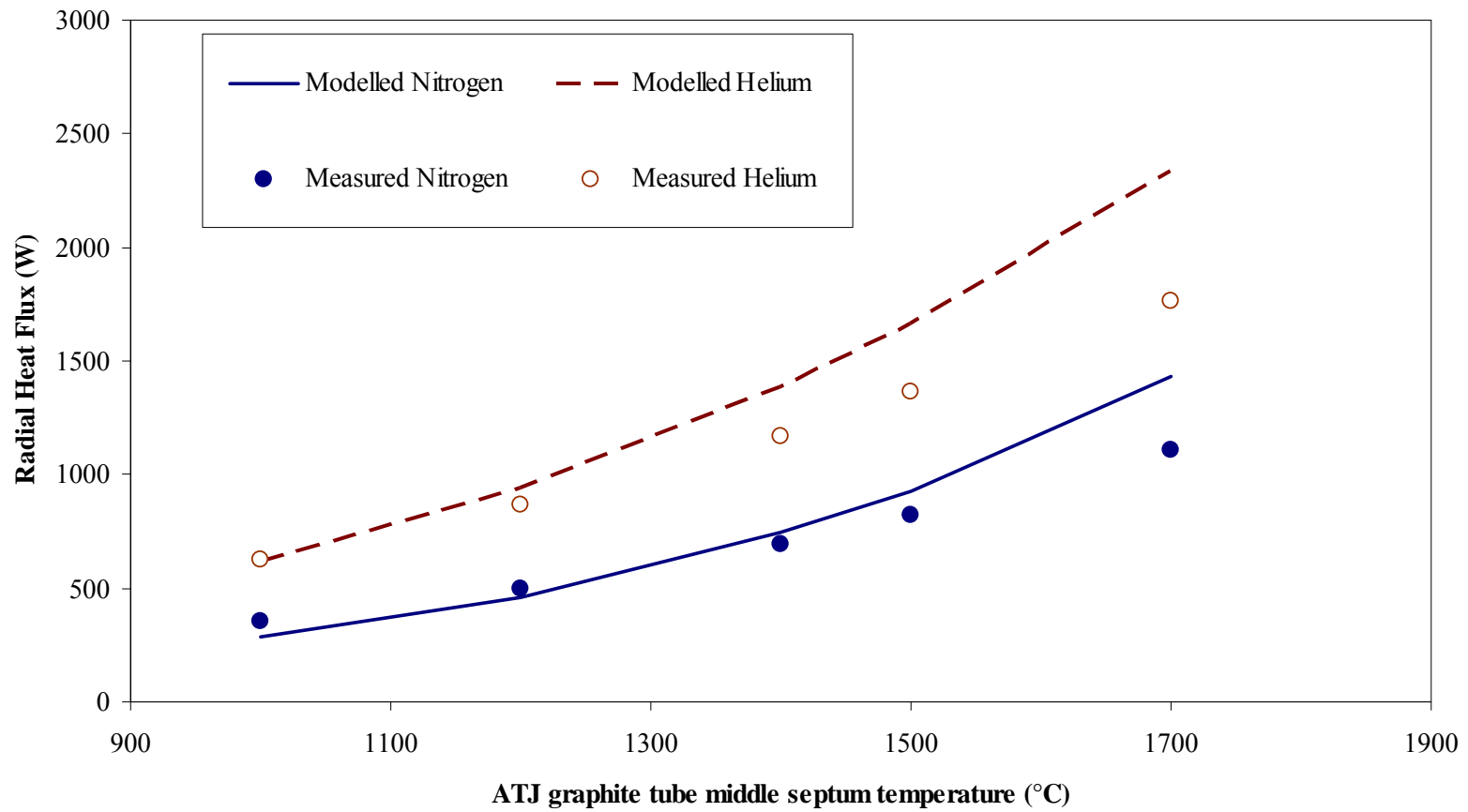
Figure 6.1. Comparison of the measured radial heat fluxes with the modelled ones at operating temperatures ranging from 1 000 to 1 700 °C using the 289 mm long ATJ graphite tube of the 48 kW Thermogage furnace at NMIA ("short tube").
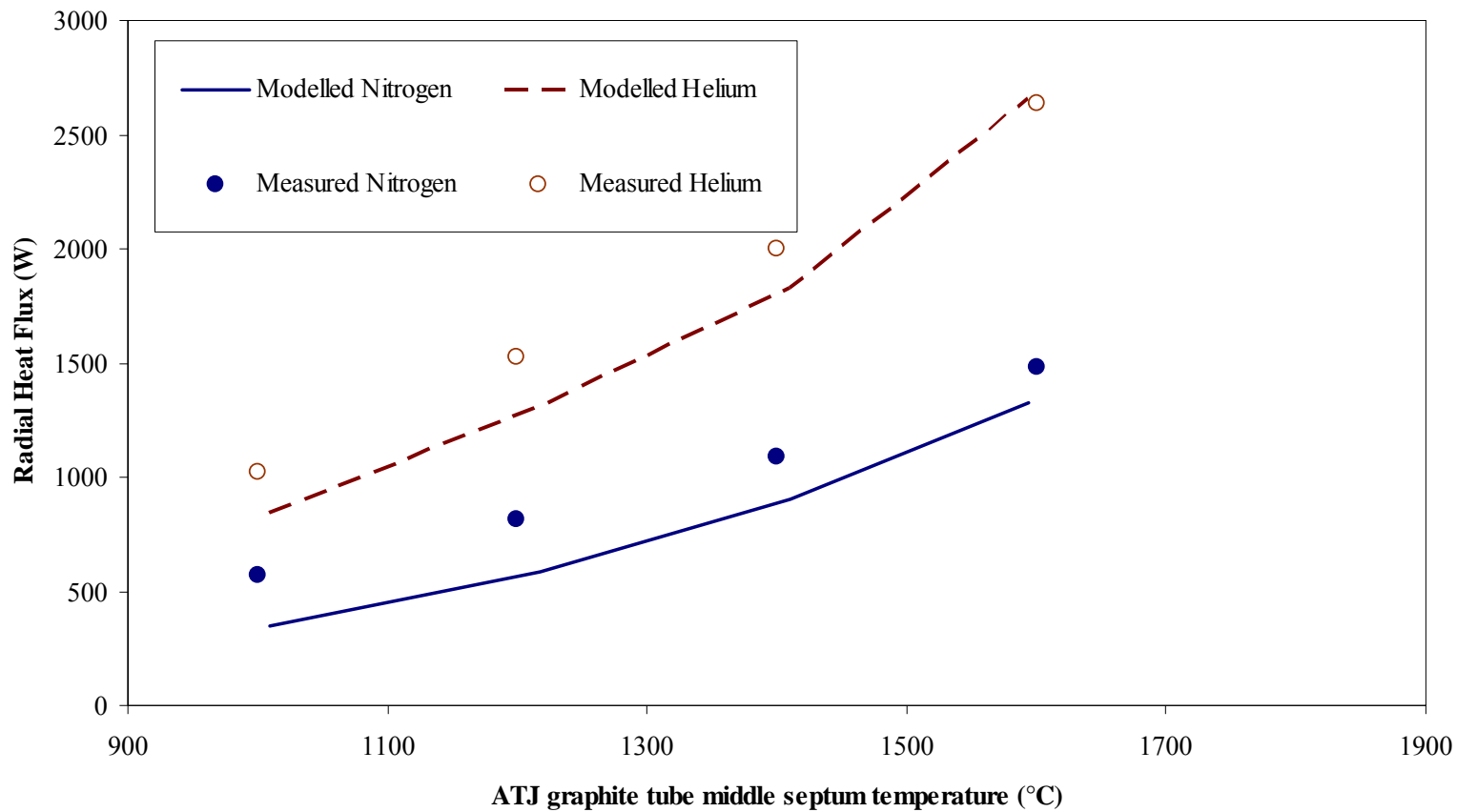
Figure 6.2. Comparison of the measured radial heat fluxes with the modelled ones at operating temperatures ranging from 1 000 to 1 700 °C using the 400 mm long ATJ graphite tube of the 48 kW Thermogage furnace at NMIA ("long tube").
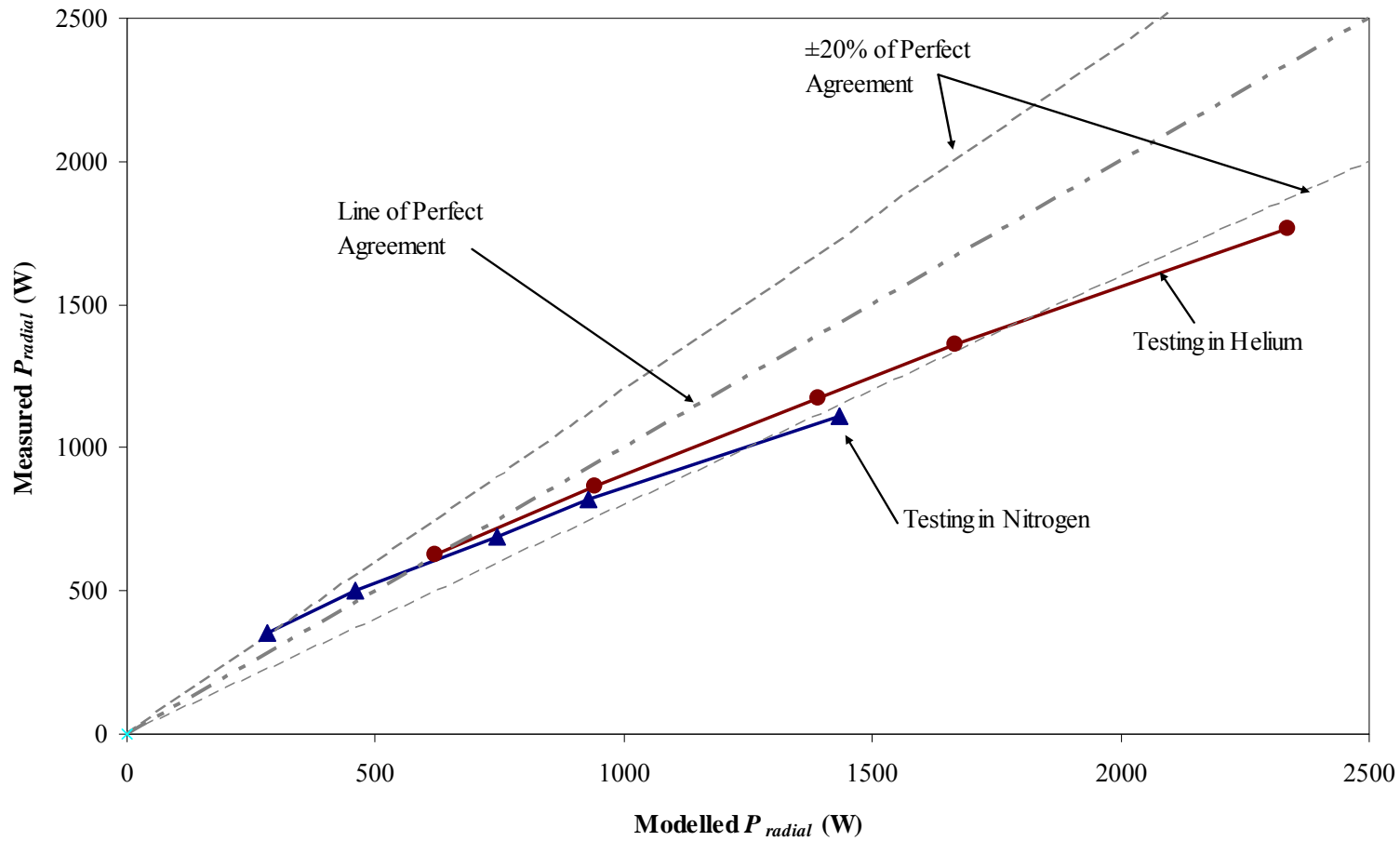
Figure 6.3. Graph of the measured heat transfer rates in the radial direction versus the modelled ones for the 289 mm ATJ graphite tube or the "short tube" at NMIA. Also, comparison is made with the line of perfect agreement (modelled=measured) along with 20% upper and lower limits.
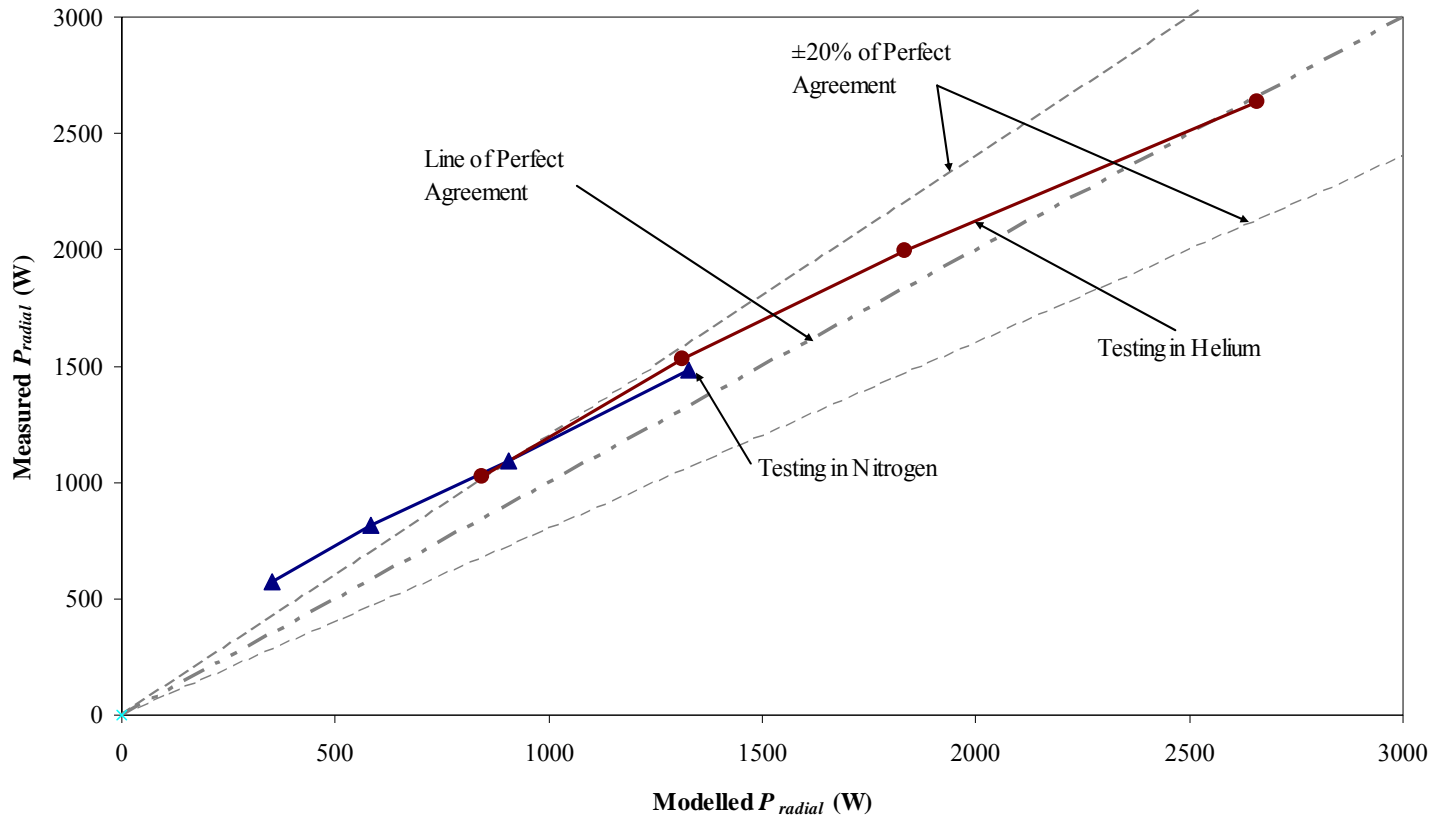
Figure 6.4. Graph of the measured heat transfer rates in the radial direction versus the modelled ones for the 400 mm ATJ graphite tube or the "long tube" at NMIA. Also, comparison is made with the line of perfect agreement (modelled=measured) along with 20% upper and lower limits.

Referring to Figure 6.1 and Figure 6.3, fo r the case of the "short tube", good agreement can be obs erved for the lower v alues of P_{radial} with th is dif ference increasing for higher values. It can also be noticed from Figure 6.3 that the m easured heat rates are in general smaller than the modelled ones. This may be explained by the heat escaping at the edges of the water cooled brass jacket and lo sses from the graphite felt to the water cooled copper electrodes (see Figure 4.1). Note that the heat balance check, conducted in chapter 4, on the "short tube" showed a difference of 18% between the input and output heat transfer rates.

With the construction of the "long tube", im provements made on the experim ental apparatus showed a better heat balance agreement between the heat transfer rates from and to the ATJ graphite tube (see chapte r 4 and Appendix B) w ith the discrep ancies between these rates dropping from around 18% to 8%. However, as it can be seen from Figure 6.2 and Figure 6.4, the differenc e between the m odelled and m easured P_{radial} at low values is larger than that of the "short tube". On the other hand, this difference becomes smaller as P_{radial} rises, especially for the case when helium is used as the purging gas of the gr aphite f elt. Th is m ay be caused by the m easurement uncertainty of the thermal c onductivity of the graphite felt (which is in the order of 10%, refer to chapter 2) and at the same time some systematic errors that could not be accounted for. These errors m ight have constant values resulting in higher percentage for low values of P_{radial} and smaller percentage at higher ones. Overall, the agreem ent between the m easured and the m odelled va lues of P_{radial} are acceptable within the specified limits of 20%.

Recall from section 3.3.1 that the radial ther mal resistance of felt is calculated using an iterative over-r elaxation method on $n+2$ finite elem ents in EXCEL (Appendix B), which can be used to ite rate for the silica tube middle te mperatures as a function of the graphite tube m iddle septum temperat ures. The silica tube m iddle tem peratures (see Figure 5.1) are m easured using K-Type therm ocouple and these m easurements can then be compared with the modelled values. Comparison of the silica tube middle temperatures for the "short tube" and th e "long tube" are shown in Figure 6.5 and Figure 6.6.
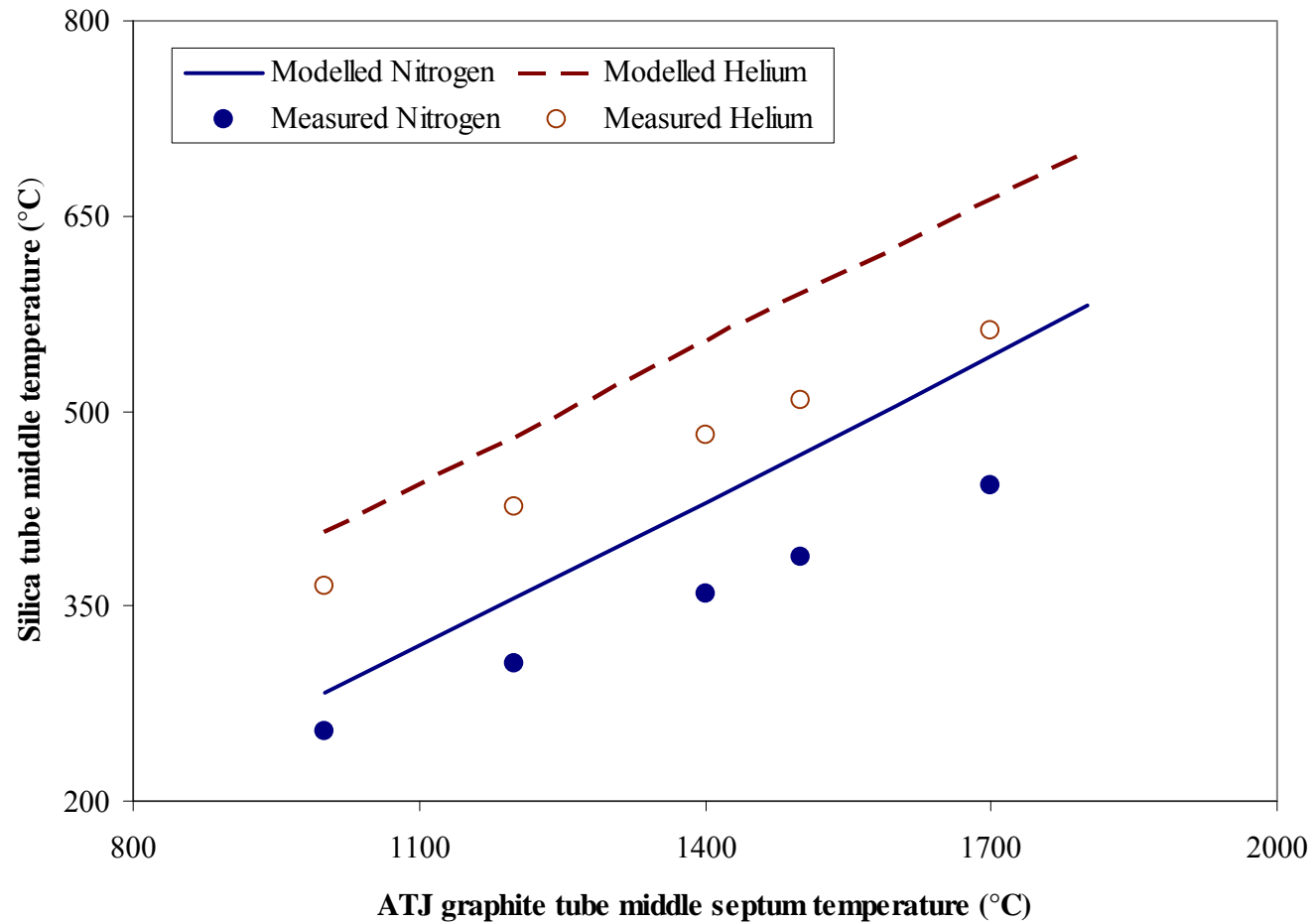
Figure 6.5. Comparison of the measured silica tube middle temperatures with the numerical model predictions at operating temperatures ranging from 1 000 to 1 700 °C for the NMIA 48 kW Thermogage furnace with 289 mm long ATJ graphite tube ("short tube").
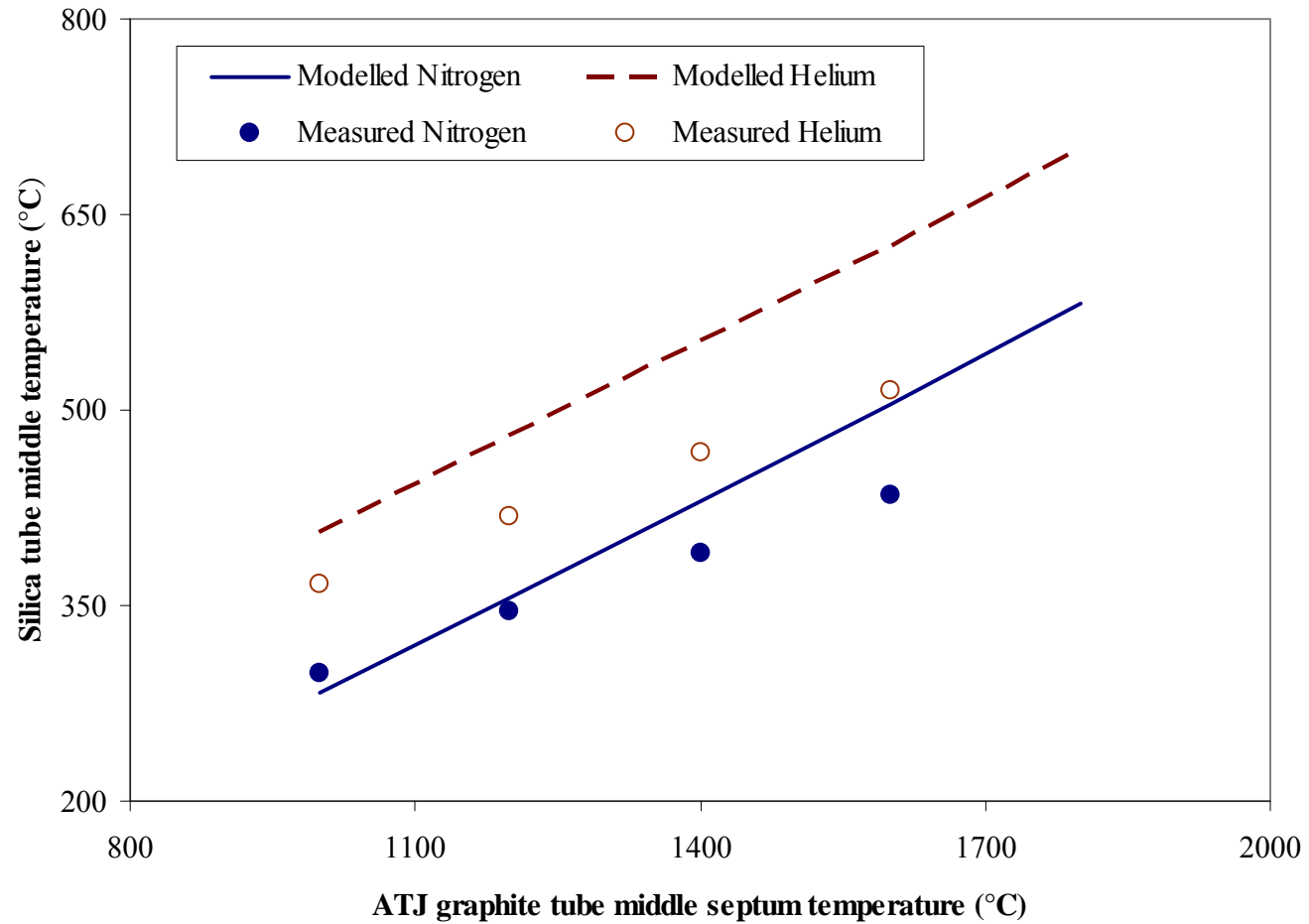
Figure 6.6. Comparison of the measured silica tube middle temperatures with the numerical model predictions at operating temperatures ranging from 1 000 to 1 700 °C for the NMIA 48 kW Thermogage furnace with 400 mm long ATJ graphite tube ("long tube").

The comparison of the modelled and m easured temperatures of the middle of the silica tube confirms that the discrepancies between the measured and modelled radial heat rates m ay be caused by the uncertainty in the values used f or the therm al conductivity of the graphite felt; the measurement uncertainty of the therm al conductivity of the felt was determined to be 10%, see chapter 2.

The comparison of th e modelled an d measured radial heat fluxes and the silica tube middle temperatu res are im portant. However, the question that arises from these measurements is: what is the effect of the thermal conductivity values of the WDF graphite felt and other qua ntities on the numerical m odels of the graphite tube temperature profile?

The answer to the above questions lies in conducting a sensitivity study on the quasi 2-D numerical model, which is discussed next.

6.3 Numerical Model Sensitivity to Input Parameters

The therm ophysical properties of A TJ graphi te and WDF graphite felt are used as input param eters in the quasi 2-D num erical m odel. In addition, the m easured temperature gradients are used in d etermining the therm al resistance at both ends of the tube, R_{cc}, (chapter 5). All of these param eters have uncertainties, which can influence the numerical model predictions.

The uncertainties in the ATJ graphite ther mophysical properties were determ ined in section 2.2. According to the literature su rvey conducted by the present author, the average thermal conductivity of ATJ graph ite was found to have a 10% uncertainty. As for the therm al conductivity of WDF graphite felt (k_{felt}), it can be noted that the major source of uncerta inty is due to the dete rmination of the rad iation constant C_{fr}, which was taken to be 15. As m entioned earlier, the value of C_{fr} was determ ined experimentally and found to vary betw een 10 and 35, and it was only by cross examining the works conducted by other i nvestigators on the m easurements of the thermal conductivity of graphite felt that the value of C_{fr} could be narrowed to 15 but

153

with a large uncertainty of 10% (s   ee section   2.1.3). On the other hand, the uncertainties in the density and specific h eat of the ATJ graphite are of no im portance in this case since the numerical model predictions are for steady state conditions only. For steady state conditions, $dT/dt =0$ and   therefore th   e right hand term   s of equation (5.2) becomes zero.

The uncer tainty in R_{cc} is m   ainly due to th   e m easurement uncertainties of the temperature gradients ($\delta T/\delta x$) with values determ   ined in section   4.2.2. The measurement uncertainty of the grap hite tube wall tem perature in the region near its ends was estimated to be 6%.

Using the above uncertainty values, num   erical m odels for the graphite tube temperature profile at an operating tem perature of 1 000 °C and with nitrogen as the felt purging gas are generated. Plots of   these num erical m odel predictions are compared with the m easured tem peratures as s hown in Figure 6.7. In   addition, th e selection of this case of ope rating temperature of 1 000 °C and with nitrogen used as the purging gas was based on having the larg   est discrepancy between the m easured and m odelled results. N ote that by selec ting th is set of m easurements, the reader is able to observe the worst case scenario of discrepancies between the modelled and the measured temperatures of the inner walls   of the graphite tube. On the other hand, other comparisons which show better agreement are presented later in this chapter.
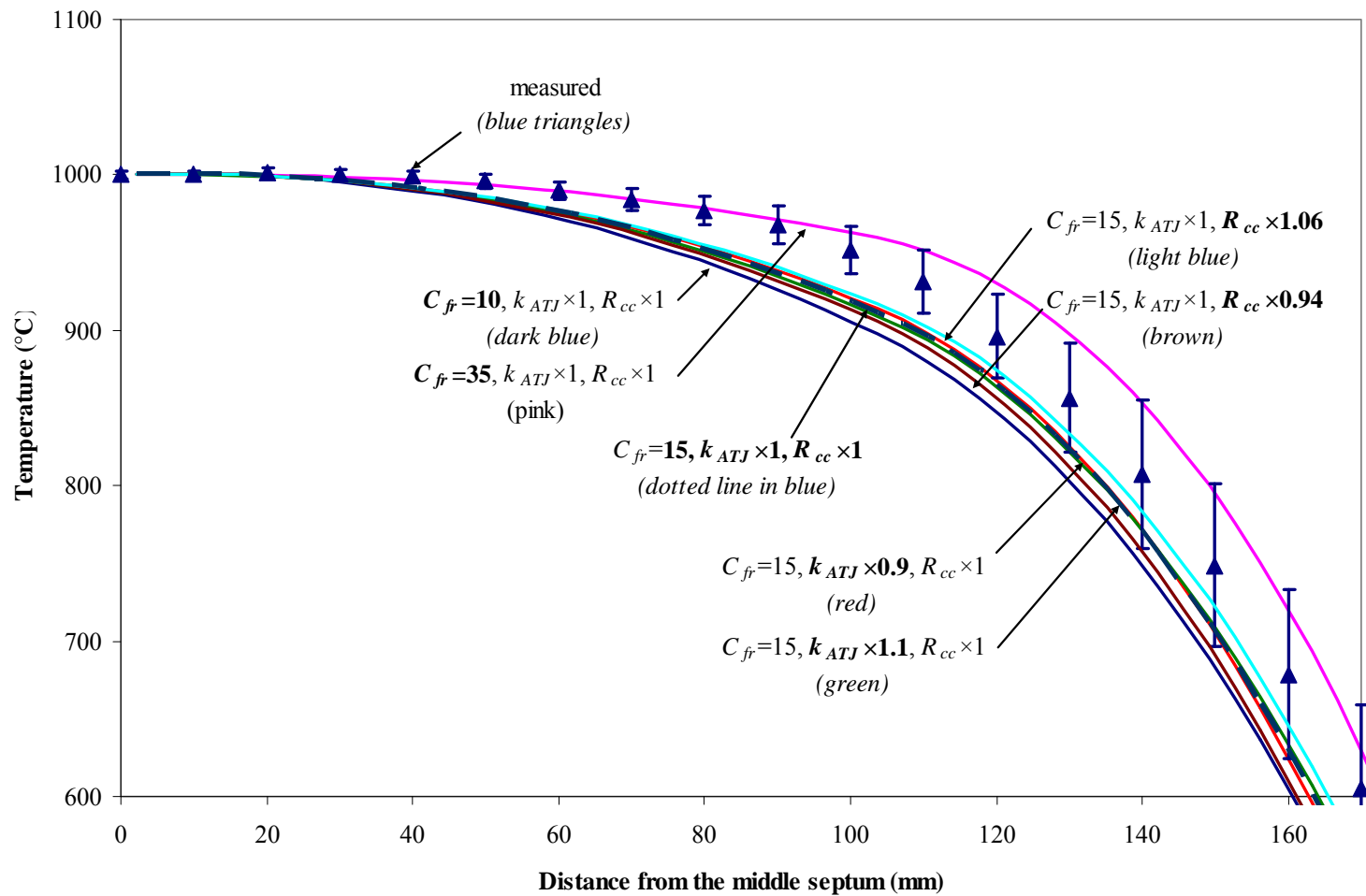
Figure 6.7. Comparison between the temperature measurements of the inner walls of the ATJ graphite tube (along with their uncertainty bars) and the numerical model predictions using various values of C_{fr}, k_{ATJ} and R_{cc}.

It can be observed from the plots, in Figur e 6.7, that the effect of varying the thermal conductivity of ATJ gr aphite on the num erical m odel predictions is sm all in comparison to other param eter uncertain ties. The c hange in the pred icted temperatures when changing values of the ATJ thermal conductivity by $\pm 10\%$, which is th e m easurement uncertainty v alue, was observed to be less than 0.5%, which is insignificant for the results presented herein.

A sm all ch ange in th e tem perature prof ile d ue to the u ncertainty o f R_{cc} can be observed from Figure 6.7. This change is less than 1% in the region within 100 mm of the tube's m iddle septum , but it increases up to 8% toward the end s of the tube. Although an 8% change in the temperature pr ofile is substantial, it m ay be noted however that th is chan ge occurs in the re gion toward the ends of the graphite tube , where it has minimal effect on the calculation of the effective emissivity of the cavity (see chapter 1). Note that the effect o f R_{cc} on the temperature profile (especially in the region near the m iddle septum) was m inimised by the fact that the cuts introduced to each tube act as hot points which pr oduce high tem perature zon es prim arily influencing the temperatures of the m iddle region of the graphite tube and creating at the sam e tim e a buffer-lik e zone where the effect of R_{cc} on the m iddle septum are minimised.

On the other hand, it can be noted that the la rgest change in the te mperature profile is caused by the change in the values of C_{fr} (from 10 to 35). W ithin 100 mm from the middle septum, the change in tem perature profile is around 6% , increasing to 20% toward the tube ends. Recall that an e xperimentally determ ined value of 15 was obtained for C_{fr}. It can be deduced that the values of the radiation constant C_{fr} can mostly influence the pre dicted va lues of the temperatu re pro files. This is of course due to the fact that m ost of the electri cally generated heat is dissipated through the graphite in the radial direc tion constituting 50-80% of the to tal heat transfer rate o ut of the tube (see Chapter 4 and Appendix B). To som e extent, influences from the other two variab le en tities, R_{cc} and k_{felt}, on the predicted tem perature profiles, especially in the regions of the tube near its middle septum, are minimal and therefore can be ignored.

Predictions of the temperature profiles generated using the quasi 2-D numerical model are validated at two operating temperatures of 1 000 a nd 1 500 °C. These are presented next.

6.4 Validation of the Temperature Profile Predictions

Validation results of the temperature profiles of the ATJ graphite tube (or the cavity inner wall temperatures) were conducted at two operating temperatures of 1 000 and 1 500 °C. The selection of these operating te mperatures was based on two reasons: (i) the m inimum tem perature at w hich th e 48kW Therm ogage furnace is used i s 1 000 °C, and (ii) the maximum temperature at which the Pt/P t-Rh circular tip thermocouple can be used, without m elting or reacting with the m easured graphite surroundings, is 1 500 °C.

Numerical models of the tem perature profil es at the two operating temperatures of 1 000 and 1 500 °C were generated with the graphite felt purged with nitrogen and helium and with a C_{fr} value of 15 (determ ined in section 2.1.3). Th ese predicted profiles are then com pared with the m easured ones. These tem perature comparisons are shown in Figures 6.8-11.
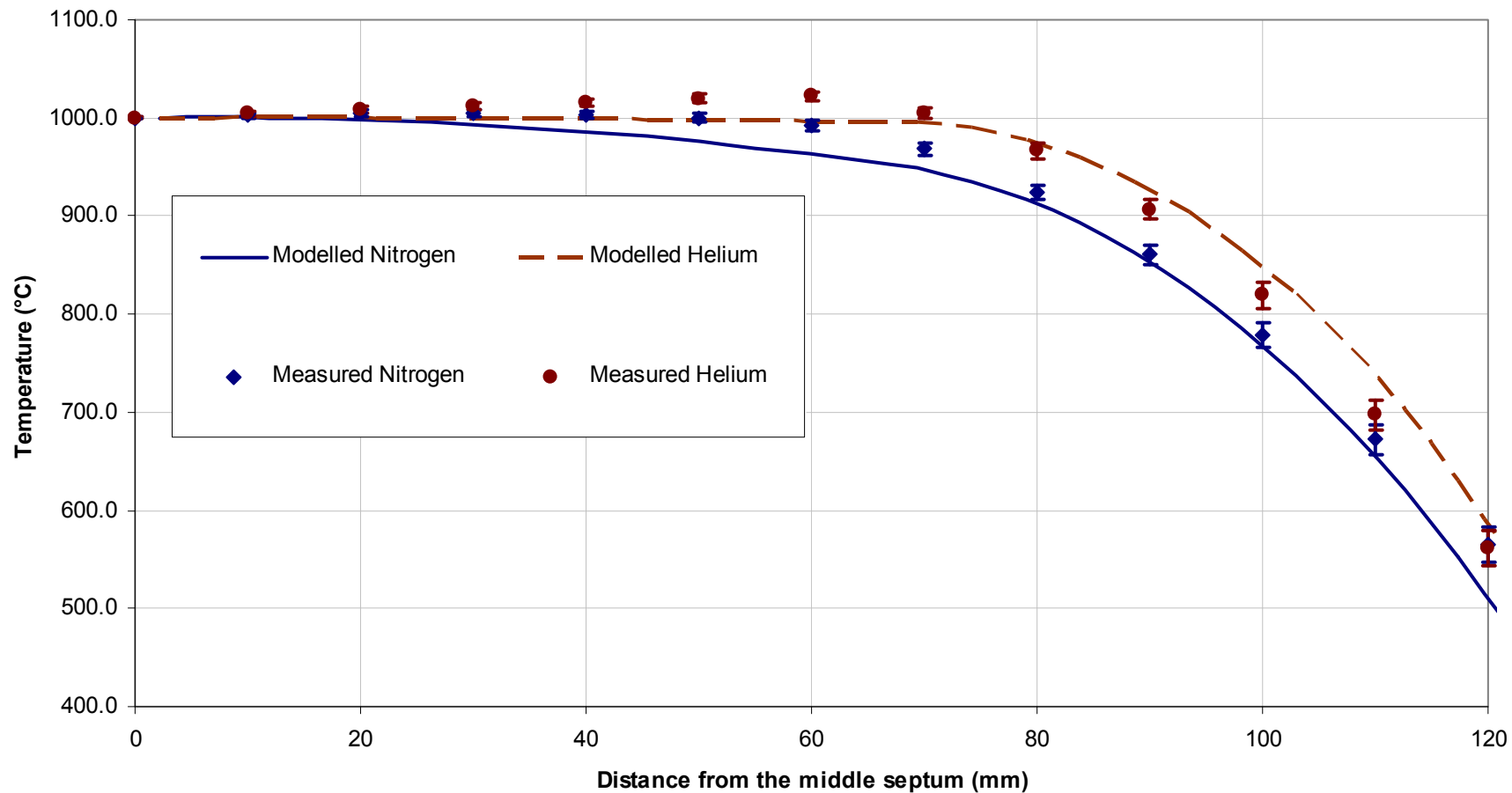
Figure 6.8. Comparison of the 289 mm ATJ graphite tube (short tube) measured temperature profiles with the numerical model predictions at an operating of 1 000 °C for the cases of the graphite felt purged with nitrogen and helium. Measurement uncertainties of the temperature are also plotted.
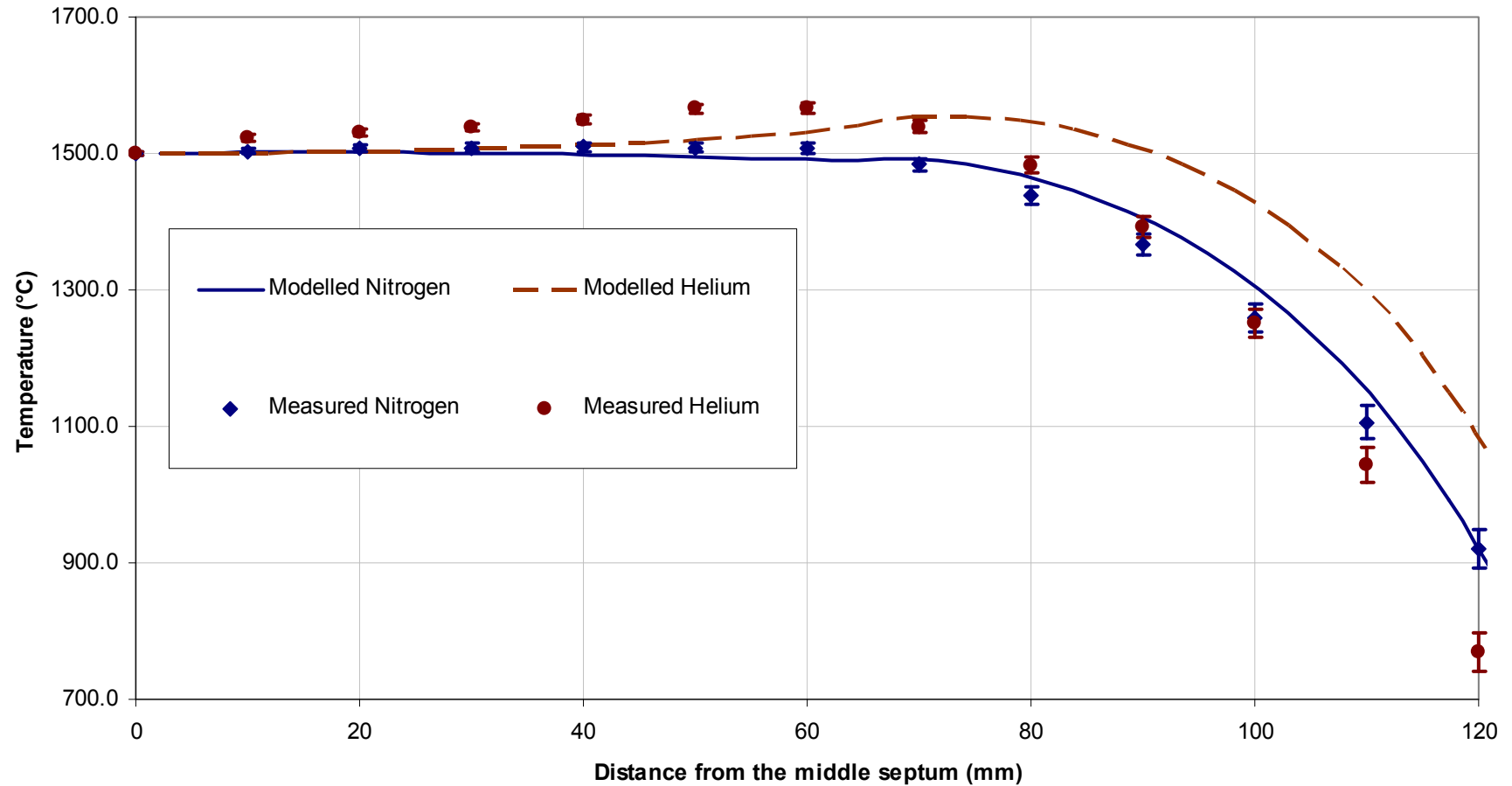
Figure 6.9. Comparison of the 289 mm ATJ graphite tube (short tube) measured temperature profiles with the numerical model predictions at an operating of 1 500 °C for the cases of the graphite felt purged with nitrogen and helium. Measurement uncertainties of the temperature are also plotted.
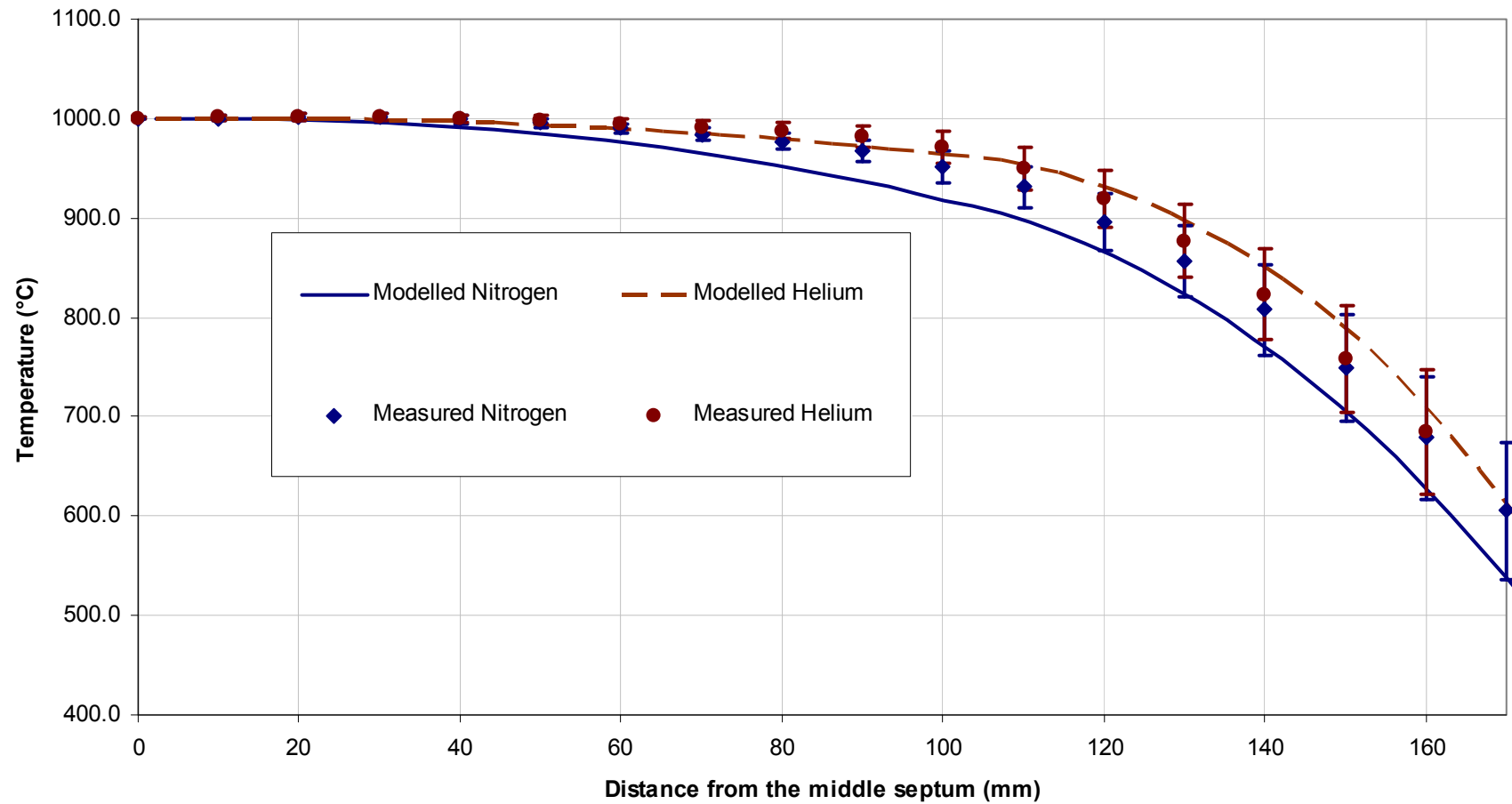
Figure 6.10. Comparison of the 400 mm ATJ graphite tube (long tube) measured temperature profiles with the numerical model predictions at an operating of 1 000 °C for the cases of the graphite felt purged with nitrogen and helium. Measurement uncertainties of the temperature are also plotted.
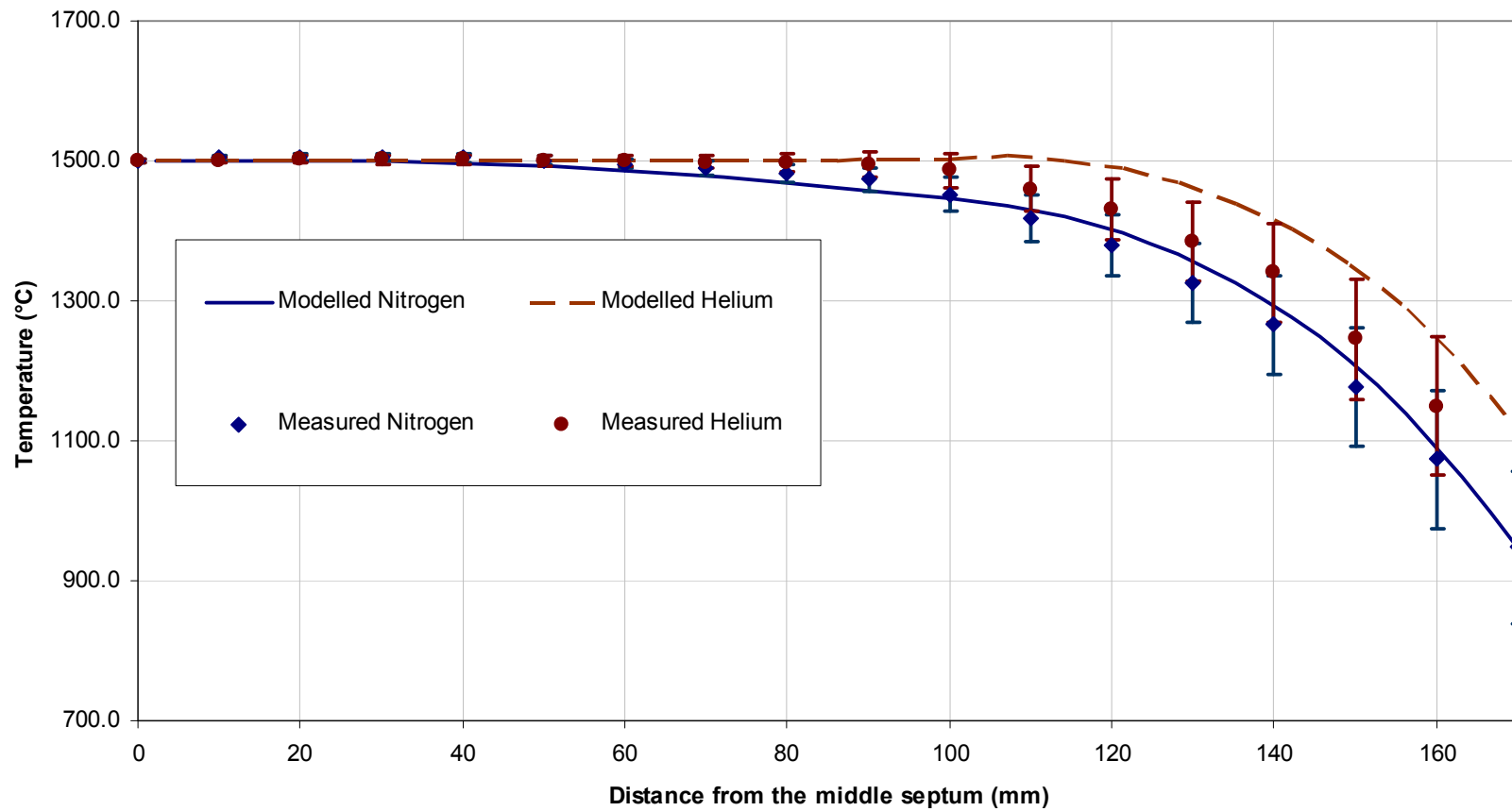
Figure 6.11. Comparison of the 400 mm ATJ graphite tube (long tube) measured temperature profiles with the numerical model predictions at an operating of 1 500 °C for the cases of the graphite felt purged with nitrogen and helium. Measurement uncertainties of the temperature are also plotted.

Recall fro m the sensitiv ity stud y conducted in the previous section that the temperature prof ile is mostly af fected by the uncerta inty in the valu e of radiation constant C_{fr}, which is used in the calculation of the thermal conductivity of the W DF graphite felt. Hence, as can be seen from the figures above, the discrepancies between the measured and m odelled resu lts can be explained p rimarily by th is uncertainty in C_{fr}. However other m easurement uncertainties of the input param eters used in the quasi 2-D numerical model such as the thermophysical properties of ATJ graphite and the therm al resis tance R_{cc} can als o contribu te to these d iscrepancies. W hile the uncertainties in the thermophysical properties of the ATJ gr aphite and specifically the thermal conductivity do not influence m uch the numerical predictions, the uncertainty in R_{cc}, on the other hand, has a la rger influence on the temperature profile predictions in the reg ion between the cut and the end of the graphite tube (as demonstrated in Figure 6.7). Hence, the larger discrepanc ies between the modelled and m easured profiles near the ends of both the "short" and "long" tubes can be explained by the uncertainty in R_{cc}.

Referring to Figure 6.8 and Figure 6.10 for th e case of operating temperature of 1 000 °C (for the long and short tube), the region up to about 70 mm is relatively uniform in tem perature, falling rapidly to about 400 °C at the junction of the CC-clamps and graphite tube, and the model pr edicts this satisfactorily. In the 1 500 °C case, presented in Figure 6.9 and Figur e 6.11, the m easured tem peratures are systematically higher than those modelled. However, in b oth cases, the predicted change in profile with change from th e lower conductance nitrogen to the higher conductance helium gas is in agreement with in the m easurement uncertainties of the temperatures and the variations in the num erical predictions due to the uncertainty in C_{fr}. Noteworthy at this s tage is that by having confirmed that the quasi 2-D numerical model can b e used to sa tisfactorily predic t a change in the tem perature profile when changing the purging gas of the felt, then th is shield g as effect can b e used as a technique to tune the temperature profile of a given tube to achieve uniform ity over a wider range of operating temperatures (discussed later in chapter 7).

In general, the num erical pred ictions of the temperature p rofile for th e case of th e "long tube" (refer to Figure 6.10 and Figure 6.11) are in better agreem ent with the measured temperature w hen compared to th e case of the "short tube". The reason for

this better agreem ent could be credite d to the im provements conducted on the experimental apparatu s when the "long t ube" was constructed. Recall from chapter 4 that ex tra care was taken by the present autho r to ensure th at the W DF graphite fel t was wrapped evenly around the A TJ graphi te tube; which is im portant in the numerical modelling of the h eat transf er r ate in the radia l direc tion and th e temperature profile of the gr aphite tube. In addition, the assumption used in chapter 5 of a quasi 2-D num erical model with the heat flows being one dim ensional along the graphite tube and radially through the graphi te felt is better realised when a longer tube is used. Note that the effect of elongating the graphite felt along the axial direction while keeping the same thickness can definitely increase heat transfer rate in the radial direction only.

It can also be noted that the nu merical predictions for the case of operatin g temperature of 1 500 °C (for both tubes) ar e in general in better agreem ent than the predictions for the case of 1 000 °C due to the increase of the heat tr ansfer rate in the radial direction. As in the case of having a longer tube, th e increase of radial heat transfer rate, caused by the increas e in the temperatures of the graphite tub e an d consequently higher therm al conductivity of gra phite felt, means that heat transfer in the radial direction is becom ing more one dim ensional when com pared to lower temperatures. Needless to rem ind the reader that this ass umption was used in the development of the quasi 2-D numerical model.

In conclusion, satisfactory agreem ents were found between the m easured temperature profiles and the numerical prediction models within the temperature uncertainties, and taking into consideration the sensitivity of the numerical model to the uncertainties of the input parameters. Therefore, th e design of a new tube can now proceed using the quasi 2-D numerical model. This is carried out in the next chapter.

7 A NEW ATJ GRAPHITE TUBE DESIGN

7.1 Introduction

As stated in chapter 1, the aim of the work presented in this thesis was to improve the effective emissivity, ε_{eff}, of the NMIA 48kW Thermogage blackbody cavity. This may be achieved by improving the cavity wall temperature uniformity. A quasi 2-D numerical model has been developed, chapter 5, and validated, chapter 6, by the present author to predict the cavity wall temperature profile. This numerical model can now be used to optimise the temperature uniformity of the inner walls of the ATJ graphite tube.

In this chapter, the design of a new ATJ graphite tube is discussed, as well as the methodologies adopted in this design being described. The temperature profile of the new graphite tube has been measured and is compared with the numerical model predictions. The effective emissivities of the cavity, at various operating temperatures and using nitrogen and helium as the felt purging gases, for the newly design tube are also presented.

7.2 Design Methodologies

Recall from chapter 1 that the cavity's wall temperature uniformity of the IKE graphite furnace was optimised by changing the furnace's heater element area profile (shown in Figure 1.10). The same principle can be applied here in the optimisation of the temperature uniformity of the inner walls of the ATJ graphite tube cavity of the NMIA 48kW Thermogage graphite furnace. In addition, measurements of the temperature profiles of the ATJ graphite tube when changing the graphite felt purging gas from nitrogen to helium showed significant changes to the temperature profile (see chapter 6). This was caused by the change in the effective thermal conductivity of the insulating felt and subsequently the radial heat transfer rate. As stated in chapter 1, this shield gas effect can also be employed in the design optimisation.

It is therefore recomm ended that to op timise the performance of the Therm ogage furnace (i) the cross s ectional area profile of the ATJ g raphite tube (the heater element) is m anipulated in order to obt ain better uniform ity of the inner wall temperatures, especially near the m iddle region of the tube, and (ii) the use of different gases used to purge the graphite fe lt (in this ca se nitrog en and helium) to "tune" the radial heat transf er rate and the tem perature profiles. In addition, design considerations are given to m odifying the ATJ graphite tube length, without affecting the useability of the Therm ogage as a te mperature calibration standard, for better performance.

7.2.1 Effect of Changing the Graphite Tube Cross Sectional Area

As shown schem atically in F igure 7.1, th e original design of the NMIA 48kW Thermogage consists of a 289 mm l ong ATJ gr aphite tube (the heater elem ent) with an inner diameter of 25.4 mm and outside diameter of 31.75 mm with a uniform cross sectional area over m ost of its length (the d iameter of th e tube decreases toward its end where the electrical copper electrodes being mounted, see Figure 1.12). To study the effect of changing the tube's cross sec tional area on th e tem perature profile, the quasi 2-D numerical model developed in chapter 5 is used to pred ict the temperature profiles of the graphite tube for various tube designs.
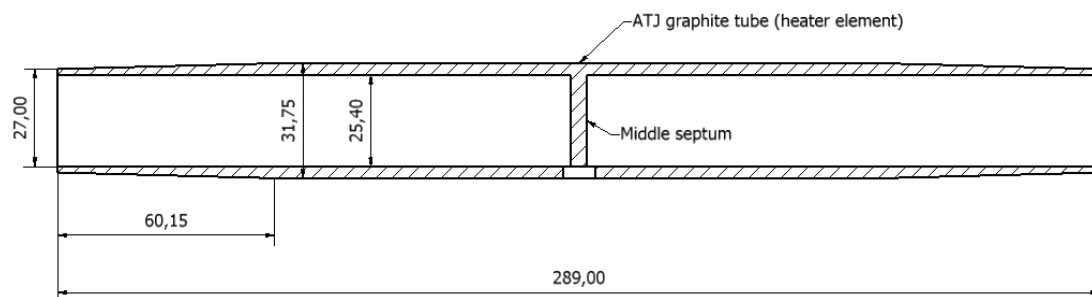
Figure 7.1. Schematic diagram of the cross sectional area of the original design of the ATJ graphite tube used as the heater element for the 48kW Thermogage furnace at the NMIA (all dimensions are in mm).

The simplest variation on the area profile from that of the original tube design is to have a 360° cut near the tube ends, where this cut acts as a "torch" heating the area around it; the cut is a reduction to the wall thickness of the tube. An example of a 289 mm long ATJ graphite tube design having a 360° cut with a width (w) of 60 mm and a depth (d) of 2 mm at 24.5 mm from the tube ends is shown in Figure 7.2.
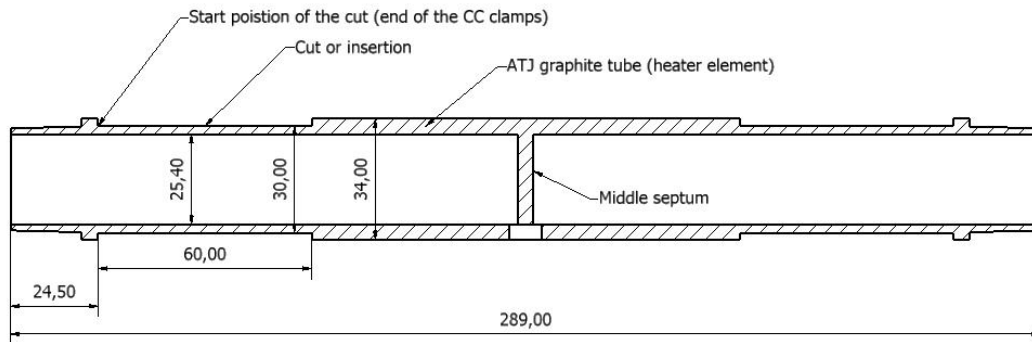
Figure 7.2. Schematic diagram of the cross sectional area of a 289 mm long ATJ graphite tube with a 60 mm wide and 2 mm deep (360°) cut at 24.5 mm from the tube ends (note that all dimensions are in mm).

To study the effect of introducing a 360° cut to the graphite tube, numerical models of temperature profiles were generated using the quasi 2-D software developed in chapter 5, with n taken as 100 nodes and dt as 0.01 sec, for the cases of graphite tubes with 60 mm wide cuts and various depths of 1.0, 2.0 and 3.0 mm. Numerical models were also generated for the cases of graphite tubes with 2.0 mm deep cuts and various widths of 40, 60 and 80 mm and for the case of nitrogen used as the felt purging gas. In addition, the graphite tube outside diameter was selected to be 34.0 mm. The results obtained were then compared with those for the case of a graphite tube with "no cut" and are plotted in Figure 7.3 and Figure 7.4.

The effect of changing the depth of the cut on the temperature profile can be seen in Figure 7.3. It is apparent from the graphs that the rise in the temperature profile is caused by the decrease in the cross sectional area of the graphite tube, resulting in a rise of the electrical resistance of this section of the tube and hence more internal heat generation. Furthermore, this rise in temperatures is also caused by the reduction of the area perpendicular to the heat transfer direction along the graphite tube; the

thermal resistance increases in the region where the 360° cut is made (reduction in the cross sectional area) and therefore if the heat transfer rate along the tube does not change but the area perpendicular to heat flow changes then a rise of temperature occurs.

Similar rises in the temperature profiles due to the increase in the width of the cut can also be observed from the graphs in Figure 7.4. However, it can be noted that this rise in profile tends to be more attenuated in comparison to the previous graphs, where an increase in the depth of the cut tends to result in a "hump-like" profile. Thus, this "wide cut" can represent an advantage, when trying to improve the temperature uniformity of the inner walls of the graphite tube, as it can provide a temperature profile rise without having the need for a deep cut. On the other hand, thinning of the cross sectional area may present a design constraint as it may weaken the graphite tube.
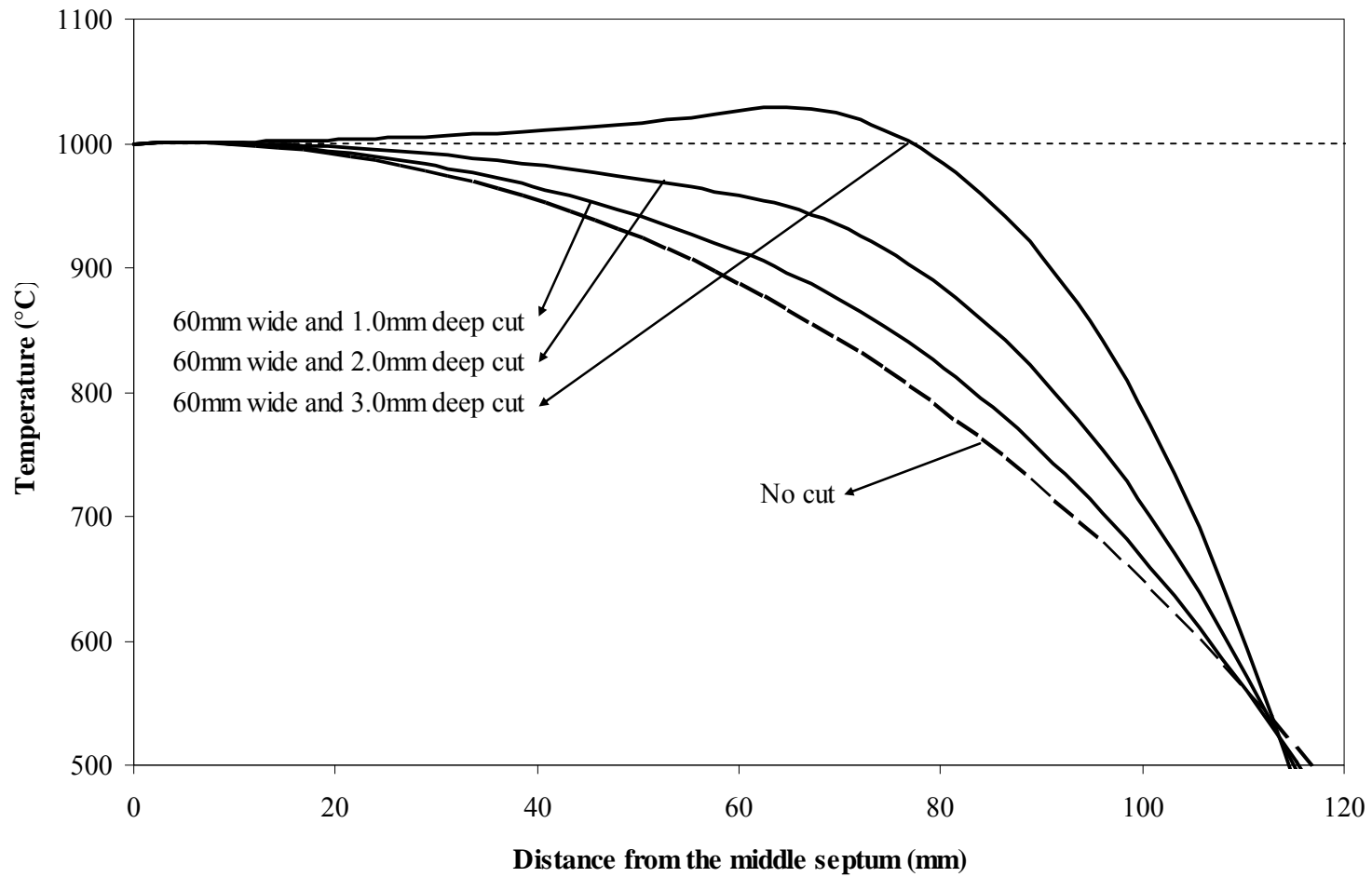
Figure 7.3. Graphs of he numerically modelled temperature profile of the 289 mm ATJ graphite tube for the cases of a tube with a 60 mm wide cut and various depths of 1.0, 2.0 and 3.0 mm and for the case of nitrogen used as the WDF felt purging gas. As well as the temperature profile for the case of a tube with "no cut".
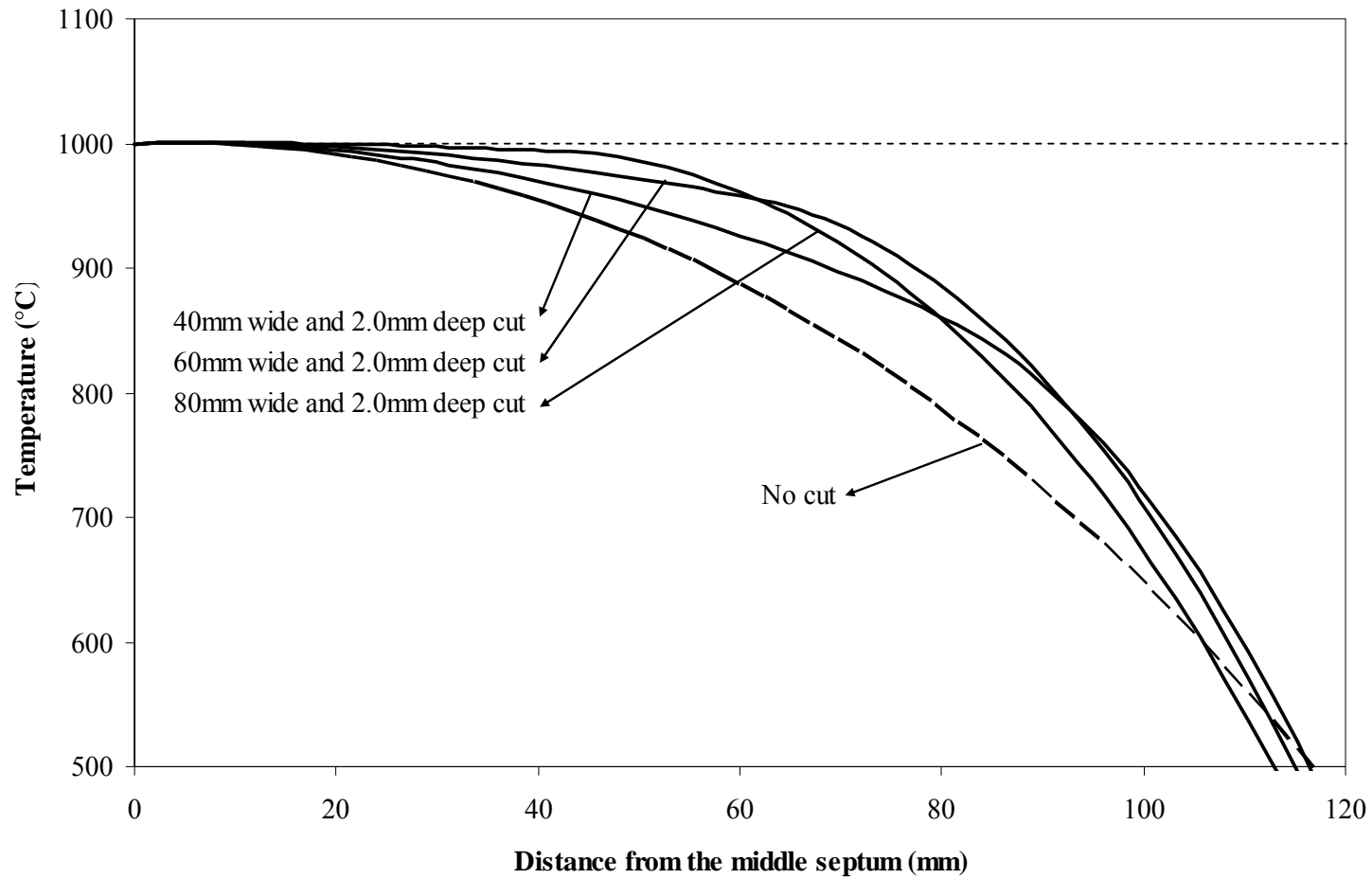
Figure 7.4. Graphs of the 289 mm ATJ graphite tube temperature numerically modelled profiles for the cases of a tube with 60 mm wide cut and various widths of 40, 60 and 80 mm and for the case of nitrogen used as the WDF felt purging gas. As well as the temperature profile for the case of a tube with "no cut".

As can be seen Figure 7.3 and Figure 7.4, the numerical predictions show that, by introducing a simple 360° cut, better temperature uniformity is obtained in the region near the middle septum of the ATJ graphite tube. Therefore, it can be deduced that this simple cut may be used in the design optimisation presented here. However, the question that may arise: what are the dimensions, width (w) and depth (d), of an optimum cut?

Before answering this question, the effect of changing the graphite felt purging gas from nitrogen to helium needs to be first investigated.

7.2.2 Effect of Changing the Graphite Felt Purging Gas

As mentioned in chapter 1, preliminary measurements showed that the graphite tube temperature profile changes substantially when changing the graphite felt purging gas from nitrogen to helium (Figure 1.13). Recall from section 2.1 that the thermal conductivity of graphite felt increases when the purging gas is changed from nitrogen to helium. Note that an increase in the thermal conductivity of the felt leads to an increase in the heat transfer rate in the radial direction and subsequently a change in the temperature profile. Luckily, this change in the temperature profile is desirable as it can be used in the optimisation of the temperature uniformity of the inner walls of the Thermogage cavity especially at low operating temperatures of 1 000 °C. Numerical model results, shown in Figure 7.5, at two operating temperatures of 1 000 and 1 500 °C with nitrogen and helium as the graphite felt purging gases reconfirm the preliminary measurements conducted (see also chapter 6). Note that these numerical models were generated for the case of the graphite tube shown schematically in
Figure 7.2 using n as 100 nodes and dt as 0.01. In addition, the graphite felt radiation coefficient C_{fr} was taken as 15.
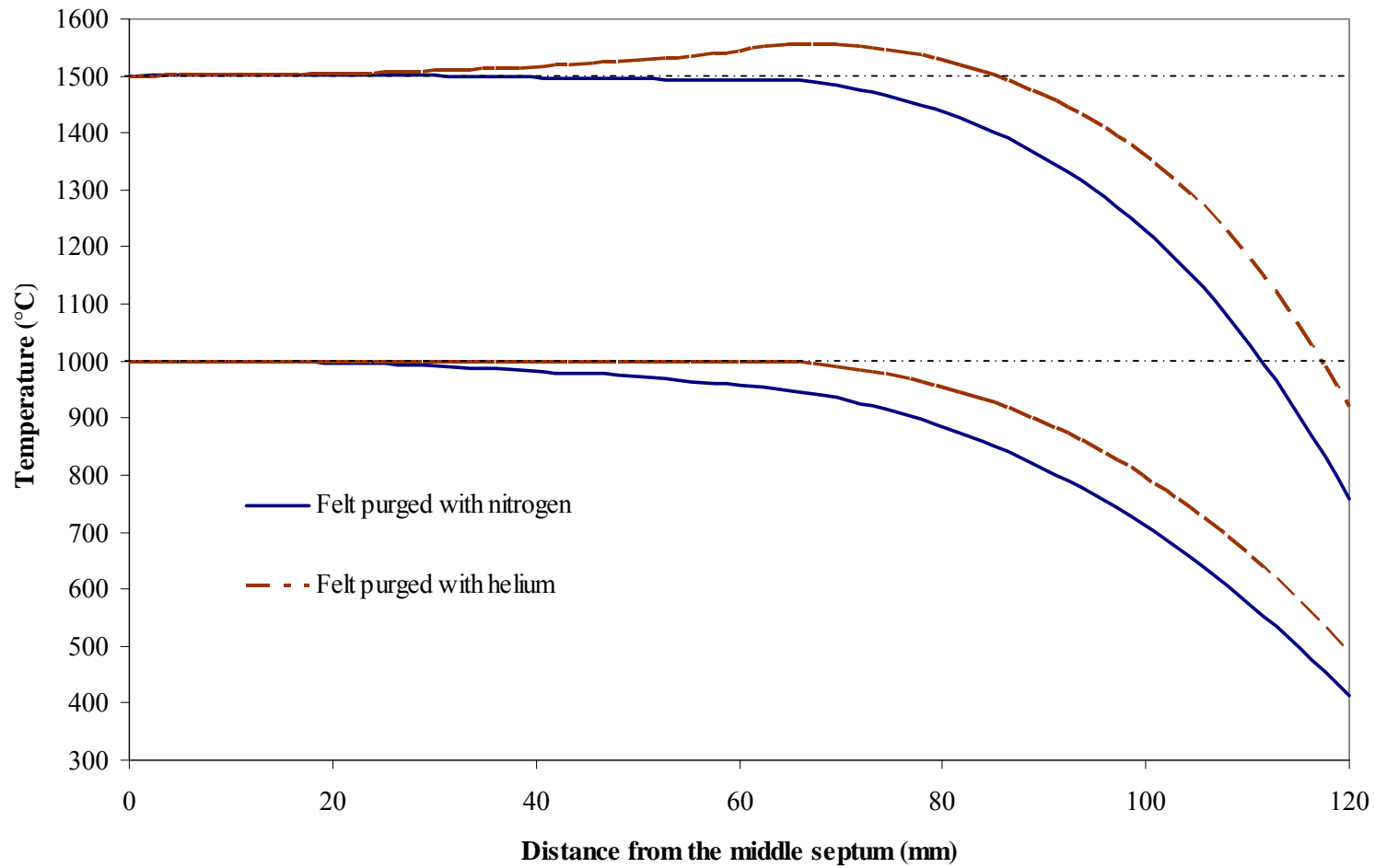
Figure 7.5. Numerical model predictions of the ATJ graphite tube temperature profiles at two operating temperatures of 1 000 and 1 500 °C for the cases of the graphite felt purged with nitrogen and helium.

As can be seen from the graphs of the numerical model predictions in Figure 7.5, at an operating temperature of 1 000 °C the area of uniform te mperature increases to around 70 mm from the m iddle septum when us ing helium. This im provement in the uniformity, as predicted by the quasi 2-D numerical model, will result in improvement in the ATJ graphite tu be's c avity ef fective e missivity, which is ca lculated u sing measurements of the temperature profile (B allico 1996). Hence, sim ilar to the case of introducing the 360° cut, changing the graphi te felt purging gas m ixture can also be employed to "tune or tweak" the tem perature profile at various operating temperatures.

7.2.3 Effect of the Tube Length

In addition to modifying the cross sectional area profile of the graphite and the use of gas m ixture, the length of the ATJ graphite tube can also be changed in order to obtain better temperature uniformity. Lengthening the graphite tube allows for longer area of tem perature p rofile uniformity by m inimising the effects of the water-cooled CC clam ps, which act as heat sink s at both ends of the tube. At the sam e, a longer tube allows for longer m iddle regions of the tube to have uniform te mperature resulting in a better cavity effective emissivity.

A length of 400 mm was selected based on the m aximum length allowed by the design constraints of the NMIA 48kW Ther mogage furnace, nam ely the distan ce between the copper electrodes. At the sam e, this selected length does not im pede the optical v iew region a vailable f or the cal ibration of pyrom eters with F/20 to F/50 viewing optics.

By adopting the three design m ethodologies above, the design of a ne w 400 mm long graphite tub e could now proceed u sing the numerical m odel developed in chapter 3. This is presented in the next section.

7.3 Design of a New Graphite Tube

As mentioned earlier, the design of an optimum cross sectional area, as in the case of the IKE furnace, can b e difficult d ue to th e in finite deg rees of freedom within th e design. Therefore, the design of a new graphite tube can be based on generating numerical model simulations of the tem perature profiles for a sim ple modification on the cross sectional; a 36 0° cut at bot h ends of the tube with a width (w) and a depth (d). Also, the quasi 2-D numerical model can be used to generate temperature profiles at various operating temperatures and for the cases of nitrogen and helium used as the graphite felt purging gases. W ith thes e num erical m odel predictions of the temperature profiles, an optimum design can then be selected.

For operating tem peratures of 1 000, 1 500 and 2 200 °C, num erical m odel predictions of the temperature profiles were generated for a 400 mm long tube with an inside diameter of 25.4 mm and an outside diam eter of 34 mm. These predictions are presented in a two dimensional table shown in Figure 7.6 for the case of nitrogen used as the felt purging gas, and in Figure 7.7 for the case of helium use d as the felt purging gas. To m ore easily compare the predicted temperature profiles, the y-axis of the plots in both figures is taken as the temperature difference in reference to th e temperature at the m iddle septum of the graphite tube, T_{septum}, versus the distance from the middle septum.

Case of 400 mm long tube with N₂ as the felt purging gas
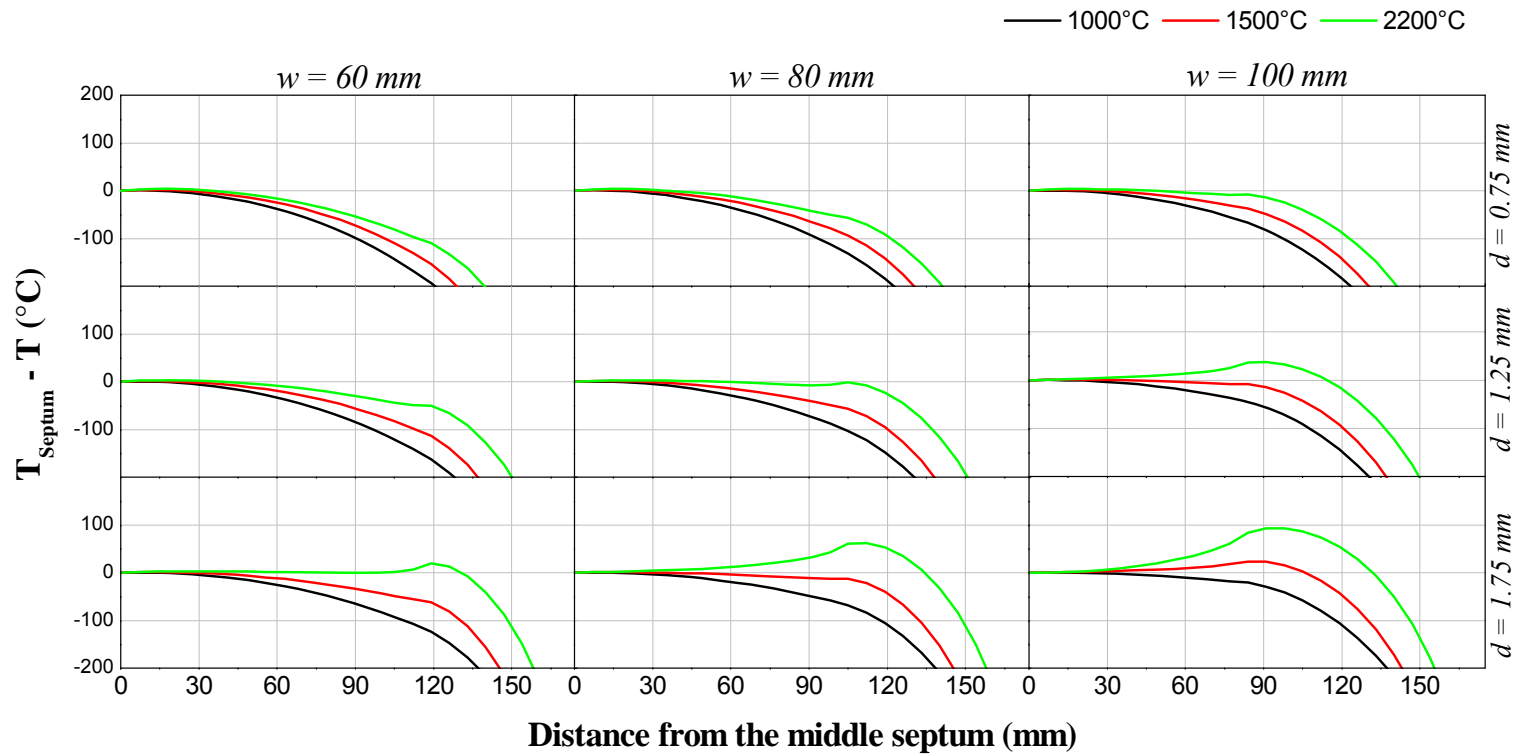
Figure 7.6. Numerical model predictions of the temperature profiles of the 400 mm long ATJ graphite tube at operating temperatures of 1000, 15000 and 2200 °C, using nitrogen as the graphite felt purging gas.

Case of 400 mm long tube with He as the felt purging gas
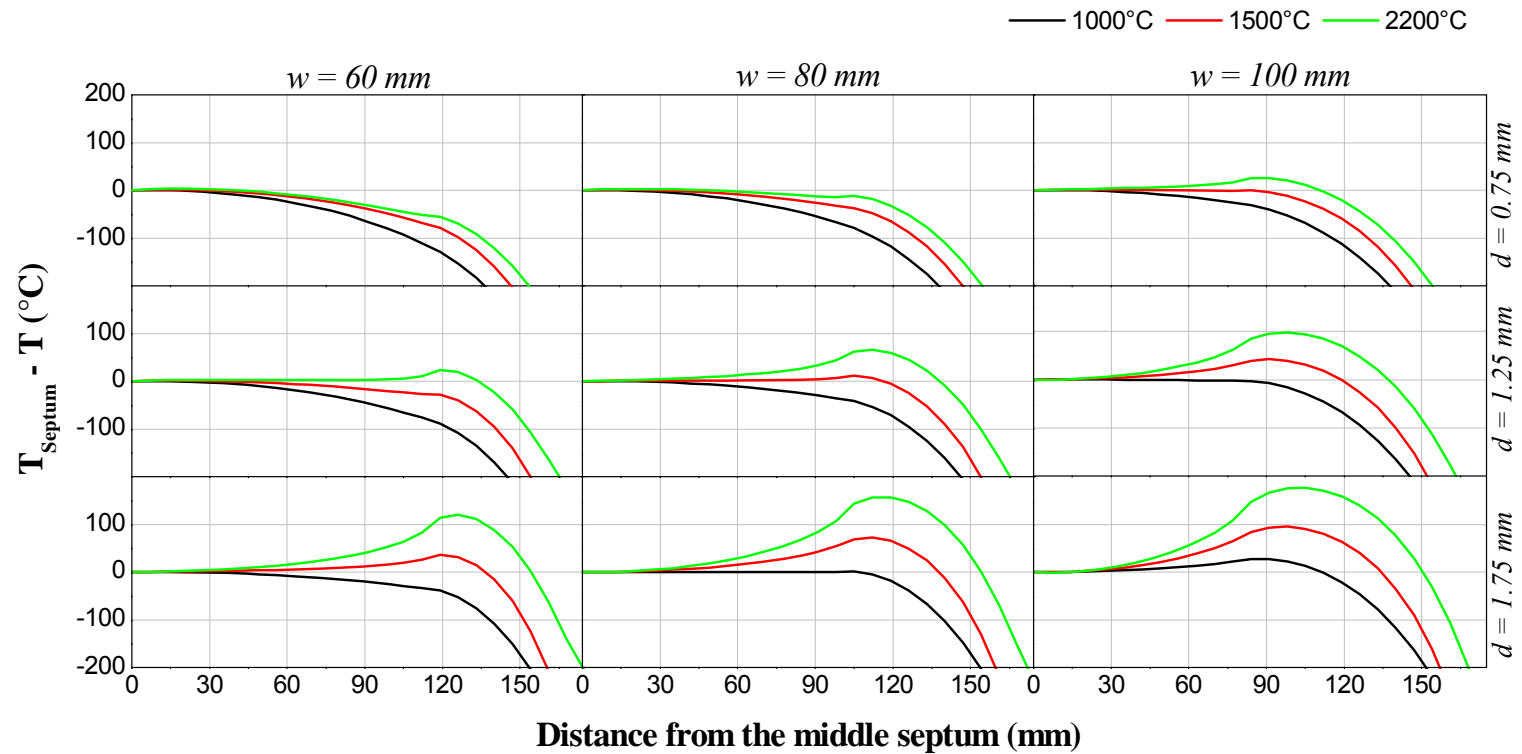
Figure 7.7. Numerical model predictions of the temperature profiles of the 400 mm long ATJ graphite tube at operating temperatures of 1 000, 1 500 and 2 200 °C, using helium as the graphite felt purging gas.

Although the aim of the work set by the present author is the optim isation of the Thermogage furnace perfor mance for tem peratures up to 1 600 °C, it is important to note tha t f uture ef forts will continue on im proving th is perf ormance f or higher temperatures. Thus, simulations are also generated for te mperatures up to 2 200 °C to allow the useability of the furnace at higher tem peratures. However, due to lim itation on the tem perature measurem ent technique s, m easurements of the tem perature profiles are only carried out at operating temperatures up to 1 600 °C.

Referring to the plots in both figures, the optimum tube design selected is for the case of an 80 mm wide and 1.25 mm 360° cut. As can be seen from thes e plots, the selection of this design is based on obtaining uniform temperature profile over a wide range of operating tem peratures, up to 2 200 °C. At an operating temperature of 1 000 °C, helium gas m ay be use d instead of nitrogen to obtain better tem perature uniformity. On the other hand, at 1 500 °C, the lower conductance nitrogen gas m ay be used instead of helium to obtain bett er temperature uniform ity. The num erical model also predicts that nitrogen can be used for optim um tem perature profile at 2 200 °C.

Based on this selection, a new ATJ graphite tube or heater el ement with a 360° cut with w=80 mm and d=1.25 mm, shown schem atically in Figure 7.8, was manufactured and installed.
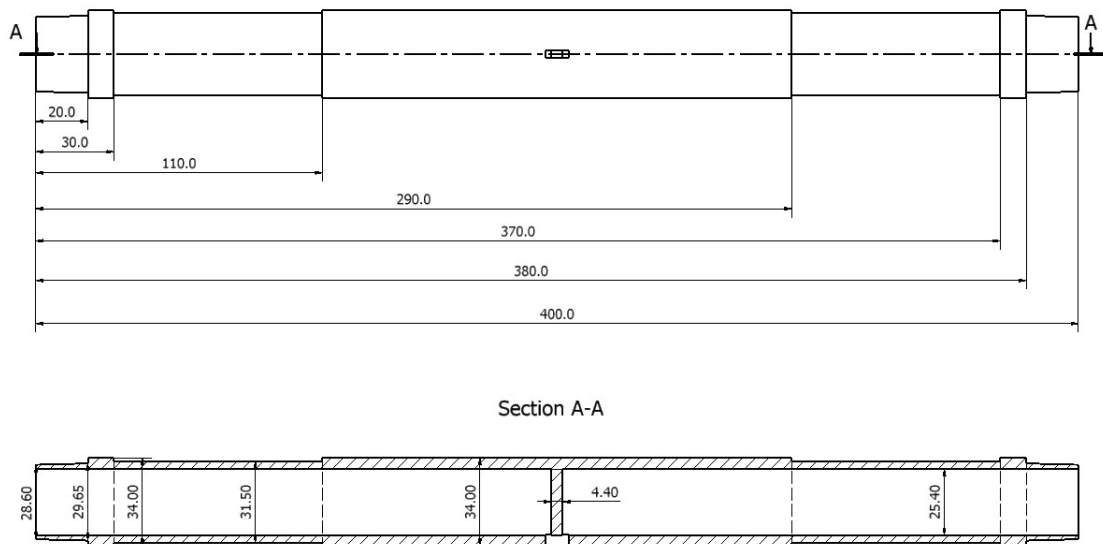
Figure 7.8. Schematic diagram of a 400 mm long ATJ graphite tube with an 80 mm wide and 1.25 mm deep cut used as the NMIA 48kW Thermogage furnace's heater element.

With the ne wly designed tube installed, m easurements of t he tem perature profiles using Pt/Pt-Rh therm ocouples at operating temperatures up to 1 500 °C were carried out. The results are presented and discussed in the next sections.

7.4 Results & Discussions

Measurements of the g raphite tube tem perature profiles were ca rried out at operating temperatures of 1 000 and 1 500 °C. Thes e m easurements were conducted with nitrogen and helium as t he graphite felt pur ging gases. The m easurements were then compared with the numerical predictions. In addition, comparisons are m ade with temperature profile m easurements of the original design of the furnace shown in Figure 7.1. The results and the numerical predictions are plotted in Figure 7.9.
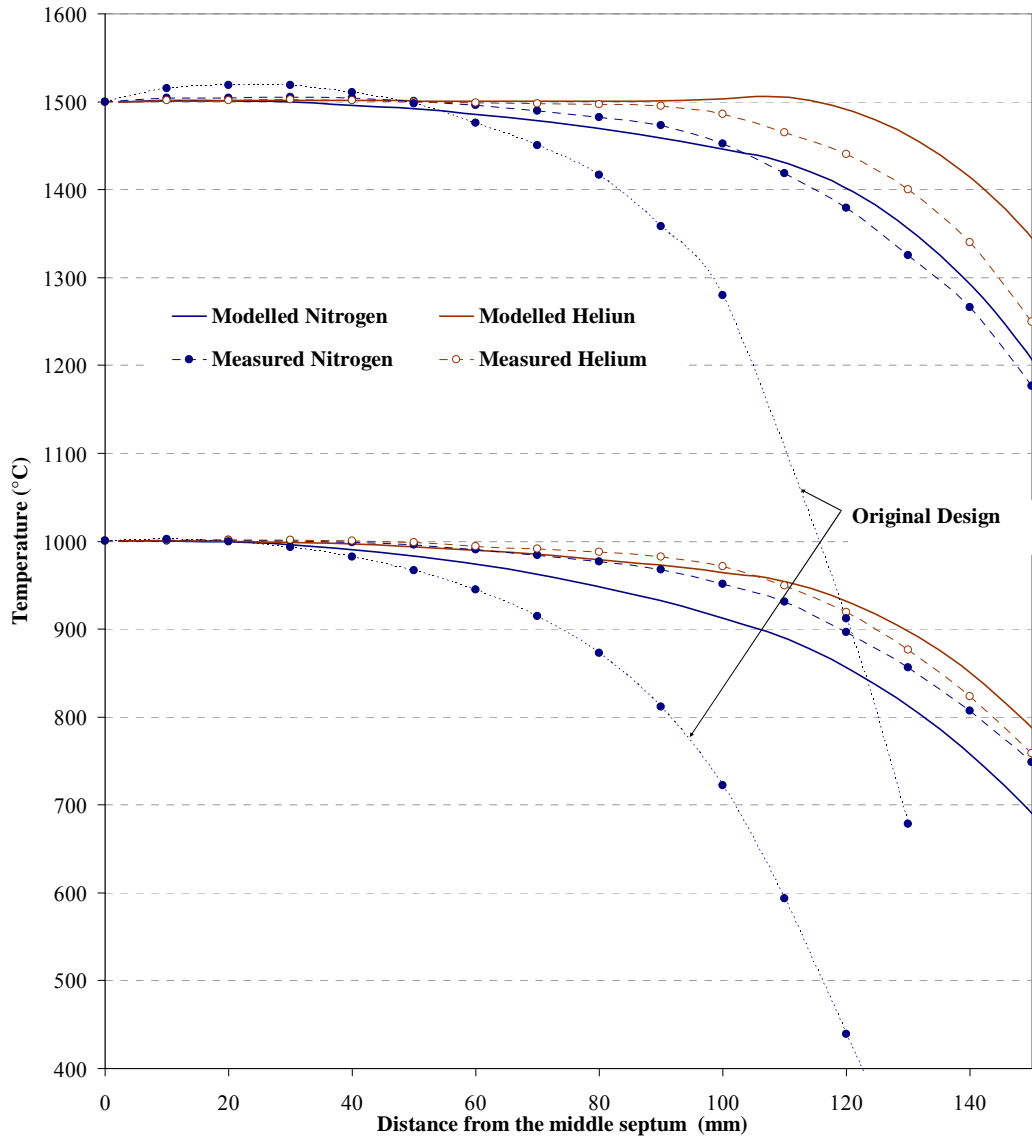
Figure 7.9. Comparison of the 400 mm long ATJ tube measured and modelled temperature profiles at 1 000 and 1 500 °C with both nitrogen and helium used as the WDF graphite felt purging gas. Comparisons are also made with the temperature profiles of the tube's original design.

As can be s een from the graphs, an incr ease is observed in the length of the tube where the tem peratures are m easured to be within 50 °C of the middle septum temperatures. At 1 000 °C, this length increases from 60 mm for the original design to more than 110 mm for the new design (t he 400 mm tube) for both cases of nitrogen and helium used as the felt purging gas. At 1 500 °C, the length of the tube with temperature within 50 °C increases to around 120 mm. Using the m easured temperature profiles together with as a value of 85 ± 5% for the emissivity of the ATJ graphite, th e cavity ef fective em issivity, ε_{eff}, is calcu lated using th e num erical

technique developed by Ballico (1998). The results are presented in Table 7.1 and compared with the effective emissivity of the original cavity. Since the use of helium gas as a "tweaking" tool to improve the uniformity of the temperature profile of the cavity is a novel idea by the present author, no values of the effective emissivity for the original tube when purged with helium could be found. Thus, comparisons of ε_{eff} are only conducted between the new design and the old design and with only nitrogen gas used as the felt purging gas.

Table 7.1. Table of the NMIA 48kW Thermogage furnace calculated cavity effective emissivities (ε_{eff}) at operating temperatures of 1 000 and 1 500 °C and for nitrogen and helium used as the WDF graphite felt purging gas.

	Original Tube Design	New Tube Design (400 mm long)	
Felt Purging Gas	Nitrogen Nitrog	en	Helium
Operating Temperature	ε_{eff}		
1000 °C	99.2 ± 0.3%	99.84 ± 0.1%	**99.98 ± 0.04%**
1500 °C	99.5 ± 0.3%	**99.97 ± 0.02%**	100.16 ± 0.1%

Using the new tube design, it can be observed from the table above that at an operating temperature of 1 000 °C and with nitrogen used as the felt purging gas the cavity effective emissivity, ε_{eff}, increased from 99.2% to 99.84%. Taking into consideration that a perfect blackbody has an effective emissivity of unity (or 100%) then this translates into a 5-fold improvement, which was calculated using the ratio of the differences (or [100%-99.2%]/[100%-99.84%]). On the other hand, ε_{eff} was improved by a factor of 40-fold when helium was used instead of nitrogen (from 99.2% to 99.98%). Similar improvements could be observed at 1 500 °C where the cavity emissivity was improved by 17-fold when nitrogen was used as the felt purging gas (from 99.5% to 99.97%). On the other hand, the results show a 100.1% emissivity when helium was used as a purging gas at an operating temperature of 1 500 °C. This was caused by the temperature "hump" near the cut in the tube (Figure 7.9).

The values of ε_{eff} in Table 7.1 can now be used to calculate the temperature uncertainty associated with using the cavity as a blackbody surface for the calibration of pyrometers. Recall that equation (1.5),

$$\frac{\Delta T}{T} = \frac{\lambda T}{C_2} \frac{\Delta \varepsilon}{\varepsilon}, (1.5)$$

could be used to com pute the relative uncertainty in temperature at a wavelength λ and an absolute tem perature T, as well as values for the re lative error in the effective emissivity $\Delta \varepsilon / \varepsilon$. The calculated values of ε_{eff} are used t o calcul ate $\Delta \varepsilon / \varepsilon$ for t he new tube design in the cases of 1 000 °C (operating tem perature) in helium gas and 1 500 °C in nitrogen to be 0.02% and 0.03% respectively. Using these values, the cavity temperature uncertainties were calcu lated, for the sa me wavelength of 650 nm, the sam e wavelength used by the NMIA's standard pyrom eters, to be 0.01 °C at 1 000 °C with helium gas and 0.02 °C at 1 500 °C with nitrogen gas. N ote that the temperature m easurement uncertainty using the original tube design is 0.6 °C at 1 000 °C and 0.7 °C at 1 500 °C (see chapter 1). As can be deduced from the uncertainties values for the orig inal and new tubes, the improvements achieved are, in the same order as ε_{eff}, 40-fold better at 1 000 °C and 17-fold at 1 500 °C.

In conclusion, the new tube design using a simple 360° cut (a diameter reduction of a width of 80 mm and a depth of 1.25 mm) along with varying the purging gas of the insulating felt from nitrogen to helium ha ve improved the perform ance of the NMIA 48kW Thermogage furnace. The m easurement uncertainties of temperatures using the NMIA 48kW Ther mogage furnace have been im proved from 0.7 °C to better than 0.02 °C for operating temperatures up to 1 600 °C. Hence, the aim of the work set in this thesis has been achieved.

In the next chapter, conclusions and recommendations arising from the work that h as been presented in this thesis are discussed.

8 CONCLUSIONS AND RECOMMENDATIONS

A new ATJ graphite tube for the NMIA's 48kW Ther mogage furnace has been designed by the present author to im prove the uncertainty of the tem perature calibration for operating te mperatures from 1 000 to 1 600 °C. The calibration uncertainty was im proved from 0.6-0.7 °C for the original tube design to better than 0.02 °C with the new one.

A survey of the available technologies used to em ulate a blackbody surface was conducted in chapter 1. As was concluded, graphite blackbody furnaces were found to be the m ost prom inent in attaining high em issivity of 0.99 or better. The different types of graphite furnaces available were also discussed, and it was found that the use of the NMI 48kW Therm ogage fur nace was a ppropriate to achieve the aim of t he research p resented h ere. It was a lso conclud ed f rom the su rvey th at by varying the area profile, as in th e case of the IK E furnace, the em issivity of the graphite furnace cavity could be improved. Furthermore, it was also deduced that this em issivity could be better improved by using different gases to purge the graphite felt used to insulate the ATJ graphite heater elem ent; the us e of different purg ing gas was a novel technique developed by the author of this thesis.

Various input param eters such as the ther mophysical properties of ATJ graphite and WDF graphite felt as f unctions of the ab solute tem peratures were needed to be investigated to be u sed in the num erical modelling of the g raphite furn ace. As was found from prelim inary investigations, the data sheet fo r the therm al conductivity of graphite felt supplied by its manufacturer was found to be in error. A literature survey was needed and therefore conducted in order to obtain better values of the therm al conductivity. In addition to th is literature survey, direct m easurements of the felt thermal conductivity were conducted at temperatures up to 1 000 °C. The results were then used to obtain an algebraic equatio n for the felt therm al conductivity as a function of the absolute temperature. This algebraic equation has m ade it possible for the first time to predict the thermal conductivity of WDF graphite felt as a function of

temperature with a relative uncertainty of 10% or less. As was concluded from the literature survey conducted, the geometrical complexity of the felt made it impossible to model the thermal conductivity from a purely deterministic point of view, and that some measurements of the thermal conductivity are always required.

In addition to the graphite felt and the ATJ graphite thermophysical properties, the numerical model developed by the author required also determinations of the carbon composite (CC) clamps thermal resistors (the ends of the ATJ graphite tube or heater element). Due to the geometric complexity of these CC clamps at both ends of the ATJ graphite tube (or the heater element), the numerical modelling of these resistors proved to be difficult. Therefore, it was decided that these special thermal resistors were to be determined experimentally. The determinations of these resistors involved direct temperature gradient measurements in order to calculate the axial heat fluxes flowing to and from these thermal resistors, as well as measuring the internal heat flux generated ohmically. On the other hand, this complexity meant that using commercial modelling packages (such as ANSYS) could add complication to the research and therefore it was decided that a simple quasi 2-D model be developed, in which the CC clamps to be modelled as special nodes.

Temperature measurement techniques, with a range up to 1 600 °C, were also developed to (i) measure the temperature gradients in order to determine the CC clamps thermal resistors, and (ii) accurately measure the graphite tube temperature profile needed in the calculation of the cavity effective emissivities, ε_{eff}. The use of conventional Pt/Pt-Rh thermocouples encased inside alumina tubes was found to have systematic errors caused by heat transfer transmission line along the thermocouple wires and alumina tube. New technique was devised using ring-shaped Pt/Pt-Rh thermocouples to minimise transmission line effects. The systematic errors using this new technique were determined. Furthermore, the new technique was validated against a novel method that involved the use of bent optical fibre to measure the surface temperature of the cavity inner walls. This technique of using a ring-shaped thermocouple wire made it possible for the first time to accurately measure the temperatures of the inner walls of the ATJ graphite tube cavity. Similarly to the case

of the ATJ graphite tube, this technique can also be used to m easure temperatures of surfaces with challenging geometries.

Having developed precise techniques to be used in the temperature measurements, the next stage of the works presented in this thesis dealt with the experimental apparatus used in the validation of the numerical m odel. The exp erimental ap paratus was validated by conducting heat balance measurements; by measuring and comparing the electrically generated h eat by the ATJ graphite with the dis sipated heat transfer rates from it. When heat balance measurements on the "short tube" were carried out, it w as found that improvem ents were needed on th e experimental apparatus. Improvem ents on the experim ental apparatus and the cons truction of a ne w gr aphite tube, "long tube", resulted in better heat balance agr eements between the i nput and output heat fluxes. The uncertainties of the heat transf er rate m easurements were als o evaluated. As could be concluded from the results, th e modified ap paratus could be used to measure heat rates an d conduct energy balance check within th e acceptable uncertainties. Most im portantly, by being able to m easure and quan tify the heat ra tes in the radial and axial direction, it was possible to confirm the assumptions m ade during the developm ent of the quasi 2-D numerical m odel; one dim ensional heat transfer radially through the felt and axially along the graphite tube.

In conclusion, the main accomplishment from the research work presented here is that there is now a better understa nding of the heat transfer mechanisms ass ociated with numerically m odelling the tem perature prof iles of the cavities of graphite f urnaces such as the 48kW Thermogage at NMIA. For the first time, a too l has been c reated that can be used to analyse and im prove the perfor mance of thes e furnaces, nam ely their emissivities.

With the aim set for the work presen ted herein having been achieved, it is recommended that further research work continues on the im provement of t he effective em issivity of the NMIA's 48kW Therm ogage furnace for tem peratures above 1 600 °C. Note that the m aximum operating tem perature of the furnace i s

2 700 °C. Hence, future work may focus on optimising the temperature profiles of the ATJ graphite tube from temperatures ranging from 1 600 to 2 700 °C.

For any future works to continue on the optimisation of the effective emissivity of the cavity of the Thermogage furnace for temperatures above 1 600 °C then the thermal conductivity of WDF graphite felt needs to be better determined for temperatures higher than 1 600 °C. The thermal conductivity was well determined by the present author for temperatures up to 1 600 °C. This however needs to be extended to temperatures up to 2 700 °C in order for it to be used for more accurate numerical predictions of the temperature profiles. It might also be very fruitful if an alternative material can be used instead of the WDF graphite felt. Materials such as graphite foam with known porosity and more uniform cross sectional area can be a good substitute to the WDF graphite felt. Note that the thermal conductivity of materials with uniform cross sectional areas, such as graphite foam, can be theoretically determined without the need for experimental measurements.

Furthermore, it is recommended that an axisymetric 3-D numerical model be used, instead of the current quasi 2-D presented in this work, so better prediction the temperature profile of the graphite tube can be achieved. This could enable better predictions of the temperature profiles at operating temperatures higher than 1600 °C.

REFERENCES

1. Anderson, J. D. (1995). Com   putational Fluid Dyna   mics: The Basics with Applications. Sydney, McGraw-Hill.

2. Ballico, M. J. (1996). "Modelling o f the e ffective em issivity of a grap hite tube black body." Metrologia 32: 259-265.

3. Ballico, M. J. (1998). Radiation   Therm ometry. Tem perature and Hum   idity Measurement. R. E. Bentley. Singapore, Springer-Verlag. 1: 67-97.

4. Ballico, M. (2000). "Simple technique for m   easuring the infrared em issivity of black-body radiators." Metrologia 37(4): 295-300.

5. Bankvall, C. (1973). "Heat Transfer in Fi brous Materials." J Test Eval 1(3): 235-243.

6. Bapat, S. G. (1973). "T   hermal Conductiv ity and Electrical Resistivity of Two Types of ATJ-S Graphite to 3500 Degree K." Carbon 11(5): 511-514.

7. Bapat, S. G. and H. Nickel (1973).   "Thermal Conductivity and Electrical Resistivity of Poco Gr ade Axf-Q1 Gr aphite to 3300 Degree K." Carbon 11(4): 323-327.

8. Barr, E. S. (1960). "Histori cal Survey of the E arly De velopment of the Infrared Spectral Region." American Journal of Physics 28: 42-54.

9. Bartell, F. O. (1989). "Blackbody, a Blackbody Sim ulator, a Blackbody Simulator Cavity, a Blackbody Simulator Cavity Aperture, and a Blackbody Sim   ulator Aperture are Each Different from   On e Another." Proceed ings of SPI E - The International Society for Optical Engineering 1110: 183-188.

10. Bardon, J.-P. and F. Danes (1994). "Heat transfer by solid conduction in a felt made of carbon fibre." High Temperatures - High Pressures 26: 323-330.

11. Bedford, R. E. and C. K. Ma (1975). "Emissivities of diffuse cavities. II: Isothermal and nonisothermal cylindro-cones." J. Opt. Soc. Am. 65: 565-575.

12. Birkebak, R. and E. Ozil (1979). Theoretical Consideration of Radiative Conductivities in Fibrous Insulation. Studies in Heat Transfer. E. R. G. Eckert and J. P. Hartnett. New York, McGraw Hill**:** 409-418.

13. Bridges, J. M. and W. R. Ott (1977). "Vacuum Ultraviolet Radiometry Em Dash 3. The Argon Mini-Arc As A New Secondary Standard Of Spectral Radiance." Appl Opt 16(2): 367-376.

14. Chahine, K., M. J. Ballico, J. Reizes and J. Madadnia (2005a). Temperature Profile Measurement of a Graphite Tube Furnace Using Optical Fibre and Platinum Thermocouples. Metrological Society of Australia, Canberra.

15. Chahine, K., M. J. Ballico, J. Reizes and J. Madadnia (2005b). Thermal Conductivity of Graphite Felt at High Temperatures. The 8th Australasia Heat and Mass Transfer Conference, Perth.

16. Chahine, K., M. J. Ballico, J. Reizes and J. Madadnia (2007). "A Simple Quasi-2D Numerical Model of a Thermogage Furnace." International Journal of Thermophysics 28(6): 2118-2127.

17. Chahine, K., M. J. Ballico, J. Reizes and J. Madadnia (2008). "Optimization of a Graphite Tube Blackbody Heater for a Thermogage Furnace." International Journal of Thermophysics 29(1): 386-394.

18. Cheng, D. K. (1983). Field and wave electromagnetics. Reading, Massachusetts, Addison Wesley.

19. Christopoulos, C. (1995). The transm ission-line m odeling m ethod : TLM. Ne w York, Institute of Electrical and Electronics Engineers ; Oxford University Press.

20. DITR. (2007). "National Meas   urement Institu te - Hom   e." 2007, from www.nmi.gov.au.

21. Bridges, J. M. and W . R. Ott (1977). "V acuum Ultraviolet Radiom etry Em Dash 3. The Argon Mini-Arc as a New Secondary Standard of Spectral Radiance." Appl Opt 16(2): 367-376.

22. Danes, F. and J.-P. Bardon (1997). "T   hermal conductivity of the carbon felts, strongly anisotropic insulants: m   odelling of heat conduction by solid phase." Revue Generale de Thermique 36(4): 302-311.

23. de Vahl Davis, G. (1983). Natural convection of air in a square cavity: an accurate numerical solution. Internat ional Journal for Num erical Methods in Fluids **3**(3): 249-264.

24. DeWitt, D. P. and G. D. Nutter (1988). Theory and practice of radiation thermometry. New York, John Wiley & Sons.

25. Dorf, R. C. (2000). The electrical engineering handbook. Boca Raton, CRC Press.

26. Hager, N. E. and R. C. Steere (1967). "R adiant Heat Transfer in Fibrous Thermal Insulation." Journal of Applied Physics 38(12): 4663-9.

27. Hattenburg, A. T. (1967). "Spectral radian   ce of a low current graphite arc." Applied Optics 6(1): 95-100.

28. Ho, C. Y., R. W. Powell, et al. (1968). Thermal conductivity of selected materials. National standard reference data series (Part 2). Washington, D.C. USGPO, 1966-1968. 2: 146.

29. Horn, T. J. and A. N. Abdelmessih (2000). Experiment al and Num erical Characterization of a Steady-S tate Cy lindrical Blackbody Cavity at 1100 °C, NASA Dryden Flight Research Center.

30. Incropera, F. P. and D. P. DeWitt (2002). Fundamentals of heat and mass transfer. New York, Wiley.

31. ISO (1993). Guide to the Expression of Uncertainty in Measurement, International Organisation for Standardisation.

32. Jones, T. P. and J. Tapping (1971). "The Suitability of Vacuum Tungsten Blackbody Lam ps as Secondary S tandard S ources in Photoelectric Pyrom etry." Metrologia 7(2): 45-49.

33. Jones, T. P. and J. Tapping (1972). "The Realization of the IPTS68 above 1064.43 °C Using the NSL Photoelectric Pyrometer." Metrologia 8: 4-11.

34. Key, P. J. and R. C. Preston (1977). "V acuum Ultraviolet Ra diation Scales: An Accurate Com parison Between Plas ma blackbody Lines and Synchrotron Radiation." Appl Opt 16(9): 2477-2485.

35. Kinchin, G. H. (1953). "The Electrical Porper ties of Graphite." Proceedings of the Royal Society of London A217: 9-26.

36. Lutkov, A. I., G. N. Za v'yalova, et al . (1975). "Therm al Conductivity of Carbon Felt and Lamp Black." High Temp 13(6): 1104-1107.

37. Mantell, C. L. (1968). Carbon and gr aphite handbook. Ne w York,, Interscience Publishers.

38. McEvoy, H. C., K. M. Raven, et al . (1996). NPL-VNIIM INTERCOM PARISON OF T UNGSTEN RIB BON LAM PS. TEMPMEKO ' 96 - 6th Symposium on Temperature and Thermal Measurement in Industry and Science, Torino, Italy.

39. Ogarev, S. A., B. B. Khlevnoy, et al. (2004). NEW HIGH-TEMPERATURE PYROLITIC BLACKBODY SOURCES FOR PRECISION MEASUREMENTS IN RADIATION THERMOMETRY. TEMPM EKO 2004 - 9th Sym posium on Temperature and Therm al Measurem ents in Industry and Science, Cavtat-Dubrovnik, Croatia.

40. Pratt, A. W. (1969). "Heat Transm ission in Low Conductivity Materials." Thermal Conductivity. R. P. Tye. London ; New York, Academic P. 1: 301- 405.

41. Raithby, G. D. and K. G. T. Hollands (1998). Natural Convection. Handbook of Heat Transfer Fundamentals. W. M. Rohsenow, J. P. Hartnett and Y. I. Cho. New York, McGraw-Hill.

42. Rasor, N. S. and J. D. McClelland (1960). "Therm al Properties of Graphite, Molybdenum and Tantalum to their Destru ction Tem peratures." J. Phys. Chem. Solids 15: 17 - 26.

43. Reynolds, W. N. (1968). Physical propertie s of graphite. Am sterdam, New Yor k [etc.], Elsevier Pub. Co.

44. Roache, P. J. (1998). Fundamentals of com putational fluid dynam ics. Albuquerque, N.M, Hermosa Publishers.

45. Sapritsky, V. I. and A. V. Prokhorov (1995). "Spectral effective em issivities of non-isothermal cavities calculated by th e Monte Carlo m ethod." Applied Optics 34(25): 5645-5652.

46. Sapritsky, V. I. (1996). "Black-body radiometry." Metrologia 32: 411-417.

47. Sapritsky, V. I., B. B. K hlevnoy, et al . (1997). "Precision blackbody sources for radiometric standards." Applied Optics 36(22): 5403-5408.

48. Sapritsky, V. I., B. B. Kh levnoy, et al. (2003). High Temperature F ixed-Point Blackbodies Based on Metal-Carbon Eutect ics for Precision Measurem ents in Radiometry, Photom etry and Radia tion Thermom etry. TEMPERATURE: Its Measurement and Control in S cience and Industry; Volum e VI I; Eighth Temperature Symposium, Chicago, Illinois (USA), AIP.

49. Sapritsky, V. I., S. A. Ogarev, et al. (2003). "Development of m etal-carbon high-temperature fixed-point blackbodies for precision photometry and radiom etry." Metrologia 40(1 SPEC.): S128-S131.

50. Sapritsky, V. L., B. B. Khlevnoy, et al. (2005). "New high-tem perature variable-temperature and fixed-point blackbodies fo r precision m easurements in radiation thermometry and radiom etry." MAPAN-J ournal of Metrology Society of India 20(2): 193.

51. Sasajima, N., Y. Ya mada, et al. (2001). Melting and Freezing Behavior of Metal-Carbon Eutectic Fixed-Point Blackbodi es. 8th International Sym posium on Temperature and Therm al Measurem ents in Industry and Science, Berlin, Germany, VDE VERLAG GMBH.

52. Saunders, R. D., C. E. Gibson, et al. (1996). "Results of a NIST/VNIIOFI comparison of spectral-radiance measurements." Metrologia 32(6 May): 449-453.

53. Schneider, A. (1998). Therm al C onduction. Te mperature and Hum idity Measurement. R. E. Bentley. Singapore, Springer-Verlag. 1: 163-183.

54. Siegel, R. and J. R. H owell (2002). Th ermal radiation heat transfer. London, Taylor & Francis.

55. Strong, H. M., F. P. Bundy, *et al*. (1960). "Flat Panel Vacuum Therm al Insulation." Journal of Applied Physics 31(1): 39 - 50.

56. Taylor, R. E. (1972). Thermophysical Properties of ATJS Graphite. West Lafayette, Purdue University, Indiana, USA.

57. Taylor, R., S. P. Turner, et al. (1993). "Thermal conductivity of carbon fibres." High Temperatures - High Pressures 25: 443 - 450.

58. Tong, T. W. and C. L. Tien (1980). "Analytical models for thermal radiation in fibrous insulations." Journal of Thermal Insulation 4: 27.

59. Tong, T. W., Q. S. Yang, *et al.* (1981). "Radiative Heat Transfer in Fibrous Insulations - 2. Experimental Study." American Society of Mechanical Engineers (Paper)(81-HT-43): 7-7.

60. Tong, T. W., C. L. Tien, *et al.* (1983). "Radiative Heat Transfer in Fibrous Insulations - 1. Analytical Study." Journal of Heat Transfer, Transactions ASME 105(1): 70-81.

61. Touloukian, Y. S. (1970). Thermal conductivity: metallic elements and alloys. New York, IFI/Plenum.

62. Touloukian, Y. S. (1970). Thermal conductivity: nonmetallic solids. New York, IFI/Plenum.

63. Tyler, W. W. and A. C. Wilson (1953). "Thermal Conductivity, Electrical Resistivity, and Thermoelectric Power of Graphite." Physical Review 89(4): 870-875.

64. Union Carbide International Company. (1964). The industrial graphite engineering handbook. New York, Union Carbide International Company.

65. Uny, G. (1986). Modelisation du Transfert Couple Rayonnement-Convection au Sein de materiaux Poreux et Identifications de leurs Properietes Radiatives.

Application aux Lain es de Verre.   Lyon, L' Institut National des   Sciences Appliquees de Lyon**:** 130.

66. Vargaftik, N. B. (1983). Handbook of physi cal properties of liquids and gases : pure substances and mixtures. Washington, Hemisphere Pub. Corp.

67. Verschoor, J. D., P. Greebler, *et al*. (1951). "Heat transfer by gas conduction and radiation in fibrous insulations." The Am erican Society of Mechanical Engineers, Atlantic City, USA, ASME.

68. Yamada, Y., N. Sasajim a, et al. (2003) . High-Tem perature Furnace Sy stems for Realizing Meta l-Carbon Eutectic   Fixed Points. TE   MPERATURE: Its Measurement and Control in S   cience   and Industry; Volum   e VI I; Eighth Temperature Symposium, Chicago, Illinois (USA), AIP.

APPENDIX A

Measurement of the Fibre Radius of the WDF Graphite Felt, r

The average fibre radius, r, of the WDF graphite felt was measured by the present author at the NMIA using a projector magnifier. Measurements of the fibre diameters were conducted on 13 fibre samples, which were picked randomly from one piece of WDF graphite felt. These measurements were then used to calculate the arithmetic average of the fibre radius. These measurements are presented in Table A.1.

Table A.1. Measurements of the diameters of WDF graphite felt fibres using a projector magnifier.

Sample Number	Measured Fibre Diameter (μm)	Calculated Fibre Radius, r (μm)
1	23.3	11.7
2	22.6	11.3
3	22.5	11.3
4	27.5	13.8
5	15.5	7.8
6	25.3	12.7
7	17.3	8.7
8	20.2	10.1
9	19.8	9.9
10	18.7	9.4
11	20.1	10.1
12	20.3	10.2
13	21.1	10.6

As may be seen from the measurements, the radii of the fibres vary from 7 to 13 μm. The arithmetic average of these measurements is calculated to be r=10.5 μm with a standard deviation of 3.2 μm.

The measurement uncertainty of the diameter measurements associated with using a projector magnifier should be better than 0.1 μm. However, as it can be seen from the large standard deviation of the measurements in Table A.1, this uncertainty is too small and can be ignored.

Measurement of the Density of the WDF Graphite Felt, ρ_{felt}

The density of the WDF graphite felt, ρ_{felt}, was calculated from measurements of the weight, w_{felt}, and volume, V_{felt}, of a piece of WDF graphite felt. This can be mathematically expressed as,

$$\rho_{felt} = \frac{w_{felt}}{V_{felt}}$$

(A.1)

To measure V_{felt}, firstly the thickness of a piece of WDF graphite felt, t_{felt}, with finely cut edges was measured, using a vernier scale, to be 5.84 mm with a standard deviation of 0.02 mm. Secondly, the felt sample area, A_{felt}, was to be measured. This was done by having the profile of the sample drawn on an A4 sized paper; A4 size paper has an area of A_{A4}=210×297 mm². Based on the assumption that all commercially produced A4 paper have a uniform thickness with minim variation, the A4 paper was firstly weighed five times and the measurements showed w_{A4}=5.104 g with a standard deviation of 0.002 g. Then, the paper was cut along the profile of the felt sample used. This profile section was then weighed five times and the measurement showed an average value for w_{cut} to be 0.352 g with a standard deviation of 0.002 g. Using the above measurements, the area of the felt may be calculated using the equation,

$$A_{felt} = \frac{w_{cut}}{w_{A4}} A_{A4} \, ,$$

(A.2)

and hence the volume of the felt can then be determined using,

$$V_{felt} = t_{felt} A_{felt}$$

(A.3)

The felt sample weight w_{felt} was measured using a high precision Sartorius balance to be 2.052 g.

Using equations (A.1-3) and the above measurements, the density of the WDF, ρ_{felt}, felt is calculated to be 80 kg·m³. The main component of uncertainty in this measurement would be caused by the fineness of the felt sample edges. Best efforts were made to ensure the sample has fine edges in order to minimise any significant contribution to the total uncertainty. Upon visual inspection by the present author, it could be safely assumed that these edges did not contribute more than 0.5% to the total uncertainty in ρ_{felt}. A 1% value for the measurement uncertainty of ρ_{felt} is considered to be acceptable.

Calculation of the volume fraction, f

Having determined the density of the graphite felt, the volume fraction of the graphite can now be calculated. The bulk density of the graphite fibres was obtained from the literature as between 1 500 and 1 770 kg·m^{-3} (Mantell 1968). The volume fraction, f, of the felt is defined as the ratio of the felt density, therefore f is calculated to be between 4.5% and 5.5%. For the works presented here, a value of 5% for f is assumed.

The measurement uncertainty of f consists of the measurement uncertainties of ρ_{felt} and the bulk density of graphite fibres, given as 1% (see above) and 2% (Mantell 1968) respectively. This gives a total uncertainty of 2.2% for f.

APPENDIX B

Measurements of the heat transfer rates of the ATJ graphite tube discussed in chapter 4 are presented in this section. Two sets of measurements were conducted using the "short" and "long" tubes described in section 4.2. Detailed descriptions of these measurements are presented next.

Measurements on the Short Tube

In order to calculate the electrical power generated by the ATJ graphite tube, measurements of the electrical current (I_{RMS}) were conducted using a (1000:1) current transformer. The voltage on the inside of the graphite tube (V_{in}) was measured using HP34401A-voltmeter. These measurements were repeated over a range of operating temperatures of the Thermogage furnace (which are also the middle septum temperatures) of 1 000, 1 200, 1 400, 1 500 and 1 700 °C with the graphite felt purged with nitrogen. Using these values of I_{RMS} and V_{in} and equation (4.2), $P_{electrical}$ was then calculated with the results presented in Table B.1.

Table B.1. List of the measurements of the current I_{RMS}, the inside voltage V_{in} and the calculated values of $P_{electrical}$ at operating temperatures of 1 000, 1 200, 1 400, 1 500 and 1 700 °C with the graphite felt purged with nitrogen.

Operating Temperature	I_{RMS}	V_{in}	$P_{electrical}$
(°C)	(A)	(VAC)	(W)
1 000	368.7	2.609	962
1 200	401.0	3.078	1 234
1 400	430.7	3.612	1 556
1 500	445.4	3.913	1 743
1 700	475.8	4.580	2 179

The heat transfer rate by radiation ($P_{radiation}$) from the inside of the graphite tube to the environment was calculated using equation (4.3) and measurements of the temperature profile of the graphite tube at 1 000 and 1 500 °C (see Figure 4.3); these were the only available measurements of the temperature profile of the "short"

graphite tube at the time of writing this thesis. It is important to point to the reader's attention that since the CC clamps are to be excluded from the numerical model then the environment is considered as the opening at the distance where these clamps are located. For the "short" tube, this distance is 117.5 m, while it is 167.8 mm for the "long" tube. On the other hand, the view factors (F_{ia} and F_{sa}) in equation (4.3) were calculated using (Siegel & Howell 2002, p. 845 and p. 848),

$$F_{ia} = \frac{X_{ia}^2 + \frac{1}{2}}{\sqrt{X_{ia}^2 + 1}} - X_{ia}, \text{ and} \qquad (B.1)$$

$$F_{sa} = \frac{1}{2}\left[X_{sa} - \sqrt{X_{sa}^2 - 4}\right], \qquad (B.2)$$

with

$$X_{ia} = \frac{x_{ia}}{2r}, \text{ and} \qquad (B.3)$$

$$X_{sa} = \frac{x_{sa}}{2r}. \qquad (B.4)$$

Here r is the inner diameter of the graphite tube (25.4 mm), x_{ia} is the distance between the ring i and the opening at the end of the graphite tube, while x_{sa} is the distance between the middle septum of the graphite tube and the outside environment (note that the distance is taken to be 117.5 mm for the "short" tube). Values of $P_{radiation}$ were calculated at operating temperatures of 1 000 and 1 500 °C, which were the two temperatures at which temperature profiles of the graphite tube were measured. These values were then used to interpolate for $P_{radiation}$ at operating temperatures of 1 200 and 1 400 °C and extrapolate for 1 700 °C with the results presented in Table B.2.

Table B.2. List of the calculated values of $P_{radiation}$ at operating temperatures varying from 1 000 to 1 700 °C with the graphite felt purged with nitrogen.

Operating Temperature	$2 \times P_{radiation}$
(°C)	(W)
1 000	8
1 200	18
1 400	27
1 500	32
1 700	42

Note that the values of $P_{radiation}$ were multiplied by two in order to take account of heat transfer rate by radiation at both ends of the graphite tube.

In order to calculate the heat transfer rate by conduction along the ATJ graphite tube ($P_{conduction}$), the temperature gradients ($\delta T/\delta x$) needed to be measured. The temperatures of the inner wall of the grahite tube were measured at distances of 100, 105, 110, 120, and 125 mm from the middle septum. The results are presented in Table B.3

Table B.3. Measurements of the inner wall of the ATJ graphite tube at various distances from the middle septum and at different operating temperatures of the Thermogage furnace at NMI.

Position from middle the septum	100 mm	105 mm	110 mm	115 mm	120 mm	125 mm
Operating Temperature	Temperature of the ATJ Graphite Wall (°C)					
1 000 °C	801	748	688	627	568	494
1 200 °C	988	925	853	775	702	609
1 400 °C	1 188	1 125	1 046	949	859	746
1 500 °C	1 291	1 223	1 138	1 035	943	819
1 700 °C	1 469	1 405	1 342	1 241	1 127	990

Using the measurements, temperatures of the inner wall of the graphite tube were then calculated at a distance of 117.5 mm from the middle septum (the location of the CC clamps). These temperatures were used in the calculation of the temperature gradients ($\delta T/\delta x$). Note that temperature measurements at 115 and 120 mm from the middle septum were used in interpolating for temperatures at 117.5 mm. and the results are presented in Table B.4

The cross sectional area of the graphite tube (A_c) was calculated to be 2.0015×10^{-4} m², and values of the thermal conductivity of ATJ graphite (k_{ATJ}) were obtained from chapter 2. Equation (4.4) was then used to calculate $P_{condcution}$ and the results are presented in Table B.4.

Table B.4. List of the calculated temperature gradients ($\delta T/\delta x$), thermal conductivity of graphite felt (k_{ATJ}) and the calculate $P_{conduction}$ at operating temperatures varying from 1 000 °C to 1 700 °C.

Operating Temperature	$\delta T/\delta x$	k_{ATJ}	$2 \times P_{conduction}$
(°C)	(°C·mm^{-1})	(W·m^{-1}·K^{-1})	(W)
1 000	14.8	65	385
1 200	18.5	58	432
1 400	22.7	52	471
1 500	24.9	49	488
1 700	27.3	44	480

Similar to $P_{radiation}$, values of $P_{conduction}$ above were multiplied also by two to take account of the heat transfer rates at both ends of the graphite tube.

According to equation (4.5), P_{radial} is calculated using measurements of the volumetric flow rate of water (V_{water}) and the temperature rise (ΔT_{water}), as well as the specific heat of water ($C_{p_{water}}$ =4 186 J·kg^{-1}·K^{-1}) and the density of water at 15 °C ($\rho_{water_{15°C}}$ =1 000 kg·m^{-3}).

On the other hand, V_{water} was measured using a timer and a calibrated domestic flowmeter. The time needed for a specified volume of water (between 5 and 20 L) to pass through the meter was recorded and used to calculate the volumetric flowrate. These measurements were repeated several times during the testings and the average value was found to be 4.16 L·min^{-1}, note that the standard deviation of the readings of the volumetric flowrate was calculated to be less than 0.22%, it can therefore be deduced that the fluctuation of these readings is small and will not significantly contribute to the uncertainty of the measurement of the flowrate.

The *emf* voltage of the K-Type differential thermocouple, which is used to measure the temperature rise of the water (ΔT_{water}), was measured at the above mentioned operating temperatures using a high accuracy HP3458A-voltmeter. Note that, for a K-type thermocouple, the measured *emf* voltages are converted into temperatures by dividing them by 40.3 $\mu V \cdot C^{-1}$. Using equation (4.5) and the above values, P_{radial} was calculated and the results are presented in Table B.5.

Table B.5. List of the calculated temperature gradients ($\partial T/\partial x$), thermal conductivity of graphite felt (k_{ATJ}) and the calculate $P_{conduction}$ at operating temperatures varying from 1 000 °C to 1 700 °C.

Operating Temperature	ΔT_{water}	P_{radial}
(°C)	(°C)	(W)
1 000	1.38	402
1 200	1.95	568
1 400	2.71	786
1 500	3.20	931
1 700	4.35	1 262

Values of the calculated heat transfer rates ($P_{electrical}$, $P_{radiation}$, $P_{conduction}$ and P_{radial}) obtained above can now be used to conduct a heat balance check and calculate the difference between the heat transfer rate going in the system ($P_{electrical}$) and the total heat transfer rate going out of the system ($P_{radiation}+P_{conduction}+P_{radial}$). The results of this comparison can be seen in Table B.6.

Table B.6. Results of the comparison between $P_{electrical}$ and $P_{radiation}+P_{conduction}+P_{radial}$.

Operating Temperature	$P_{electrical}$	$P_{radiation}+P_{conduction}+P_{radial}$	Difference	
(°C)	(W)	(W)	(W)	(%)
1 000	962	795	167	17
1 200	1 234	1 017	217	18
1 400	1 556	1 284	272	18
1 500	1 743	1 451	292	17
1 700	2 179	1 784	396	18

Measurements on the Long Tube

Similar to the previous section, measurements were also carried out on the "long" tube but at operating temperatures of 1 000, 1 200, 1 400 and 1 600 °C with nitrogen used as the graphite felt purging gas. In addition, it is important to note that with the "Long" tube the CC clamps are located at a distance of 167.8 mm from its middle septum. Another difference to the previous section is that the temperature profiles for the "long" tube were measured at each of the above mentioned operating temperatures and were directly used in the calculations of $P_{radiation}$ (see section 4.3.2). Similar to the results shown in Tables B.1-6, Tables B.7-12 below present the results of the measurements conducted on the "long" tube.

Table B.7. List of the measurements of the current I_{RMS}, the inside voltage V_{in} and the calculated values of $P_{electrical}$ at operating temperatures of 1 000, 1 200, 1 400 and 1 600 °C with the graphite felt purged with nitrogen (long tube).

Operating Temperature	I_{RMS}	V_{in}	$P_{electrical}$
(°C)	(A)	(VAC)	(W)
1 000	368.6	2.620	966
1 200	406.8	3.076	1 251
1 400	441.6	3.600	1 590
1 600	475.8	4.236	2 015

Table B.8. List of the calculated values of $P_{radiation}$ at operating temperatures varying from 1 000 to 1 700 °C with the graphite felt purged with nitrogen (long tube).

Operating Temperature	$2 \times P_{radiation}$
(°C)	(W)
1 000	4
1 200	6
1 400	11
1 600	17

Table B.9. Measurements of the inner wall of the ATJ graphite tube at various distances from the middle septum and at different operating temperatures of the Thermogage furnace at NMI (long tube).

Position from middle the septum	150 mm	160 mm	170 mm
Operating Temperature	Temperature of the ATJ Graphite Wall (°C)		
1 000 °C	774	686	583
1 200 °C	946	839	709
1 400 °C	1140	1020	869
1 600 °C	1322	1204	1026

Table B.10. List of the calculated temperature gradients ($\delta T/\delta x$), thermal conductivity of graphite felt (k_{ATJ}) and the calculate $P_{conduction}$ at operating temperatures varying from 1 000 °C to 1 600 °C (long tube).

Operating Temperature	$\delta T/\delta x$	k_{ATJ}	$2 \times P_{conduction}$
(°C)	(°C·mm^{-1})	(W·m^{-1}·K^{-1})	(W)
1 000	10.3	56	316
1 200	13.1	51	361
1 400	15.1	46	376
1 600	17.8	42	403

Table B.11. List of the calculated temperature gradients ($\delta T/\delta x$), thermal conductivity of graphite felt (k_{ATJ}) and the calculate $P_{conduction}$ at operating temperatures varying from 1 000 °C to 1 600 °C (long tube).

Operating Temperature	ΔT_{water}	P_{radial}
(°C)	(°C)	(W)
1 000	2.87	574
1 200	4.09	818
1 400	5.44	1 089
1 600	7.40	1 481

Note that the flowrate of the coolant water for the "long" tube was measured to be 2.85 L·min^{-1}.

Table B.12. Results of the comparison between $P_{electrical}$ and $P_{radiation}+P_{conduction}+P_{radial}$ (long tube).

Operating Temperature	$P_{electrical}$	$P_{radiation}+P_{conduction}+P_{radial}$	Difference	
(°C)	(W)	(W)	(W)	(%)
1 000	966	894	72	7
1 200	1 251	1186	65	5
1 400	1 590	1476	114	7
1 600	2 015	1901	114	6

APPENDIX C

In order to simplify the calculations of the radial thermal resistance in the quasi 2-D numerical model presented in chapter 5, it is recommended that the equivalent (or effective) radial thermal resistance, R_{radial}, is calculated as a function of the absolute temperature T, which is taken to be the cavity wall temperature. In this section, the calculations of R_{radial} and examples of these calculations are presented.

As described in section 3.3.1, R_{radial} consists of a series of thermal resistances, R_i, representing the graphite felt, the aluminium foils and the silica tube and the air gaps among them. In order to compute R_{radial} as a function of T, an iterative over-relaxation numerical method on $n+2$ finite elements in EXCEL is used. The analogy to electromagnetic wave theory is used to solve for the temperatures inside the felt insulation. The graphite felt insulation (including felt, graphite foils and silica tube) is equated to a series of electrical resistors R_i with an electrical current flowing through them (the electrical equivalent to heat flux). The temperature T_i, which is equivalent to the electrical voltage, can be calculated using the following equation:

$$T_i = T_o + \left(T_{WJ} - T_o\right)\frac{\displaystyle\sum_{j=1}^{i} R_j}{\displaystyle\sum_{i=1}^{n} R_i} \tag{C.1}$$

Here T_o and T_{WJ} are the ATJ graphite surface and the water jacket absolute temperatures (see Figure 5.4). Note that T_{WJ} is maintained at 15 °C (or 288.2 K) by using a heat exchanger (see chapter 4).

According to Figures 5.1 and 5.4, the thickness of the graphite felt is 14.5 mm surrounded by two 0.5 graphite foils. These are encapsulated inside 2 mm thick silica tube. A water cooled brass jacket is also constructed around the silica tube in order to (i) capture all the radial heat flux and (ii) to prevent the user from accidentally coming into contact with the silica tube hot surface (see section 5.2).

Using equations (C.1) and (5.4-11), an EXCEL spreadsheet can be constructed to iterate for values of R_{radial} for a temperature range from 22 °C to 2 200 °C. An example of this spreadsheet is given in Table C.1.

Table C.1. Example of an EXCEL spreadsheet table used in the calculation of R_{radial}, using an iterative over relaxation method on n+2 finite elements, as a function of the absolute temperature T.

Thermal Conductivity	r	k_f	k	Σk	T
	mm	$W \cdot m^{-1} \cdot K^{-1}$	$W \cdot m^{-1} \cdot K^{-1}$	$W \cdot m^{-1} \cdot K^{-1}$	K
	17	0.3 976			1 273.2 (T_{WJ})
	18	0.3 740	0.024	0.024	1 241.5
	19	0.3 514	0.024	0.047	1 209.7
	20	0.3 296	0.024	0.071	1 177.5
	21	0.3 087	0.024	0.096	1 144.9
	22	0.2 885	0.025	0.120	1 111.7
	23	0.2 690	0.025	0.146	1 077.6
Graphite Felt	24	0.2 501	0.026	0.172	1 042.6
	25	0.2 317	0.027	0.199	1 006.5
	26	0.2 139	0.028	0.227	968.9
	27	0.1 966	0.029	0.256	929.6
	28	0.1 798	0.031	0.287	888.4
	29	0.1 635	0.033	0.319	844.8
	30	0.1 477	0.035	0.354	798.3
	31	0.1 325	0.037	0.391	748.3
	31.5	0.1 177	0.041	0.432	693.7
Felt/Foils			0.041	0.473	638.1
Foils			0.009	0.483	625.5
Foils/Silica			0.048	0.531	561.2
Silica		17.0	0.0006	0.531	560.4
Water Jacket			0.2030	**0.734**	**288.2 (T_o)**

R_{Radial} (K·W^{-1}·m)=   1.362

According to the table, the graphite felt section of the insulation is divided into small layers with 1 mm thickness to ensure that the numerical iteration converges; it has been observed that a 1 mm thick layer of graphite (grid size) ensures that the numerical model is stable. Note also that the graphite thermal conductivity, which is a function of T, is calculated using equation (2.13) with C_{fr} taken as 15.0 and N_2 as the felt purging gas. Furthermore, the graphite fibre radius is measured to be 11.5 μm and the graphite volume felt is calculated from direct measurements of the felt density,

80 kg·m^{-3}, and the bulk graphite density, 1 500 kg·m^{-3}, to be 5%. These values are also in equation (2.13).

As it can be seen from for this example, the nodes thermal conductivity values are used instead of thermal resistors since these values are more readily available.

The felt/foils, foils and foils/silica sections are considered as 0.5 mm air/gas gaps between two surfaces filled with either N_2 or He. Their thermal resistances are calculated using equations (5.5a-c).

The water jacket thermal resistance, which consists of radiative and convective components, is calculated using equations (5.8-11). Values of the water jacket thermal resistances versus the silica tube surface temperatures are plotted in Figure 3.6.

The entries under the term Σk in Table C.1 denotes the aggregate sum of the thermal conductivities. For example, the value of 0.734 W·m^{-1}·K^{-1} is the sum of all the thermal conductivities, under the table entry titled k. In this case, the radial resistance R_{radial} is taken as the inverse value of 0.734 W·m^{-1}·K^{-1}, which is computed to be 1.362 K·W^{-1}·m.

Also, in the example given in Table C.1, the values for T_o and T_{WJ} are set to 15 °C (or 288.2 K) and 1 000 °C (or 1 273.2 K) consecutively. Values of R_{radial} as a function of the absolute temperature T can be obtained by varying the values of T_o from 22 °C to 2200 °C. These are calculated and plotted in Figure C.1.
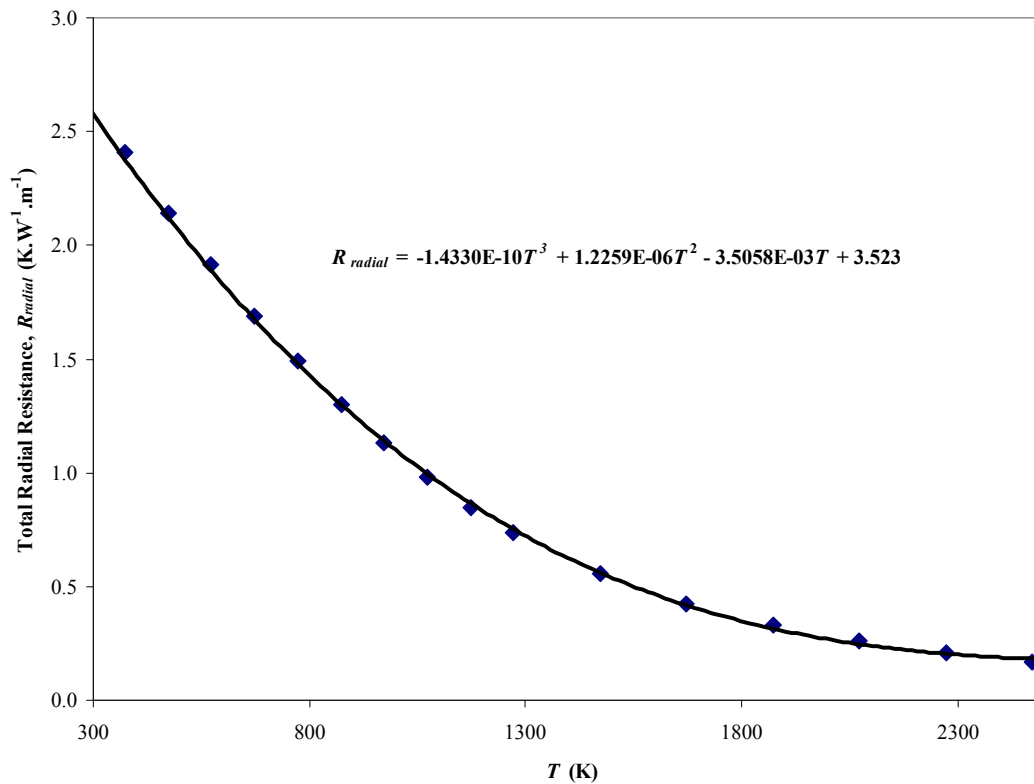
Figure C.1. Graph of the calculated values of the radial thermal resistance R_{radial} of the NMIA 48kW Thermogage furnace's insulation (felt, foils and silica tube) as a function of the absolute temperature T. The best fit curve is also plotted its equation is given.

As mentioned earlier, the values of R_{radial} plotted in the figure above are calculated for values of the graphite felt thermal conductivity with C_{fr} taken as 15 and using N_2 as the graphite felt purging gas. In the literature survey conducted by the present author in chapter 2, the values of C_{fr} was found to vary between 10 and 35. A value of 15.0 for C_{fr} was selected based on this literature survey. As mentioned earlier, equation (2.13) can be used to calculate the graphite felt thermal conductivities for a given value of C_{fr} as well as the graphite felt purging gas thermal conductivities. These gases thermal conductivities are fitted to 5th degree polynomials with their coefficients listed in Table 2.1. However, it is important to note that only values of N_2 and He are used as all measurements carried out in this work are conducted using these two gases.

It follows from the above that values of the graphite felt thermal conductivity can be generated as a function of the absolute temperature T for values of C_{fr} of 10, 15 and

35 for both cases of N_2 and He used as the felt purging gas. These values are plotted in Figure C.2.
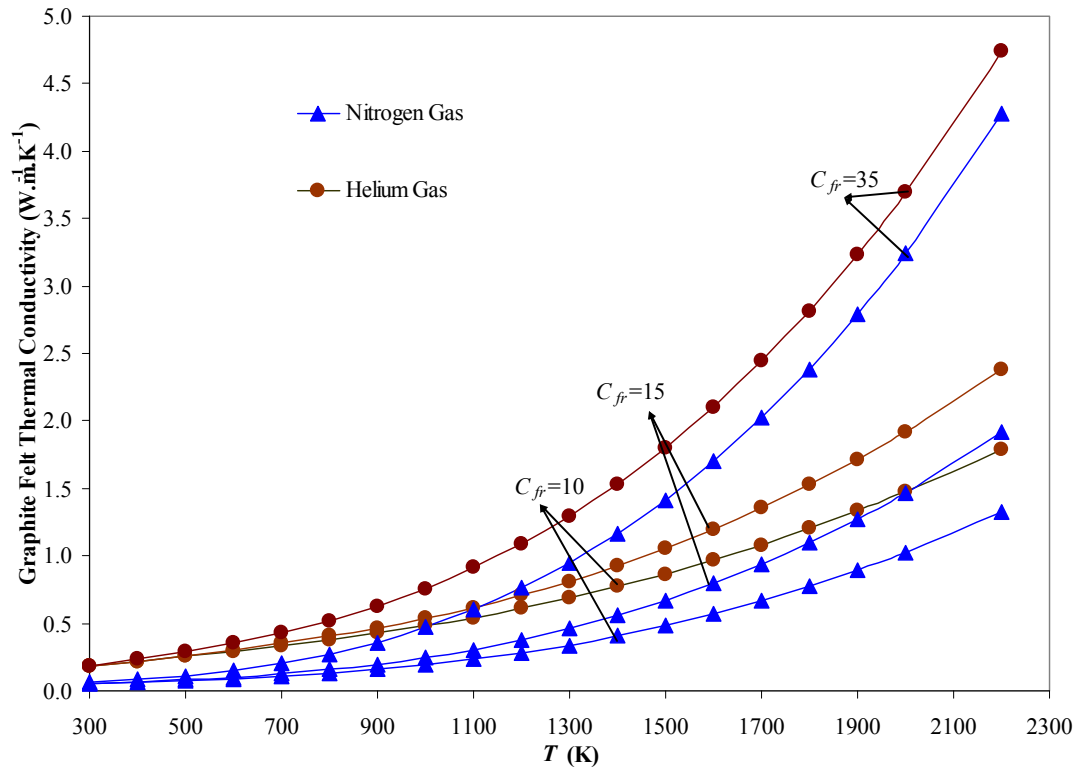
Figure C.2. Plots of the graphite felt thermal conductivity with C_{fr}=10, 15 and 35 for both cases of N_2 and He used as the felt purging versus the absolute temperature T.

The thermal conductivity values in the figure above are fitted to a 3rd degree polynomial, $k(T)=c_3T^3+c_2T^2+c_1T+c_0$, in order to be used in the calculations of the graphite felt thermal conductivities (k column). The polynomial coefficients of these fits are listed in Table C.2. Noteworthy, the residuals of these polynomial, which presents the uncertainties due their use, are less than 0.5% at all temperature ranges. These are substantially smaller than the total graphite felt thermal conductivity uncertainty, which is 10% (see section 2.1).

Table C.2. List of the 3rd degree polynomial coefficients used to calculate the graphite felt thermal conductivity k as a function of the absolute temperature T for specific values of C_{fr} and using N_2 and He as the felt purging gases.

k_{felt}	$C_{fr} = 10$		$C_{fr} = 15$		$C_{fr} = 35$	
Gas Used	N_2	He	N_2	He	N_2	He
c_3	1.0189×10^{-10}	1.0218×10^{-10}	1.5075×10^{-10}	1.5104×10^{-10}	3.9167×10^{-10}	3.9196×10^{-10}
c_2	-4.0014×10^{-9}	-4.8929×10^{-8}	-4.0014×10^{-9}	-4.8929×10^{-8}	-4.0014×10^{-9}	-4.8929×10^{-8}
c_1	4.0744×10^{-5}	3.3657×10^{-4}	4.0744×10^{-5}	3.3657×10^{-4}	4.0744×10^{-5}	3.3657×10^{-4}
c_0	4.1075×10^{-2}	8.1706×10^{-2}	4.1075×10^{-2}	8.1706×10^{-2}	4.1075×10^{-2}	8.1706×10^{-2}

Using the coefficients in the table above, values of the radial thermal resistance R_{radial} as a function of T are calculated and plotted in Figure C.3.
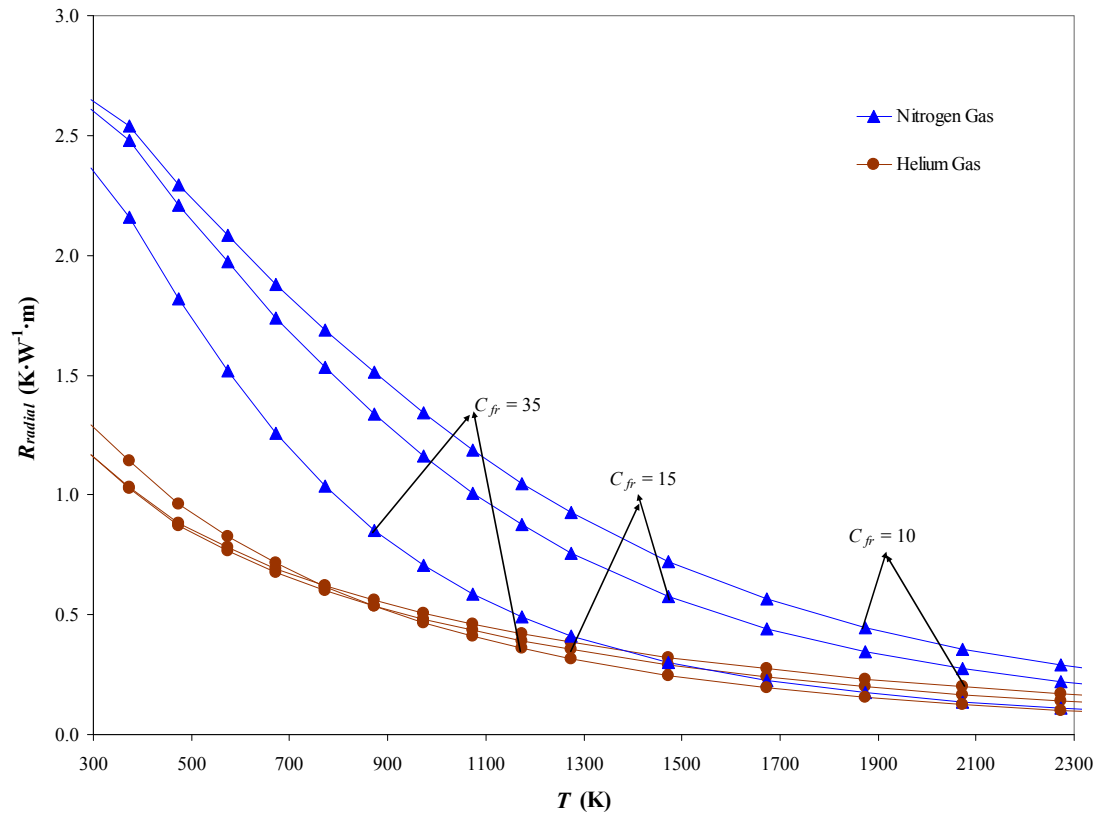

Figure C.3. Plots of total radial resistance R_{radial} versus the absolute temperature T with C_{fr} values of 10, 15 and 35 and using N_2 and He as the graphite felt purging gases.

Finally, the values of R_{radial} in the above plots can also be fitted to 3rd degree polynomial, $R_{radial}(T) = c_3 T^3 + c_2 T^2 + c_1 T + c_0$, in order to be used in the quasi 2-D

numerical model developed in chapter 2. Values of these coefficients are listed in Table C.3.

Table C.3. List of the 3rd degree polynomial coefficients used to calculate the total or effective thermal resistance R_{radial} as a function of the absolute temperature T for specific values of C_{fr} and using N$_2$ and He as the felt purging gases.

R_{radial}	$C_{fr} = 10$		$C_{fr} = 15$		$C_{fr} = 35$	
Gas Used	N$_2$	He	N$_2$	He	N$_2$	He
c_3	-6.6502×10^{-11}	-1.6535×10^{-10}	-1.5097×10^{-10}	-1.6403×10^{-10}	-4.1931×10^{-10}	-1.9895×10^{-10}
c_2	8.2965×10^{-7}	9.3588×10^{-7}	1.2761×10^{-6}	9.4446×10^{-7}	2.5085×10^{-6}	1.1692×10^{-6}
c_1	-2.9595×10^{-3}	-1.9065×10^{-3}	-3.6231×10^{-3}	-1.9494×10^{-3}	-5.1048×10^{-3}	-2.4078×10^{-3}
c_0	3.5026	1.6192	3.6312	1.6281	3.6957	1.8813

The table above summarises the polynomial coefficients used in the quasi 2-D numerical model for the graphite felt thermal conductivities. Values of C_{fr} are selected based on their relevance to the works presented in sections 2.1 and 6.4.

APPENDIX D

(Publications)

Processors note: full text removed due to copyright restrictions.

Chahine, K., Ballico, M., Reizes, J. & Madadnia, J. 2005, 'Thermal Conductivity of Graphite Felt at High Temperatures', Proceedings of 8th Australasian Heat & Mass Transfer Conference (8AHMTC), Curtin University of Technology, July 2005 in Proceedings of 8th Australasian Heat & Mass Transfer Conference (8AHMTC), ed Chandratilleke, T and Narayanaswamy, R, Curtin University of Technology, Curtin University of Technology, pp. 1-4.

Chahine, K., Ballico, M., Reizes, J. & Madadnia, J. 2005, 'Temperature Profile Measurement of a Graphite Tube Furnace Using Optical Fibre and Platinum Thermocouples', Metrology Society of Australia's Biennial Conference (MSA), ACT, Australia, October 2005 in Proceedings of Metrology Society of Australia's 6th Bienial Conferene (MSA), ed N/A, Australian National University (ANU), Canberra, Australia, pp. 163-168.

Chahine, K., Ballico, M., Reizes, J. & Madadnia, J. 2007, 'A Simple Quasi-2D Numerical Model of a Thermogage Furnace', International Journal of Thermophysics, vol. 28, no. 6, pp. 2118-2127.